Nuclear Schiff Moment Search in Thallium Fluoride Molecular Beam: Rotational Cooling

Konrad Wenz

Submitted in partial fulfillment of the
requirements for the degree of
Doctor of Philosophy
under the Executive Committee
of the Graduate School of Arts and Sciences

COLUMBIA UNIVERSITY

2021

ABSTRACT

Nuclear Schiff Moment Search in Thallium Fluoride Molecular Beam: Rotational Cooling

Konrad Wenz

The search for physics beyond the Standard Model has been a main focus of the scientific community for several decades. Unknown physics in the form of new interactions violating the simultaneous reversal of charge and parity symmetries (CP) would, for example, provide a significant step towards understanding the baryon matter-antimatter asymmetry observed in the Universe. Such parameters are predicted to also manifest themselves in atomic and molecular systems in the form of both: permanent electric dipole moments and nuclear charge distribution asymmetries described by the nuclear Schiff moment. Both can be measured to a high degree of precision in modern experiments, allowing us to place stringent limits on parameters appearing in new fundamental theories.

The Cold Molecule Nuclear Time Reversal Experiment (CeNTREX) is the latest approach to probing these effects. CeNTREX is a molecular beam experiment that uses thallium fluoride (^{205}Tl^{19}F) as its test species to measure energy shifts induced by the interaction of thallium's nuclear Schiff moment. It does so by performing nuclear magnetic resonance using a separate oscillatory fields technique. The precision of this measurement is dictated by the free precession time and the number of interrogated molecules, and is significantly enhanced by thallium fluoride's inherent properties.

Employing novel methods, CeNTREX strives to achieve significant improvements to limits

placed on the fundamental parameters. One such method is rotational cooling. It was thoroughly analyzed, simulated and experimentally confirmed - with the help of optical and microwave pumping, we collapsed the initial Boltzmann distribution of molecules amongst their rotational states into one chosen hyperfine state of the ground rotational state manifold.

The efficiency of this process depends on multiple factors, the most crucial being the approach towards dark state destabilization and remixing. After careful investigation, we chose the most appropriate method and devised an efficient rotational cooling scheme. Experimental confirmation showed an enhancement factor of $r_f = 23.70 \pm 1.13$, very close to our theoretical predictions. This allows us to conclude that CeNTREX should provide a 2500-fold improvement over the current best measurements of the nuclear Schiff moment in thallium nucleus.

Table of Contents

List of Figures

List of Tables

Acknowledgments

First and foremost I would like to thank professor Tanya Zelevinsky for her guidance, support, patience and for providing me with an opportunity to join her group and to work on this project. Amongst others in the Zelevinsky Lab, I would like to extend my special thanks to Rees McNally who provided much support and, just as crucially, stimulating conversation. Without him the work would not have been the same. I am also very grateful to other ZLab members I met throughout the PhD program and who offered me their help and support: Geoff Iwata, Chih-Hsi Lee, Mick Aitken, Kon H. Leung, Stan Kondov, Sebastian Vazquez-Carson, Emily Tiberi and Ivan Kozyryev.

This work, being part of the CeNTREX collaboration, could not have been completed without the leadership of Professor David DeMille whose advice has always proven to be helpful. Furthermore, my thanks goes to Olivier Grasdijk, Oskari Timgren and Jakob Kastelic, all of whom contributed greatly to the experiment.

Graduate school was not always easy, and so I would also like to thank professor Jeremy Dodd for all the counsel he provided. The same goes to my classmates, especially Alexander Kerelsky, Heather McCarrick, Björn Kjellstrand and Stefan Countryman, as well as other Columbia physics PhD students including Giuliano Chiracó, Angelo Esposito, Joey Howlett and Steve Harrellson, to whom I am very thankful for making the dark pandemic times in New York City much more bearable. Moreover, I am grateful to Shirley Zhang and Evan Martinez for their friendship and encouragement.

Finally, I would like to thank all the people that contributed to my journey here, both on academic and personal level. For the former, I would like to credit my high school chemistry teacher Mrs. Teresa Kołogrecka-Bajek who taught me, believed in me and set me on the academic path, while for the latter, I am deeply thankful to my close friends, including Lucjan Szubert and Piotr Furmaniak, as well as to my brother, mom and dad who have always, regardless of my decisions, been there for me.

Chapter 1

Introduction

1.1 The Puzzle

Symmetries play one of the major roles in physics. One of the best examples is the so-called CPT-symmetry which, to the best of our knowledge, is one of the most basic symmetries in nature. However, only half a century ago it was assumed that CP was a good symmetry as well. If that was the case, as was pointed by Landau [1], elementary particles would not be able to have permanent electric dipole moments (EDM) along their spin axis, and so detecting one would be an unambiguous sign of CP-violation.

As we know now, the Standard Model (SM) already predicts small amounts of CP-violating interactions. Namely, it is violated by certain weak interactions and it has been observed in K-, B-, and D-meson decays [2, 3]. Contributions from SM come from the Cabibbo-Kobayashi-Maskawa (CKM) quark-mixing matrix [4, 5]. This so-called Kobayashi-Maskawa mechanism introduces the third quark generation to explain the CP-violation [6], and the so-called CKM phase has been the only source of CP-violation observed so far [3]. To be more precise, in the SM lagrangian the CKM matrix appears when describing the weak coupling between quarks:

$$\mathcal{L}_{\text{CKM}} = -\frac{ig}{\sqrt{2}} \sum_{p,q} V^{pq} \bar{U}_L^p \not{W}^+ D_L^q + \text{h.c.},$$

where g is the weak coupling constant, W^+ is the charged weak gauge field, U_L^p and D_L^q represent p- and q-generation left-handed up and down quarks, and V^{pq} is an element of CKM matrix. Due to certain constraints, the matrix

$$V = \begin{bmatrix} V^{ud} & V^{us} & V^{ub} \\ V^{cd} & V^{cs} & V^{cb} \\ V^{td} & V^{ts} & V^{tb} \end{bmatrix}$$

has only four independent elements: 3 non-CP-violating mixing angles and the aforementioned CP-violating phase. The CP-violating effects can be written as proportional to the so-called Jarlskog invariant $\bar{\delta} = \mathrm{Im}(V_{us}V_{cs}^*V_{cb}V_{ub}^*)$ [7].

One of the main motivations for searches for the CP-symmetry-violating effects is related to the baryon asymmetry in the Universe. From observations it is known that the antimatter-to-matter density ratio is bounded by a number between 10^{-15} to 10^{-6} [8], and no mechanism responsible for this asymmetry has been experimentally proven to be true. It was speculated by Sakharov [9] that this baryon imbalance necessitates violation of the CP-symmetry, and because the CP-violating effects in SM are not enough to account for the observed antimatter-to-matter ratios, new and unknown sources of CP-violation have to exist.

One of the most commonly used examples of a flavor-netural CP-violation can be already found in the QCD lagrangian describing gluon fields. The CP-violating term is proportional to the QCD-theta parameter $\bar{\theta}$ [10]:

$$\mathcal{L}_{\bar{\theta}} = \frac{g^2}{32\pi^2}\bar{\theta}\,\mathrm{Tr}\left(G^{\mu\nu}\widetilde{G}_{\mu\nu}\right), \tag{1.1.1}$$

where G is the gluon field tensor, g here is the strong coupling constant, and $\bar{\theta}$ is dimensionless. Currently the upper bound placed on $\bar{\theta}$, with respect to the usual strong interaction, is $\left|\bar{\theta}\right| < 9{\cdot}10^{-11}$ as concluded from experiments in neutral ^{199}Hg atoms [11] and ultracold neutrons [12, 13]. Such a low value of this parameter is puzzling and has its own name - the strong CP problem. One of the known solutions to it is the Peccei-Quinn mechanism with an accompanying elementary scalar particle: the axion [14]. The axion would then lead to $\bar{\theta} \approx 0$, and is one of the leading candidates for dark matter [15, 16, 17, 18].

1.2 From Particle Physics to Schiff Moments

Physics beyond the SM or new interactions in the QCD sector can lead to effective charge asymmetries along the spin of a particle, and eventually create observable effects in more macroscopic systems. EDMs are one of the manifestations of this particle charge asymmetry. Another one is the so-called Schiff moment [19], which appears in finite-size composite particles such as nuclei. Both EDMs and nuclear Schiff moments (NSM) would have to be very small if only contributions from SM were included. However, additional effects originating in the beyond SM theories can lead to larger EDMs and NSMs, and so searches for either provide a nearly background-free signal for new physics (the background expected from SM would only become apparent when probing effects beyond the energy scale of $\sim 10^5$ TeV [20]).

To understand how the observable effects arise in macroscopic systems, we start with the electron and quarks' EDMs. In the electron, EDM arises at four-loop level [21], and is estimated to be [22]:

$$d_e^{\mathrm{CKM}} \approx \frac{eG_F}{\pi^2}\left(\frac{\alpha}{2\pi}\right)^3 m_e\bar{\delta} \approx 10^{-38}\ e\,\mathrm{cm}. \tag{1.2.1}$$

Similarly, we can compute EDMs for quarks: $d_d \approx -0.7\times10^{-34}\ e\,\mathrm{cm}$ and $d_u \approx -0.15\times10^{-34}\ e\,\mathrm{cm}$ for the down and up quark respectively, from which we can obtain proton's and neutron's EDMs. For example, for neutron:

$$d_n^{\mathrm{CKM}} = \frac{4}{3}d_d - \frac{1}{3}d_u \approx -1.1\times10^{-34}\ e\,\mathrm{cm}.$$

A much bigger contribution to neutron's and proton's EDM arises from "long distance" meson-exchange interactions [7], not from EDMs of their constituents. These interactions appear in an effective, non-relativistic lagrangian:

$$\mathcal{L}_{\pi NN} = \bar{N}\left[\bar{g}_\pi^{(0)}\vec{\tau}\cdot\vec{\pi} + \bar{g}_\pi^{(1)}\pi^0 + \bar{g}_\pi^{(2)}(3\tau_3\pi^0 - \vec{\tau}\cdot\vec{\pi})\right]N$$

where $g^{(1,2,3)}$ are coupling constants between nucleons N and pions π. These couplings appear in the so-called Penguin process [23], where one of the vertices is CP-violating. Forgetting about the $g^{(2)}$, which is expected to be at least two orders of magnitude smaller than other two constants [24], the contributions to nucleon's EDM can be written as:

$$d_N = d_N^{\mathrm{CKM}} + \left(\alpha_{N,0}\,\bar{g}_\pi^{(0)} + \alpha_{N,1}\,\bar{g}_\pi^{(1)}\right). \tag{1.2.2}$$

The $\alpha_{(p,n),(0,1)}$ are proportionality constants for nucleons. The nucleon-pion couplings are also an important element of the mentioned NSM, to which many EDM experiments are sensitive to. The Schiff moment itself is a measure of charge asymmetry in the nucleus defined as r^2-weighted dipole distribution [25]:

$$\mathcal{S} \equiv \frac{e}{10}\left[\left\langle r^2\mathbf{r}\right\rangle - \frac{5}{3Z}\left\langle r^2\right\rangle\left\langle \mathbf{r}\right\rangle\right]. \tag{1.2.3}$$

In the definition, the expectation values $\langle r^n\rangle \equiv \int \rho(\mathbf{r}) r^n d^3r$ are the moments of the nuclear charge density ρ. The second term is then the electric dipole moment of the nucleus and is unobservable in a neutral atom, and is therefore subtracted from $\mathcal{S}$ [7]. It can then be written as [7]:

$$\mathcal{S} = s_N d_N + \frac{m_N g_A}{F_\pi}\left(a_0\bar{g}_\pi^{(0)} + a_1\bar{g}_\pi^{(1)} + a_2\bar{g}_\pi^{(2)}\right),$$

where s_N parametrize contributions of the unpaired nucleon's dipole moment, g_A is the nucleon axial-vector coupling, F_π is pion decay constant and $a_{1,2,3}$ parametrize direct contributions from nucleon-pion coupling constants. Using Eq. (1.2.2) we obtain:

$$\mathcal{S} = s_N d_N^{\mathrm{CKM}} + \left(\frac{m_N g_A}{F_\pi}a_0 + s_N\alpha_{N,0}\right)\bar{g}_\pi^{(0)} + \left(\frac{m_N g_A}{F_\pi}a_1 + s_N\alpha_{N,1}\right)\bar{g}_\pi^{(1)}. \tag{1.2.4}$$

The contributions to both the Schiff moment, and nucleons' or leptons' EDM can arise also from QCD lagrangian describing gluon fields of Eq. (1.1.1) and the parameter $\bar{\theta}$, which contributes the most to the coupling constant $g_\pi^{(0)}$. Beyond Standard Model physics can change values of these couplings and parameters as well. However, the new physics can also create additional CP-violating contributions to the nucleons' and leptons' EDMs directly, i.e. not through quarks' EDMs. The most important contributions which are usually taken into account are the effective nucleon-spin-independent and nucleon-spin-dependent electron-nucleon interactions described by the scalar (S):

$$\mathcal{L}_S = -\frac{G_F}{\sqrt{2}}\,\bar{e}\,i\gamma_5\,e\,\bar{N}\left(C_S^{(0)} + C_S^{(1)}\tau_3\right)N$$

and tensor (T) interactions:

$$\mathcal{L}_T = -\frac{8G_F}{\sqrt{2}}\,\bar{e}\,\sigma_{\mu\nu}\,ev^\nu\,\bar{N}\left(C_T^{(0)} + C_T^{(1)}\tau_3\right)S^\mu N,$$

The former, described by the $C_S^{(0,1)}$ constants, is crucial in paramagnetic systems, while the latter, with $C_T^{(0,1)}$ constants, is of importance in diamagnetic systems.

In general, following [7], we can summarize all the contributions to EDM systems which are accessible to experiments using following parameters:

- Electron's EDM d_e, which contributes in the first order to EDMs of paramagnetic atoms and molecules.
- Nuclear-spin-indpendent electron-nucleon couplings $C_S^{(0,1)}$, which contributes mostly to the paramagnetic systems.
- Nuclear-spin-dependent electron-nucleon couplings $C_T^{(0,1)}$ important mostly in diamagnetic systems.
- Schiff moment $\mathcal{S}$ important in diamagnetic atoms and molecules, which is related to unpaired nucleon's EDM and pion-nucleon couplings.

To the first order, we can write that for paramagnetic atoms:

$$d_{\text{para}} \approx \eta_{d_e} d_e + k_{C_S^{(0)}} C_S^{(0)}$$

and for diamagnetic ones:

$$d_{\text{dia}} = \kappa_{\mathcal{S}} \mathcal{S}(\bar{g}_\pi^{(0,1)}, d_N) + k_{C_T^{(0)}} C_T^{(0)} + ... \tag{1.2.5}$$

While experiments searching for EDMs and NSMs can in principle provide very stringent constraints on beyond SM physics, they have their limitations. As was pointed out by Schiff [19], the CP-violating asymmetric charge distribution does not manifests itself in a linear term in the interaction energy of non-relativistic electric dipoles that are bound in a neutral system while also residing in an external electrostatic potential - the system "rearranges" itself to screen the external field completely [26]. This so-called Schiff's theorem is an obstacle that needs to be bypassed in order to allow detection of the CP-violating effects in various constituents. Two such mechanisms are: relativistic constituent motion and finite constituent size.

In case of atoms or molecules, the latter mechanism is the dominant one. After all, a nucleus is non-relativistic, but has a finite size. This can cause a residual electromagnetic moment to appear in the form of the already-mentioned Schiff moment $\mathcal{S}$ defined in Eq. (1.2.3) as a measure of charge asymmetry, and which depends on the CP-violating parameters shown in Eq. (1.2.4). According to

Eq. (1.2.5), in heavy diamagnetic atoms and diatomic molecules with such an atom (e.g. thallium fluoride), this finite-size effect is responsible for the biggest contribution to the CP-violating signals.

The nuclear spin $\mathbf{I}$ is the only parameter in a nucleus with a preferred directions, and so the quantum NSM $\boldsymbol{\mathcal{S}}$ has to be parallel to this axis, i.e. $\boldsymbol{\mathcal{S}} = \mathcal{S}\,\mathbf{I}/I$. Therefore, NSM inherits all symmetries of the nuclear spin - parity-reversing transformation P does not affect it, but the time reversal T changes its sign (in comparison, the classical Schiff moment, being a static charge distribution, changes sign under parity reversal, but not under the time reversal transformation). If CPT symmetry is indeed a true symmetry of nature, then a non-zero Schiff moment, which violates both T and P symmetries, has to be a signature of CP-violation.

The various contributions to NSM elucidated before play a bigger or smaller role depending on the character of the atom or molecule. In the case of the thallium ^{205}Tl nucleus [25, 27]:

$$\begin{aligned}
\mathcal{S}\left(^{205}\mathrm{Tl}\right) &\approx \left(0.13 g_A \bar{g}_\pi^{(0)} - 0.004 g_A \bar{g}_\pi^{(1)} - 0.27 g_A \bar{g}_\pi^{(2)}\right) e\,\mathrm{fm}^3; \\
\mathcal{S}\left(^{205}\mathrm{Tl}\right) &\approx 0.027\,\bar{\theta}\; e\,\mathrm{fm}^3; \\
\mathcal{S}\left(^{205}\mathrm{Tl}\right) &\approx \left(12\,\widetilde{d}_d + 9\,\widetilde{d}_u\right) e\,\mathrm{fm}^2; \\
\mathcal{S}\left(^{205}\mathrm{Tl}\right) &\approx 0.4\,d_p\,\mathrm{fm}^2,
\end{aligned} \tag{1.2.6}$$

where $\widetilde{d}_d$ and $\widetilde{d}_u$ are quark chromo-EDMs (including contributions from the gluon fields). We should note here that the lack of d_n contribution comes from the fact that this particular nucleus has closed neutron shells. We can see that a nonzero NSM $\mathcal{S}\left(^{205}\mathrm{Tl}\right)$ would provide evidence for a non-zero value of one or more of these fundamental CP-violating parameters.

1.3 Energy Shifts and Measured Quantities

Existence of a permanent electric dipole moment or the nuclear Schiff moment will cause energy shifts if the systems is subject to external electric fields. These shifts can be significant in polar molecules, where the internuclear axis $\hat{\mathbf{n}}$ adds an additional direction in the system other than the nuclear spin. In thallium fluoride (TlF), which is the species of choice in our and previous experiments looking for NSM, we define this vector as pointing from fluorine to thallium atom. This vector is related to molecule's permanent and internal dipole moment, and so a strong gradient of electron density exists along it. It is this density gradient, creating effective electric field, that

NSM (and other CP-violating effects [28]) of molecular nuclei interacts with. This interaction can be described by an effective CP-violating hamiltonian [25]:

$$\mathcal{H}_{\mathrm{CPV}} = W_{\mathcal{S}}\, \mathcal{S}\, \hat{\mathbf{n}} \cdot \frac{\mathbf{I}}{I}, \tag{1.3.1}$$

where $W_{\mathcal{S}}$ is the proportionality constant between $\mathcal{S}$ and the CP-violating contribution to the molecular energy, for a fully polarized molecule. This constant is usually obtained from ab initio calculations and is determined by properties of the electronic wavefunctions [25, 29, 30, 31]. One of its important features is its quadratic scaling with the atomic number Z of the nucleus [32].

While the interaction of NSM with the effective internal electric field, described by Eq. (1.3.1), exists without submitting the molecule to any external fields $\boldsymbol{\mathcal{E}}$, it does not create any observable first-order effects in any of system's eigenstates. As was pointed out in previous searches for NSM in TlF [33, 34], the internuclear axis vector $\hat{\mathbf{n}}$ averages to zero due to unpolarized molecule's rotation, and thus the expectation value $\langle \mathcal{H}_{\mathrm{CPV}} \rangle = 0$. The situation changes when an external electric field is applied. The field polarizes the molecule and changes the expectation value of $\hat{\mathbf{n}}$, and therefore the expectation value of the effective hamiltonian of Eq. (1.3.1) as well, to a non-zero value. In fact, the expectation value of the internuclear axis vector becomes parallel to the direction of the external electric field, i.e. $\langle \hat{\mathbf{n}} \rangle \parallel \boldsymbol{\mathcal{E}}$, and from the combination of both we can define the degree of electrical polarization of molecule:

$$\mathbf{P} \equiv \frac{\langle \hat{\mathbf{n}} \cdot \boldsymbol{\mathcal{E}} \rangle}{\mathcal{E}}.$$

With such definition $-1 \leq \mathbf{P} \leq 1$ and the energy shifts from Eq. (1.3.1) can be written as:

$$\langle \mathcal{H}_{\mathrm{CPV}} \rangle = W_{\mathcal{S}}\, \mathcal{S}\, \mathbf{P} \frac{\langle \boldsymbol{\mathcal{E}} \cdot \mathbf{I} \rangle}{\mathcal{E}\, I}. \tag{1.3.2}$$

It was already 50 years ago that Sandars suggested [35] that a molecular beam experiment and a resonance measurement could be used to find proton's EDM, if a molecule with a heavy diamagnetic atom, i.e. with an unpaired proton in its nucleus, is used, e.g. ^{205}Tl. Such an experiment is possible, because polar molecules can be quite easily polarized in modest and realistically realizable electric fields (due to their small rotational level spacing of $\sim 10^{-4}$ eV), which allows us to achieve a near-maximal NSM-induced energy shifts. The actual value of $\mathcal{S}$ can be measured by probing energy difference of spin-up and spin-down states relative to $\langle \hat{\mathbf{n}} \rangle$, and therefore relative to polarizing electric field $\boldsymbol{\mathcal{E}}$. Because magnitude of the external electric fields determines the degree of polarization, the

NSM-induced splitting between these states changes with changing field's magnitude. Moreover, if direction of the electric field were to reverse, the energy splitting would either decrease or increase depending on relative orientation of spins and field's direction. Following Eq. (1.3.2), this difference in level splittings is proportional to the electric polarization $\mathbf{P}$, the interaction strength $W_{\mathcal{S}}$, and $\mathcal{S}$ (Fig. 1.3.1), and it is exactly what can be measured experimentally.

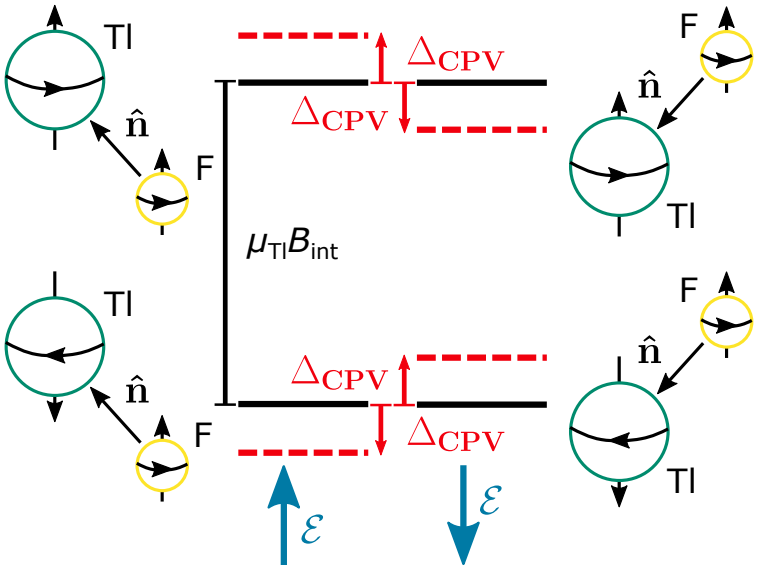

Figure 1.3.1: Energy shift $\Delta_{\rm CPV} = W_{\mathcal{S}}\,\mathcal{S}\,\mathbf{P}$ associated with CP-violating effects, and created as a result of a non-zero NSM given by the effective interaction $\mathcal{H}_{\rm CPV} = W_{\mathcal{S}}\,\mathcal{S}\,\mathbf{I}\cdot\hat{\mathbf{n}}/I$, shown for opposite orientations of the external electric field $\boldsymbol{\mathcal{E}}$. Here μ_{Tl} is the Tl magnetic moment and $B_1^{\rm int}$ is the effective internal magnetic field at the Tl nucleus due to the spin-rotation interaction.

To better understand the principle behind the NSM measurement, we can look at the magnetic resonance measurement, which provides an oversimplified picture. Magnetic dipole moments, as it is well known, are aligned with the angular momentum vector $\boldsymbol{\mu}_B = \gamma\mathbf{J}$. When exposed to a static magnetic field the effective hamiltonian $\mathcal{H} = -\boldsymbol{\mu}\cdot\mathbf{B}$ describes the interaction and yields an equation:

$$\frac{d\mathbf{J}}{dt} = \gamma\mathbf{J}\times\mathbf{B},$$

which describes angular momentum vector precession with frequency $\omega_R = \gamma B/\hbar$. The angle of precession is therefore equal to $\phi = \gamma BT/\hbar$, where T is the total interaction (precession) time. In the simplest case with $|\mathbf{J}| = 1/2$ the magnetic field splits the state into two

states of different energy ($\Delta E = 2\mu_B B$). If we prepare an atom or molecule in the initial state $|\psi_i\rangle = (|J,+M_J\rangle + |J,-M_J\rangle)/\sqrt{2}$, after the interaction the state will evolve to $|\psi_f\rangle = (e^{-i\phi}|J,+M_J\rangle + e^{i\phi}|J,-M_J\rangle)/\sqrt{2}$. We can measure the precession angle by accessing transition related to only one of the basis state, i.e. we can project the final state on a particular state, for example the initial one. Then the probability of detection is proportional to cosine-squared of the precession angle, i.e. $P(\phi) \propto \cos^2\phi$.

The electric dipole moment (or NSM), similarly to the magnetic dipole moment, should be aligned with the angular momentum of the system. While in paramagnetic atoms it is aligned with spin of the unpaired electron $\mathbf{d} \propto \mathbf{S}$, in diamagnetic atoms (such as ^{205}Tl) it is aligned with the spin of the nucleus $\mathbf{d} \propto \mathbf{I}$ as was previously mentioned. In analogy to the shift experienced by magnetic moments in a static magnetic field, a non-zero electric dipole moment would simply be described by an interaction hamiltonian:

$$\mathcal{H} = -\mathbf{d}\cdot\boldsymbol{\mathcal{E}} = -d\frac{\mathbf{I}\cdot\boldsymbol{\mathcal{E}}}{I}$$

creating energy difference of $\Delta E = 2d\mathcal{E}$ between the two states. The electric dipole moment can be aligned or anti-aligned with respect to the electric field, and so the precession angle is simply $\phi = -d\mathcal{E}_{\text{eff}}T/\hbar$, where we emphasized that the electric field magnitude that is taken into consideration in this case is the *effective* electric field probed by the spin (and part of the interaction constant $W_{\mathcal{S}}$ in our system). From the equation above we can see that changing the direction of the electric field, if the electric dipole moment exists in the system, changes the precession angle accumulated. Modern beam experiments, exploit this fact and measure these changes, which in general are equal to [7]:

$$\phi = T\frac{|d\mathcal{E}_{\text{eff}}|}{2\pi\hbar J}|\Delta M_J| \propto \Delta E.$$

In the case of our NSM measurement, we use the effective interaction $\mathcal{H}_{\text{CPV}}$ and observe that the shift in the energy splitting between states with Tl spin-up and spin-down states, relative to the quantization axis, can be written as:

$$\Delta E = 2\Delta_{\text{CPV}} = 2W_{\mathcal{S}}\,\mathcal{S}\,\text{sgn}(\mathcal{E})\,\mathbf{P}, \tag{1.3.3}$$

where the sign of $\mathcal{E}$ refers to the direction of $\boldsymbol{\mathcal{E}}$ relative to a fixed quantizing axis $\mathbf{z}$.

The Cold Molecule Nuclear Time Reversal Experiment (CeNTREX) is a molecular beam experiment with a goal of measuring this energy splitting with unparalleled precision. It uses a cold beam

of thallium fluoride to measure CP-violating effects in the ^{205}Tl nucleus that appear due to the existence of NSM. This particular nucleus is one of the most well-suited to measure CP-violating effects: it is a polar diatomic molecule, that can be easily polarized; it has high electron density gradient at the site of nuclei ($\mathcal{E}_{\text{eff}}$) and therefore the $W_{\mathcal{S}}$ constant; and it is a heavy nucleus with $A = 205$ and $Z = 81$ leading to high NSM-induced energy shifts, which scale $\propto A^{2/3}Z^2$ [35, 36]. Our species was also chosen due to several other reasons - its cold molecular beam can be obtained using known experimental procedures, and its molecular states and transitions have already been described in scientific publications. Finally, the ^{205}Tl nucleus contains an unpaired proton in its outer shell. Hence, CeNTREX will be mostly sensitive to proton EDM effects, as opposed to other leading experiments which are more sensitive to the neutron EDM [11]. TlF is also not sensitive to the electron EDM due to its zero total electron spin [37].

1.4 Precision of the Measurement

The precision of the measurement depends on the interrogation time T (in our case the free precession time) and the signal-to-noise ratio, which depends on the technique used. In most experiments one is limited by the count rate. Its statistical uncertainty of single frequency measurement is:

$$\sigma_f = \frac{1}{2\pi T\sqrt{N}},$$

where N is number of particles probed. Following the oversimplified picture of interaction described by $\mathcal{H} = -\mathbf{d}\cdot\boldsymbol{\mathcal{E}}$, the overall uncertainty of electric dipole moment measurement for a pair of frequency measurements with opposite electric field and identical interrogation times is simply given by:

$$\sigma_d = \frac{\hbar I}{2\sqrt{2}\mathcal{E}_{\text{eff}}}\frac{1}{T\sqrt{N}}. \tag{1.4.1}$$

This already shows that the experiment becomes more sensitive to EDMs when electric fields, interaction times and number of molecules are increased. As was mentioned before, the strength of the effective electric field is mostly determined by the features of the chosen system, such as TlF. Increases in sensitivity can therefore be achieved differently by different class of experiments. While trapping experiments confine atoms or molecules and allow for long interaction times, their sensitivity is limited by a relatively small number of trapped molecules. CeNTREX, being a beam

experiment, tries to increase the number of molecules on which the measurement is performed, while simultaneously sacrificing the interrogation time.

Currently, the best limits put on T-violating interactions associated with the Schiff moment $\mathcal{S}\left(^{205}\mathrm{Tl}\right)$ were found by Cho, Sangster and Hinds in 1991 [33, 34], who measured a NSM-induced frequency shift of $\Delta E = 2\Delta_{\mathrm{CPV}} = (1.4 \pm 2.4) \times 10^{-4}$ Hz, consistent with zero. In the TlF system $W_{\mathcal{S}} = 40539\,\mathrm{a.u.}$, polarization $\mathbf{P} = \langle \hat{\mathbf{n}} \cdot \boldsymbol{\mathcal{E}}/\mathcal{E} \rangle = 0.547$ (in 30 kV/cm external field), which leads to [27, 30]:

$$\mathcal{S}\left(^{205}\mathrm{Tl}\right) = (3.6 \pm 6.1) \times 10^{-11}\, e\,\mathrm{fm}^3.$$

With Eq. (1.2.6), the following limits can be then placed:

$$\begin{aligned} \bar{\theta} &= (1.3 \pm 2.3) \times 10^{-9}, \\ 12\widetilde{d}_d + 9\widetilde{d}_u &= (3.6 \pm 6.1) \times 10^{-24} e\,\mathrm{cm}, \\ d_p &= (0.9 \pm 1.5) \times 10^{-23}\, e\,\mathrm{cm}, \\ 0.13 g_A \bar{g}_\pi^{(0)} - 0.004 g_A \bar{g}_\pi^{(1)} - 0.27 g_A \bar{g}_\pi^{(2)} &= (3.6 \pm 6.1) \times 10^{-11}. \end{aligned} \tag{1.4.2}$$

1.5 Increasing Experimental Sensitivity

Comparing to previous experiments, we plan to utilize several methods that will improve our signal and allow us to put more stringent limits on the sought-after parameters. One of the first major advancements has already been demonstrated in other molecular beam experiments and will be used in our experiment as well. Namely, we are using a cryogenic molecular beam source, which allows us to achieve a cold beam with higher intensity and lower velocity spread compared to the jet source used in the previous work. Another signal enhancement method that has been shown to work is beam collimation with the help of a quadrupole electrostatic field - this technique increases the total number of interrogated molecules that reach the detection area.

Particular properties of TlF allowed us to additionally develop new techniques for CeNTREX that can further increase the signal by increasing the number of probed molecules. The first of these methods is a rotational cooling process, which will be performed with optical and microwave pumping. It collapses much of the initial Boltzmann distribution into one state, which increases the number of molecules accessible for measurement by at least an order of magnitude. Then, the final state detection, which will be performed through a laser-induced fluorescence, can achieve a

near-unity detection efficiency with the help of a optical quasi-cycling (nearly-closed) transitions.

While both of these approaches are seemingly easy to implement, peculiarities of TlF make both of these processes quite difficult to achieve experimentally. Specifically, low natural energy splittings in molecular ground states, and high energy splittings in the excited state lead to creation of coherent dark states - if the techniques are not implemented with care and precision, instead of increasing our signal, we might lose a big number of molecules to non-interacting state superpositions. The problem of understanding, and efficient remixing and destabilization of these dark states, optimal schemes for optical cycling detection and rotational cooling, as well as experimental realization of the rotational cooling process are the main topics of this thesis.

First, in Chapter 2, we will derive and discuss thallium fluoride's peculiar structure and lay ground for further analysis of the system. Then, in Chapter 3 we will go over different parts of CeNTREX, show the progress that has already been made and problems that still remain to be solved. In Chapter 4 we will briefly introduce the mathematical framework that will be used to analyze light-molecule interaction of TlF. Dark states and their analysis in the context of our experiment's processes will be shown in Chapter 5. Conclusions drawn from it will be then implemented in both Chapters 6 and 7, where we will propose, discuss and numerically simulate different schemes for optical cycling and rotational cooling in TlF. From there, we will step into the experimental realization of the rotational cooling process and start with describing the necessary apparatus: first, in Chapter 8, our frequency-quadrupling laser system will be presented, and a further depiction of the remainder of the setup will follow in Chapter 9. In Chapter 10 we will show specific experimental predictions, as well as obtained results. Final conclusion will be drawn in Chapter 11, where we will talk about the impact of our rotational cooling experiment on the final molecule yield, and what the eventual CeNTREX sensitivity to NSM might be.

Chapter 2

Thallium Fluoride Structure

2.1 Rotational and Hyperfine Levels in TlF

In our study it is important to first understand the molecule we are working with. Thallium fluoride has already been studied [36, 38, 39] and used in experiments [40], so its structure and many of the physical constants associated with it are already known. What is left for us is to thoroughly evaluate the rotational and hyperfine structure as well as understand Stark and Zeeman shifts, and the dipole transitions. We will also do so in both coupled and uncoupled bases - solutions in coupled basis are needed in modeling of rotational cooling, while the uncoupled basis can be used for calculations related to state transfer in other parts of our experiment.

The TlF molecule is diatomic and is described by its electronic state, vibrational and rotational motion, plus the Tl and F nuclear spin states. In the experiment we use TlF in its ground vibrational state, both in its ground electronic state $X^1\Sigma^+$ ($\nu = 0$), and in an electronically excited $B^3\Pi_1$ ($\nu = 0$) state. In both cases, the angular momentum couplings are best described in a Hund's case (c) basis, where the energy eigenstates are usually written in terms of the basis states $|\eta, J, F_1, F, M_F\rangle$. In this notation η represents both the electronic and vibrational quantum numbers, $\mathbf{J}$ is the total angular momentum (excluding the nuclear spins), $\mathbf{F_1} = \mathbf{J} + \mathbf{I_1}$, with $I_1 = 1/2$ being thallium's (^{205}Tl) nuclear spin, $\mathbf{F} = \mathbf{F_1} + \mathbf{I_2}$ is the total angular momentum, with $I_2 = 1/2$ being the nuclear spin for ^{19}F, and M_F is its projection along a quantization axis in the lab frame. Field-free eigenstates are close to these basis states in the ground $X^1\Sigma^+$ state. However, in the $B^3\Pi_1$ state, strong hyperfine interactions strongly mix states with different J and F_1 values. We

describe these eigenstates with a modified notation $\left|\eta', \widetilde{J}', \widetilde{F}_1', F', M_F'\right\rangle$, where $\widetilde{J}'$ and $\widetilde{F}_1'$ correspond to the largest component in their basis-state decomposition, and primes here simply indicate that the quantum numbers refer to the $B^3\Pi_1$ excited state.

We begin here with the hyperfine and rotational structure of the electronic ground state - the electronic and vibrational structure of the molecule are of smaller importance in the context of the models presented in this thesis. Thallium fluoride's hyperfine structure together with appropriate constants (including its rotational constant) have already been presented in [36]. The rotational structure is easy to evaluate. In Hund's case (c) the rotational levels [41], up to first order, are given as:

$$\mathcal{H}_{\mathrm{rot}} = hB_{\mathrm{rot}}\left[J(J+1) + J_a(J_a+1) - 2\Omega^2\right],$$

with B_{rot} being the effective rotational constant. In our case, $B_{\mathrm{rot}} = B_e + \alpha_e(\nu + 1/2) + \ldots$ with $B_e = 6.68987$ GHz and $\alpha_e = -45.084$ MHz [42], which gives effective $B_{\mathrm{rot}} = 6.66733$ GHz (corresponding to temperature of $T \approx 0.3$ K) for vibrational level $\nu = 0$. We also have $\mathbf{J}_a = \mathbf{L} + \mathbf{S}$, $\mathbf{J} = \mathbf{J}_a + \mathbf{R}$ and Ω being projection of $\mathbf{J}_a$ and $\mathbf{J}$ on the internuclear axis. In the ground state $X^1\Sigma^+$ both $J_a = 0$ and $\Omega = 0$, therefore the energy levels scale as $J(J+1)$. Molecules in the beam are assumed to be in the vibrational ground state ($\nu = 0$), since the beam temperature is much lower than the energy scales associated with the electronic and vibrational excitations. However, even at cryogenic temperatures, there is a Boltzmann distribution over many rotational and nuclear spin states.

The hyperfine interaction is more difficult to evaluate. In [36] authors provide:

$$\mathcal{H}_{\mathrm{sr}} = c_{\mathrm{Tl}}\left(\mathbf{I_1}\cdot\mathbf{J}\right) + c_F\left(\mathbf{I_2}\cdot\mathbf{J}\right) \tag{2.1.1}$$

$$\mathcal{H}_{\mathrm{ss}} = 5c_3\frac{3\left(\mathbf{I_1}\cdot\mathbf{J}\right)\left(\mathbf{I_2}\cdot\mathbf{J}\right) + 3\left(\mathbf{I_2}\cdot\mathbf{J}\right)\left(\mathbf{I_1}\cdot\mathbf{J}\right) - 2\left(\mathbf{I_1}\cdot\mathbf{I_2}\right)\mathbf{J}^2}{(2J+3)(2J-1)} + c_4\left(\mathbf{I_1}\cdot\mathbf{I_2}\right). \tag{2.1.2}$$

Hyperfine interactions split sublevels with different F values ($F = J-1, J, J, J+1$, except $F = 0, 1$ only for $J = 0$) in each rotational state, and there is a $(2F+1)$-fold degeneracy of each state with total angular momentum F, corresponding to the quantum numbers $M_F = -F, \ldots, 0, \ldots, F$. Thus, each rotational level has $4(2J+1)$ magnetic sublevels. The provided constants have following numerical values [36]: $c_{\mathrm{Tl}}/h = 126.03$ kHz, $c_{\mathrm{F}}/h = 17.89$ kHz, $c_3/h = 0.70$ kHz and $c_4/h = -13.30$ kHz. The first part, nuclear spin-rotation interaction, has already been evaluated [39], and it will

be provided here as well. The second term describing nuclear spin-spin interaction can be divided into two components: the first part is in fact a so-called dipolar interaction (evaluated for various molecules in [41]), and the second term is the spin-spin interaction.

Including rotation, spin-rotation and spin-spin interactions, plus interactions with external electric ($\boldsymbol{\mathcal{E}}$) and magnetic ($\mathbf{B}$) fields, the system is then described by the effective hyperfine hamiltonian [36]:

$$\mathcal{H}_{\mathrm{TlF}} = \mathcal{H}_{\mathrm{rot}} + \mathcal{H}_{\mathrm{sr}} + \mathcal{H}_{\mathrm{ss}} + \mathcal{H}_{\mathrm{S}} + \mathcal{H}_{\mathrm{Z}}, \tag{2.1.3}$$

where the last two terms correspond to Stark and Zeeman hamiltonians respectively:

$$\begin{aligned}\mathcal{H}_{\mathrm{S}} &= -\boldsymbol{\mu}\cdot\boldsymbol{\mathcal{E}}\\ \mathcal{H}_{\mathrm{Z}} &= -\frac{\mu_J}{J}(\mathbf{J}\cdot\mathbf{B}) - \frac{\mu_1}{I_1}(\mathbf{I_1}\cdot\mathbf{B}) - \frac{\mu_2}{I_2}(\mathbf{I_2}\cdot\mathbf{B}),\end{aligned}$$

both of which will be discussed in this chapter as well.

2.2 Zero-field Hyperfine Structure

We begin with evaluating the terms Eq. (2.1.1) and Eq. (2.1.2) in the coupled basis following [41]. First, we look at the spin-rotation interaction for thallium nucleus forgetting about Ω (it does not play any role in these particular interactions; the matrix element will simply contain a $\delta_{\Omega,\Omega'}$ pre-factor):

$$\begin{aligned}\left\langle J, I_1, F_1, I_2, F, M_F \middle| T^1(\mathbf{I_1})\cdot T^1(\mathbf{J}) \middle| J', I_1', F_1', I_2', F', M_F' \right\rangle &\overset{(A.6)}{=} \delta_{F,F'}\delta_{M_F,M_F'}\delta_{I_2,I_2'}\\ &\left\langle J, I_1, F_1 \middle\| T^1(\mathbf{I_1})\cdot T^1(\mathbf{J}) \middle\| J', I_1', F_1' \right\rangle.\end{aligned}$$

Next, we use formula Eq. (A.5) with our coupling scheme, where, as mentioned earlier, $\mathbf{F_1} = \mathbf{J} + \mathbf{I_1}$ and $\mathbf{F} = \mathbf{F_1} + \mathbf{I_2}$. To do that, we write the scalar product in the opposite order, so that $\mathbf{J}$

corresponds to j_1 in the formula we want to use.

$$\left\langle J, I_1, F_1 \middle\| T^1(\mathbf{J}) \cdot T^1(\mathbf{I_1}) \middle\| J', I_1', F_1' \right\rangle \overset{(A.5)}{=} \delta_{F_1,F_1'} (-1)^{J'+F_1+I_2} \begin{Bmatrix} I_1' & J & F_1 \\ J & I_1 & 1 \end{Bmatrix} \left\langle J \middle\| T^1(\mathbf{J}) \middle\| J' \right\rangle$$

$$\left\langle I_1 \middle\| T^1(\mathbf{I_1}) \middle\| I_1' \right\rangle$$

$$\overset{(A.2)}{=} \delta_{F_1,F_1'} \delta_{I_1,I_1'} \delta_{J,J'} (-1)^{J'+F_1+I_2} \sqrt{J(J+1)(2J+1)}$$

$$\sqrt{I_1(I_1+1)(2I_1+1)} \begin{Bmatrix} I_1' & J & F_1 \\ J & I_1 & 1 \end{Bmatrix}.$$

Using the fact that $I_1 = I_1' = 1/2$ and $I_2 = I_2' = 1/2$ we obtain:

$$\left\langle J, I_1, F_1, I_2, F, M_F \middle| T^1(\mathbf{I_1}) \cdot T^1(\mathbf{J}) \middle| J', I_1', F_1', I_2', F', M_F' \right\rangle = \delta_{M_F,M_F'} \delta_{F,F'} \delta_{F_1,F_1'} \delta_{J,J'}$$
$$(-1)^{J'+F_1+1/2} \sqrt{\frac{3}{2}} \sqrt{J(J+1)(2J+1)} \begin{Bmatrix} \frac{1}{2} & J' & F_1 \\ J & \frac{1}{2} & 1 \end{Bmatrix}. \tag{2.2.1}$$

In a very similar manner we can evaluate the fluorine spin-rotation term. Like before, we will also change the order of the scalar product in order to easily follow spherical tensor algebra formulas in our coupling scheme. We begin with:

$$\left\langle J, I_1, F_1, I_2, F, M_F \middle| T^1(\mathbf{J}) \cdot T^1(\mathbf{I_2}) \middle| J', I_1', F_1', I_2', F', M_F' \right\rangle =$$

$$\overset{(A.5)}{=} \delta_{F,F'} \delta_{M_F,M_F'} (-1)^{F_1'+I_2+F} \begin{Bmatrix} I_2' & F_1' & F \\ F_1 & I_2 & 1 \end{Bmatrix} \left\langle I_2 \middle\| T^1(\mathbf{I_2}) \middle\| I_2' \right\rangle \left\langle J', I_1', F_1' \middle\| T^1(\mathbf{J}) \middle\| J', I_1', F_1' \right\rangle$$

$$\overset{(A.7)}{=} \delta_{F,F'} \delta_{M_F,M_F'} \delta_{J,J'} (-1)^{F_1'+I_2+F} \begin{Bmatrix} I_2' & F_1' & F \\ F_1 & I_2 & 1 \end{Bmatrix} \left\langle I_2 \middle\| T^1(\mathbf{I_2}) \middle\| I_2' \right\rangle (-1)^{J+I_1+F_1'+1}$$
$$\sqrt{(2F_1+1)(2F_1'+1)} \begin{Bmatrix} J' & F_1' & I_1 \\ F_1 & J & 1 \end{Bmatrix} \left\langle J \middle\| T^1(\mathbf{J}) \middle\| J' \right\rangle.$$

Using Eq. (A.2) and the fact that both nuclei have spins of 1/2 we obtain:

$$\left\langle J, I_1, F_1, I_2, F, M_F \middle| T^1(\mathbf{I_2}) \cdot T^1(\mathbf{J}) \middle| J', I_1', F_1', I_2', F', M_F' \right\rangle = \sqrt{\frac{3}{2}} \delta_{M_F,M_F'} \delta_{F,F'} \delta_{J,J'} (-1)^{J+F+2F_1'+2}$$
$$\sqrt{(2F_1+1)(2F_1'+1)} \sqrt{J(J+1)(2J+1)} \begin{Bmatrix} \frac{1}{2} & F_1' & F \\ F_1 & \frac{1}{2} & 1 \end{Bmatrix} \begin{Bmatrix} J' & F_1' & \frac{1}{2} \\ F_1 & J & 1 \end{Bmatrix}. \tag{2.2.2}$$

The same way one can calculate the spin-spin interaction matrix element. We obtain:

$$\left\langle J, I_1, F_1, I_2, F, M_F \middle| T^1(\mathbf{I_1}) \cdot T^1(\mathbf{I_2}) \middle| J', I_1', F_1', I_2', F', M_F' \right\rangle =$$

$$\overset{(A.5)}{=} \delta_{F,F'}\delta_{M_F,M_F'}(-1)^{F_1'+I_2+F} \begin{Bmatrix} I_2' & F_1' & F \\ F_1 & I_2 & 1 \end{Bmatrix} \left\langle I_2 \middle\| T^1(\mathbf{I_2}) \middle\| I_2' \right\rangle \left\langle J, I_1, F_1 \middle\| T^1(\mathbf{I_1}) \middle\| J', I_1', F_1' \right\rangle$$

$$\overset{(A.7)}{=} \delta_{F,F'}\delta_{M_F,M_F'}(-1)^{F_1'+I_2+F} \begin{Bmatrix} I_2' & F_1' & F \\ F_1 & I_2 & 1 \end{Bmatrix} \left\langle I_2 \middle\| T^1(\mathbf{I_2}) \middle\| I_2' \right\rangle (-1)^{J+I_1'+F_1+1} \sqrt{(2F_1+1)(2F_1'+1)}$$
$$\begin{Bmatrix} I_1' & F_1' & J \\ F_1 & I_1 & 1 \end{Bmatrix} \left\langle I_1 \middle\| T^1(\mathbf{I_1}) \middle\| I_1' \right\rangle .$$

And yet again using Eq. (A.2) and the fact that both nuclei have spins of 1/2 we end up with:

$$\left\langle J, I_1, F_1, I_2, F, M_F \middle| T^1(\mathbf{I_1}) \cdot T^1(\mathbf{I_2}) \middle| J', I_1', F_1', I_2', F', M_F' \right\rangle = \frac{3}{2}\delta_{M_F,M_F'}\delta_{F,F'}\delta_{J,J'}(-1)^{J+F+F_1'+F_1+2}$$
$$\sqrt{(2F_1+1)(2F_1'+1)} \begin{Bmatrix} \frac{1}{2} & F_1' & F \\ F_1 & \frac{1}{2} & 1 \end{Bmatrix} \begin{Bmatrix} \frac{1}{2} & F_1' & J \\ F_1 & \frac{1}{2} & 1 \end{Bmatrix} . \tag{2.2.3}$$

The final contribution comes from the dipolar coupling of nuclear spins. The term can be translated into spherical tensor representation. We write it as $\mathcal{H}_{\text{dip}} = 5c_3\sqrt{10}\ T^1(\mathbf{C^2}, \mathbf{I_1}) \cdot T^1(\mathbf{I_2})$, where $T^2(\mathbf{C})$ is a spherical tensor constructed from spherical harmonics, and its expectation value for the ground electronic state is already taken into account in the constant c_3 [41]. We should also note that $T^1(\mathbf{C^2}, \mathbf{I_1}) = T^2(\mathbf{C}) \times T^1(\mathbf{I_1})$. We begin with:

$$\left\langle \eta; J, \Omega, I_1, F_1, I_2, F, M_F \middle| T^1(\mathbf{C^2}, \mathbf{I_1}) \cdot T^1(\mathbf{I_2}) \middle| \eta'; J', \Omega', I_1', F_1', I_2', F', M_F' \right\rangle =$$

$$\overset{(A.5)}{=} \delta_{F,F'}\delta_{M_F,M_F'}(-1)^{F_1'+I_2+F} \begin{Bmatrix} I_2' & F_1' & F \\ F_1 & I_2 & 1 \end{Bmatrix} \left\langle I_2 \middle\| T^1(\mathbf{I_2}) \middle\| I_2' \right\rangle$$
$$\left\langle \eta; J, \Omega, I_1, F_1 \middle\| T^1(\mathbf{C^2}, \mathbf{I_1}) \middle\| \eta'; J', \Omega', I_1', F_1' \right\rangle ,$$

which then, using Eq. (A.3), leads to:

$$\left\langle \eta; J, \Omega, I_1, F_1, I_2, F, M_F \middle| T^1(\mathbf{C^2}, \mathbf{I_1}) \cdot T^1(\mathbf{I_2}) \middle| \eta'; J', \Omega', I_1', F_1', I_2', F', M_F' \right\rangle =$$

$$= \delta_{F,F'} \delta_{M_F, M_F'} (-1)^{F_1' + I_2 + F} \begin{Bmatrix} I_2' & F_1' & F \\ F_1 & I_2 & 1 \end{Bmatrix} \sqrt{I_2(I_2+1)(2I_2+1)} \sqrt{(2+1)(2F_1+1)(2F_1'+1)}$$

$$\begin{Bmatrix} F_1 & F_1' & 1 \\ J & J' & 2 \\ I_1 & I_1' & 1 \end{Bmatrix} \left\langle \eta; J, \Omega \middle\| T^2(\mathbf{C}) \middle\| \eta'; J', \Omega' \right\rangle \left\langle I_1 \middle\| T^1(\mathbf{I_1}) \middle\| I_1' \right\rangle .$$

In the equation above η represents an electronic state (in our case $X^1\Sigma^+$) and other quantum numbers. To evaluate the reduced matrix element of the spherical tensor $T^2(\mathbf{C})$, we need to bring the tensor into the molecule's frame of reference and then use Eq. (A.9). Hence:

$$\left\langle \eta; J, \Omega \middle\| T^2(\mathbf{C}) \middle\| \eta'; J', \Omega' \right\rangle = \left\langle \eta; J, \Omega \middle\| \sum_{q=-2}^{2} \mathscr{D}^{(2)}_{.q}(\omega)^* T^2_q(\mathbf{C}) \middle\| \eta'; J', \Omega' \right\rangle = \sum_{q=-2}^{2} \left\langle \eta \middle\| C^2_q(\theta, \phi) \middle\| \eta' \right\rangle$$

$$(-1)^{J-\Omega} \sqrt{(2J+1)(2J'+1)} \begin{pmatrix} J & 2 & J' \\ -\Omega & q & \Omega \end{pmatrix} .$$

The term $\left\langle \eta \middle\| C^2_q(\theta, \phi) \middle\| \eta' \right\rangle$, as mentioned before, is included in the c_3 constant. Therefore, after dropping this term:

$$\left\langle \eta; J, \Omega, I_1, F_1, I_2, F, M_F \middle| T^1(\mathbf{C^2}, \mathbf{I_1}) \cdot T^1(\mathbf{I_2}) \middle| \eta'; J', \Omega', I_1', F_1', I_2', F', M_F' \right\rangle =$$

$$= \delta_{F,F'} \delta_{M_F, M_F'} (-1)^{F_1' + I_2 + F + J - \Omega} \sqrt{I_1(I_1+1)(2I_1+1)} \sqrt{I_2(I_2+1)(2I_2+1)} \sqrt{(2J+1)(2J'+1)}$$

$$\sqrt{(2+1)(2F_1+1)(2F_1'+1)} \begin{Bmatrix} I_2' & F_1' & F \\ F_1 & I_2 & 1 \end{Bmatrix} \begin{Bmatrix} F_1 & F_1' & 1 \\ J & J' & 2 \\ I_1 & I_1' & 1 \end{Bmatrix} \sum_{q=-2}^{2} \begin{pmatrix} J & 2 & J' \\ -\Omega & q & \Omega \end{pmatrix}$$

Here, we are only considering the electronic ground state $X^1\Sigma^+$, in which $\Omega = 0$, so in the sum

only $q = 0$ term survives. Including $I_1 = I_2 = 1/2$ finally gives us:

$$\left\langle \eta; J, \Omega, I_1, F_1, I_2, F, M_F \middle| T^1(\mathbf{C^2}, \mathbf{I_1}) \cdot T^1(\mathbf{I_2}) \middle| \eta'; J', \Omega', I_1', F_1', I_2', F', M_F' \right\rangle =$$

$$= \frac{3\sqrt{3}}{2} \delta_{M_F, M_F'} \delta_{F,F'} (-1)^{F_1'+F+J+1/2} \sqrt{(2F_1'+1)(2F_1+1)(2J+1)(2J'+1)} \tag{2.2.4}$$

$$\begin{pmatrix} J & 2 & J' \\ 0 & 0 & 0 \end{pmatrix} \begin{Bmatrix} \frac{1}{2} & F_1' & F \\ F_1 & \frac{1}{2} & 1 \end{Bmatrix} \begin{Bmatrix} F_1 & F_1' & 1 \\ J & J' & 2 \\ \frac{1}{2} & \frac{1}{2} & 1 \end{Bmatrix}$$

By looking at all the evaluated contributions, one can see that there will be some mixing between different states. One of it will happen between different rotational states due to the dipolar coupling given in Eq. (2.2.4). However, because the constant c_3 is 6 orders of magnitude smaller then the rotational constant B_{rot}, this mixing will be very miniscule and its contribution to energies of these levels is negligible. We will also get mixing between levels of the same $\mathbf{J}$, $\mathbf{F}$ and $\mathbf{M_F}$, and different $\mathbf{F_1}$. For TlF in the ground electronic state this mixing moves the levels by approximately 1 kHz - the states with lower $\mathbf{F_1}$ have their energy lowered and states with larger $\mathbf{F_1}$ have it made larger.

Next, we would like to evaluate the same terms in the uncoupled basis, which is proper to use in the presence of external fields. Here, the proper quantum numbers are $|J, \Omega, M_J; I_1, M_{I_1}; I_2, M_{I_2}\rangle$. In this basis the old notation formulas of Eq. (2.1.1) and Eq. (2.1.2) are actually easier to use in practice, but for the sake of completeness we will use the approach used for the coupled basis. Just like before, we start with the spin-rotation interaction. Because now both terms of the scalar product act on uncoupled angular momenta with separate projections, we have to pay special attention to the scalar product (as before, in these terms we ignore Ω and the resulting $\delta_{\Omega,\Omega'}$ pre-factor):

$$\left\langle J, M_J; I_1, M_{I_1}; I_2, M_{I_2} \middle| T^1(\mathbf{I_1}) \cdot T^1(\mathbf{J}) \middle| J', M_J'; I_1', M_{I_1}'; I_2', M_{I_2}' \right\rangle =$$

$$\delta_{I_2, I_2'} \delta_{M_{I_2}, M_{I_2}'} \left\langle J, M_J; I_1, M_{I_1} \middle| \sum_p (-1)^p T_p^1(\mathbf{J}) \cdot T_{-p}^1(\mathbf{I_1}) \middle| J', M_J'; I_1', M_{I_1}' \right\rangle .$$

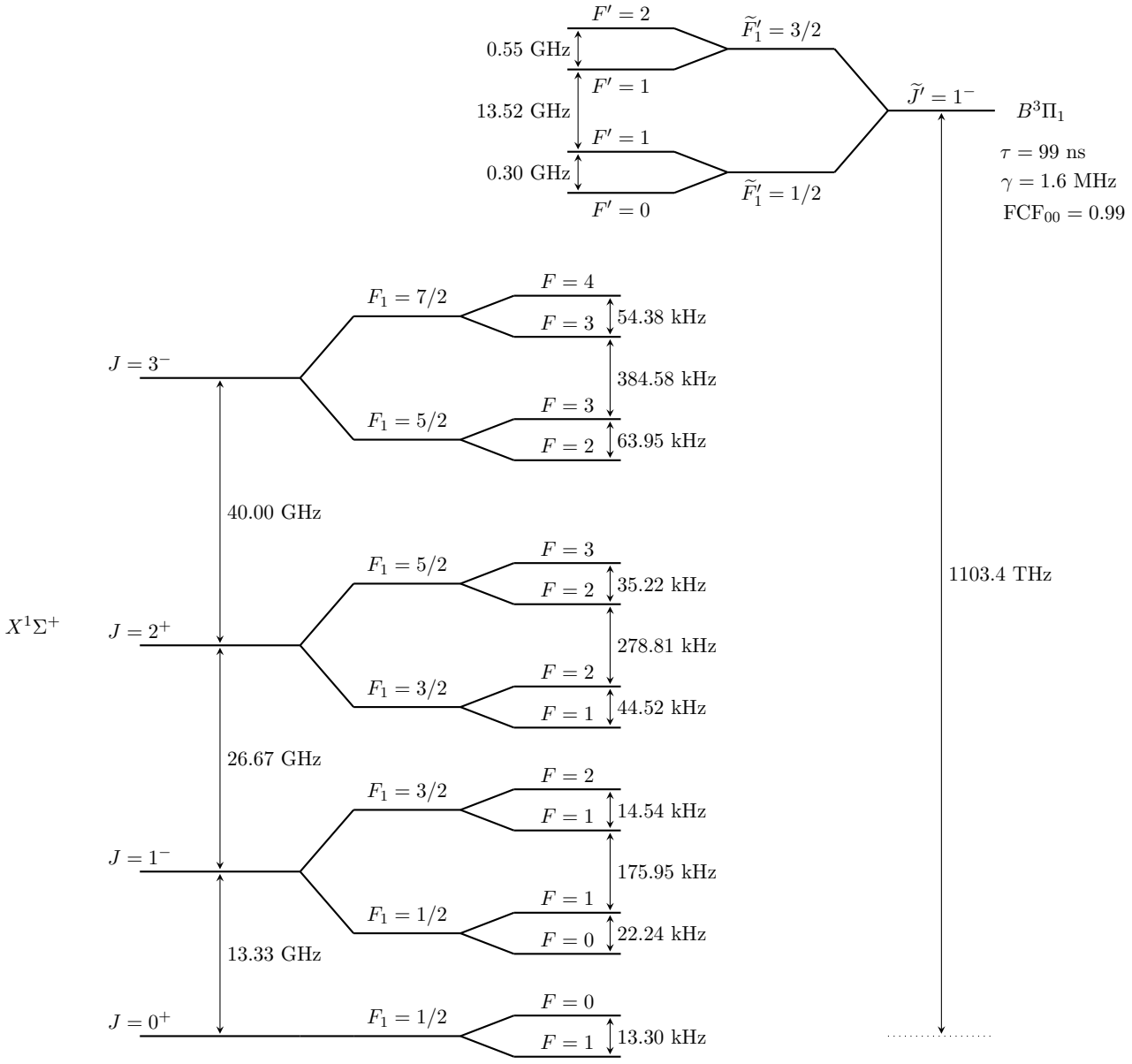

Figure 2.2.1: Diagram of TlF states $X^1\Sigma^+$ and $B^3\Pi_1$ that are considered in the coupled basis, with no applied fields. Splittings for the excited electronic states are obtained from spectroscopic measurements. All numbers are provided in linear frequency units (i.e. $E = hf$).

Because both operators act on uncoupled angular momenta, we can just simply separate the scalar product. From there:

$$\sum_p (-1)^p \left\langle J, M_J \middle| T^1_p(\mathbf{J}) \middle| J', M'_J \right\rangle \left\langle I_1, M_{I_1} \middle| T^1_{-p}(\mathbf{I_1}) \middle| I'_1, M'_{I_1} \right\rangle \overset{(A.1)}{=} \sum_p (-1)^p (-1)^{J-M_J} \begin{pmatrix} J & 1 & J' \\ -M_J & p & M'_J \end{pmatrix}$$

$$\left\langle J \middle\| T^1_p(\mathbf{J}) \middle\| J' \right\rangle (-1)^{I_1 - M_{I_1}} \begin{pmatrix} I_1 & 1 & I'_1 \\ -M_{I_1} & -p & M'_{I_1} \end{pmatrix} \left\langle I_1 \middle\| T^1_{-p}(\mathbf{I_1}) \middle\| I'_1 \right\rangle$$

$$\overset{(A.2)}{=} \sum_p (-1)^p \delta_{J,J'} \delta_{I_1,I'_1} (-1)^{J-M_J} (-1)^{I_1 - M_{I_1}} \sqrt{J(J+1)(2J+1)} \sqrt{I_1(I_1+1)(2I_1+1)}$$

$$\begin{pmatrix} J & 1 & J' \\ -M_J & p & M'_J \end{pmatrix} \begin{pmatrix} I_1 & 1 & I'_1 \\ -M_{I_1} & -p & M'_{I_1} \end{pmatrix}.$$

Once we put everything together and remember that $I_1 = I'_1 = I_2 = I'_2 = 1/2$ we obtain:

$$\left\langle J, M_J; I_1, M_{I_1}; I_2, M_{I_2} \middle| T^1(\mathbf{I_1}) \cdot T^1(\mathbf{J}) \middle| J', M'_J; I'_1, M'_{I_1}; I'_2, M'_{I_2} \right\rangle = \sqrt{\frac{3}{2}} \delta_{M_{I_2}, M'_{I_2}} (-1)^{J+1/2-M_J-M_{I_1}}$$

$$\sqrt{J(J+1)(2J+1)} \sum_p (-1)^p \begin{pmatrix} J & 1 & J \\ -M_J & p & M'_J \end{pmatrix} \begin{pmatrix} \frac{1}{2} & 1 & \frac{1}{2} \\ -M_{I_1} & -p & M'_{I_1} \end{pmatrix}. \tag{2.2.5}$$

Analogically, for the second spin-rotation term we get:

$$\left\langle J, M_J; I_1, M_{I_1}; I_2, M_{I_2} \middle| T^1(\mathbf{I_2}) \cdot T^1(\mathbf{J}) \middle| J', M'_J; I'_1, M'_{I_1}; I'_2, M'_{I_2} \right\rangle = \sqrt{\frac{3}{2}} \delta_{M_{I_1}, M'_{I_1}} (-1)^{J+1/2-M_J-M_{I_2}}$$

$$\sqrt{J(J+1)(2J+1)} \sum_p (-1)^p \begin{pmatrix} J & 1 & J \\ -M_J & p & M'_J \end{pmatrix} \begin{pmatrix} \frac{1}{2} & 1 & \frac{1}{2} \\ -M_{I_2} & -p & M'_{I_2} \end{pmatrix}. \tag{2.2.6}$$

The direct spin-spin interaction term is trivial to evaluate in the uncoupled basis as well:

$$\left\langle J, M_J; I_1, M_{I_1}; I_2, M_{I_2} \middle| T^1(\mathbf{I_1}) \cdot T^1(\mathbf{I_2}) \middle| J', M'_J; I'_1, M'_{I_1}; I'_2, M'_{I_2} \right\rangle = \frac{3}{2} \delta_{M_J, M'_J} \delta_{J,J'} (-1)^{1-M_{I_1}-M_{I_2}}$$

$$\sum_p (-1)^p \begin{pmatrix} \frac{1}{2} & 1 & \frac{1}{2} \\ -M_{I_1} & p & M'_{I_1} \end{pmatrix} \begin{pmatrix} \frac{1}{2} & 1 & \frac{1}{2} \\ -M_{I_2} & -p & M'_{I_2} \end{pmatrix}. \tag{2.2.7}$$

The dipolar term in the uncoupled basis is, on the other hand, truly messy. First, we use the explicit form of scalar product of two rank-1 tensors and then combine this with Wigner-Eckart

theorem and reduced matrix element for a rank-1 tensor:

$$\left\langle \eta; J, \Omega, M_J; I_1, M_{I_1}; I_2, M_{I_2} \middle| T^1(\mathbf{C^2}, \mathbf{I_1}) \cdot T^1(\mathbf{I_2}) \middle| \eta'; J', \Omega', M'_J; I'_1, M'_{I_1}; I'_2, M'_{I_2} \right\rangle =$$

$$= \sum_p (-1)^p \left\langle I_2, M_{I_2} \middle| T^1_{-p}(\mathbf{I_2}) \middle| I'_2, M'_{I_2} \right\rangle \left\langle \eta; J, \Omega, M_J; I_1, M_{I_1} \middle| T^1_p(\mathbf{C^2}, \mathbf{I_1}) \middle| \eta'; J', \Omega', M'_J; I'_1, M'_{I_1} \right\rangle$$

$$= \sum_p (-1)^p (-1)^{I_2 - M_{I_2}} \sqrt{I_2(I_2+1)(2I_2+1)} \begin{pmatrix} I_2 & 1 & I_2 \\ -M_{I_2} & -p & M'_{I_2} \end{pmatrix}$$

$$\left\langle \eta; J, \Omega, M_J; I_1, M_{I_1} \middle| T^1_p(\mathbf{C^2}, \mathbf{I_1}) \middle| \eta'; J', \Omega', M'_J; I'_1, M'_{I_1} \right\rangle$$

$$\overset{(A.4)}{=} \sum_p (-1)^p (-1)^{1/2 - M_{I_2}} \sqrt{\frac{3}{2}} \begin{pmatrix} \frac{1}{2} & 1 & \frac{1}{2} \\ -M_{I_2} & -p & M'_{I_2} \end{pmatrix} \sum_{p_1 p_2} (-1)^{2-1+p} \sqrt{2+1} \begin{pmatrix} 1 & 2 & 1 \\ p_1 & p_2 & -p \end{pmatrix}$$

$$\left\langle \eta; J, \Omega, M_J; I_1, M_{I_1} \middle| T^2_{p_1}(\mathbf{C}) T^1_{p_2}(\mathbf{I_1}) \middle| \eta'; J', \Omega', M'_J; I'_1, M'_{I_1} \right\rangle .$$

In the last line we decomposed the tensor product as well, which will allow us to easily evaluate two spherical tensors separately. Namely (with $I_1 = 1/2$):

$$\left\langle \eta; J, \Omega, M_J; I_1, M_{I_1} \middle| T^2_{p_1}(\mathbf{C}) T^1_{p_2}(\mathbf{I_1}) \middle| \eta'; J', \Omega', M'_J; I'_1, M'_{I_1} \right\rangle =$$

$$= \left\langle \eta; J, \Omega, M_J \middle| T^2_{p_1}(\mathbf{C}) \middle| \eta'; J', \Omega', M'_J \right\rangle (-1)^{I_1 - M_{I_1}} \sqrt{I_1(I_1+1)(2I_1+1)} \begin{pmatrix} I_1 & 1 & I_1 \\ -M_{I_1} & p_2 & M'_{I_1} \end{pmatrix}$$

$$\overset{(A.1)}{=} (-1)^{J - M_J} \begin{pmatrix} J & 1 & J' \\ -M_J & p_1 & M'_J \end{pmatrix} \left\langle \eta; J, \Omega \middle\| T^2(\mathbf{C}) \middle\| \eta'; J', \Omega' \right\rangle (-1)^{1/2 - M_{I_1}} \sqrt{\frac{3}{2}} \begin{pmatrix} \frac{1}{2} & 1 & \frac{1}{2} \\ -M_{I_1} & p_2 & M'_{I_1} \end{pmatrix} .$$

The reduced matrix element above has already been evaluated. We can now put everything together and note that, like before, in the electronic state we are considering $\Omega = 0$ and the reduced matrix

element of tensor $T^2(\mathbf{C})$ is already included in the constant, and obtain:

$$\left\langle \eta; J, \Omega, M_J; I_1, M_{I_1}; I_2, M_{I_2} \middle| T^1(\mathbf{C^2}, \mathbf{I_1}) \cdot T^1(\mathbf{I_2}) \middle| \eta'; J', \Omega', M'_J; I'_1, M'_{I_1}; I'_2, M'_{I_2} \right\rangle =$$

$$= \sum_{p,p_1,p_2} \frac{3\sqrt{3}}{2} (-1)^{2+2J-M_J-M_{I_1}-M_{I_2}} (-1)^p \sqrt{(2J+1)(2J'+1)} \begin{pmatrix} 1 & 2 & 1 \\ p_1 & p_2 & -p \end{pmatrix}$$

$$\begin{pmatrix} \frac{1}{2} & 1 & \frac{1}{2} \\ -M_{I_1} & p_2 & M'_{I_1} \end{pmatrix} \begin{pmatrix} \frac{1}{2} & 1 & \frac{1}{2} \\ -M_{I_2} & p & M'_{I_2} \end{pmatrix} \begin{pmatrix} J & 1 & J' \\ -M_J & p_1 & M'_J \end{pmatrix} \begin{pmatrix} J & 2 & J' \\ 0 & 0 & 0 \end{pmatrix}. \tag{2.2.8}$$

2.3 Zeeman Effect in TlF

Thallium fluoride's ground state $X^1\Sigma^+$ having $\mathbf{L} = 0$ and $\mathbf{S} = 0$ is not expected to experience a strong Zeeman effect. Nevertheless, in the experiment the regions where state transfer and projection occur will not be magnetically shielded, so it is crucial that we evaluate the magnetic field contributions. Following [41], we effectively have the following terms contributing to the Zeeman effect:

1. $g_S \mu_B B_z T^1_0(\mathbf{S})$ - electron spin isotropic contribution
2. $g_l \mu_B B_z \sum_{q=\pm1} \mathscr{D}^{(1)}_{0q}(\omega)^* T^1_q(\mathbf{S})$ - electron spin anisotropic contribution
3. $g'_L \mu_B B_z T^1_0(\mathbf{L})$ - electron orbital angular momentum (g'_L is assumed to account for relativistic, diamagnetic and non-adiabatic effects)
4. $-g_r \mu_B B_z T^1_0(\mathbf{R})$ - rotational magnetic moment contribution
5. $-\sum_\alpha g^\alpha_N \mu_N B_z T^1_0(\mathbf{I}^\alpha)$ - nuclear spins
6. $\mu_B B_Z \sum_{q=\pm1} e^{-2iq\phi} \left[g'_L \mathscr{D}^{(1)}_{0,-q}(\omega)^* T^1_q(\mathbf{S}) - g^{e'}_r \sum_p (-1)^p \mathscr{D}^{(1)}_{-p,-q}(\omega)^* T^1_p(\mathbf{R}) \mathscr{D}^{(1)}_{0,-q}(\omega)^* \right]$ - parity-dependent contributions for Π states
7. $T^2(\chi) \cdot T^2_0(B, B)$ - anisotropic magnetic susceptibility contribution

We will evaluate contributions 1 through 5 - we are considering a $^1\Sigma$ state and look only at linear terms. We shall do so in the basis with coupled nuclear spins, which is true only for small fields, and in the uncoupled basis, and we will always assume that B-field defines a z-axis. We begin

with the coupled basis and the electron spin isotropic contribution, which for the considered state will be 0, but will be evaluated regardless. Remembering that in Hund's case (c) $\mathbf{J} = \mathbf{R} + \mathbf{J_a}$ and $\mathbf{J_a} = \mathbf{L} + \mathbf{S}$. Our matrix element will be:

$$\begin{aligned}\left\langle g_S \mu_B B_z T_0^1(\mathbf{S}) \right\rangle &= \left\langle J_a; J, \Omega, F_1, F, M_F \middle| g_S \mu_B B_z T_0^1(\mathbf{S}) \middle| J_a'; J', \Omega', F_1', F', M_F' \right\rangle \\ &= \left\langle J_a; J, \Omega, F_1, F, M_F \middle| g_S \mu_B B_z \sum_{q=-1,0,1} \mathscr{D}_{0,q}^{(1)}(\omega)^* \, T_q^1(\mathbf{S}) \middle| J_a'; J', \Omega', F_1', F', M_F' \right\rangle .\end{aligned}$$

It is worth noting that the operator $\mathscr{D}_{0,q}^{(1)}(\omega)^*$, as we saw before, will act on $\mathbf{J}$ and Ω, while the spin operator $T_q^1(\mathbf{S})$ will act on $\mathbf{J_a}$ and Ω. We now obtain:

$$\begin{aligned}\left\langle g_S \mu_B B_z T_0^1(\mathbf{S}) \right\rangle &= \left\langle J_a; J, \Omega, F_1, F, M_F \middle| g_S \mu_B B_z \sum_{q=-1,0,1} \mathscr{D}_{0,q}^{(1)}(\omega)^* T_q^1(\mathbf{S}) \middle| J_a'; J', \Omega', F_1', F', M_F' \right\rangle \\ &= g_S \mu_B B_z (-1)^{F - M_F + F' + F_1 + F_1' + J + 3} \sqrt{(2F+1)(2F'+1)(2F_1+1)(2F_1'+1)} \\ &\begin{pmatrix} F & 1 & F' \\ -M_F & 0 & M_F' \end{pmatrix} \begin{Bmatrix} F_1' & F' & \frac{1}{2} \\ F & F_1 & 1 \end{Bmatrix} \begin{Bmatrix} J' & F_1' & \frac{1}{2} \\ F_1 & J & 1 \end{Bmatrix} \\ &\sum_{q=-1,0,1} \left\langle J, \Omega \middle\| \mathscr{D}_{.,q}^{(1)}(\omega)^* \middle\| J', \Omega' \right\rangle \left\langle L, S, J_a, \Omega \middle| T_q^1(\mathbf{S}) \middle| L', S', J_a', \Omega' \right\rangle .\end{aligned}$$

Due to Ω-doubling in some cases (for example in the $B^3\Pi_1$ state) normally we should include parity of the states as well, but because we are considering the Σ state we will simply calculate the matrix element for a single pure Ω state, not their superpositions with defined $|\Omega|$. We can now use Eq. (A.9) together with the Wigner-Eckart theorem to obtain:

$$\begin{aligned}\left\langle L, S, J_a, \Omega \middle| T_q^1(S) \middle| L', S', J_a', \Omega' \right\rangle &= (-1)^{J_a - \Omega} \begin{pmatrix} J_a & 1 & J_a' \\ -\Omega & q & \Omega' \end{pmatrix} \left\langle L, S, J_a \middle\| T^1(\mathbf{S}) \middle\| L', S', J_a' \right\rangle \\ &= (-1)^{J_a - \Omega} \begin{pmatrix} J_a & 1 & J_a' \\ -\Omega & q & \Omega' \end{pmatrix} (-1)^{J_a + L + S + 1} \delta_{L,L'} \sqrt{(2J_a+1)(2J_a'+1)} \\ &\begin{Bmatrix} S' & J_a' & L \\ J_a & S & 1 \end{Bmatrix} \delta_{S,S'} \sqrt{S(S+1)(2S+1)}.\end{aligned}$$

Putting it all together we get:

$$\left\langle g_S \mu_B B_z T^1_0(\mathbf{S}) \right\rangle = g_S \mu_B B_z \delta_{L,L'} \delta_{S,S'} (-1)^{F-M_F+F'+F_1+F_1'+2J+2J_a-2\Omega+L+S+4} \sqrt{(2F+1)(2F'+1)}$$
$$\sqrt{(2F_1+1)(2F_1'+1)(2J+1)(2J'+1)(2J_a+1)(2J_a'+1)S(S+1)(2S+1)}$$
$$\begin{pmatrix} F & 1 & F' \\ -M_F & 0 & M_F' \end{pmatrix} \begin{Bmatrix} F_1' & F' & \frac{1}{2} \\ F & F_1 & 1 \end{Bmatrix} \begin{Bmatrix} J' & F_1' & \frac{1}{2} \\ F_1 & J & 1 \end{Bmatrix} \begin{Bmatrix} S & J_a' & L \\ J_a & S & 1 \end{Bmatrix}$$
$$\sum_{q=-1,0,1} \begin{pmatrix} J & 1 & J' \\ -\Omega & q & \Omega' \end{pmatrix} \begin{pmatrix} J_a & 1 & J_a' \\ -\Omega & q & \Omega' \end{pmatrix}. \tag{2.3.1}$$

In a very similar way, we can evaluate the orbital magnetic moment contribution:

$$\left\langle g_L' \mu_B B_z T^1_0(\mathbf{L}) \right\rangle = g_L' \mu_B B_z \delta_{L,L'} \delta_{S,S'} (-1)^{F-M_F+F'+F_1+F_1'+2J+2J_a-2\Omega+L+S+4} \sqrt{(2F+1)(2F'+1)}$$
$$\sqrt{(2F_1+1)(2F_1'+1)(2J+1)(2J'+1)(2J_a+1)(2J_a'+1)L(L+1)(2L+1)}$$
$$\begin{pmatrix} F & 1 & F' \\ -M_F & 0 & M_F' \end{pmatrix} \begin{Bmatrix} F_1' & F' & \frac{1}{2} \\ F & F_1 & 1 \end{Bmatrix} \begin{Bmatrix} J' & F_1' & \frac{1}{2} \\ F_1 & J & 1 \end{Bmatrix} \begin{Bmatrix} L' & J_a' & S \\ J_a & L & 1 \end{Bmatrix}$$
$$\sum_{q=-1,0,1} \begin{pmatrix} J & 1 & J' \\ -\Omega & q & \Omega' \end{pmatrix} \begin{pmatrix} J_a & 1 & J_a' \\ -\Omega & q & \Omega' \end{pmatrix}. \tag{2.3.2}$$

As can be seen, both terms Eq. (2.3.1) and Eq. (2.3.2) are 0 for $\mathbf{S} = 0$ and $\mathbf{L} = 0$ respectively. The anisotropic contribution will have an identical form to Eq. (2.3.1), though the sum will go over $q = \pm 1$ and the g-factor will be changed to g_l from g_S. That term is also 0 for a $^1\Sigma$ state.

To evaluate the rotational magnetic moment contribution, first let's point out that $\mathbf{R} = \mathbf{J} - \mathbf{J_a} = \mathbf{J} - \mathbf{L} - \mathbf{S}$. This means, that the rotational contribution will change the effective g-factors in spin and orbital contributions: Eq. (2.3.1) will effectively have a g-factor of $g_S + g_r$ and Eq. (2.3.2) a g-factor of $g_L' + g_r$. A new contribution will come from coupling to the total angular momentum.

We have:

$$\left\langle -g_r\mu_B B_z T^1_0(\mathbf{J})\right\rangle = -g_r\mu_B B_z(-1)^{F-M_F+F'+F_1+F_1'+J+3}\sqrt{(2F+1)(2F'+1)(2F_1+1)(2F_1'+1)}$$

$$\begin{pmatrix} F & 1 & F' \\ -M_F & 0 & M_F' \end{pmatrix}\begin{Bmatrix} F_1' & F' & \frac{1}{2} \\ F & F_1 & 1 \end{Bmatrix}\begin{Bmatrix} J' & F_1' & \frac{1}{2} \\ F_1 & J & 1 \end{Bmatrix}\left\langle J\middle\| T^1(\mathbf{J})\middle\| J\right\rangle$$

$$= -g_r\mu_B B_z\delta_{J,J'}(-1)^{F-M_F+F'+F_1+F_1'+J+3}\sqrt{(2F+1)(2F'+1)(2F_1+1)(2F_1'+1)}$$

$$\sqrt{J(J+1)(2J+1)}\begin{pmatrix} F & 1 & F' \\ -M_F & 0 & M_F' \end{pmatrix}\begin{Bmatrix} F_1' & F' & \frac{1}{2} \\ F & F_1 & 1 \end{Bmatrix}\begin{Bmatrix} J' & F_1' & \frac{1}{2} \\ F_1 & J & 1 \end{Bmatrix}. \tag{2.3.3}$$

Contribution from the nuclear spin in coupled basis are also quite easy to evaluate. For $\mathbf{I_2}$ we obtain:

$$\left\langle -g_N^{(2)}\mu_N B_z T^1_0(\mathbf{I_2})\right\rangle = \left\langle J; F_1, I_2, F, M_F\middle| -g_N^{(2)}\mu_N B_z T^1_0(\mathbf{I_2})\middle| J; F_1', I_2', F', M_F'\right\rangle$$

$$= -g_N^{(2)}\mu_N B_z(-1)^{F-M_F+F'+F_1+3/2}\sqrt{(2F+1)(2F'+1)}\begin{pmatrix} F & 1 & F' \\ -M_F & 0 & M_F' \end{pmatrix}$$

$$\begin{Bmatrix} I_2' & F' & F_1 \\ F & I_2 & 1 \end{Bmatrix}\delta_{F_1,F_1'}\delta_{I_2,I_2'}\delta_{J,J'}\sqrt{I_2(I_2+1)(2I_2+1)}$$

$$= -\sqrt{\frac{3}{2}}g_N^{(2)}\mu_N B_z\delta_{J,J'}\delta_{F_1,F_1'}(-1)^{F-M_F+F'+F_1+3/2}\sqrt{(2F+1)(2F'+1)}$$

$$\begin{pmatrix} F & 1 & F' \\ -M_F & 0 & M_F' \end{pmatrix}\begin{Bmatrix} \frac{1}{2} & F' & F_1 \\ F & \frac{1}{2} & 1 \end{Bmatrix}. \tag{2.3.4}$$

Analogically, for $\mathbf{I_1}$ we have:

$$\left\langle -g_N^{(1)}\mu_N B_z T^1_0(\mathbf{I_1})\right\rangle = \left\langle J, I_1, F_1, I_2, F, M_F\middle| -g_N^{(1)}\mu_N B_z T^1_0(\mathbf{I_1})\middle| J', I_1', F_1', I_2', F', M_F'\right\rangle$$

$$= -\sqrt{\frac{3}{2}}g_N^{(1)}\mu_N B_z\delta_{J,J'}(-1)^{F-M_F+F'+F_1+F_1'+J+3}\sqrt{(2F+1)(2F'+1)(2F_1+1)(2F_1'+1)}$$

$$\begin{pmatrix} F & 1 & F' \\ -M_F & 0 & M_F' \end{pmatrix}\begin{Bmatrix} F_1' & F' & \frac{1}{2} \\ F & F_1 & 1 \end{Bmatrix}\begin{Bmatrix} \frac{1}{2} & F_1' & J \\ F_1 & \frac{1}{2} & 1 \end{Bmatrix}. \tag{2.3.5}$$

If we were now working in decoupled basis, we would obtain simpler results. For example, nuclear spins will not contribute to spin and orbital Zeeman effects:

$$\begin{aligned}\left\langle g_S\mu_B B_z T^1_0(\mathbf{S})\right\rangle =& \left\langle J_a; J,\Omega,M_J; I_1,M_{I_1}; I_2,M_{I_2}\middle| g_S\mu_B B_z T^1_q(\mathbf{S})\middle| J'_a; J',\Omega',M'_J; I_1,M'_{I_1}; I_2,M'_{I_2}\right\rangle \\ &= g_S\mu_B B_z \delta_{L,L'}\delta_{S,S'}\delta_{M_{I_1},M'_{I_1}}\delta_{M_{I_2},M'_{I_2}}(-1)^{2J-M_J+2J_a-2\Omega+L+S+1}\sqrt{(2J+1)(2J'+1)} \\ &\sqrt{(2J_a+1)(2J'_a+1)S(S+1)(2S+1)}\begin{pmatrix} J & 1 & J' \\ -M_J & 0 & M'_J\end{pmatrix}\begin{Bmatrix} S & J'_a & L \\ J_a & S & 1\end{Bmatrix} \\ &\sum_{q=-1,0,1}\begin{pmatrix} J & 1 & J' \\ -\Omega & q & \Omega'\end{pmatrix}\begin{pmatrix} J_a & 1 & J'_a \\ -\Omega & q & \Omega'\end{pmatrix},\end{aligned} \tag{2.3.6}$$

for the spin contribution and:

$$\begin{aligned}\left\langle g_S\mu_B B_z T^1_0(\mathbf{L})\right\rangle =& \left\langle J_a; J,\Omega,M_J; I_1,M_{I_1}; I_2,M_{I_2}\middle| g'_L\mu_B B_z T^1_0(\mathbf{L})\middle| J'_a; J',\Omega',M'_J; I_1,M'_{I_1}; I_2,M'_{I_2}\right\rangle \\ &= g_S\mu_B B_z \delta_{L,L'}\delta_{S,S'}\delta_{M_{I_1},M'_{I_1}}\delta_{M_{I_2},M'_{I_2}}(-1)^{2J-M_J+2J_a-2\Omega+L+S+1}\sqrt{(2J+1)(2J'+1)} \\ &\sqrt{(2J_a+1)(2J'_a+1)L(L+1)(2L+1)}\begin{pmatrix} J & 1 & J' \\ -M_J & 0 & M'_J\end{pmatrix}\begin{Bmatrix} L & J'_a & S \\ J_a & L & 1\end{Bmatrix} \\ &\sum_{q=-1,0,1}\begin{pmatrix} J & 1 & J' \\ -\Omega & q & \Omega'\end{pmatrix}\begin{pmatrix} J_a & 1 & J'_a \\ -\Omega & q & \Omega'\end{pmatrix},\end{aligned} \tag{2.3.7}$$

for the orbital angular momentum. Both terms are 0 for the $^1\Sigma$ state. The rotational magnetic moment contribution in the decoupled basis becomes much simpler:

$$\begin{aligned}\left\langle -g_r\mu_B B_z T^1_0(\mathbf{J})\right\rangle =& -g_r\mu_B B_z \delta_{J,J'}\delta_{I_1,I'_1}\delta_{I_2,I'_2}\delta_{M_{I_1},M'_{I_1}}\delta_{M_{I_2},M'_{I_2}} \\ &(-1)^{J-M_J}\sqrt{J(J+1)(2J+1)}\begin{pmatrix} J & 1 & J' \\ -M_J & 0 & M'_J\end{pmatrix} \\ &= -g_r\mu_B B_z M_J\,\delta_{J,J'}\delta_{M_{I_1},M'_{I_1}}\delta_{M_{I_2},M'_{I_2}}.\end{aligned} \tag{2.3.8}$$

The nuclear spin contributions have the same form in the decoupled basis:

$$\left\langle -g_N^{(1)}\mu_N B_z T_0^1(\mathbf{I_1})\right\rangle = -g_N^{(1)}\mu_B B_z M_{I_1}\,\delta_{J,J'}\delta_{M_{I_2},M'_{I_2}} \tag{2.3.9}$$

$$\left\langle -g_N^{(2)}\mu_N B_z T_0^1(\mathbf{I_2})\right\rangle = -g_N^{(2)}\mu_B B_z M_{I_2}\,\delta_{J,J'}\delta_{M_{I_1},M'_{I_1}}\,. \tag{2.3.10}$$

Finally, we provide mean values [36] for TlF g-factors relevant here and in $\mathcal{H}_\mathrm{Z}$ of Eq. (2.1.3): $\mu_J \equiv g_r\mu_B = 35$ Hz/G, $\mu_1^{205} \equiv g_N^{(1)}\mu_B = 1.2405$ kHz/G and $\mu_2 \equiv g_N^{(2)}\mu_B = 2.004$ kHz/G, where (1) and (2) correspond to thallium and fluorine respectively. As can be seen, all the factors are very small, and so we would potentially require fields of couple hundred to a thousand Gauss to efficiently remix our dark states or to decouple our spins.

2.4 Stark Effect in TlF

The next crucial piece is the Stark hamiltonian $\mathcal{H}_\mathrm{S}$. In CeNTREX apparatus, TlF molecules experience a non-zero electric and (nominally) zero magnetic field, and, in general, the contribution to the hamiltonian is simply equal to $-\boldsymbol{\mu}\cdot\boldsymbol{\mathcal{E}}$, where $\boldsymbol{\mu}$ is molecule's permanent dipole moment equal to $\mu_0 = 4.2282$ Debye [36]. The character of the energy eigenstates changes significantly depending on the magnitude of the electric field $\mathcal{E}$, which varies extremely between different stages of the experiment. Therefore, we will describe the energy eigenstates of the molecule's electronic ground state in different regimes of $\mathcal{E}$-field strength (with $B = 0$), as defined by the ratio of Stark shifts, $\Delta E_\mathrm{S} = \langle\mathcal{H}_\mathrm{S}\rangle \sim \mu_0^2\mathcal{E}^2/B_\mathrm{rot}$, to the strength of hyperfine interactions, $E_\mathrm{hf} = \langle\mathcal{H}_\mathrm{sr} + \mathcal{H}_\mathrm{ss}\rangle \sim c_j$, or rotational energies, $E_\mathrm{rot} = \langle\mathcal{H}_\mathrm{rot}\rangle \sim B_\mathrm{rot}$. In all regimes, the total angular momentum projection M_F along the quantization axis (usually defined by the local direction of $\boldsymbol{\mathcal{E}}$) is an exact quantum number.

In the low-field regime, where $\Delta E_\mathrm{S} \ll E_\mathrm{hf}$, energy eigenstates can be still approximately described by the J, F, and F_1 quantum numbers. However, already in the mid-field regime, where $E_\mathrm{hf} \ll \Delta E_\mathrm{S} \ll E_\mathrm{rot}$, both J and M_J are approximate quantum numbers. We also have two distinct cases. For $M_J = \pm 1$, $\mathbf{J}$ is strongly coupled to the molecular axis $\hat{\mathbf{n}}$, and therefore also to $\boldsymbol{\mathcal{E}}$, and both nuclear spins are coupled to $\mathbf{J}$ (and so they are coupled to $\boldsymbol{\mathcal{E}}$ as well) by the spin-rotation interaction. Thus, in this case the approximate nuclear spin quantum numbers are M_{I_1} and M_{I_2} and the fully decoupled basis is the one to use. When $M_J = 0$ (including the $J = 0$ case), the nuclear spins decouple from $\mathbf{J}$ and $\boldsymbol{\mathcal{E}}$. Nonetheless, they are still coupled to each other through the

Regime	Definition	Field strength	Approx. eigenstates
Low	$\Delta E_{\mathrm{S}} \ll E_{\mathrm{hf}}$	$\mathcal{E} \lesssim 50\,\mathrm{V/cm}$	$\lvert J, F_1, F, M_F\rangle$
Mid	$E_{\mathrm{hf}} \ll \Delta E_{\mathrm{S}} \ll E_{\mathrm{rot}}$	$50\,\mathrm{V/cm} \ll \mathcal{E} \lesssim 5\,\mathrm{kV/cm}$	$\lvert J, M_J \neq 0\rangle \lvert M_{I_1}, M_{I_2}\rangle$ $\lvert J, M_J = 0\rangle \lvert I_t, M_{I_t}\rangle$
High	$E_{\mathrm{hf}} \ll E_{\mathrm{rot}} \lesssim \Delta E_{\mathrm{S}}$	$5\,\mathrm{kV/cm} \ll \mathcal{E}$	$\left\lvert \widetilde{J}, M_J \neq 0 \right\rangle \lvert M_{I_1}, M_{I_2}\rangle$ $\left\lvert \widetilde{J}, M_J = 0 \right\rangle \lvert I_t, M_{It}\rangle$

Table 2.4.1: Regimes of electric field strength and associated eigenstates in TlF. Table prepared by the CeNTREX collaboration.

spin-spin interaction, and so the state can be described by $\mathbf{I}_t = \mathbf{I}_1 + \mathbf{I}_2$ (the total nuclear spin) and M_{I_t} (its projection) in addition to J and $M_J = 0$.

In the high-field regime where $E_{\mathrm{hf}} \ll E_{\mathrm{rot}} \lesssim \Delta E_{\mathrm{S}}$, the rotational states J are significantly mixed, and separations between M_J states are on the order of E_{rot}. Here, just like in the mid-field regime, the decoupled basis represents the approximate quantum numbers - the eigenstates are defined by the same quantum numbers, aside from J. For these strongly mixed states we usually use a notation $\widetilde{J}$. This quantum number corresponds to the value of J that any given state connects to adiabatically, if the $\mathcal{E}$-field is reduced. Table 2.4.1 summarizes the different regimes and associated eigenstates.

We will now evaluate the Stark effect for any electric field direction and start with the low-field coupled basis. We have:

$$\langle -\boldsymbol{\mu}\cdot\boldsymbol{\mathcal{E}}\rangle = -\sum_p \left\langle J,\Omega,F_1,F,M_F\right|(-1)^p\, T^1_p(\boldsymbol{\mu})T^1_{-p}(\boldsymbol{\mathcal{E}})\left|J',\Omega',F_1',F',M_F'\right\rangle$$

$$\overset{(A.1)}{=} -\sum_p (-1)^p(-1)^{F-M_F}\mathcal{E}_{-p}\begin{pmatrix} F & 1 & F' \\ -M_F & p & M_F'\end{pmatrix}\left\langle J,\Omega,F_1,F\right\|T^1(\boldsymbol{\mu})\left\|J',\Omega',F_1',F'\right\rangle.$$

Next, to evaluate the reduced matrix element of the tensor related to the permanent dipole we use

Eq. (A.7) and obtain:

$$\left\langle J,\Omega,F_1,F\middle\|T^1(\boldsymbol{\mu})\middle\|J',\Omega',F_1',F'\right\rangle = (-1)^{F'+F_1+F_1'+J+3}\sqrt{(2F+1)(2F'+1)(2F_1+1)(2F_1'+1)}$$
$$\begin{Bmatrix} F_1' & F' & \frac{1}{2} \\ F & F_1 & 1 \end{Bmatrix}\begin{Bmatrix} J' & F_1' & \frac{1}{2} \\ F_1 & J & 1 \end{Bmatrix}\left\langle J,\Omega\middle\|T^1(\boldsymbol{\mu})\middle\|J',\Omega'\right\rangle.$$

The next step requires us to move from the space-fixed coordinate system to the molecule-fixed coordinate system. We do that using Wigner D-function remembering that the permanent dipole has the component along the internuclear axis only ($q=0$) and that for the $^1\Sigma$ state $\Omega=0$:

$$\begin{aligned}\left\langle J,\Omega\middle\|T^1(\boldsymbol{\mu})\middle\|J',\Omega'\right\rangle &= \sum_q \left\langle J,\Omega\middle\|\mathscr{D}^{(k)}_{.q}(\omega)^* T^1_q(\boldsymbol{\mu})\middle\|J',\Omega'\right\rangle \\ &= \mu_0\left\langle J,\Omega\middle\|\mathscr{D}^{(k)}_{.0}(\omega)^*\middle\|J',\Omega'\right\rangle \\ &\overset{(A.9)}{=} (-1)^J\sqrt{(2J'+1)(2J+1)}\begin{pmatrix} J & 1 & J' \\ 0 & 0 & 0\end{pmatrix}.\end{aligned}$$

Finally, combining all the terms gives us:

$$\langle -\boldsymbol{\mu}\cdot\boldsymbol{\mathcal{E}}\rangle = -\mu_0\sum_p (-1)^p(-1)^{F-M_F+F'+F_1+F_1'+2J+3}\mathcal{E}_{-p}\sqrt{(2F+1)(2F'+1)(2F_1+1)(2F_1'+1)}$$
$$\sqrt{(2J+1)(2J'+1)}\begin{pmatrix} F & 1 & F' \\ -M_F & p & M_F'\end{pmatrix}\begin{Bmatrix} F_1' & F' & \frac{1}{2} \\ F & F_1 & 1 \end{Bmatrix}\begin{Bmatrix} J' & F_1' & \frac{1}{2} \\ F_1 & J & 1 \end{Bmatrix}\begin{pmatrix} J & 1 & J' \\ 0 & 0 & 0\end{pmatrix}. \tag{2.4.1}$$

The term above is also a term used to evaluate the off-diagonal contributions to the hamiltonian for microwave transitions between states within the $X^1\Sigma^+$ electronic state. This comes from the fact that the rotational transitions are induced by interaction of electric dipole moment of the whole molecule with the electric field of microwaves. For the purpose of modeling the rotational cooling and optical cycling this term will be used extensively. Finally, in the uncoupled basis the Stark

effect term is:

$$\langle -\boldsymbol{\mu}\cdot\boldsymbol{\mathcal{E}}\rangle = -\mu_0\delta_{M_{I_1},M'_{I_1}}\delta_{M_{I_2},M'_{I_2}}\sum_p(-1)^p(-1)^{2J-M_J}\mathcal{E}_{-p}\sqrt{(2J+1)(2J'+1)}$$

$$\begin{pmatrix} J & 1 & J' \\ -M_J & p & M'_J \end{pmatrix}\begin{pmatrix} J & 1 & J' \\ 0 & 0 & 0 \end{pmatrix}. \tag{2.4.2}$$

It is worth noting that the last term in the formulas for Stark effect in $^1\Sigma$ state of TlF are non-zero for $J' = J \pm 1$. There is no first-order Stark effect in TlF, but mixing of adjacent rotational level due to the existence of an electric field will lead to quadratic Stark shift, which we use to our advantage in the experiment. If we assume that the field defines the quantization axis ($p = 0$), after diagonalization of a 3-by-3 matrix (including $|J-1\rangle$, $|J\rangle$ and $|J+1\rangle$ states) one obtains an expression for the second-order Stark energy in the decoupled basis (strong field regime):

$$\Delta E_{\mathrm{S}}^{(2)} = -\frac{\mu_0^2\mathcal{E}_z^2}{2B_{\mathrm{rot}}}\frac{J(J+1)-3M_J^2}{J(J+1)(2J-1)(2J+3)}, \tag{2.4.3}$$

with B_{rot} being the effective rotational constant. In figures below we show TlF energy eigenstates with changing electric field magnitudes, which are of huge importance in CeNTREX. Not only we need to understand how the energy eigenstates behave in large electric fields to model the behavior of a focusing component (quadrupole lens discussed later in Chapter 3) that operates in fields of up to 50 kV/cm, but also to analyze the evolution of our $\widetilde{J} = 1$, $M_J = \pm 1$ science states in the ^{205}Tl NSM measurement that is carried out at $\mathcal{E} = 30$ kV/cm. Moreover, the state manipulation in CeNTREX is performed mostly in the low- and mid-field environments and Fig. 2.4.1 shows how the relevant energies and eigenstates evolve in those regimes for $J = 1$ and $J = 2$ states. Bold curves are states directly relevant to CeNTREX. Fig. 2.4.2 shows behavior of states up to $J = 2$ from low to high fields.

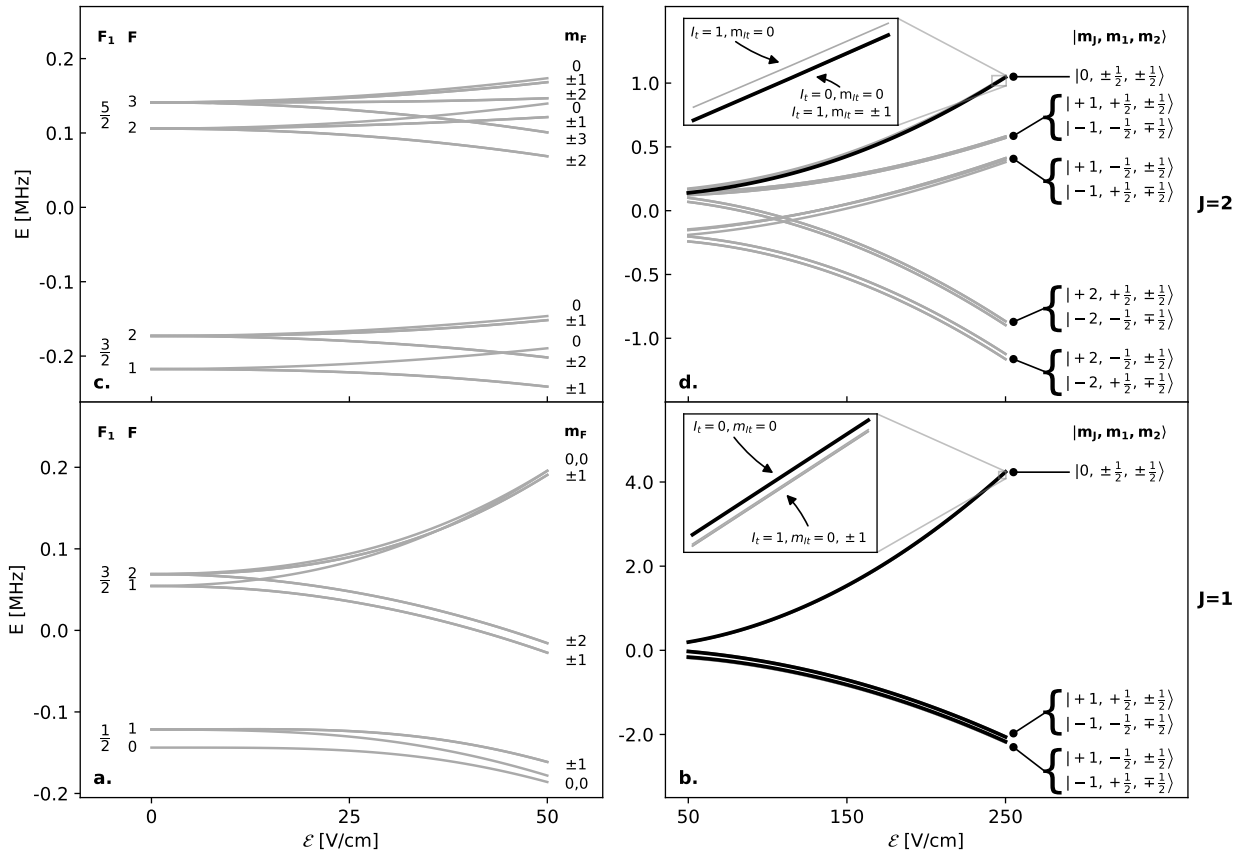

Figure 2.4.1: Overview of the energy eigenstates for changing $\mathcal{E}$-field magnitudes. The low-field regime, where $\Delta E_S \ll E_{hf}$, where energy eigenstates retain J, F, and F_1 as approximate quantum numbers is shown in **a)** for $J = 1$ and **c)** for $J = 2$. The mid-field regime, where $E_{hf} \ll \Delta E_S \ll E_{rot}$, where both J and M_J are approximate quantum numbers is shown in **b)** for $J = 1$ and **d)** for $J = 2$. States used in CeNTREX are shown in bold.

2.5 Dipole Transitions

In CeNTREX, lasers will be tuned to $X^1\Sigma^+(\nu = 0) \rightarrow B^3\Pi_1(\nu = 0)$ transitions in order to manipulate and read out ground state hyperfine and rotational sublevels. Details of the $B^3\Pi_1$ state structure are given in [39, 43]. Here, only a few main features of this state's substructure are important. First, the B state hyperfine splittings are very large ($\gtrsim$ 100 MHz) compared to the natural linewidth of the transition ($\gamma \approx 1.6$ MHz), which is in turn much larger than the hyperfine splittings in the ground X state ($c_j \lesssim 100$ kHz). This means that hyperfine structure is fully resolved in the excited state, but completely unresolved in the ground state. Thus, optical

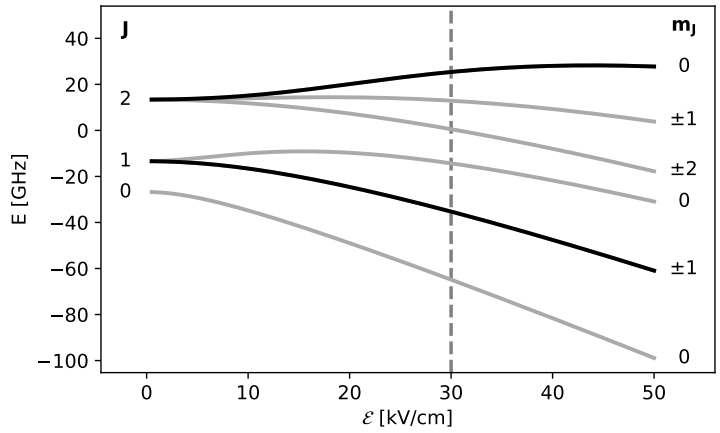

Figure 2.4.2: Evolution of the energy eigenstates of the TlF Hamiltonian (Eq. (2.1.3)) for $\mathcal{E}$ ranging from 0 V/cm to 50 kV/cm, for $J = 0, 1, 2$. States used in CeNTREX are shown in bold. Hyperfine structure is unresolved in this plot.

transitions in TlF couple a large number of hyperfine levels (with a given value of J) in the ground state to a single hyperfine state with quantum numbers $\widetilde{J}, \widetilde{F}_1$ and exact quantum number F in the excited state. Another important feature of the B state is that its matrix of Franck-Condon factors (FCFs) for decay to the X state is extremely diagonal [44], such that $\sim 99\%$ of the time the $B(\nu = 0)$ vibrational state decays back to the vibrational ground state $X(\nu = 0)$, which enables optical pumping and optical cycling processes to take place with almost no loss. However, the mixing of J and F_1 due to B-state hyperfine interaction substantially modifies rotational selection rules in $B - X$ decays. It must be taken into account when describing optical excitation and emission in TlF, and it will be addressed here.

In simulations and modeling of both rotational cooling and optical cycling it is important to understand the dipole transitions between the ground and excited electronic states. In order to find correct off-diagonal terms in the hamiltonian, we need to find the Rabi frequencies. Such an off-diagonal element will then be proportional to Ω_R, where for a dipole transition from state $|i\rangle$ to $|f\rangle$ it is given as:

$$\Omega_R = \frac{\mathcal{E}}{\hbar} \langle f|\vec{\varepsilon}\cdot \mathbf{d}|i\rangle = \frac{e\mathcal{E}}{\hbar} \langle f|\vec{\varepsilon}\cdot \mathbf{r}|i\rangle \tag{2.5.1}$$

where $\vec{\varepsilon}$ is light polarization vector, $\mathcal{E}$ is electric field's amplitude and $\mathbf{d}$ is the effective transition dipole, which is not the same as the molecule's permanent dipole moment μ_0. We will evaluate this

matrix element assuming that we are given polarization ε_p ($p = \pm 1$ corresponds to two circular polarizations, and $p = 0$ corresponds to linear polarization along the quantization axis), and using a rank 1 spherical tensor $T^1_p(\mathbf{d})$. We can then re-write the expression for the Rabi rate:

$$\Omega_R = \sum_{p=-1,0,1} (-1)^p \frac{\mathcal{E}_{-p}}{\hbar} \langle f|T^1_p(\mathbf{d})|i\rangle. \tag{2.5.2}$$

We have:

$$\langle f|T^1_p(\mathbf{d})|i\rangle = \left\langle J, \Omega, F_1, F, M_F, \mathcal{P}\middle|T^1_p(\mathbf{d})\middle|J', \Omega', F_1', F', M_F', \mathcal{P}'\right\rangle,$$

where $\mathcal{P}$ is a number identifying state's parity type - 0 for e-parity states and 1 for f-parity states. We then use Eq. (A.1) to obtain:

$$\left\langle J, \Omega, F_1, F, M_F, \mathcal{P}\middle|T^1_p(\mathbf{d})\middle|J', \Omega', F_1', F', M_F', \mathcal{P}'\right\rangle = (-1)^{F-M_F} \begin{pmatrix} F & 1 & F' \\ -M_F & p & M_F' \end{pmatrix} \left\langle J, \Omega, F_1, F, \mathcal{P}\middle\|T^1(\mathbf{d})\middle\|J', \Omega', F_1', F', \mathcal{P}'\right\rangle.$$

Because the spherical tensor being evaluated acts on angular momentum $\mathbf{J}$, in order to simplify the equation above we need to take into account the couplings between $\mathbf{J}$ and nuclear spins.

$$\begin{aligned}\langle f|T^1_p(\mathbf{d})|i\rangle &= (-1)^{F-M_F} \begin{pmatrix} F & 1 & F' \\ -M_F & p & M_F' \end{pmatrix} \left\langle J, \Omega, F_1, F, \mathcal{P}\middle\|T^1(\mathbf{d})\middle\|J', \Omega', F_1', F', \mathcal{P}'\right\rangle \\ &= (-1)^{F-M_F+F'+F_1+F_1'+J+3} \sqrt{(2F+1)(2F'+1)(2F_1+1)(2F_1'+1)} \\ &\begin{pmatrix} F & 1 & F' \\ -M_F & p & M_F' \end{pmatrix} \begin{Bmatrix} F_1' & F' & \frac{1}{2} \\ F & F_1 & 1 \end{Bmatrix} \begin{Bmatrix} J' & F_1' & \frac{1}{2} \\ F_1 & J & 1 \end{Bmatrix} \left\langle J, \Omega, \mathcal{P}\middle\|T^1(\mathbf{d})\middle\|J', \Omega', \mathcal{P}'\right\rangle\end{aligned}$$

Finally, to correctly evaluate the remaining reduced matrix element, we need to move the dipole from the lab frame to the molecule-fixed frame. We do that, like before, using reduced Wigner-D functions:

$$T^1(\mathbf{d}) = \sum_{q=-1,0,1} \mathscr{D}^1_{\cdot,q} T^1_q(\mathbf{d}).$$

Then, by explicitly introducing electronic states η we get:

$$\begin{aligned}\left\langle \eta, J, \Omega, \mathcal{P}\middle\|T^1(\mathbf{d})\middle\|\eta', J', \Omega', \mathcal{P}'\right\rangle &= \sum_{q=-1,0,1} \left\langle \eta, J, \Omega, \mathcal{P}\middle\|(\mathscr{D}^1_{\cdot,q})^* T^1_q(\mathbf{d})\middle\|\eta', J', \Omega', \mathcal{P}'\right\rangle \\ &= \sum_{q=-1,0,1} \left\langle J, \Omega, \mathcal{P}\middle\|(\mathscr{D}^1_{\cdot,q})^*\middle\|J', \Omega', \mathcal{P}'\right\rangle e \left\langle \eta\middle|\mathbf{r}\middle|\eta'\right\rangle.\end{aligned}$$

Now, to evaluate the last (angular) part of the matrix element, we have to consider Ω-doubling, which occurs in the excited $B^3\Pi_1$ state. Using our convention for $\mathcal{P}$ for states of e-parity and f-parity, the positive and negative parity superposition states can be written as:

$$|+\rangle = \frac{1}{\sqrt{2}}\left(|\Omega\rangle + (-1)^J |-\Omega\rangle\right)$$
$$|-\rangle = \frac{1}{\sqrt{2}}\left(|\Omega\rangle - (-1)^J |-\Omega\rangle\right),$$

where parity of the state ($|+\rangle$ or $|-\rangle$) is determined by the type of the parity and the angular momentum J, namely parity is equal to $(-1)^{J+\mathcal{P}}$. We can then write that in general:

$$|J, |\Omega|, \mathcal{P}, \pm\rangle = \frac{1}{\sqrt{2}}\left(|\Omega\rangle + (-1)^{J+\mathcal{P}}(-1)^J |-\Omega\rangle\right) = \frac{1}{\sqrt{2}}\left(|\Omega\rangle + (-1)^{\mathcal{P}} |-\Omega\rangle\right). \tag{2.5.3}$$

We can look at the formula above in the following way: given a parity type, the superposition is well defined (sum for e-parity states and difference for f-parity). Such state will then have parity dependent on J. For example, the f-parity state is $(|\Omega\rangle - |-\Omega\rangle)/\sqrt{2}$, and for $J = 1$ such state will have positive parity ($(-1)^{1+1} = 1$). If we compare this with the standard definition $|+\rangle = (|\Omega\rangle + (-1)^1 |-\Omega\rangle)/\sqrt{2}$ we get the same superposition state. Therefore, in this scheme we will be using states written as in Eq. (2.5.3). Then, the dipole transition matrix element's last term can be written as:

$$\left\langle J, \Omega, \mathcal{P}\middle\| (\mathscr{D}^1_{\cdot,q})^* \middle\| J', \Omega', \mathcal{P}'\right\rangle = \sum_{q=-1,0,1} \frac{1}{2}\sqrt{(2J+1)(2J'+1)} \left[(-1)^{J-\Omega}\begin{pmatrix} J & 1 & J' \\ -\Omega & q & \Omega' \end{pmatrix} + \right.$$
$$+ (-1)^{J+\Omega}(-1)^{\mathcal{P}}\begin{pmatrix} J & 1 & J' \\ \Omega & q & \Omega' \end{pmatrix} + (-1)^{J-\Omega}(-1)^{\mathcal{P}'}\begin{pmatrix} J & 1 & J' \\ -\Omega & q & -\Omega' \end{pmatrix} +$$
$$\left. +(-1)^{J+\Omega}(-1)^{\mathcal{P}+\mathcal{P}'}\begin{pmatrix} J & 1 & J' \\ \Omega & q & -\Omega' \end{pmatrix}\right].$$

Therefore, the dipole transition matrix element for a transition from initial state i (here, primed quantum numbers, even though throughout the thesis primes will mark the excited state) to state

f is given by:

$$\langle f|T_p^1(\mathbf{d})|i\rangle = \frac{1}{2}e\langle \mathbf{r}\rangle (-1)^{F-M_F+F'+F_1+F_1'+2J-\Omega+3}\sqrt{(2F+1)(2F'+1)(2F_1+1)(2F_1'+1)}$$

$$\sqrt{(2J+1)(2J'+1)}\begin{pmatrix} F & 1 & F' \\ -M_F & p & M_F' \end{pmatrix}\begin{Bmatrix} F_1' & F' & \frac{1}{2} \\ F & F_1 & 1 \end{Bmatrix}\begin{Bmatrix} J' & F_1' & \frac{1}{2} \\ F_1 & J & 1 \end{Bmatrix}$$

$$\sum_{q=-1,0,1}\left[\begin{pmatrix} J & 1 & J' \\ -\Omega & q & \Omega' \end{pmatrix} + (-1)^{\mathcal{P}}\begin{pmatrix} J & 1 & J' \\ \Omega & q & \Omega' \end{pmatrix} + (-1)^{\mathcal{P}'}\begin{pmatrix} J & 1 & J' \\ -\Omega & q & -\Omega' \end{pmatrix} + \right.$$

$$\left. +(-1)^{\mathcal{P}+\mathcal{P}'}\begin{pmatrix} J & 1 & J' \\ \Omega & q & -\Omega' \end{pmatrix}\right] \tag{2.5.4}$$

For our specific electronic states, assuming the ground state is the initial state, this reduces to:

$$\langle f|T_p^1(\mathbf{d})|i\rangle = \frac{1}{\sqrt{2}}e\langle \mathbf{r}\rangle (-1)^{F-M_F+F'+F_1+F_1'+2J-1+3}\sqrt{(2F+1)(2F'+1)(2F_1+1)(2F_1'+1)}$$

$$\sqrt{(2J+1)(2J'+1)}\begin{pmatrix} F & 1 & F' \\ -M_F & p & M_F' \end{pmatrix}\begin{Bmatrix} F_1' & F' & \frac{1}{2} \\ F & F_1 & 1 \end{Bmatrix}\begin{Bmatrix} J' & F_1' & \frac{1}{2} \\ F_1 & J & 1 \end{Bmatrix}$$

$$\sum_{q=-1,0,1}\left[\begin{pmatrix} J & 1 & J' \\ -1 & q & 0 \end{pmatrix} + (-1)^{\mathcal{P}}\begin{pmatrix} J & 1 & J' \\ 1 & q & 0 \end{pmatrix}\right]. \tag{2.5.5}$$

We can evaluate most of Eq. (2.5.4) for our states - all quantum numbers are given. The exception is the electronic part $\left\langle B^3\Pi_1\middle|\mathbf{r}\middle|X^1\Sigma^+\right\rangle$ (we're assuming the that the vibrational part, the Franck-Condon, factor is equal to 1, while its real value, as mentioned, is approximately 0.99), which should be on the order of Bohr's radius a_0. It can also be evaluated using known decay rate from the excited electronic states. Finally, it is also worth noting that, because of mixing in the excited state, in order to evaluate these dipole transition matrix elements for a state $\widetilde{J}$, we need to use formula Eq. (2.5.4) for all states that contribute to the state being evaluated.

2.5.1 Decay Rates and Branching Ratios

Using the dipole transition matrix element, we are now able to find the decay rates for different decay paths, as well as various rotational branching ratios, all of which will be needed in modeling

and simulations. A decay rate from state i to state f is defined as:

$$\Gamma_{i\to f} = \frac{\omega_{if}^3}{3\pi\varepsilon_0\hbar c^3} |\langle f|\mathbf{d}|i\rangle|^2.$$

Firstly, we see that decay rates between rotational states in the same electronic state will be totally negligible comparing to decay rates from the excited electronic state to ground state. Secondly, we see that we could use Eq. (2.5.4) to find those rates, if we sum over all possible polarizations. Then, branching ratio will be given as (assuming that frequencies for all the decays are equal, which for our system is close to truth; differences are on the order of 10 GHz comparing to transition frequency of $\sim 10^6$ GHz):

$$b_{fi} = \frac{\Gamma_{i\to f}}{\sum_f \Gamma_{i\to f}} = \frac{\sum_{p=-1,0,1} |\langle f|d_p|i\rangle|^2}{\sum_f \left(\sum_{p=-1,0,1} |\langle f|d_p|i\rangle|^2\right)}.$$

Because we know value of Γ_i for the $B^3\Pi_1$ state ($\Gamma = 1/\tau \approx 2\pi \times 1.6$ MHz), we can also find the electronic part of transition dipole moment $\langle \mathbf{r}\rangle$ assuming that all the decays emit photons of the same energy and decays go only to the vibrational level $\nu = 0$ (which is approximately true). Then:

$$\Gamma_i = \sum_f \Gamma_{i\to f} = \frac{\omega^3}{3\pi\varepsilon_0\hbar c^3} \sum_f \left(\sum_{p=-1,0,1} |\langle f|d_p|i\rangle|^2 \right) \propto \langle \mathbf{r}\rangle^2$$

For pure states the sum is equal to 1, and we obtain:

$$\left|\left\langle B^3\Pi_1 \middle| \mathbf{r} \middle| X^1\Sigma^+ \right\rangle\right|^2 = \frac{1}{e^2} \frac{3\pi\varepsilon_0\hbar c^3}{(2\pi\nu)^3} \Gamma, \tag{2.5.6}$$

with $\nu \approx 1103.4$ THz being the transition frequency (not the vibrational state). We can calculate that $\left\langle B^3\Pi_1 \middle| \mathbf{r} \middle| X^1\Sigma^+ \right\rangle \approx 0.32\, a_0$, which translated into value of induced electric dipole moment μ for this transition is equal to about 0.81 Debye (as mentioned before, for microwave transitions between rotational states in the ground electronic state we will use $\mu_0 = 4.2282$ Debye, which is the permanent electric dipole moment of TlF).

Using the formulas above we can evaluate branching ratios for *pure* states in $B^3\Pi_1$ of both e- and f-type parity (while for rotational cooling we will be using the mentioned e-parity states, when looking at the optical cycling, we will concentrate on transitions from $J = 1^-$ in the electronic ground state to $\widetilde{J} = 1^+$ in the excited electronic state; such state is a state of f-type parity with $\mathcal{P} = 1$). Tables of branching ratios are provided in the appendix - table B.1 presents them for e-parity states, while table B.2 for f-parity states for $\widetilde{J} = 1$.

Unfortunately, the pure states do not represent the reality and their rotational branching ratios are of limited use. In the excited electronic state rotational states are experiencing hyperfine mixing. For the states that we are interested in, we are getting a following mixing matrix [39] for e-parity states:

$$
\begin{array}{c}
 \\
|1,1/2,0\rangle \\
|1,1/2,1\rangle \\
|1,3/2,1\rangle \\
|1,3/2,2\rangle
\end{array}
\begin{array}{c}
\begin{array}{cccccccc}
|1,1/2,0\rangle & |1,1/2,1\rangle & |1,3/2,1\rangle & |1,3/2,2\rangle & |2,3/2,1\rangle & |2,3/2,2\rangle & |2,5/2,2\rangle & |3,5/2,2\rangle
\end{array} \\
\begin{pmatrix}
1 & 0 & 0 & 0 & 0 & 0 & 0 & 0 \\
0 & 0.9996 & 0.0203 & 0 & 0.018 & 0 & 0 & 0 \\
0 & -0.0267 & 0.8518 & 0 & 0.5232 & 0 & 0 & 0 \\
0 & 0 & 0 & 0.8482 & 0 & 0.5294 & 0.0138 & 0.0064
\end{pmatrix}
\end{array},
$$

where rows represent the mixed eigenstates, while columns correspond to pure states.Including the mixing, changes branching ratios slightly. Finally, from Eq. (2.5.4) we can obtain two selection rules that are true for all polarizations and are dictating the decay paths: $\Delta J = \pm 1$ (for e-type parity) $\Delta F_1 = 0, \pm 1$ and $\Delta F = 0, \pm 1$. However, the real states $\widetilde{J} = 1$ have a small admixture of the $|J = 3, F_1 = 5/2, F = 2\rangle$ state, which allows them to decay into $|J = 4, F_1 = 7/2, F = 3\rangle$ in the electronic ground state. Note, that even though there also is an admixture of $J = 2$ states in $B^3\Pi_1$, molecules will not decay into $J = 1$ or $J = 3$ states in $X^1\Sigma^+$, because the overall state $\widetilde{J} = 1$ has the same parity as the mentioned $J = 1$ and $J = 3$ states. Table B.3 in the appendix presents these modified branching ratios for e-type parity states and table B.4 for f-type parity states.

Chapter 3

Overview of Full Experimental Setup

3.1 Overview

Our experiment is divided into interconnected modules which we will describe in this chapter in order that a TlF molecule would encounter on its path. First, a cryogenic buffer gas beam source (BS) creates a slow, cold and bright molecular beam, which then passes through a rotational cooling region (RC) where molecules are transferred from their initial thermal distribution in rotational states into a single hyperfine state in $J = 0$. Afterwards, in the state preparation region A (SPA) the molecules are coherently moved into the $|J = 2, M_J = 0\rangle$ state that allows us to focus the beam into the final detection region downstream with the electrostatic quadrupole lens (EQL). After the lens, TlF molecules are transferred into the Schiff moment measurement $|J = 1, M_J = \pm 1\rangle$ "science state" in the state preparation region B (SPB). The Schiff moment measurement is performed in the main interaction region (MI), where a nuclear magnetic resonance (NMR) process is performed using a separated oscillatory fields (SOF) technique [45, 46] with a strong polarizing $\boldsymbol{\mathcal{E}}$-field present. There, first a superposition of thallium nuclear spin states is created by a short RF magnetic field subregion, then molecules undergo a period of free precession in electric field $\boldsymbol{\mathcal{E}}$, and finally another RF field subregion maps the accumulated phase into a population difference between two spin states. It is the energy difference between the spin states, including a Schiff moment contribution, that leads to this phase accumulation. After the main interaction region, the state preparation region C (SPC) is where each spin state is transferred to a different rotational state. These final rotational populations are then read out using a laser-induced fluorescence (LIF) technique through

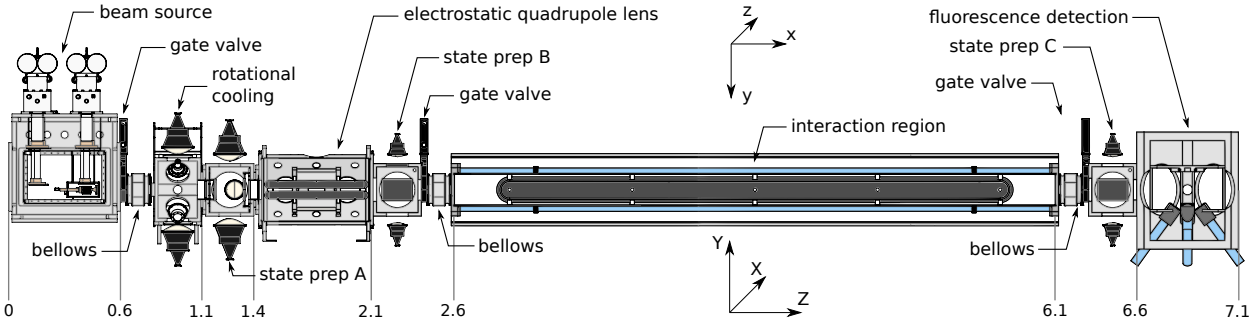

Figure 3.1.1: Overview of the planned CeNTREX beamline. Distance in meters is shown on the bottom. Modules following the electrostatic quadrupole lens are currently being designed, so few details are given.

optical quasi-cycling transitions in the fluorescence detection region (FD). We present overview of the beamline design in Fig. 3.1.1 and Fig. 3.1.2.

Because the quantizing fields in CeNTREX change direction throughout the apparatus, we find it useful to use two different coordinate systems. We use $(\mathbf{X}, \mathbf{Y}, \mathbf{Z})$ to denote "beamline" coordinates, where $\mathbf{Z}$ points in the average direction of the molecular beam and $\mathbf{Y}$ is vertical. Similarly, we use $(\mathbf{x}, \mathbf{y}, \mathbf{z})$ to denote "interaction region" coordinates, where $\mathbf{z}$ lies along the average $\boldsymbol{\mathcal{E}}$-field in the interaction region, and $\mathbf{x}$ is the vector closest to the average beam velocity that is also perpendicular to $\mathbf{z}$.

3.2 Beam Source

The thallium fluoride molecular beam is obtained from a cryogenic neon buffer gas beam source [47]. There, a solid TlF target cooled to 16-20 K is kept within a copper cell, and is ablated with a pulsed Nd:YAG laser operating at up to 50 Hz. The ablation occurs with a continuous Ne flow through the cell with a typical rate of 25-40 sccm (standard cubic centimeters per minute). The cell is surrounded by a shield kept at 4 K that cryopumps the neon. The Ne buffer gas and ablated TlF reach thermal equilibrium before the cell exit, where the beam cools even further by expanding into vacuum. The cell has an exit aperture with a diameter of 6.35 mm (it defines the zero position along the beamline axis $\mathbf{Z}$), and the beam source itself has two more apertures (one in a 4 K layer, and one in a blackbody shield), both with a 1" diameter, that collimate the molecular beam.

Properties of TlF beam's velocity distributions were already measured. We placed an additional

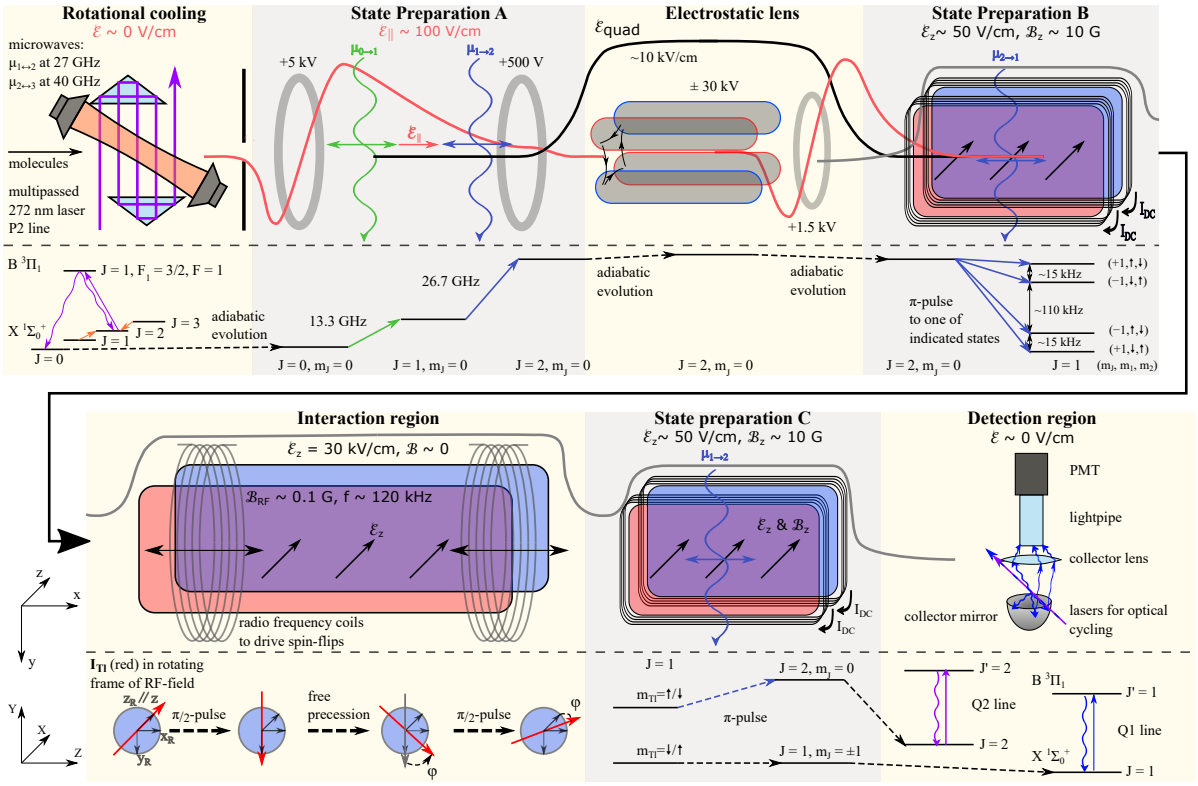

Figure 3.1.2: Overview of the regions the TlF molecules traverse as they move through the CeNTREX beamline. After emerging from the beam source (not shown), the molecules enter the rotational cooling region, where the population in the rotational levels $J = 1$, 2, and 3 is optically pumped to $|J = 0, F = 0\rangle$. (Chapter 7 and Fig. 3.3.1 provide more detail). From there, they move into state preparation region A, where they are coherently transferred into a $|J = 2, M_J = 0\rangle$ state, which is focused by the electrostatic lens. In state preparation region B, the molecular state is transferred into one of the $|J = 1, M_J = \pm 1\rangle$ states before proceeding to the interaction region. Here, using NMR with the SOF technique, we transform the frequency shift between Tl spin-up and spin-down states into a population difference between these states. Subsequently, in state preparation region C, one of the Tl spin state populations is transferred to a $J = 2$ state. Finally, in the detection region, optical cycling and fluorescence collection are used for efficient, quasi-simultaneous detection of the two populations. The red, grey, and black curves in the figure indicate the magnitude of the electric field along, respectively, the beam direction $\mathbf{Z}$, the interaction region field direction $\mathbf{z}$, and the transverse electric quadrupole field directions $\mathbf{X}, \mathbf{Y}$.

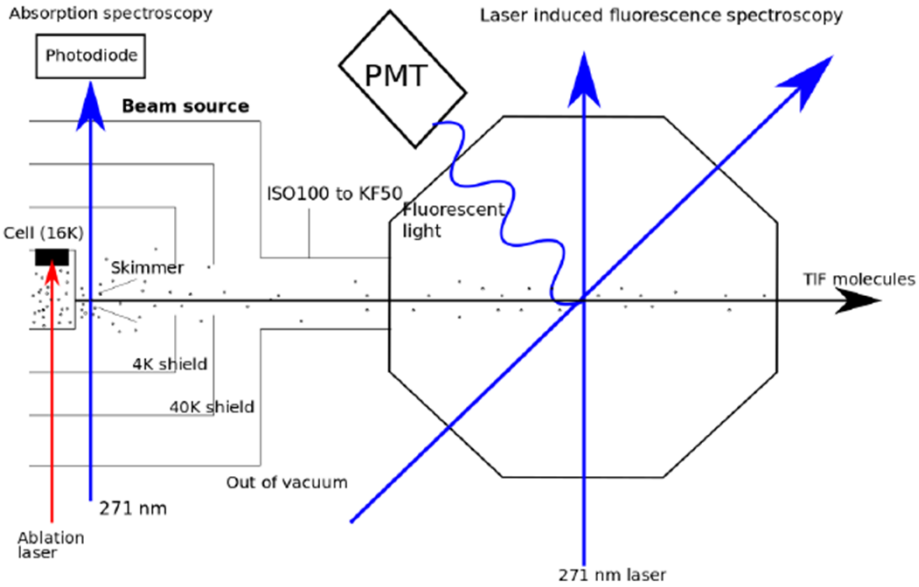

Figure 3.2.1: Schematic of an experimental setup that was used to measure properties of the molecular beam.

collimator downstream and allowed a laser beam to cross the molecular beam. It was tuned to a Q1 line ($\widetilde{J}' = J = 1$) of the $X - B$ transition (detailed in Chapter 6). Using a photomultiplier tube (PMT) we collected laser-induced fluorescence and analyzed the LIF signal as a function of laser detuning with the laser beam perpendicular or at 45° with respect to the TlF beam (Fig. 3.2.1). This allowed us to deduce properties of the velocity distributions. The longitudinal distribution was very nearly Gaussian, with mean $\bar{v}_Z = 184 \pm 17$ m/s and Gaussian width $\sigma_{v_Z} = 16.1 \pm 0.8$ m/s. The latter corresponds to translational temperature $T_{\rm tr} = 7.0 \pm 0.7$ K.

The TlF beam divergence was determined from the shape of an isolated Q-branch absorption line, probed upstream of any collimation. The FWHM (full width at half-maximum) spread in transverse velocity here was 93 ± 3 m/s, corresponding to a divergence cone half-angle of $14.0 \pm 1.5°$.

To determine the rotational temperature of TlF we measured the population in different rotational states by looking at LIF signal sizes with lasers tuned to R-branch transitions ($\widetilde{J}' = J + 1$). Because the laser can resolve hyperfine structure in the excited but not in the ground state, by targeting the excited-state sublevel with the largest possible angular momentum, $\widetilde{F}' = \widetilde{J}' + 1 = J + 2$, we could ensure that only a single ground state hyperfine level, with $F = J + 1$, was excited. Such

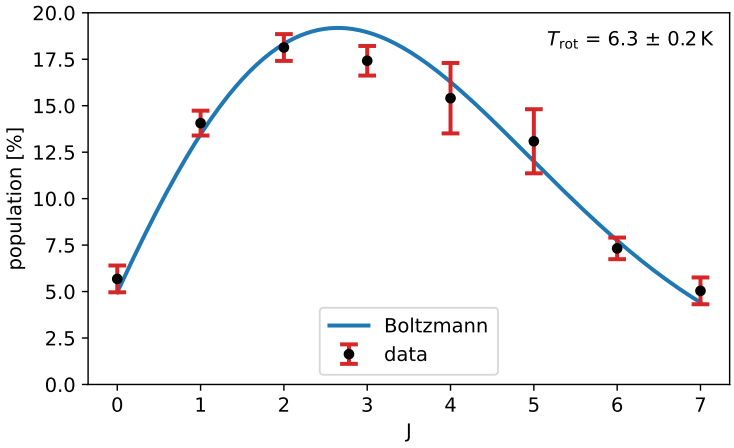

Figure 3.2.2: Relative rotational state populations of TlF in the CeNTREX beam source with typical conditions as described in the text, overlaid with a fit to a Boltzmann distribution. From the fit, we find the rotational temperature $T_{\mathrm{rot}} = 6.3 \pm 0.2$ K.

an approach greatly simplified the extraction of rotational level populations from LIF signals. The relative populations were then fit to a Boltzmann distribution,

$$P(J) = g(J) \exp\left(-\frac{BJ(J+1)}{k_B T_{\mathrm{rot}}}\right), \tag{3.2.1}$$

where $g(J) = 4(2J+1)$ is the degeneracy of each rotational level, as shown in Fig. 3.2.2. From the fit we obtained $T_{\mathrm{rot}} = 6.3 \pm 0.2$ K.

From known line strengths [39, 43, 48], calculated solid angle of fluorescence detection, and calibrated PMT sensitivity, we found a time-averaged beam intensity of 5×10^{12} molecules/state/sr/s. Here, each M_F sublevel is considered a one state, and the time average is taken over 1 second when operating at 50 Hz pulse repetition rate. This is comparable to intensities found in other cryogenic buffer gas beam sources [47].

3.3 Rotational Cooling

In a Boltzmann distribution at $T_{\mathrm{rot}} = 6.3$ K, about 50% of the TlF population is in states with $J = 0$ through $J = 3$. To maximize the Schiff moment measurement sensitivity in CeNTREX, this population can be dissipatively pumped to the $|J = 0, F_1 = 1/2, F = 0\rangle$ level, which can become the initial state for all further steps in the experiment. This rotational cooling can be accomplished

using a single optical pumping laser and two microwave driving fields. The laser can couple the $J = 2$ state to an excited state with $\widetilde{J}' = 1^-$. We calculate that about half of the decays from the excited $\widetilde{J}' = 1^-$ state end in the $J = 0$ state; nearly all of the remainder returns to the $J = 2$ state, and branching to other vibrational states is $\lesssim 1\%$ [38, 44], as was mentioned in the previous chapter. The microwaves could then resonantly couple $J = 1 \leftrightarrow J = 2$ and $J = 2 \leftrightarrow J = 3$. Repeated excitation-decay cycles should then lead to accumulation of population from $J = 1,\ 2,$ and 3 into the $J = 0$ state, as shown in Fig. 3.3.1.

The presence of hyperfine structure adds considerable complexity to rotational cooling in TlF. While the ground-state hyperfine splitting is smaller than the laser linewidth, the excited-state hyperfine levels are well separated. We tune the $J = 2$ optical pumping laser to resonance with the $\left|\widetilde{J}' = 1^-, \widetilde{F_1}' = 3/2, F' = 1\right\rangle$ level and refer to this line as the P2F1 transition (P-branch transitions have $\widetilde{J}' = J - 1$). Without a considerable effort, this level structure will only support an extremely low excitation and pumping rate due to the formation of long-lived coherent dark states [49] within the manifold of unresolved ground-state hyperfine and Zeeman sublevels. It is this problem that is a major part of this thesis. In Chapter 5 we look at dark state creation and methods of their destabilization, and then in Chapter 7 we analyze and simulate different approaches towards the rotational cooling. Finally, in Chapter 10 we present results of experimental realization of this process.

3.4 State Preparation Region A

In CeNTREX, the electrostatic quadrupole lens is designed to selectively focus molecules in the $|J = 2, M_J = 0\rangle$ state. As we just mentioned, rotational cooling should bring majority of the population into the $|J = 0, F_1 = 1/2, F = 0\rangle$ state, which is a pure $I_t = 0$ (singlet) state of the nuclear spins. A coherent transfer of this state's population into the $|J = 2, M_J = 0\rangle$ state will be achieved in the state preparation region A, where a two-stage adiabatic passage (AP) protocol will be utilized. In both stages, the population is moved to the next rotational state (J increases by one), while its projection M_J remains unchanged, with (nominally) $I_t = 0$ throughout.

The driving field will be provided by two CW, single-frequency free-space microwave beams, tuned to near-resonance with the $J = 0 \leftrightarrow J = 1$ and $J = 1 \leftrightarrow J = 2$ transitions. The beams

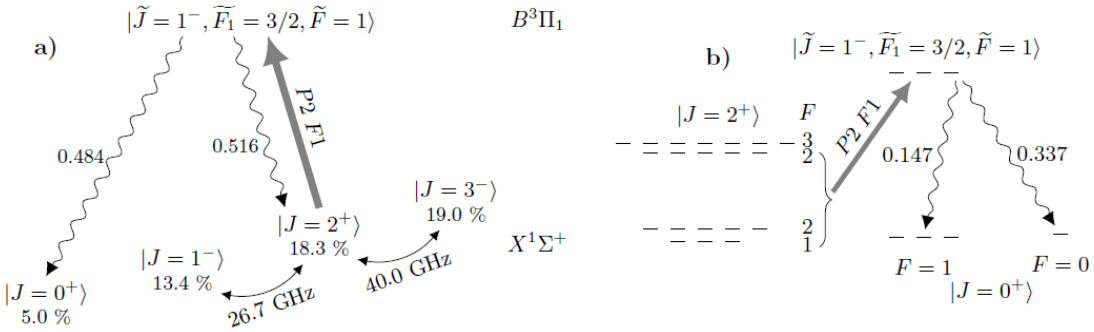

Figure 3.3.1: Rotational cooling scheme. **a)** The thick solid arrow marks a UV laser driving the P2F1 transition; bent arrows represent microwaves, and wavy arrows indicate spontaneous emission. The odd-parity $\widetilde{J}' = 1^-$ excited state can only decay to states with $J = 0^+, 2^+$. Percentages under the ground-state kets are the thermal population at temperature $T_{\rm rot} = 6.3$ K, prior to rotational cooling. **b)** Hyperfine structure relevant to optical pumping. Decays back to $J = 2^+$ are not shown. The P2F1 transition does not excite $|J = 2^+, F = 3\rangle$. The nearest optical transition that couples to the $J = 2^+$ hyperfine manifold is separated from this line by about 550 MHz.

can be produced by spot-focusing horns, spatially offset so the beam profiles have no significant overlap. We plan to provide the time-varying detuning of each beam from its respective resonance by the quadratic Stark shift due to a spatially varying DC electric field as the molecules fly through the region. The desired $\Delta M_J = \Delta I_t = 0$ transitions will be then selectively driven by π-polarized microwaves. Due to geometric constraints, this will require the DC electric field, $\boldsymbol{\mathcal{E}}$, to lie along the molecular beamline, $\mathbf{Z}$ (Fig. 3.1.2 provides an overview of this region).

For adiabatic passasge to provide an efficient population transfer, the adiabaticity condition has to be fulfilled [50]:

$$\frac{d\Delta}{dt} \ll \Delta^2 + \Omega_\mu^2, \tag{3.4.1}$$

where Δ is the detuning and Ω_μ the Rabi rate of the microwave drive. Furthermore, the detuning at large times before and after the AP interaction must be larger than the microwave Rabi rate. This will be accomplished with fields as shown in Fig. 3.4.1.

Our collaboration simulated the TlF state evolution in the SPA region with peak Rabi rates $\Omega_\mu = 70$ kHz, perfectly pure π-polarization, microwave intensity profile as measured from the focusing horns, $\mathcal{E}_Z$ field from finite element calculations, and including the effect of the Earth's

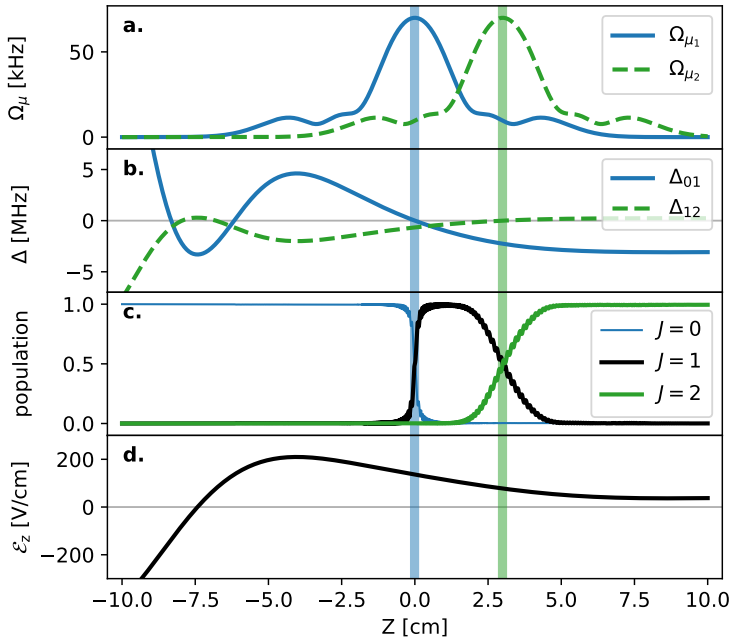

Figure 3.4.1: Rabi rates, detunings, state populations and field amplitudes versus position in state preparation region A, where **Z** is the molecular beam direction. **a)** Calculated Rabi rates $\Omega(Z)$, based on the measured intensity profile from the spot-focusing horns. **b)** Stark-shifted detunings Δ_{01} and Δ_{12} of the transitions $J = 0 \leftrightarrow J = 1$ and $J = 1 \leftrightarrow J = 2$, respectively. **c)** Calculated populations of relevant states as the molecules travel through the SPA region, showing a simulated transfer efficiency from $J = 0$ to $J = 2$ of 99%. **d)** Electric field $\mathcal{E}_\mathrm{Z}$, based on finite element simulations.

magnetic field. With these assumptions, it was found that the state transfer efficiency is close to 99%. We are confident that high transfer efficiency can also be reached in the real experiment - as long as the adiabaticity condition is fulfilled, the state transfer occurs with an efficiency close to 100% [50]. By making sure it is satisfied within a safe margin, the effects of various factors that might lower the efficiency can be mitigated.

3.5 Electrostatic Quadrupole Lens

The molecular beam exiting the source is spread over a wide solid angle, and the beam intensity decreases as the square of the distance from the source. The total distance from beam source to final detection in CeNTREX is about 6.4 m, so beam focusing can substantially improve the signal

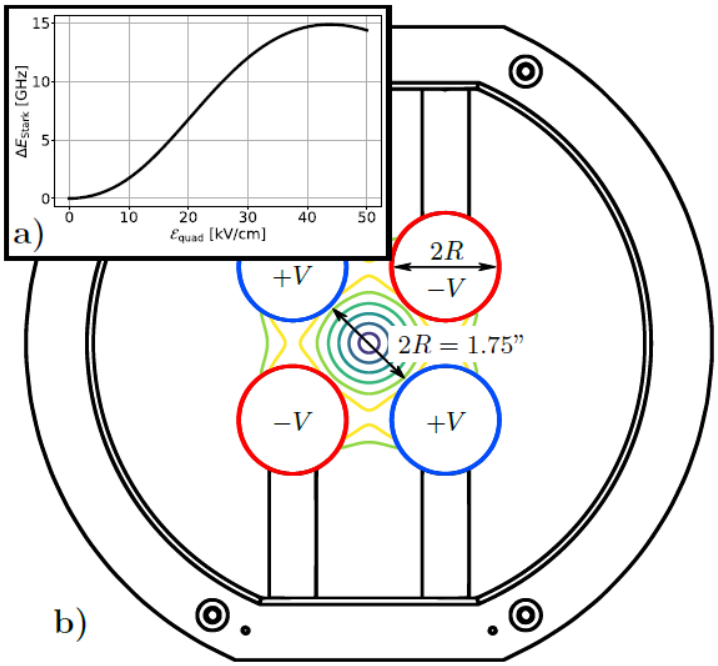

Figure 3.5.1: **a)** Stark shift of the $|J = 2, M_J = 0\rangle$ hyperfine manifold of states. **b)** Front view of the electrostatic quadrupole lens. Colored curves are equipotential surfaces. The electrodes have length $l = 60$ cm, and applied potentials $\pm V$ up to ± 30 kV. The electrode support structure is mounted on translation stages (not shown) that allow for alignment of the lens under vacuum.

strength. To accomplish this, an electrostatic quadrupole lens (EQL) will be employed.

An EQL with four equidistant cylindrical electrode rods, held at alternating positive and negative potentials of the same magnitude V, generates an electric quadrupole field of magnitude

$$|\mathcal{E}_{\text{quad}}(r)| = \frac{2Vr}{R^2}, \tag{3.5.1}$$

where $2R$ is both the bore diameter of the lens and the electrode diameter, and r is the distance from the central axis of the quadrupole. A front view of the lens is shown in Fig. 3.5.1b. The $|J = 2, M_J = 0\rangle$ states in TlF have a quadratic Stark shift in fields up to $\mathcal{E}_{\text{quad}} \approx 20$ kV/cm as shown in Eq. (2.4.3), and slightly slower than quadratic to ~ 30 kV/cm (Fig. 3.5.1a). For electrode potentials of $\pm V = \pm 30$ kV, the fields inside the lens do not exceed 30 kV/cm, and so most molecules in the lens remain in the quadratic Stark shift regime.

A quadrupole field acting on molecules with a quadratic Stark shift produces a harmonic po-

tential along the radial direction within the lens. Under these conditions, the electrostatic lens acts as an analogue to a thick optical lens [51]: the lens can be thought of as imaging the molecular beam from the source to the detection region. The trajectories of the molecules can be described by the ray transfer matrices of a thick optical lens [52, 53]. To understand it better we can begin by re-writing the Stark shift term using Eq. (3.5.1):

$$\Delta E_{\mathrm{S}}^{(2)} = \frac{C(\Delta V)^2}{2R^4} r^2 \tag{3.5.2}$$

where the J, M_J dependence of Eq. (2.4.3) is included in the constant C and ΔV is the potential difference between two electrodes. Now, let's suppose a molecule of mass m is emitted from a source with initial distance r_0 from the axis with longitudinal speed v_Z and transverse speed $\dot{r_0}$. After traveling for a distance z_0, it enters the EQL of length l and radius R. After it leaves the lens, it travels for a distance z_f and finally enters the detection region at a distance r_f from axis with transverse speed $\dot{r_f}$. By solving the equations of motion a relationship between the initial and final distance from the axis and transverse velocities can be put into a matrix form:

$$\begin{pmatrix} r_f \\ \dot{r}_f/v_Z \end{pmatrix} = \begin{pmatrix} 1 & z_f \\ 0 & 1 \end{pmatrix} \begin{pmatrix} \cos pl & p^{-1}\sin pl \\ -p\sin pl & \cos pl \end{pmatrix} \begin{pmatrix} 1 & z_0 \\ 0 & 1 \end{pmatrix} \begin{pmatrix} r_0 \\ \dot{r}_0/v_Z \end{pmatrix}, \tag{3.5.3}$$

where

$$p = \left(\frac{C(\Delta V)^2}{R^4 m v_Z^2} \right)^{\frac{1}{2}}$$

Setting the upper-right element of the transformation matrix in Eq. (3.5.3) to zero, we obtain the focusing condition:

$$z_0 \cos pl + \frac{\sin pl}{p} - p z_0 z_f \sin pl + z_f \cos pl = 0. \tag{3.5.4}$$

This sets the condition for a molecule emitted from a given initial off-axis distance r_0 to be focused at the final off-axis distance $r_f = M r_0$, regardless of its initial transverse speed $\dot{r}_0$. Here M is understood as "magnification" defined as:

$$M = \cos pl - p z_f \sin pl,$$

and it determines the degree to which the beam diverges after traveling through the lens. Finally, once the focusing condition is applied to Eq. (3.5.3), a mentioned thick optical lens equation is obtained:

$$\begin{pmatrix} r_i \\ \dot{r}_i/v_Z \end{pmatrix} = \begin{pmatrix} 1 & z_i' \\ 0 & 1 \end{pmatrix} \begin{pmatrix} 1 & 0 \\ -f^{-1} & 1 \end{pmatrix} \begin{pmatrix} 1 & z_o' \\ 0 & 1 \end{pmatrix} \begin{pmatrix} r_o \\ \dot{r}_o/v_Z \end{pmatrix}, \tag{3.5.5}$$

where $r_{o/i}$ is the radial position of the molecule in the object/image plane (in our case beam source/detection region) corresponding to $r_{0,f}$ notation used before and changed here for emphasis, $z'_{o,i}$ is the distance from the object/image plane to the entrance/exit principal plane of the lens, and f is the effective focal length given by

$$f = \frac{1}{p \sin(pl)}. \tag{3.5.6}$$

As shown in Eq. (3.5.6), the focal length depends on velocity of the molecules. The spread of longitudinal velocities in the molecular pulse thus gives a range of focal lengths. This chromatic aberration increases the focal spot size. Aberrations due to deviation of the Stark shift from a purely quadratic spatial dependence have a similar effect.

Due to the complexity added by the aberrations, the length and diameter of the lens were optimized with Monte Carlo simulations of molecular trajectories through the entire apparatus. These simulations were done before much of the beamline was designed and prior to measurements of the molecular beam properties, and thus educated guesses had to be made for the parameters. For the molecular beam we assumed a Gaussian distribution with $\bar{v}_Z = 200$ m/s and $\sigma_{v_Z} = 13$ m/s for the longitudinal velocities. The beamline was taken to have a distance of 0.81 m from the molecular source to the start of the lens, and 3.63 m from the end of the lens to detection. The detection region was taken to have an acceptance area of 10 mm $\times$ 30 mm. The source was taken to have a diameter of 20 mm, and was located 0.25" downstream from the cold cell exit aperture. This was based on an estimate of the molecular cloud size at the "zone of freezing" where interactions between molecules are assumed to have ceased [47]. The length and diameter of the lens were then optimized by maximizing the expected number of detected molecules when the electrodes were at $\pm$30 kV. The optimal combination was found to be a diameter $2R = 1.75$", and a $l = 60$ cm length. The simulated gain in the number of molecules making it to detection was a factor of 24.

Some of the beamline and molecular beam properties are now known better than when the lens was designed. The measured molecular beam velocity is slightly lower, at $\bar{v}_Z = 184$ m/s, than previously assumed. To compensate for the lower velocity, the electrode voltages will be lowered to $\pm$27 kV. The source-to-lens-distance will be 1.01 m, and the lens-to-detection-distance 4.45 m. With these parameters, the simulated gain in the number of molecules reaching the detection region is a factor of 23.2 ± 0.9 where the uncertainty is based on Poisson statistics in the simulation.

From the simulations, we have also estimated TlF accumulation on the MI region electrodes - knowing it is crucial for proper maintenance of the apparatus. The simulations show that if additional beam-collimating apertures are not installed, a monolayer of TlF can form in under a month of continuous operation assuming measured beam's brightness. Installing an aperture just before the EQL, and just before the MI region, might help us mitigate this problem. To understand how small an aperture can be without being detrimental we can first estimate acceptance distance from the axis for the EQL. We do that by putting a limit on distance r_0 from the center of the lens at lens' entrance, for given distance z_0 and parameters R, p and l, for which no molecules will reach amplitude of oscillation inside the lens large enough to hit or escape the lens.

Inside the lens, molecules travel according to the equation of motion:

$$r = r_0 \cos pz + \frac{\dot{r}_0}{pv_Z} \sin pz. \tag{3.5.7}$$

At the same time, assuming that a molecule leaves the source at $r = 0$ (a point source), the distance r_0 is related to z_0 and angle θ between the **Z**-axis along the setup and molecule's trajectory through $r_0 = z_0 \tan\theta$. Tangent of angle θ is also related to transverse velocity $\dot{r}_0$ at the lens' entrance and molecule's longitudinal velocity v_Z. Namely, $\dot{r}_0 = v_Z \tan\theta$. Knowing that, we can re-write equation Eq. (3.5.7) as:

$$r = r_0 \cos pz + \frac{\tan\theta}{p} \sin pz = r_0 \cos pz + \frac{r_0}{z_0 p} \sin pz = \sqrt{r_0^2 + \frac{r_0^2}{z_0^2 p^2}} \cos(pz + \phi), \tag{3.5.8}$$

where the last form of the equation allows us to clearly see what the amplitude of the movement is (as well as its phase ϕ, which is not relevant to our discussion). We do not want this amplitude to reach a value larger than radius of the lens R. Therefore:

$$r_0 \leq \frac{pz_0}{\sqrt{1 + p^2 z_0^2}} R \tag{3.5.9}$$

which provides a rough estimate for size of a proper aperture before the EQL. Adding a 4 mm wide slit before the MI region is projected to help as well without substantially decreasing the number of molecules reaching the detection region. Including the apertures in the simulation shows that a monolayer of TlF should form after 4 months of continuous beam operation.

3.6 State Preparation Region B

In order to perform the nuclear Schiff moment measurement we need the molecules to be in the $J = 1$ state with $M_J = \pm 1$ [36, 38]. However, after the EQL TlF is in the $|J = 2, M_J = 0\rangle$ state. We plan to perform the state transfer in the state preparation region B and will do that by using resonant microwaves with x-polarization (perpendicular to the quantization axis). The microwave fields will be applied in the presence of a magnetic field $B_{\rm SPB} \approx 10$ G, as well as a quantization-axis-defining electric field $\mathcal{E}_{\rm SPB} \approx 50$ V/cm. Both fields will be parallel to one another and pointing along the **z**-axis (in the "interaction region" coordinates), and will allow to distinguish between two $\pm M_J$ states. Unlike in SPA, adiabatic passage here could potentially drive transitions to undesired states that might be nearby in energy. Therefore, here we plan to use a microwave π-pulse. We estimate that with a peak Rabi rate $\Omega_\mu = 1.5$ kHz, the transfer efficiency should approach $\sim$96%, although imperfections of electric and magnetic fields causing the transition frequencies to shift away from the microwave frequency, are likely to reduce it. To achieve high efficiency, B needs to be uniform to within $\delta B/B < 10^{-3}$ and $\mathcal{E}$ to within $\delta\mathcal{E}/\mathcal{E} < 10^{-4}$.

3.7 Main Interaction Region

The Schiff moment measurement requires a large and uniform external electric field, which in our case will be $\mathcal{E}_{\rm MI} = 30$ kV/cm, along **z**, and it will polarize the molecules. Such large field causes the energies of the $\widetilde{J} = 1,\ M_J = \pm 1$ manifold of hyperfine states to be well-described by the effective Hamiltonian [34]:

$$\begin{aligned}\mathcal{H}_{\rm eff} =&(-\mu_J J_z - \mu_1 \mathbf{I}_1 - \mu_2 \mathbf{I}_2)B_z - \mu_1 \mathbf{I}_{1z} J_z B_1^{\rm int} - \mu_2 I_{2z} J_z B_2^{\rm int} + C_S I_{1z} I_{2z} \\ &+ C_T (J_+^2 I_{-,1} I_{-,2} + h.c.) + W_{\mathcal{S}}\, \mathcal{S} \frac{\mathbf{I}_1}{I_1} \cdot \hat{\mathbf{n}},\end{aligned} \tag{3.7.1}$$

where $B^{\rm int}$ is the effective intra-molecular magnetic field along $\langle \mathbf{J} \rangle$ that arises from the spin-rotation terms in Eq. (2.1.1), while C_S and C_T are effective scalar and tensor spin-spin interactions, respectively, that arise from the spin-spin terms in Eq. (2.1.2). The subscripts $z, +, -$ on operators refer to the angular momentum projection, raising, and lowering operators, respectively.

As was shown in the introduction, the electric polarization, **P**, can be described by:

$$\mathbf{P} = \left\langle \hat{\mathbf{n}} \cdot \hat{\mathcal{E}} \right\rangle = \langle \cos\theta \rangle \,,$$

with $\hat{\mathcal{E}} \equiv \boldsymbol{\mathcal{E}}/\mathcal{E}$. Here, θ is the angle between $\hat{\mathbf{n}}$ and the $\mathbf{z}$-axis defined by $\boldsymbol{\mathcal{E}}_{\rm MI}$. For our science state in the $J = 1,\ M_J = \pm 1$ manifold $\mathbf{P} = 0.547$ in $\mathcal{E}_{\rm MI} = 30$ kV/cm. By measuring changes in energy splittings of two states with identical values of M_J and opposite Tl spin projections $M_1 = \pm 1/2$, we should be able to determine thallium's nuclear Schiff moment $\mathcal{S}$. These changes will occur when we reverse the direction of the electric field in the MI region $\boldsymbol{\mathcal{E}}_{\rm MI}$ with respect to the magnetic field $\mathbf{B}_{\rm SPB}$ in the SPB region. If the Schiff moment $\mathcal{S} \neq 0$, then, as was mentioned in Chapter 1, the energy splitting will shift by $\pm 2\Delta_{\rm CPV} = \pm 2 W_{\mathcal{S}}\, \mathcal{S}\, \mathbf{P}$. In Fig. 3.7.1 we show the science states in the $\widetilde{J} = 1,\ M_J = \pm 1$ manifold for electric field $\mathcal{E}_{\rm MI} = 30$ kV/cm. We can see that pairs of states that only flip thallium's spin ($\mathbf{I}_1$) are the j/e and k/h pairs. Because of the effective internal magnetic field and the scalar spin-spin interaction, both are separated by 119.517 kHz.

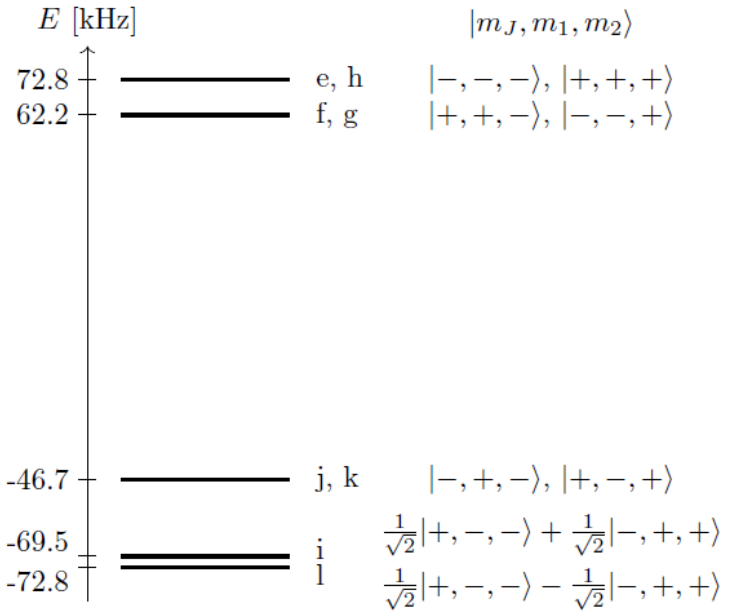

Figure 3.7.1: Hyperfine level structure of TlF $\left|\widetilde{J} = 1, M_J = \pm 1\right\rangle$ states in $\mathcal{E} = 30$ kV/cm and $B = 0$ that are present in the Main Interaction Region. Only the sign of the quantum numbers is shown - the full values are $M_J = \pm 1$, $M_1 = \pm 1/2$, $M_2 = \pm 1/2$, where M_1 and M_2 correspond to thallium's and fluorine's nuclear spin respectively. The zero of energy is arbitrary.

Using a SOF method for nuclear magnetic resonance [45, 46], but with no external magnetic field, one can measure this energy splitting. First, we will need to set the RF drive frequency to

the j↔e or k↔h transition resonance $\hbar\omega_{\mathrm{RF}} \approx \mu_1 B_{\mathrm{int}} - C_s/2$, which will cause the first RF pulse in the sequence to create a superposition of thallium's spin-up and spin-down states. For example, if we start in state e, a $\pi/2$-pulse would create a superposition of e and j states. This state would then undergo a free precession for time T, which would lead to phase accumulation between the spin-up and spin-down states:

$$\phi \approx \frac{1}{\hbar}\left[-\mu_1 B_{\mathrm{int}}\mathrm{sgn}(M_J) + C_s M_{I_2} + 2W_{\mathcal{S}}\,\mathcal{S}\,\mathbf{P}\,\mathrm{sgn}(\mathcal{E}_{\mathrm{MI}})\right]T. \tag{3.7.2}$$

After the free precession, the relative populations in spin-up and spin-down states can be obtained through a second RF pulse, which can map this accumulated phase. Transition from the spin-up to the spin-down state has probability [46]:

$$P_{\uparrow\to\downarrow} = \sin^2\left(2\Omega_{\mathrm{RF}}\tau\right)\,\cos^2\left[\frac{1}{2}\left(\phi_{\mathrm{CPV}} + \phi_{\mathrm{SOF}}\right)\right].$$

In the equation above Ω_{RF} is the Rabi frequency of the RF pulse, τ is time a molecule spends in the RF field, and the phase offset between the first and second RF pulses is given by ϕ_{SOF}. The CPV phase is defined as:

$$\phi_{\mathrm{CPV}} = 2W_{\mathcal{S}}\,\mathcal{S}\,\mathbf{P}\,\mathrm{sgn}(\mathcal{E}_{\mathrm{MI}})\frac{T}{\hbar} = \frac{2\Delta_{\mathrm{CPV}}T}{\hbar},$$

and it is the quantity that we would like to determine. Having its value, and knowing the value of T, the energy shift Δ_{CPV} can be obtained. To reach maximum sensitivity to the measured shift, we plan to set the SOF phase difference to $\pi/2$ magnitude and to alternate its sign, i.e. $\phi_{\mathrm{SOF}} = \pm\pi/2$.

Ideally, the free precession would occur with no magnetic field present and its accumulation would be attributed only to nuclear Schiff moment's precession in the electric field $\boldsymbol{\mathcal{E}}_{\mathrm{MI}}$. Unfortunately, the reality is often disappointing and magnetic fields cannot be completely eliminated from the interaction region thus generating spurious energy shifts. In CeNTREX we plan to minimize these magnetic fields by adding several layers of magnetic shielding in the shape of concentric cylinders. With a 4-cylinder shield and 12 layers of Metglas (a high-permeability material [54]) on each cylinder we aim to achieve residual fields of at most 10 μG.

It is also very crucial to generate the interaction region's electric field with high uniformity. To do that we have started constructing two quartz electrodes 3 m in length, which in CeNTREX will be separated by 2 cm. Both of these electrodes will have the so-called Rogowski profile [55, 56]

that should prevent formation of large edge fields. They will also have a conductive water-based colloidal graphite coating. We decided to use coated quartz electrodes to minimize electrodes' electrical conductance that could lead to magnetic Johnson noise [57, 58, 59]. To reduce it even further, the electrodes will be placed in a quartz vacuum chamber - a 3.5 m quartz tube with 26 cm outer diameter and 2 cm wall thickness. Its inner surface will be then grounded by adding a conductive coating or placing a thin conducting sheet.

Finally, the oscillatory RF fields required for the measurement will be placed outside the vacuum chamber. They will be position symmetrically away from the center of the electrodes, and will be separated by about 2.5 m. We plan to add a few additional coils that would be able to generate small magnetic field and its gradients, and help us with diagnostic and search for systematic effects.

3.8 State Preparation Region C

Once the molecules leave the interaction region, they will be in $|J=1, M_J, M_{I_1}=+1/2, M_{I_2}\rangle$ and $|J=1, M_J, M_{I_1}=-1/2, M_{I_2}\rangle$ states. These, due to their proximity in energy, cannot be resolved optically. Therefore, we plan to move population from one of these states into the $J=2$ rotational manifold, which is separated from the $J=1$ level by about 26.6 GHz and is optically resolvable. An efficient way to perform such population is transfer is currently being investigated and will probably involve a microwave π-pulse similarly to what we plan to do in SPB region.

3.9 Fluorescence Detection Region

The information about the accumulated phase is imprinted onto populations in $J=1,2$ rotational states after the SPC region. To retrieve it, we plan to perform a laser-induced fluorescence measurement on two optical quasi-cycling transitions in order to maximize the number of emitted photons from each molecule. We plan to use Q-line transition ($\widetilde{J}'=J$) which, in the case of $J=1$, has been demonstrated experimentally to provide a near-unity detection efficiency, albeit with scattering rates lower than expected. The problems with scattering rates occur due to creation of coherent dark states in ground state manifolds, and are identical in nature to problems we expect to see in the rotational cooling process, which is the main topic of this thesis. In Chapter 5 we will thoroughly investigate mechanisms of dark state creation and their destabilization, remixing, and

in Chapter 6 we will try to understand both cycling transitions (for $J = 1$ and $J = 2$) and propose the most efficient methods for their realization.

CeNTREX is a molecular beam experiment with a shot-to-shot variation in signal. Hence, we will address both cycling transition quasi-simultaneously by rapidly switching between two UV detection lasers. This will allow us to readout both the spin-up and the spin-down populations in a single molecular beam pulse, and will in effect mitigate the influence of fluctuations within and between these pulses [60]. We are confident we will be able to accomplish this using acousto-optic modulators. We will allow for enough dead time between switches for the decay from the excited state to happen, but also switch quickly enough for a single molecule to interact with both lasers multiple times. This scheme has already been used in the ACME experiment [61].

Currently, we are designing the LIF collection apparatus. The design includes a combination of lenses with high numerical apertures and mirrors that will cover a total solid angle of approximately $0.3 \times 4\pi$ sr. The photomultiplier tube (described later in Chapter 10) with quantum efficiency of 25% will allow to detect every emitted photon with about 7.5% efficiency. Therefore, scattering $\gtrsim 30$ photons per molecule should be sufficient for every molecule to be detected with $\gtrsim 90\%$ probability.

The actual quantity that we will calculate using the obtained $S_\uparrow$ and $S_\downarrow$ fluorescence signals, will be the asymmetry parameter $\mathcal{A}$ defined as:

$$\mathcal{A} \equiv \frac{S_\uparrow - S_\downarrow}{S_\uparrow + S_\downarrow},$$

which for the on-resonance SOF drive frequency is:

$$\mathcal{A} \approx 1 - 2\sin^2(2\Omega_{\mathrm{RF}}\tau)\,\cos^2\left[\frac{1}{2}\left(\phi_{\mathrm{CPV}} + \phi_{\mathrm{SOF}}\right)\right]. \tag{3.9.1}$$

Finally, in our experiment we will use $\phi_{\mathrm{SOF}} = \pm\pi/2$ and $2\Omega_{\mathrm{RF}}\tau = \pi/2$, which will simplify Eq. (3.9.1) to $\mathcal{A} \approx \pm\sin\phi_{\mathrm{CPV}} \approx \pm\phi_{\mathrm{CPV}}$.

3.10 State Evolution Between Regions

At the end of this chapter it is worth mentioning that spaces between different regions of CeNTREX will be filled by spatially-varying fields due to different regions requiring $\boldsymbol{\mathcal{E}}$- and $\mathbf{B}$-fields of varying magnitude and orientation. These fields can lead to a reduction of statistical sensitivity of our

experiment and can potentially produce additional systematic errors - in molecules' rest frame they will appear as time-varying fields that could move the populations to undesired states. Therefore, we have been trying to understand how the relevant quantum states evolve when molecules travel between experiment's regions, and to that extent we have performed extensive numerical simulations to identify optimized schemes for transfer between regions in CeNTREX, and to understand how undesired states can be populated here. Fortunately, it was found that it should be possible to achieve near 100% efficiency in all cases.

Chapter 4

Lindblad Master Equation

4.1 The Master Equation

In order to understand and simulate the light-matter interaction in TlF, we need to use an appropriate mathematical framework. While the hamiltonian of the interaction can be obtained from Eq. (2.5.4), simply solving Schrödinger's equations will not provide a full picture - it does not take into account any dissipative and decohering effects. For that, we need to look at time evolution of the density matrix that can be found using the Liouville - von Neumann master equation in the Lindblad form. In this chapter, we will briefly discuss this mathematical framework.

For a closed quantum mechanical system, if we consider pure states $|\psi(t)\rangle$, their time evolution can be described by a unitary transformation $|\psi(t_f)\rangle \equiv U(t_f, t_i)\,|\psi(t_i)\rangle$. If one substitutes that transformation into Schrodinger's equation, an equation for the operator U is obtained:

$$i\frac{dU(t,t_0)}{dt} = H(t)U(t,t_0).$$

For a system that is isolated a time-independent hamiltonian gives us a simple form for the operator (assuming $\hbar = 1$):

$$U(t,t_0) = e^{-iH(t-t_0)}$$

For a density matrix ρ, which is a proper way of describing quantum statistical ensembles, and defined as $\rho(t) = \sum_k c_k\,|\psi_k(t)\rangle\,\langle\psi_k(t)|$, the time evolution can be obtained from the time evolution

of a state. We then have:

$$\rho(t_f) = \sum_k c_k U(t_f, t_i) \left|\psi_k(t_i)\right\rangle \left\langle\psi_k(t_i)\right| U^\dagger(t_f, t_i) = U(t_f, t_i)\rho(t_i)U^\dagger(t_f, t_i).$$

Differentiating both sides with respect to time leads to Liouville - von Neumann equation:

$$\begin{aligned}\frac{d\rho(t)}{dt} &= \frac{dU(t,t_i)}{dt}\rho(t_i)U^\dagger(t,t_i) + U(t,t_i)\rho(t_i)\frac{dU^\dagger(t,t_i)}{dt} \\ &= -iH(t)U(t,t_i)\rho(t_i)U^\dagger(t,t_i) + iU(t,t_i)\rho(t_i)U^\dagger(t,t_i)H(t) \\ &= -i[H(t), \rho(t)].\end{aligned}$$

Deriving master equation for time evolution of density matrix in an open quantum system is a non-trivial problem. The equation is obtained by considering one-parameter dynamical maps V_t acting on algebras of bounded operators on Hilbert space. These dynamical maps are defined as transformations such that:

$$\rho(t) = V_t\rho(0).$$

For example, for a closed system described before

$$V_t\rho(0) = U(t,0)\rho(0)U(t,0)^\dagger.$$

These maps are also defined to be trace-preserving, complete positive and satisfy Markov property ($V_{t_1}V_{t_2} = V_{t_1+t_2}$ for $t_1,\, t_2 \geq 0$). These maps create a Markov semigroup that preserves positivity and normalization of density matrix [62].

We can then write the map in terms of its generators: $V_t = \exp(\mathcal{L}t)$. For the Liouville - von Neumann equation we simply obtain $\mathcal{L}\rho = -i[H, \rho]$. This can be seen by looking at $\rho(t) = \exp(\mathcal{L}t)\rho(0)$ for infinitesimal time steps $s \to 0$. We have $\rho(t+s) \approx (1 + \mathcal{L}s)\rho(t)$, which leads to the quantum master equation:

$$\frac{d\rho(t)}{dt} = \mathcal{L}\rho(t).$$

The most general form of these generators was first determined in the seventies [63, 64]. In those seminal papers, a completely orthonormal operator basis F_i was defined and equipped with a trace norm, i.e. $\langle F_i, F_j\rangle \equiv \mathrm{Tr}\left(F_i^\dagger F_j\right) = \delta_{ij}$, and consisted of N^2 operators for a Hilbert space of dimension N. Authors eventually determined that the operator $\mathcal{L}$ can be written as:

$$\mathcal{L}\rho = -i[H, \rho] + \frac{1}{2}\sum_{i,j=1}^{N^2-1} \alpha_{ij}\left([F_i, \rho F_j^\dagger] + [F_i, \rho F_j^\dagger]\right).$$

Because the matrix of coefficients α_{ij} is positive and hermitian, it can be diagonalized. We obtain eigenvalues γ_i and a different complete set of orthonormal operators C_i, which are linear combinations of operators F_i. We can then write the quantum master equation in the so-called Lindblad form:

$$\mathcal{L}\rho = -i[H,\rho] + \sum_{i=1}^{N^2-1} \gamma_i \left(C_i \rho C_i^\dagger - \frac{1}{2} \left\{ C_i^\dagger C_i, \rho \right\} \right). \tag{4.1.1}$$

4.2 Unitary Transformation

The non-hermitian part of Eq. (4.1.1) is sometimes referred to as dissipator, and from now on we will use $\mathcal{L}$ to refer to it. The equation with re-defined $\mathcal{L}$ can be then written as:

$$\frac{d\rho}{dt} = -i\hbar[H,\rho] + \mathcal{L}, \tag{4.2.1}$$

which for a 2-level system can be shown to have the same form as optical Bloch equations. Quite often it is easier to work in a rotating basis, where hamiltonian has a much simpler form. Such a transformation can be described using a unitary matrix T and it leads to:

$$\begin{aligned} \tilde{\rho} &= T^\dagger \rho T \\ H' &= T^\dagger H T \\ \tilde{\mathcal{L}} &= T^\dagger \mathcal{L} T. \end{aligned}$$

The whole equation will then transform accordingly (setting $\hbar = 1$):

$$T^\dagger \frac{d\rho}{dt} T = -i(T^\dagger H \rho T - T^\dagger \rho H T) + T^\dagger \mathcal{L} T,$$

which after inserting an identity matrix $TT^\dagger$ and some algebra gives us:

$$T^\dagger \frac{d\rho}{dt} T = -i[H', \tilde{\rho}] + \tilde{\mathcal{L}}. \tag{4.2.2}$$

Next, we can look at how ρ and its derivative transforms:

$$\frac{d\rho}{dt} = \frac{d}{dt}(T\tilde{\rho}T^\dagger) = \frac{dT}{dt}\tilde{\rho}T^\dagger + T\tilde{\rho}\frac{dT^\dagger}{dt} + T\frac{d\tilde{\rho}}{dt}T^\dagger.$$

After performing a unitary transformation this gives us:

$$T^\dagger \frac{d\rho}{dt} T = T^\dagger \frac{dT}{dt}\tilde{\rho} + \tilde{\rho}\frac{dT^\dagger}{dt}T + \frac{d\tilde{\rho}}{dt}. \tag{4.2.3}$$

We also know that for unitary matrices

$$\frac{dT^\dagger}{dt}T = -T^\dagger\frac{dT}{dt},$$

which together with Eq. (4.2.3) allows us to write

$$T^\dagger\frac{d\rho}{dt}T = \frac{d\tilde{\rho}}{dt} + \left[T^\dagger\frac{dT}{dt}, \tilde{\rho}\right].$$

We can then substitute the above formula into Eq. (4.2.2) and find

$$\frac{d\tilde{\rho}}{dt} = -i[H', \tilde{\rho}] - \left[T^\dagger\frac{dT}{dt}, \tilde{\rho}\right] + \tilde{\mathcal{L}}.$$

Finally, we can define $\tilde{H} = H' - iT^\dagger dT/dt$, which after substituting into the equation above, gives us an equation in the same form as Eq. (4.2.1):

$$\frac{d\tilde{\rho}}{dt} = -i[\tilde{H}, \tilde{\rho}] + \tilde{\mathcal{L}}. \tag{4.2.4}$$

When solving the master equation we will in fact be solving Eq. (4.2.4) in a basis where $\tilde{H}$ has a simple form. Basis that we will be using is a kind of rotating basis, where the unitary transformation for a system with n states can be written as:

$$T = \begin{pmatrix} e^{i\alpha_1 t} & & & \\ & \ddots & & 0 \\ & & \ddots & \\ 0 & & & e^{i\alpha_n t} \end{pmatrix}$$

for some real parameters α_i. It can be easily found that:

$$-iT^\dagger\frac{dT}{dt} = \begin{pmatrix} \alpha_1 & & & \\ & \ddots & & 0 \\ & & \ddots & \\ 0 & & & \alpha_n \end{pmatrix}.$$

To obtain $\tilde{H}$, we just need to look at H'. First,

$$(HT)_{il} = \sum_{j=1}^{n} H_{ij}T_{jl} = H_{il}T_{ll} = H_{il}e^{i\alpha_l t},$$

and then

$$H'_{kl} = (T^\dagger(HT))_{kl} = \sum_{i=1}^{n} T^\dagger_{ki}(HT)_{il} = T^\dagger_{kk}(HT)_{kl} = H_{kl}e^{i(\alpha_l-\alpha_k)t}.$$

Finally, combining found expressions, we see that for our choice of unitary transformation the hamiltonian is given by:

$$\tilde{H}_{kl} = H_{kl}e^{i(\alpha_l-\alpha_k)t} + \alpha_k\delta_{kl}. \tag{4.2.5}$$

We will always try to find such unitary transformation that eliminates all the oscillatory time dependence from the hamiltonian.

4.3 Dissipator

One of the valid choices of Lindblad operators in Eq. (4.1.1) are the projection operators P_i having properties $P_i^2 = P_i$ and $P_i^\dagger = P_i$, used for example in [65]. Authors there divide the dissipator into two parts. The first one contains dephasing effects, which include influence of finite laser linewidths and various broadening effects such as transit time broadening and collision-induced broadening, and is evaluated using the mentioned projection operators. The second one is related to spontaneous decay processes where the diagonal terms describe transfer between populations, and the off-diagonal terms are related to decoherence effects. Here, only that second part of the dissipator will be included, and it will be evaluated using quantum jump operators [65].

For states i and j we define quantum jump operators as $C_{i\to f} = |f\rangle\langle i|$. For spontaneous decays from i to f with rate $\Gamma_{i\to f}$ we will be using operators $G_{i\to f} = \sqrt{\Gamma_{i\to f}}C_{i\to f} = \sqrt{\Gamma_{i\to f}}\,|f\rangle\langle i|$. In matrix form these will look like:

$$G_{i\to f} = \begin{array}{c} \\ f \end{array} \begin{array}{c} \begin{array}{ccccc} & & & i & \end{array} \\ \begin{pmatrix} 0 & \cdots & & & 0 \\ & & & \sqrt{\Gamma_{i\to f}} & \\ \vdots & & & & \vdots \\ 0 & \cdots & & & 0 \end{pmatrix} \end{array}.$$

Because $G_{i\to f}$ is real, $G^\dagger_{i\to f} = G^{\mathrm{T}}_{i\to f}$, and (dropping lower indices)

$$G^\dagger G = \begin{array}{c} \\ i \end{array} \overset{\qquad\qquad i}{\begin{pmatrix} 0 & \cdots & 0 \\ \vdots & & \vdots \\ & \Gamma_{i\to f} & \\ 0 & \cdots & 0 \end{pmatrix}}.$$

With these, we can easily evaluate the part of $\mathcal{L}$ related to spontaneous decay, which will include both decoherence and population transfer. First, let's look at the anticommutator part $\{G^\dagger G, \rho\}$ knowing that the only non-zero element of $G^\dagger G$ is $(G^\dagger G)_{ii}$. The first term is:

$$(G^\dagger G\rho)_{kl} = \sum_j (G^\dagger G)_{kj}\rho_{jl} = \delta_{ki}(G^\dagger G)_{ki}\rho_{il},$$

so the non-zero elements have indices $\{i, l\}$ for $1 \le l \le n$ equivalent to a non-zero row:

$$G^\dagger G\rho = \begin{array}{c} \\ i \end{array} \begin{pmatrix} 0 & \cdots & 0 \\ \vdots & & \vdots \\ \Gamma_{i\to f}\rho_{i1} & \cdots & \Gamma_{i\to f}\rho_{in} \\ \vdots & & \vdots \\ 0 & \cdots & 0 \end{pmatrix}.$$

Analogically, the second term is:

$$(\rho G^\dagger G)_{kl} = \sum_j \rho_{kj}(G^\dagger G)_{jl} = \rho_{ki}(G^\dagger G)_{il}\delta_{li},$$

giving us a non-zero column:

$$\rho G^\dagger G = \overset{\qquad\qquad i}{\begin{pmatrix} 0 & \cdots & \Gamma_{i\to f}\rho_{1i} & \cdots & 0 \\ \vdots & & \vdots & & \vdots \\ 0 & \cdots & \Gamma_{i\to f}\rho_{ni} & \cdots & 0 \end{pmatrix}}.$$

Now we just need to evaluate the second term in $\mathcal{L}$ knowing that the only non-zero element of G is G_{fi} and the only non-zero element of $G^\dagger$ is $G^\dagger_{if}$:

$$\begin{aligned}(G\rho G^\dagger)_{rs} &= \sum_j G_{rj}(\rho G^\dagger)_{js} = \delta_{rf} G_{ri}(\rho G^\dagger)_{is} \\ &= \delta_{rf} G_{ri} \left(\sum_m \rho_{im} (G^\dagger)_{ms} \right) = \delta_{rf} G_{ri} \rho_{ii} (G^\dagger)_{if} \delta_{sf} \\ &= \delta_{rf} \delta_{sf} \Gamma_{i\to f} \rho_{ii},\end{aligned}$$

which gives a matrix with only one non-zero element:

$$G\rho G^\dagger = \begin{array}{c} \\ f \end{array} \begin{array}{c} \begin{array}{ccc} f & & \end{array} \\ \begin{pmatrix} 0 & \cdots & 0 \\ & \Gamma_{i\to f}\rho_{ii} & \\ \vdots & & \vdots \\ 0 & \cdots & 0 \end{pmatrix} \end{array}.$$

This finally allows us to obtain a matrix that represents contribution to $\mathcal{L}$ from a spontaneous decay from state i to f:

$$\mathcal{L}_{i\to f} = -\frac{1}{2}\{G^\dagger_{i\to f} G_{i\to f}, \rho\} + G_{i\to f}\rho G^\dagger_{i\to f} = \begin{array}{c} \\ f \\ \\ \\ \\ i \\ \\ \end{array} \begin{array}{c} \begin{array}{ccccccc} & & f & & i & & \end{array} \\ \begin{pmatrix} 0 & & & -\frac{\Gamma_{i\to f}}{2}\rho_{1i} & & 0 \\ & \Gamma_{i\to f}\rho_{ii} & & \vdots & & \\ & & & & & \\ & & 0 & \vdots & & \\ -\frac{\Gamma_{i\to f}}{2}\rho_{i1} & \cdots & \cdots & -\Gamma_{i\to f}\rho_{ii} & \cdots & -\frac{\Gamma_{i\to f}}{2}\rho_{in} \\ & & & \vdots & & \\ 0 & & & -\frac{\Gamma_{i\to f}}{2}\rho_{ni} & & 0 \end{pmatrix} \end{array}.$$

We see that we properly obtain a decrease of population ρ_{ii} with rate $\Gamma_{i\to f}$ with simultaneous increase of population ρ_{ff} equal to that loss, which results in the matrix having a zero trace. That is equivalent to a closed system, where the trace of density matrix ρ is preserved. The off-diagonal terms correspond to evolving coherence between two states. Despite the fact that this method gives

us a correct result, computationally it can be quite challenging. For large systems the initial state i can have multiple decay paths. For a single initial state, we'd have to calculate matrices above for every final state separately. However, the calculation can simplified.

A single initial state decaying into multiple different states will have a total decay rate $\Gamma_i = \sum_f \Gamma_{i\to f}$, so for a single final state, the corresponding decay rate is $\Gamma_{i\to f} = b_{fi}\Gamma_i$, where b_{fi} is the branching ratio. We also note that all the coherence (off-diagonal) terms were generated by the anticommutator, which is a bilinear operator. So:

$$\sum_f \{G^\dagger_{i\to f} G_{i\to f}, \rho\} = \left\{ \sum_f G^\dagger_{i\to f} G_{i\to f}, \rho \right\} \equiv \{M_i^\dagger M_i, \rho\},$$

where we have defined a operator M_i

$$(M_i)_{kl} = \begin{cases} \sqrt{\Gamma_i} & \text{if } k = l = i \\ 0 & \text{otherwise} \end{cases}$$

for which $M_i^\dagger = M_i$. We can do that, because every matrix $G^\dagger_{i\to f} G_{i\to f}$ will have $b_{fi}\Gamma_{i\to f}$ in its $\{i,i\}$-th cell, so after the summation the term in that cell will be $\sum_f b_{fi}\Gamma_{i\to f} = \Gamma_i$. Using matrix M instead of G will, however, not give us the same result in the second term of $\mathcal{L}_i \equiv \sum_f \mathcal{L}_{i\to f}$. Instead, we will obtain:

$$M_i \rho M_i^\dagger = \begin{array}{c} \\ i \end{array} \begin{array}{c} \begin{array}{cccc} & & i & \end{array} \\ \begin{pmatrix} 0 & \cdots & & 0 \\ \vdots & & & \vdots \\ & & \Gamma_i \rho_{ii} & \\ 0 & \cdots & & 0 \end{pmatrix} \end{array}$$

so, in the end:

$$\mathcal{L}_i = -\frac{1}{2}\{M_i^\dagger M_i, \rho\} + M_i \rho M_i^\dagger = \begin{array}{c} \\ \\ \\ i \\ \\ \\ \\ \end{array} \begin{pmatrix} 0 & & -\frac{\Gamma_i}{2}\rho_{1i} & & 0 \\ & & \vdots & & \\ -\frac{\Gamma_i}{2}\rho_{i1} & \cdots & 0 & \cdots & -\frac{\Gamma_i}{2}\rho_{in} \\ & & \vdots & & \\ 0 & & -\frac{\Gamma_i}{2}\rho_{ni} & & 0 \end{pmatrix}.$$

We, therefore, obtain correct decoherence terms, but no population transfer terms. However, having branching ratios we can quite easily fill in the diagonal terms without performing any matrix operations. Finally, if we have several initial states we can create operator $M = \sum_i M_i$, for which $M^2 = \sum_i M_i^2$, because $M_i M_j$ is zero for $i \neq j$. Again, the off-diagonal terms will be determined correctly, because of the linearity of anticommutator. The other term, however, has to be determined separately for every initial state. Hence, the fastest way to calculate all the off-diagonal contributions to $\mathcal{L}$ from spontaneous decays is:

$$\mathcal{L}_\Gamma = \sum_i \mathcal{L}_i = -\frac{1}{2}\left\{\sum_i M_i^2, \rho\right\} + \sum_i M_i \rho M_i = -\frac{1}{2}\{M^2, \rho\} + \sum_i M_i \rho M_i \tag{4.3.1}$$

4.4 Example - EIA in a Four-level System

Modeling and simulations of toy models and experimental procedures required solving the equations multiple times. To streamline the process, we wrote a package in MATLAB that allows for a quick setup of a quantum system and appropriate equations, and fast solutions to the master equation.[1] As a benchmark test and an example of setting up the master equation using the described method we chose a four-level system in N-configuration, which in weak probe limit should exhibit electromagnetically induced absorption (EIA). In that system we have two lower lying states $|A\rangle$ and $|B\rangle$ with energies ω_A and ω_B that are connected to a common excited state $|E_1\rangle$ with energy ω_{E_1}. The laser connecting state $|B\rangle$ with $|E_1\rangle$ is the probe laser with frequency ω_p and Rabi frequency Ω_p. In a general case it is assumed to be detuned from the transition by

[1] Code is available at: https://github.com/kwenz/OBE-solver.

Δ_p. The transition from $|A\rangle$ to $|E_1\rangle$ is due to the control laser 1, and transition from $|B\rangle$ to $|E_2\rangle$ is due the control laser 2. Both of them are in general case detuned by Δ_{c_1} and Δ_{c_2} respectively. The state $|E1\rangle$ has a total decay rate $\Gamma_A + \Gamma_{B_1}$ and the state $|E2\rangle$ decays into state $|B\rangle$ with rate Γ_{B_2}. The system is shown in the Fig. 4.4.1.

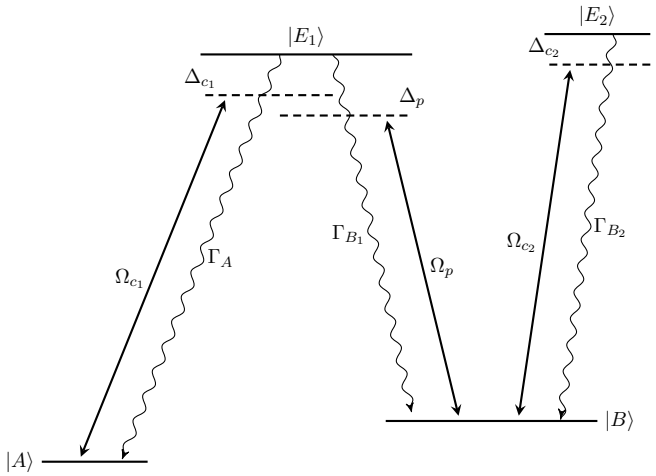

Figure 4.4.1: Diagram of a four-level system in N configuration.

For such system we obtain hamiltonian of the form:

$$H = \begin{array}{c} \begin{array}{cccc} |A\rangle & |B\rangle & |E_1\rangle & |E_2\rangle \end{array} \\ \begin{pmatrix} \omega_A & 0 & \frac{\Omega_{c_1}}{2}e^{i\omega_{c_1}t} & 0 \\ 0 & \omega_B & \frac{\Omega_p}{2}e^{i\omega_p t} & \frac{\Omega_{c_2}}{2}e^{i\omega_{c_2}t} \\ \frac{\overline{\Omega}_{c_1}}{2}e^{-i\omega_{c_1}t} & \frac{\overline{\Omega}_p}{2}e^{-i\omega_p t} & \omega_{E_1} & 0 \\ 0 & \frac{\overline{\Omega}_{c_2}}{2}e^{-i\omega_{c_2}t} & 0 & \omega_{E_2} \end{pmatrix} \end{array},$$

where we have already used rotating wave approximation ($\Omega = \Omega_0 \cos\omega t \approx \Omega_0 e^{i\omega t}/2$). We then perform unitary transformation, where we find coefficients α_i in Eq. (4.2.5) by trying to remove oscillating terms from off-diagonal elements of the hamiltonian. We get a set of linear equations:

$$\begin{cases} \alpha_3 - \alpha_1 = & -\omega_{c_1} \\ \alpha_3 - \alpha_2 = & -\omega_p \\ \alpha_4 - \alpha_2 = & -\omega_{c_2} \end{cases},$$

which is solved for

$$\begin{cases} \alpha_1 = & \omega_{c_1} - \omega_p \\ \alpha_2 = & 1 \\ \alpha_3 = & -\omega_p \\ \alpha_4 = & -\omega_{c_2} \end{cases}.$$

This allows us to use unitary transformation with matrix

$$T = \begin{pmatrix} e^{i(\omega_{c_1}-\omega_p)t} & 0 & 0 & 0 \\ 0 & 1 & 0 & 0 \\ 0 & 0 & e^{-i\omega_p t} & 0 \\ 0 & 0 & 0 & e^{-i\omega_{c_2} t} \end{pmatrix},$$

giving us

$$\tilde{H} = \begin{pmatrix} \Delta_p - \Delta_{c_1} + \omega_B & 0 & \Omega_{c_1}/2 & 0 \\ 0 & \omega_B & \Omega_p/2 & \Omega_{c_2}/2 \\ \overline{\Omega}_{c_1}/2 & \overline{\Omega}_p/2 & \Delta_p + \omega_B & 0 \\ 0 & \overline{\Omega}_{c_2}/2 & 0 & \Delta_{c_2} + \omega_B \end{pmatrix}.$$

The diagonal terms of hamiltonian $\tilde{H}$ show us that the natural choice for the energy scale is $\omega_B = 0$.

To find matrix $\mathcal{L}$ we first define two matrices M_{E_1} and M_{E_2}, where:

$$M_{E_1} = \begin{pmatrix} 0 & 0 & 0 & 0 \\ 0 & 0 & 0 & 0 \\ 0 & 0 & \sqrt{\Gamma_A + \Gamma_{B_1}} & 0 \\ 0 & 0 & 0 & 0 \end{pmatrix}, \; M_{E_2} = \begin{pmatrix} 0 & 0 & 0 & 0 \\ 0 & 0 & 0 & 0 \\ 0 & 0 & 0 & 0 \\ 0 & 0 & 0 & \sqrt{\Gamma_{B_2}} \end{pmatrix}.$$

We can then also find

$$M^2 = M_{E_1}^2 + M_{E_2}^2 = \begin{pmatrix} 0 & 0 & 0 & 0 \\ 0 & 0 & 0 & 0 \\ 0 & 0 & \Gamma_A + \Gamma_{B_1} & 0 \\ 0 & 0 & 0 & \Gamma_{B_2} \end{pmatrix}$$

and plug those three matrices into Eq. (4.3.1) to obtain decoherence terms. Population transfer (diagonal) terms can be easily added by hand. Eventually, we obtain:

$$\mathcal{L} = \begin{pmatrix} \Gamma_A \rho_{e_1 e_1} & 0 & -\frac{\Gamma_A+\Gamma_{b_1}}{2}\rho_{ae_1} & -\frac{\Gamma_{B_2}}{2}\rho_{ae_2} \\ 0 & \Gamma_{B_1}\rho_{e_1e_1} + \Gamma_{B_2}\rho_{e_2e_2} & -\frac{\Gamma_A+\Gamma_{B_1}}{2}\rho_{be_1} & -\frac{\Gamma_{B_2}}{2}\rho_{be_2} \\ -\frac{\Gamma_A+\Gamma_{B_1}}{2}\rho_{e_1a} & -\frac{\Gamma_A+\Gamma_{B_1}}{2}\rho_{e_1b} & -(\Gamma_A+\Gamma_{B_1})\rho_{e_1e_1} & -\frac{\Gamma_A+\Gamma_{B_1}+\Gamma_{B_2}}{2}\rho_{e_1e_2} \\ -\frac{\Gamma_{B_2}}{2}\rho_{e_2a} & -\frac{\Gamma_{B_2}}{2}\rho_{e_2b} & -\frac{\Gamma_A+\Gamma_{B_1}+\Gamma_{B_2}}{2}\rho_{e_2e_1} & -\Gamma_{B_2}\rho_{e_2e_2} \end{pmatrix}.$$

To look at the accuracy of numerical solutions, we solved the equations in the weak probe limit for which analytical solutions exist. In such limit the system should exhibit the mentioned EIA effect. First, however, we looked at the evolution of populations. Even for zero probe laser detuning Δ_p, we expect that the population in the steady state will consist of only states $|B\rangle$ and $|E_2\rangle$. Indeed, that is the case as shown in Fig. 4.4.2 depicting populations as function of time.

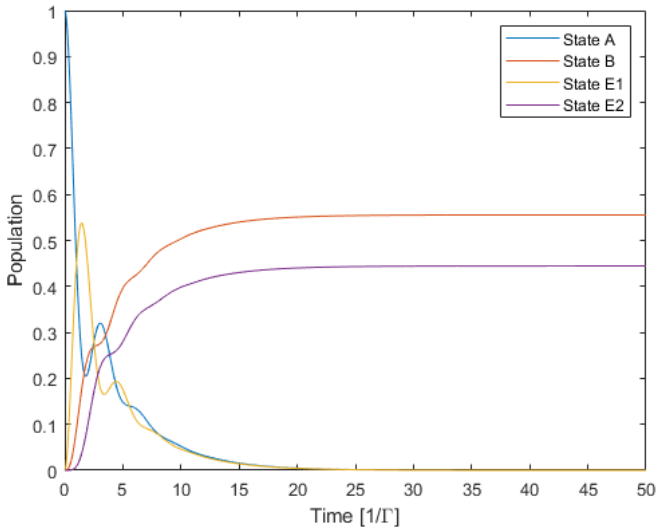

Figure 4.4.2: Populations as function of time for a four-level system in weak probe limit. Solution was obtained for $2\Gamma_A = 2\Gamma_{B_1} = \Gamma_{B_2} \equiv \Gamma$, $\Omega_{c_1} = \Omega_{c_2} = 2\Gamma$ and $\Omega_p = 0.00025\,\Gamma$ with $\Delta_{c_1} = \Delta_{c_2} = \Delta_p = 0$.

Finally, we were able to check for the existence of EIA. This effect is visible once we inspect imaginary part of ρ_{be_1}. In general, the analytical solution is given by [66]:

$$\rho_{be_1} = -\frac{i\Omega_p\rho_{bb}}{2\beta_{be_1}\alpha_2} + \frac{i\Omega_p\Omega_{c_2}^2(\rho_{bb}-\rho_{e_2e_2})}{8\beta_{e_2e_1}\beta_{be_1}\beta_{e_2b}\alpha_2} - \frac{i\Omega_p\Omega_{c_1}^2\Omega_{c_2}^2(\rho_{bb}-\rho_{e_2e_2})}{32\beta_{e_2e_1}\beta_{be_1}\beta_{e_2a}\beta_{e_2b}\alpha_1\alpha_2}\left(\frac{1}{\beta_{ba}}+\frac{1}{\beta_{e_2e_1}}\right),$$

where

$$\begin{aligned}
\rho_{e_2e_2} &= \frac{\Omega_{c_2}^2}{\Gamma^2+2\Omega_{c_2}^2}\\
\rho_{bb} &= 1-\rho_{e_2e_2}\\
\beta_{ba} &= -i\Delta_p\\
\beta_{be_1} &= -\frac{\Gamma}{2}-i\Delta_p\\
\beta_{e_2a} &= -\frac{\Gamma}{2}-i\Delta_p\\
\beta_{e_2e_1} &= -\Gamma-i\Delta_p\\
\beta_{e_2b} &= -\frac{\Gamma}{2}\\
\alpha_1 &= 1+\frac{\Omega_{c_1}^2}{4\beta_{e_2a}\beta_{e_2e_1}}+\frac{\Omega_{c_2}^2}{4\beta_{e_2a}\beta_{ba}}\\
\alpha_2 &= 1+\frac{\Omega_{c_1}^2}{4\beta_{ba}\beta_{be_1}}+\frac{\Omega_{c_2}^2}{4\beta_{e_2e_1}\beta_{be_1}}-\frac{\Omega_{c_1}^2\Omega_{c_2}^2}{16\beta_{be_1}\beta_{e_2a}\alpha_1}\left(\frac{1}{\beta_{ba}}+\frac{1}{\beta_{e_2e_1}}\right)^2.
\end{aligned}$$

We can now compare this ungainly analytical solution with the numerical solution. The comparison is shown in Fig. 4.4.3, where we can see that the two results are identical.

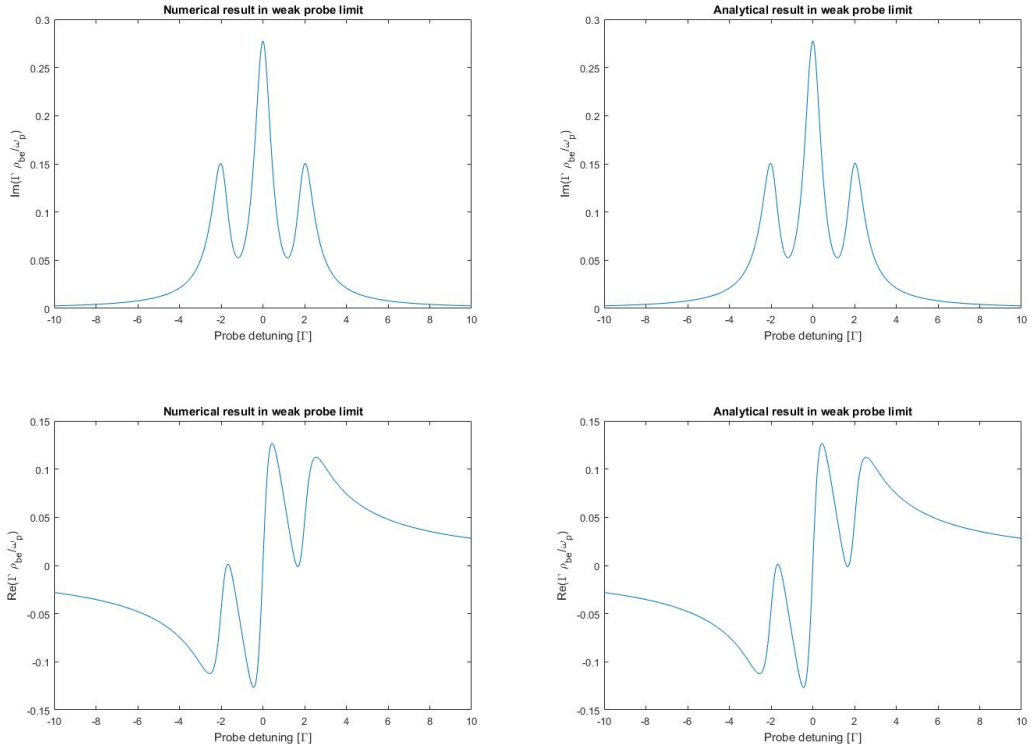

Figure 4.4.3: Numerical (left) and analytical (right) results showing electromagnetically induced absorption by plotting $\Gamma\rho_{be_1}/\Omega_p$ as a function of probe detuning Δ_p. Solution was obtained for $2\Gamma_A = 2\Gamma_{B_1} = \Gamma_{B_2} \equiv \Gamma$, $\Omega_{c_1} = \Omega_{c_2} = 2\,\Gamma$ and $\Omega_p = 0.00025\,\Gamma$ with $\Delta_{c_1} = \Delta_{c_2} = 0$.

Chapter 5

Dark States

5.1 Problems with Dark States in TlF

In molecular systems a new problem arises that is usually ignored in atoms. Due to higher number of degrees of freedom, the system is described by more quantum numbers, and the number of distinct states is much larger. In TlF in a single rotational manifold there are already $4(2J+1)$ levels. If these levels are close to degenerate, dark states can appear. In atoms such problems are usually ameliorated by using a so-called type I transition - coupling states with a quantum number F in the ground state to states with $F' = F + 1$ in the excited state. Given there is a higher multiplicity of states in the excited state manifold, no dark states are created.

In molecules it is usually impossible to use type I transitions - they are not closed with respect to the quantum number considered. Therefore, type II transitions are utilized with $F' = F - 1$. Usually, such transitions do not immediately create dark states, because states in the ground state manifold are not close-to-degenerate (with respect to the decay rate Γ, which is a natural energy unit in the system, or the natural linewidth $\gamma = \Gamma/2\pi$). Known rule of a thumb is that the number of dark states is equal to $n_g - n_e$, where n_e and n_g are number of close-to-degenerate excited and ground states respectively that are coupled to each other. Because of energy differences in the ground state manifold, n_g quite often is just the number of states in a coupled sub-manifold and can be made larger or equal to n_e.

Sometimes, however, we do have multiple dark states in the system. These can then be remixed using various methods. One of the most commonly used ones is lifting the degeneracy by inducing

Zeeman splitting. This leads to magnetic field effectively remixing dark and bright states. It requires the g-factor to be substantial in order to be able to use this method with just modest magnetic fields. States with $\mathbf{S} > 0$ or $\mathbf{L} > 0$ should be good candidates for this remixing method.

Thallium fluoride is unfortunately a pretty nasty molecule and we do not have its toxicity in mind. In its ground electronic state, states within every rotational manifold have energy differences couple of orders of magnitude smaller than the natural linewidth, which makes them close to degenerate. On the other hand, the hyperfine manifolds in the excited electronic state are split by several orders of magnitude more than the natural linewidth (Fig. 2.2.1). Therefore, a laser could couple a whole rotational state manifold to only one hyperfine manifold in the excited state. For example, in rotational cooling we need to couple $J = 2$ states in the ground state with $F' = 1$ states in the excited electronic state, which will create $20 - 3 = 17$ dark states!

TlF in its ground state is also a $^1\Sigma$ state with $\mathbf{S}$ and $\mathbf{L}$ both equal to 0, so its effective g-factor is quite small as was shown in Chapter 2. We need to find other methods of dark state destabilization. In this chapter we will investigate the dark states - understand how they are created and behave, and then look at the best ways of remixing them with the bright states.

5.2 A Simplified 3-level System

We begin with analysis of two 3-state systems - a standard Λ-type system, and its simpler version with only one coupling light field. We will begin with the latter. We chose such system to represent a simple situation where two possibly unresolved states are coupled by one light field to an excited state (Fig. 5.2.1 depicts the level structure).

In the context of optical cycling and rotational cooling, we have two problems that already appear in this very simple system and we would like to solve - how to avoid creating the dark state and how to reach optimal scattering rate, which is also crucial in CeNTREX in the context of the detection transitions. We start with the former. To begin the analysis we analytically solve the master equation described in the previous chapter and, for simplicity, assume real Rabi rates. We begin by writing a hamiltonian in a frame where the time dependence has been eliminated and

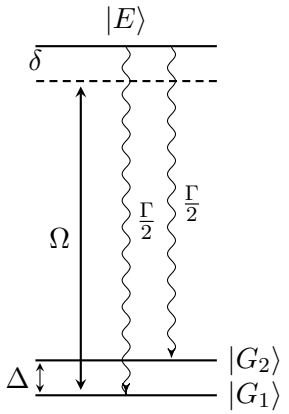

Figure 5.2.1: Diagram of a simplified three-level system.

energy of the excited state set to zero:

$$\tilde{H} = \begin{pmatrix} -\delta & 0 & -\frac{\Omega}{2} \\ 0 & \Delta - \delta & -\frac{\Omega}{2} \\ -\frac{\Omega}{2} & -\frac{\Omega}{2} & 0 \end{pmatrix}.$$

Solving the equations to obtain the steady state solution of the population of state $|E\rangle$ gives us:

$$\rho_{ee} = \frac{\Omega^2}{4} \frac{1}{\left(\delta - \frac{\Delta}{2}\right)^2 + \left(\frac{\Gamma'}{2}\right)^2}, \tag{5.2.1}$$

with

$$\Gamma' = \sqrt{\Gamma^2 + \Delta^2 + \Omega^2 \left(1 + \frac{\Omega^2}{\Delta^2}\right)}. \tag{5.2.2}$$

We would expect that the existence of a dark state would cause the excited state population (and hence the scattering rate $R_{\text{scatt}} \equiv \Gamma \rho_{ee}$) in the steady state to reach 0 (the population would end up accumulating in the dark state). Indeed, when states are almost degenerate ($\Delta \to 0$):

$$\rho_{ee} = \frac{\Omega^2/4}{\left(\delta - \frac{\Delta}{2}\right)^2 + \Gamma^2 + \Delta^2 + \Omega^2 \left(1 + \frac{\Omega^2}{\Delta^2}\right)} \xrightarrow{\Delta \to 0} \frac{\Delta^2}{4},$$

the scattering rate drops to 0. From Eq. (5.2.2) we can also see that the lineshape is power-broadened, although that power broadening has an unusual term that is inversely proportional to the ground state splitting. That term is also responsible for decreasing scattering rate with increasing power and it is the term that survives when splitting becomes small.

To better understand how bright and dark states are connected with each other, we move the hamiltonian to a different basis with:

$$|B\rangle = \frac{|G_1\rangle + |G_2\rangle}{\sqrt{2}}$$
$$|D\rangle = \frac{|G_1\rangle - |G_2\rangle}{\sqrt{2}},$$

which leads to:

$$\tilde{H} = -\begin{pmatrix} \delta - \frac{\Delta}{2} & \frac{\Delta}{2} & \frac{\Omega}{\sqrt{2}} \\ \frac{\Delta}{2} & \delta - \frac{\Delta}{2} & 0 \\ \frac{\Omega}{\sqrt{2}} & 0 & 0 \end{pmatrix}.$$

We first notice the bright state $|B\rangle$ (column and row 1) has a direct coupling to the excited state $|E\rangle$ (column and row 3), while the dark state $|D\rangle$ (column and row 2) does not. However, the dark state has an indirect coupling to the excited state - it is coupled to the bright state with coupling strength Δ. The smaller that splitting is, the weaker the coupling and at $\Delta = 0$ the dark state becomes completely decoupled. In a more realistic situation, both ground states are still coupled by the same light field, but their matrix elements for the dipole transition to the excited state are different, and hence their Rabi rates are. Assuming $\Omega_{g_1} = a\Omega$ and $\Omega_{g_2} = b\Omega$, we obtain hamiltonian:

$$\tilde{H} = -\begin{pmatrix} \delta - \frac{b^2}{a^2+b^2}\Delta & \frac{ab}{a^2+b^2}\Delta & \frac{\Omega\sqrt{a^2+b^2}}{\sqrt{2}} \\ \frac{ab}{a^2+b^2}\Delta & \delta - \frac{a^2}{a^2+b^2}\Delta & 0 \\ \frac{\Omega\sqrt{a^2+b^2}}{\sqrt{2}} & 0 & 0 \end{pmatrix}.$$

The dark state appearing at $\Delta = 0$ is still there, though we see that the strength of the coupling enters in a non-trivial way. If we were perhaps able to shift one of the states by a different amount than the other, for example by coupling another state to these ground states with different strengths, we could be able to change the way the dark state evolves. Here, it evolves (remixes) with rate proportional to the splitting Δ, but shifting one state with respect to the other would create a slightly different superposition and, therefore, affect the state's evolution. We will explore that idea later, once we include microwaves. In general, as was mentioned and as we can see from the example above, lifting the degeneracy allows for better dark state remixing.

To find the maximum scattering rate in such simple system, we note that Eq. (5.2.1) will reach maximum at $\delta = \Delta/2$. Then, as it happens, the peak occurs at:

$$\Omega_{\text{opt}} = \sqrt[4]{\Delta^4 + \Delta^2\Gamma^2} \overset{\Delta \gg \Gamma}{\longrightarrow} \Delta,$$

for which (at high splittings Δ) the excited state population ρ_{ee} reaches value of 1/3. Fig. 5.2.2 shows the behavior of ρ_{ee} as a function of the Rabi rate with splitting $\Delta = 2\,\Gamma$. The result shown here is pretty interesting - it shows that the scattering rate is highest, when the Rabi rate is comparable to the remixing rate. Note, that unlike in a 2-level system, the scattering rate does *not* saturate at high Rabi rates.

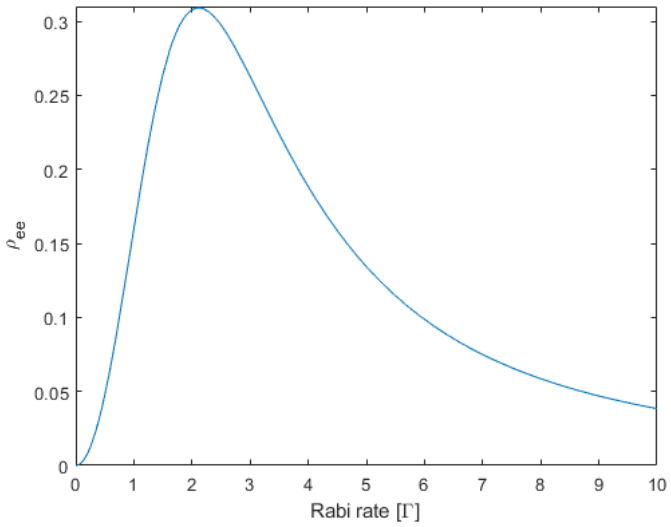

Figure 5.2.2: Excited state population as a function of Rabi rate for $\Delta = 2\,\Gamma$.

Indeed, such result has already been shown in [49]. In a system, where we explicitly have bright and dark states (Fig. 5.2.3) remixed with rate R and the excited state decaying to the dark state with rate $\alpha\Gamma$ (decay rate to the bright state is then $(1-\alpha)\Gamma$), we obtain an optimal Rabi rate:

$$\Omega_{\text{opt}}^2 = \sqrt{\frac{8\,\Gamma^2 R^2 + 32 R^4}{\alpha}} \overset{R \ll \Gamma}{\longrightarrow} \frac{2\sqrt{2}}{\sqrt{\alpha}}\,\Gamma R,$$

where we assumed remixing rate smaller than the natural linewidth, which is quite often the case in the experiments that try to remix the dark states. Alternatively, the remixing rate should be on the order of $\alpha\Omega^2/\Gamma$ in order to obtain high scattering rate. To put it in words, the rate with which

we are remixing dark and bright states (the rate of moving the population from a dark to a bright state) has to be on the order of the rate with which the dark states are re-populated through the spontaneous decay. It is an important result, which should hold for larger systems as well.

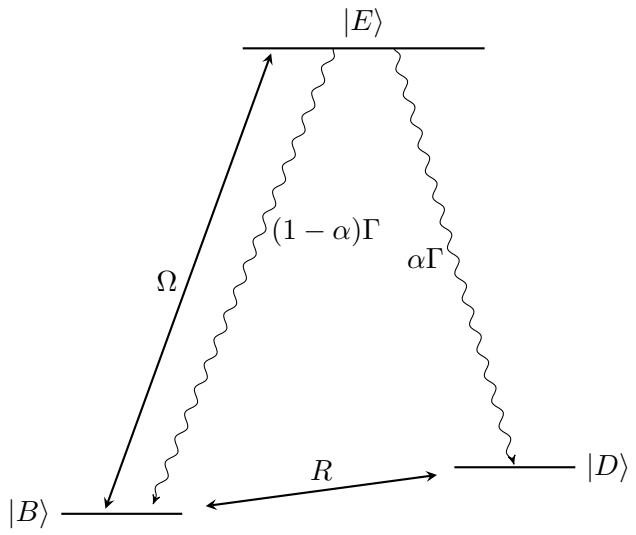

Figure 5.2.3: Diagram of a three-level system in Λ configuration with explicit dark and bright states actively remixed with rate R. Here, the decay to dark state happens with rate $\alpha\Gamma$.

5.3 Λ-system

A standard Λ-type system is quite often described in textbooks to present the effects of electromagnetically induced transparency (EIT). There, one of the lasers is much weaker than the other. In our situation, however, we will assume that both lasers have comparable Rabi rates, and no approximations can be made. We also assume a general case, where energies of the low-lying levels are $\hbar\omega_{G_1}$ and $\hbar\omega_{G_2}$, and a substitution $\omega_{G_2} = \omega_{G_1} + \Delta$ can be made if necessary. The excited state is again assumed to have 0 energy. The decays are assumed to have equal rates to both ground states.

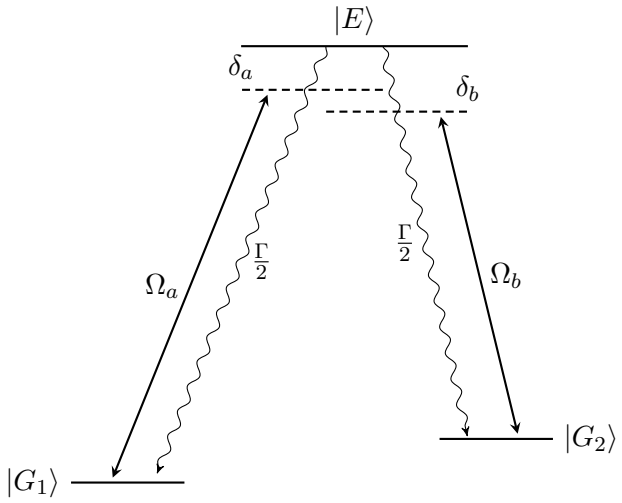

Figure 5.3.1: Diagram of a three-level system in Λ configuration.

After eliminating time dependence from the hamiltonian, it takes form of:

$$\tilde{H} = \begin{pmatrix} -\delta_a & 0 & -\frac{\Omega_a}{2} \\ 0 & -\delta_b & -\frac{\Omega_b}{2} \\ -\frac{\Omega_a}{2} & -\frac{\Omega_b}{2} & 0 \end{pmatrix}.$$

The solution for the excited state population in the steady state in this case is very inelegant, but the important part, its numerator, is small enough to include here.

$$\rho_{ee} \propto \Omega_a^2 \Omega_b^2 (\delta_a - \delta_b)^2 \tag{5.3.1}$$

We see that the scattering rate goes to zero, if both lasers are detuned the same from their respective resonances, regardless of what the energies of the ground states $|G_1\rangle$ and $|G_2\rangle$ are. In the previous system, where the energies of these states were split by Δ and coupled to the excited state using one laser, detunings for the states were δ and $\delta - \Delta$. These are equal only when splitting $\Delta = 0$, and that is exactly when scattering rate given by Eq. (5.2.1) goes to zero.

However, as we see in Eq. (5.3.1), if those states were coupled by separate light fields, the scattering rate could be non-zero. In other words, if the levels are degenerate ($\Delta = 0$), we can avoid zero scattering rate in the steady state, if we use two different lasers detuned differently from their respective resonances. What we are doing is effectively lifting the degeneracy - now state $|G_1\rangle$

has energy δ_a and state $|G_2\rangle$ energy δ_b. By keeping these different, we are avoiding a dark state by making the remixing rate equal to the difference in energies.

Like before, we can look at the hamiltonian in a different basis. We first define $\Omega = \sqrt{\Omega_a^2 + \Omega_b^2}$ and transform states to a different basis using transformation:

$$U = \begin{pmatrix} \frac{\Omega_a}{\Omega} & \frac{\Omega_b}{\Omega} & 0 \\ \frac{\Omega_b}{\Omega} & -\frac{\Omega_a}{\Omega} & 0 \\ 0 & 0 & 1 \end{pmatrix},$$

which can be interpreted as rotation of states $|G_1\rangle$ and $|G_2\rangle$ about the state $|E\rangle$ by an angle $\theta = \arcsin(\Omega_a/\Omega)$. As a result we will obtain following states:

$$|B\rangle = \frac{\Omega_a |G_1\rangle + \Omega_b |G_2\rangle}{\Omega}$$
$$|D\rangle = \frac{\Omega_b |G_1\rangle - \Omega_a |G_2\rangle}{\Omega}.$$

The Hamiltonian after the transformation takes form of:

$$\tilde{H} = -\begin{pmatrix} \frac{\Omega_a^2\delta_a + \Omega_b^2\delta_b}{\Omega^2} & \frac{\Omega_a\Omega_b}{\Omega^2}(\delta_a - \delta_b) & \frac{\Omega}{2} \\ \frac{\Omega_a\Omega_b}{\Omega^2}(\delta_a - \delta_b) & \frac{\Omega_a^2\delta_b + \Omega_b^2\delta_a}{\Omega^2} & 0 \\ \frac{\Omega}{2} & 0 & 0 \end{pmatrix}. \tag{5.3.2}$$

State $|B\rangle$ is coupled to the excited state by light field with Rabi rate Ω. The dark state $|D\rangle$ has no direct coupling to the excited state, although it is coupled to the state $|B\rangle$ as long as the detunings are different. If $\delta_a = \delta_b$ the state becomes completely decoupled and the system is pumped from the coupled state to the dark state, which results in zero scattering rate in the steady state. So, just like before, the remixing rate is proportional to the energy splitting between the states.

5.3.1 Effects of Phase Modulation

There is one other detail that we have not mentioned yet. Both lasers considered here are assumed to be phase coherent, but in reality that does not need to be the case. We consider the phase difference between the lasers to be any time-dependent function, i.e. we will assume that one of

the light coupling is described by $\Omega \exp(i\varphi(t))$. The hamiltonian after unitary transformation takes form:

$$\tilde{H} = \begin{pmatrix} -\delta_a & 0 & -\frac{\Omega_a}{2} e^{i\varphi(t)} \\ 0 & -\delta_b & -\frac{\Omega_b}{2} \\ -\frac{\Omega_a}{2} e^{-i\varphi(t)} & -\frac{\Omega_b}{2} & 0 \end{pmatrix}.$$

If the phase difference changes with time, we expect that the steady state will never be reached. Even if the phase difference is simply attributed to the phase noise, it influences the results - when there is no phase noise (so phase difference is constant), then the excited state population for lasers with equal detunings ($\delta_a = \delta_b$) quite quickly goes down to zero. However, once the time dependence of phase is added, the situation changes. Fig. 5.3.2 depicts the new behavior, where the phase difference was modeled as $\varphi(t) = \beta \sin(\omega_m t)$ for $\beta = \pi$ rad and $\omega_m = \Gamma$ corresponding to sinusoidal phase modulation of one of the laser beams, which can be achieved experimentally with the help of an electro-optical modulator. Fig. 5.3.2 shows how such modulation influences the result. If we averaged the excited state population over time, we would obtain a non-zero result. In general, the time dependence of the phase of one of the laser helps, because the previously-dark state's direct coupling to the excited changes with the changing phase. The hamiltonian in the previously used rotated basis is:

$$\tilde{H} = -\begin{pmatrix} \frac{\Omega_a^2 \delta_a + \Omega_b^2 \delta_b}{\Omega^2} & \frac{\Omega_a \Omega_b}{\Omega^2}(\delta_a - \delta_b) & \frac{\Omega_a^2 e^{i\varphi(t)} + \Omega_b^2}{2\Omega} \\ \frac{\Omega_a \Omega_b}{\Omega^2}(\delta_a - \delta_b) & \frac{\Omega_a^2 \delta_b + \Omega_b^2 \delta_a}{\Omega^2} & \frac{\Omega_a \Omega_b \left(e^{i\varphi(t)} - 1\right)}{2\Omega} \\ \frac{\Omega_a^2 e^{-i\varphi(t)} + \Omega_b^2}{2\Omega} & \frac{\Omega_a \Omega_b \left(e^{-i\varphi(t)} - 1\right)}{2\Omega} & 0 \end{pmatrix}.$$

If the phase difference between the lasers is constant, it can be assumed that $\varphi = 0$, so the dark state loses the direct coupling to the excited state and we obtain situation described previously. However, if the phase difference changes with time, the dark state remains constantly coupled to the excited state, albeit with varying strength.

Finally, we can also look at the averaged result for various depths and modulation frequencies shown in Fig. 5.3.3. It shows that even though the detunings for both transitions are equal, such that for phase-coherent lasers the excited state population would be identically zero, we get an average population reaching the limit of 1/3 for quite a wide range of modulation depths and

frequencies. This was actually shown in [49] for a larger system and was framed as destabilization of dark states by phase modulation.

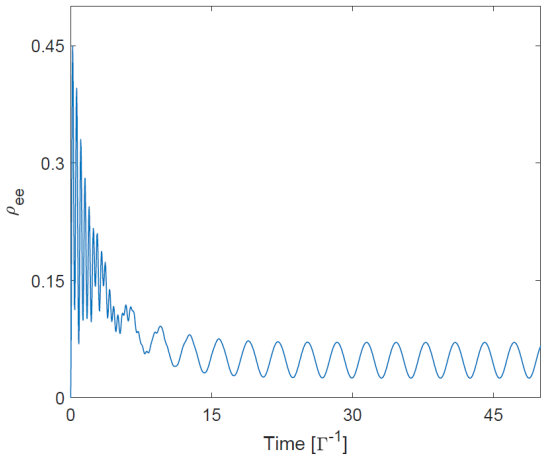

Figure 5.3.2: Evolution of excited state population with phase of one of the lasers modulated. Solution was obtained for $\Omega_a = \Omega_b = 10\,\Gamma$, $\delta_a = \delta_b = 0$, $\beta = \pi$ rad and $\omega_m = \Gamma$.

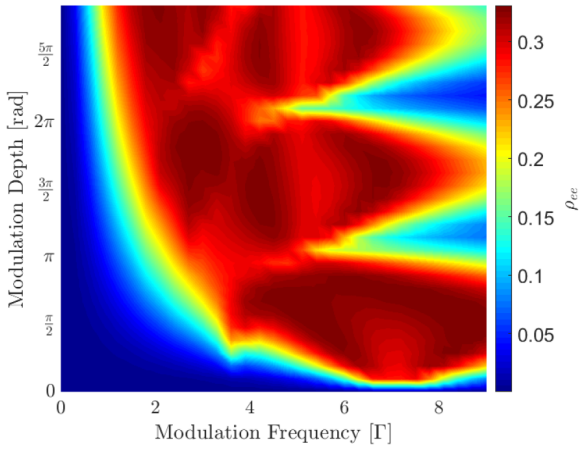

Figure 5.3.3: Averaged excited state population as a function of modulation depth and frequency of one of the lasers. Solution was obtained for $\Omega_a = \Omega_b = 10\,\Gamma$ and $\delta_a = \delta_b = 0$.

The method described here can also be investigated from a different point of view. Instead of using previous definitions of bright and dark states, we define them as:

$$|B\rangle = \frac{\Omega_a e^{i\varphi(t)}\,|G_1\rangle + \Omega_b\,|G_2\rangle}{\Omega}$$

$$|D\rangle = \frac{\Omega_b\,|G_1\rangle - \Omega_a e^{i\varphi(t)}\,|G_2\rangle}{\Omega}.$$

Modulating the phase can now be interpreted as simply changing what dark and bright states are. In a very simple situation when $\Omega_a = \Omega_b \equiv \Omega$, for $\varphi = 0$ we have:

$$|B_{\varphi=0}\rangle = \frac{|G_1\rangle + |G_2\rangle}{2}$$
$$|D_{\varphi=0}\rangle = \frac{|G_1\rangle - |G_2\rangle}{2},$$

while for $\varphi = \pi$:

$$|B_{\varphi=\pi}\rangle = \frac{-|G_1\rangle + |G_2\rangle}{2} = -|D_{\varphi=0}\rangle$$
$$|D_{\varphi=\pi}\rangle = \frac{|G_1\rangle + |G_2\rangle}{2} = |B_{\varphi=0}\rangle\,.$$

So by simply flipping the phase difference by π, we are completely rotating the basis - bright state becomes the dark state and vice-versa. Exactly this mechanism is the reason behind another dark state destabilization method - polarization switching, which will be discussed later.

5.4 Four-state System Based on TlF

In thallium fluoride the optical cycling scheme can be seen as, in a very simplified version, a three-level system with ground state splitting Δ that we described at the beginning. The ground states in this system belong to the $J = 1$ rotational manifold. In this section, we will generalize some results regarding the dark states and look at one way of destabilizing the dark states - we will consider using microwaves to couple the ground rotational state $J = 0$ with $J = 1$ states in order to either lift the degeneracy in $J = 1$ or to induce an indirect remixing mechanism. Diagram of the system is depicted in Fig. 5.4.1.

This system is designed in a way to provide an insight into creation and destabilization of dark states. We will assume that states $|G_1\rangle$ and $|G_2\rangle$ are coupled differently both through the laser and microwaves. Let's assume that laser couplings are $a\Omega$ and $b\Omega$ for states $|G_1\rangle$ and $|G_2\rangle$ respectively. For microwaves, we can assume couplings $\alpha\Omega_\mu$ and $\beta\Omega_\mu$ (all real). Then, the hamiltonian takes form[1]:

$$H = \begin{array}{c} \begin{array}{cccc} |A\rangle & |G_1\rangle & |G_2\rangle & |E\rangle \end{array} \\ \begin{pmatrix} -\delta_L - \delta_\mu & -\frac{\alpha\Omega_\mu}{2} & -\frac{\beta\Omega_\mu}{2} & 0 \\ -\frac{\alpha\Omega_\mu}{2} & -\delta_L & 0 & -\frac{a\Omega_L}{2} \\ -\frac{\beta\Omega_\mu}{2} & 0 & \Delta - \delta_L & -\frac{b\Omega_L}{2} \\ 0 & -\frac{a\Omega_L}{2} & -\frac{b\Omega_L}{2} & 0 \end{pmatrix} \end{array}.$$

[1]For clarity, from now on we will use H instead of $\tilde{H}$ to mark a hamiltonian in a rotating basis and obtained via a unitary transformation described before.

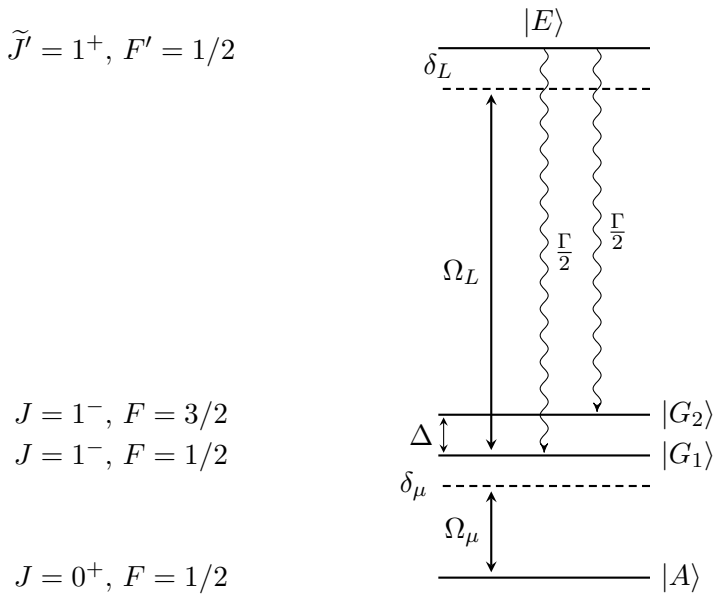

Figure 5.4.1: Diagram of a simplified four-level system with microwave coupling. Two ground states $|G_1\rangle$ and $|G_2\rangle$ are coupled via laser to the excited state, while also being coupled to an auxiliary state $|A\rangle$ via microwaves.

First, we will look at dark and bright states in the system by creating them with respect to the laser transition (as was easily done in a Λ-type system) and analyzing their couplings to each other and to state $|A\rangle$. Hence, we move to basis:

$$|B_L\rangle = \frac{\Omega_a |G_1\rangle + \Omega_b |G_2\rangle}{\Omega} = \frac{a |G_1\rangle + b |G_2\rangle}{\sqrt{a^2+b^2}}$$
$$|D_L\rangle = \frac{b |G_1\rangle - a |G_2\rangle}{\sqrt{a^2+b^2}}.$$

and obtain:

$$H = \begin{array}{c} \begin{array}{cccc} |A\rangle & |B_L\rangle & |D_L\rangle & |E\rangle \end{array} \\ \begin{pmatrix} -\delta_L - \delta_\mu & -\frac{\Omega_\mu}{2\sqrt{a^2+b^2}}(a\alpha + b\beta) & \frac{\Omega_\mu}{2\sqrt{a^2+b^2}}(a\beta - b\alpha) & 0 \\ -\frac{\Omega_\mu}{2\sqrt{a^2+b^2}}(a\alpha + b\beta) & \frac{b^2}{a^2+b^2}\Delta - \delta_L & -\frac{ab}{a^2+b^2}\Delta & -\frac{\Omega_L\sqrt{a^2+b^2}}{2} \\ \frac{\Omega_\mu}{2\sqrt{a^2+b^2}}(a\beta - b\alpha) & -\frac{ab}{a^2+b^2}\Delta & \frac{a^2}{a^2+b^2}\Delta - \delta_L & 0 \\ 0 & -\frac{\Omega_L\sqrt{a^2+b^2}}{2} & 0 & 0 \end{pmatrix} \end{array}.$$

When the splitting $\Delta = 0$ and both states become degenerate, the dark state becomes decoupled from the bright state; for a non-zero splitting there is no dark state - state $|D_L\rangle$ evolves with rate Δ into bright state $|B_L\rangle$, although for small splittings this evolution can be very slow making state $|D_L\rangle$ effectively dark. This dark state, however, is coupled to the state $|A\rangle$ through microwaves as long as $a\beta - b\alpha \neq 0$. State $|A\rangle$, on the other hand, is coupled to the bright state $|B_L\rangle$ as long as $a\alpha + b\beta \neq 0$. Therefore, as long as $a/b \neq \alpha/\beta$ and $a/b \neq -\beta/\alpha$, the state $|D_L\rangle$ never becomes decoupled from the excited state $|E\rangle$. Fig. 5.4.2 shows the results for $a = b = 1$, $\alpha = 1/3$, $\beta = 2/3$, and $\delta_L = \delta_\mu = 0$. We can clearly see that at both $\Delta = 4\,\Gamma$ and $\Delta = 0$ the microwaves increase the scattering rate. At $\Delta = 0$ the rate is visibly 0 if the microwaves are off, but increasing their intensity quickly fixes the problem.

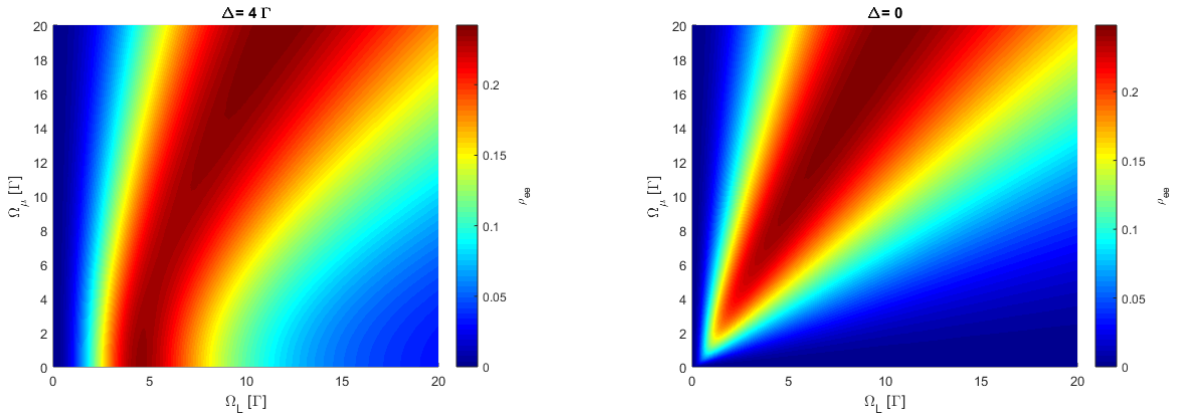

(a) Excited state population as a function of laser and microwave Rabi rates with different strengths of microwave couplings. Splitting $\Delta = 4\,\Gamma$.

(b) Excited state population as a function of laser and microwave Rabi rates with different strengths of microwave couplings. Splitting $\Delta = 0$.

Figure 5.4.2: Results for a 4-state system with microwaves coupled with different strengths. Existence of the dark states **a)** limits the scattering rate or **b)** brings it completely to zero. This can be alleviated if microwave couplings to an auxiliary state are added.

To better understand behavior and creation of the dark states, we can first look at the geometry of spaces spanned by bright and dark states created from states $|G_1\rangle$ and $|G_2\rangle$. As shown before, we can create bright and dark states with respect to the optical transition. We can do the same with respect to transitions to state $|A\rangle$, which we can treat as an excited state with no decays.

Then:

$$|B_\mu\rangle = \frac{\alpha\,|G_1\rangle + \beta\,|G_2\rangle}{\sqrt{\alpha^2+\beta^2}}$$
$$|D_\mu\rangle = \frac{\beta\,|G_1\rangle - \alpha\,|G_2\rangle}{\sqrt{\alpha^2+\beta^2}}.$$

Spaces spanned by $|B_L\rangle$ or $|B_\mu\rangle$ and, similarly, $|D_L\rangle$ or $|D_\mu\rangle$ are one-dimensional. Depending on their orientation with respect to one another, the population might be trapped in a dark state or not. In this simple system we can draw both spaces as shown in Fig. 5.4.3. In our case two situations will lead to trapping of population in dark states: states $|B_L\rangle$ and $|B_\mu\rangle$ belong to the same subspace; or states $|B_L\rangle$ and $|D_\mu\rangle$ belong to the same subspace, which is equivalent to saying that space spanned by $|B_L\rangle$ is perpendicular to the space spanned by $|B_\mu\rangle$. In the first case the dark states with respect to both transitions form the same space, i.e. system's dark state is not coupled to either $|E\rangle$ or $|A\rangle$, which means that neither of the transitions can remove its population accumulated due to the decay from excited state $|E\rangle$. The second case is where laser and microwave transitions address completely different states - our 4 state system can then be divided into two 2-state systems that do not talk to each other.

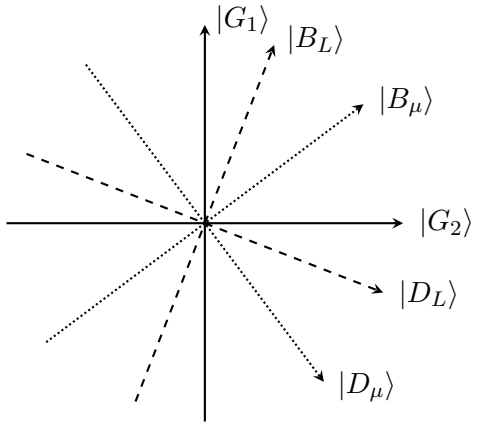

Figure 5.4.3: Dark and bright state spaces.

Because $|B_L\rangle$ can be neither parallel nor perpendicular to $|B_\mu\rangle$, we can write both discussed conditions as:

$$\langle B_L|B_\mu\rangle \neq 0$$
$$\frac{|\,\langle B_L|B_\mu\rangle\,|}{|\,\langle B_L|B_L\rangle\,||\,\langle B_\mu|B_\mu\rangle\,|} \neq 1,$$

which for our system is equivalent to $a\alpha + b\beta \neq 0$ and $a\beta - b\alpha \neq 0$ just as was found before. Next, we can re-write the hamiltonian as:

$$H = \begin{array}{c} \begin{matrix} |G_1\rangle & |G_2\rangle & |A\rangle & |E\rangle \end{matrix} \\ \begin{pmatrix} -\delta_L & 0 & -\frac{\alpha\Omega_\mu}{2} & -\frac{a\Omega_L}{2} \\ 0 & \Delta - \delta_L & -\frac{\beta\Omega_\mu}{2} & -\frac{b\Omega_L}{2} \\ -\frac{\alpha\Omega_\mu}{2} & -\frac{\beta\Omega_\mu}{2} & -\delta_L - \delta_\mu & 0 \\ -\frac{a\Omega_L}{2} & -\frac{b\Omega_L}{2} & 0 & 0 \end{pmatrix} \end{array}.$$

In a system with equal number of ground ($|G_1\rangle$ and $|G_2\rangle$) and excited ($|A\rangle$ and $|E\rangle$) states, to obtain a dark state we have to have degeneracy in the ground state (states can create a dark superposition, if they have the same eigenvalues), which happens for $\Delta = 0$, and $\det \mathbf{\Omega} = 0$ (that condition is universal and is mathematically derived in [67]), where we defined:

$$\mathbf{\Omega} = \begin{pmatrix} -\frac{\alpha\Omega_\mu}{2} & -\frac{\beta\Omega_\mu}{2} \\ -\frac{a\Omega_L}{2} & -\frac{b\Omega_L}{2} \end{pmatrix}.$$

which corresponds to the ground-excited state "interaction" part of the matrix. A zero value of the determinant is equivalent to saying that the matrix does not have a full rank, or that both bright states that are represented as rows in this matrix are co-linear. Now, that condition will lead to $a\beta - b\alpha \neq 0$ found before. If the $|A\rangle$ state was a "real" excited state with non-zero decays to ground states that couple to the other excited state $|E\rangle$, such condition would be sufficient to avoid creation of dark states. In that case even if both bright states were perpendicular to one another, decays from $|A\rangle$ would populate state $|B_L\rangle$ and vice-versa - decays from $|E\rangle$ would populate $|B_\mu\rangle$. Here, however, we find that the second condition, $a\alpha + b\beta \neq 0$, is equivalent to saying that $\det(\mathbf{\Omega}/|\mathbf{\Omega}|) \neq 1$, where by $\mathbf{\Omega}/|\mathbf{\Omega}|$ we understand the interaction matrix where rows represent bright states *normalized* to 1.

Finally, one can look at this system as a system with three ground non-decaying states and one excited state. The ground states would be dressed states in space spanned by $|A\rangle$, $|G_1\rangle$ and $|G_2\rangle$ obtained by diagonalizing:

$$H_g = \begin{array}{c} \begin{matrix} |A\rangle & |G_1\rangle & |G_2\rangle \end{matrix} \\ \begin{pmatrix} -\delta_L - \delta_\mu & -\frac{\alpha\Omega_\mu}{2} & -\frac{\beta\Omega_\mu}{2} \\ -\frac{\alpha\Omega_\mu}{2} & -\delta_L & 0 \\ -\frac{\beta\Omega_\mu}{2} & 0 & \Delta - \delta_L \end{pmatrix} \end{array}.$$

In such case, interaction part $\mathbf{\Omega}$ would be a 1-by-3 matrix which can result in 1 bright state and 2 dark states ($\dim(\ker \mathbf{\Omega}) = 2$) if the condition of degeneracy is met, which is equivalent to saying that a pair of eigenvalues of H_g is equal to each other. After diagonalization, one can see that the eigenvalues cannot be equal to each other and all the eigenstates have direct couplings to the excited state (the eigenvalues and eigenvectors have forms too ungainly to provide here). The only way to have dark states created is to bring those couplings to 0. One of the states is coupled as long as Ω_L and Ω_μ are non-zero, the second one becomes dark when $a\alpha + b\beta = 0$ and the third one when $a\beta - b\alpha = 0$. In this picture it also becomes clear that the states $|G_1\rangle$ and $|G_2\rangle$ effectively acquire an uneven AC Stark shift due to their coupling to state $|A\rangle$, which leads to faster dark state's evolution. We also notice that the eigenstates become completely dark, if they are fully withing the ground state manifold and do not posses a component in the excited state manifold [67], i.e. if an eigenstate, represented by the corresponding eigenvector, is a superposition of $|G_1\rangle$ and $|G_2\rangle$ states only.

Even though before we looked at increasing the scattering rate in the steady state, we could also try a scheme where microwaves are turned on once the optical fields are turned off. Then, the microwaves would remove population from $|D_L\rangle$ and put it into $|B_L\rangle$ allowing the optical field to yield a non-zero scattering rate. To avoid population transfer between state $|A\rangle$ and states $|G_1\rangle$ and $|G_2\rangle$, and to ensure high AC Stark shift of those states, we need to choose detuning δ_μ and Rabi rate Ω_μ correctly. Given that population transfer is proportional to $\Omega_\mu^2/\delta_\mu^2$ and the AC Stark shift $\propto \Omega_\mu^2/\delta_\mu$, choosing very large detunings and somewhat large Rabi rates should allow us to reach the desired effect. Indeed, Fig. 5.4.4 shows results for $a = b = 1$, $\alpha = 1/3$, $\beta = 2/3$, $\Delta = \Gamma/1000$, $\delta_L = 0$, $\Omega_L = 1\,\Gamma$, $\delta_\mu = 120\,\Gamma$ and $\Omega_\mu = 15\,\Gamma$. We see that indeed the population can be moved this way from dark to bright state.

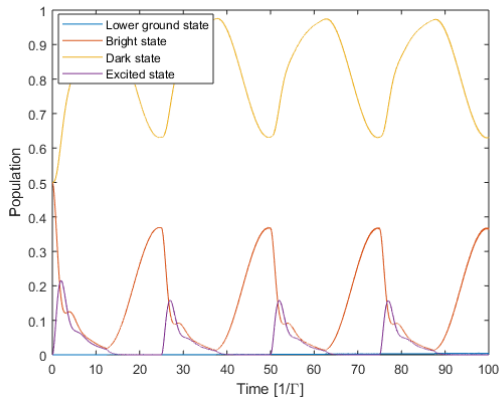

(a) Evolution of all states in dark and bright state basis (with respect to optical transition).

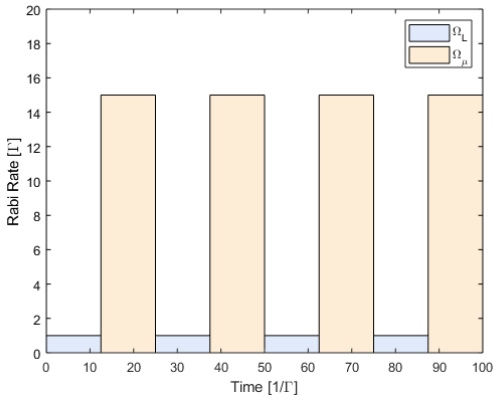

(b) Pulse timing.

Figure 5.4.4: Results for an arbitrary set of parameters: $a = b = 1$, $\alpha = 1/3$, $\beta = 2/3$, $\Delta = \Gamma/1000$, $\delta_L = 0$, $\Omega_L = 1\,\Gamma$, $\delta_\mu = 120\,\Gamma$ and $\Omega_\mu = 15\,\Gamma$. Strong off-resonance pulses of microwaves are able to move the population from the dark state and into the bright state without an intermediate population transfer to the auxiliary state $|A\rangle$.

This system is also small enough to allow us to understand the mixing between bright and dark states quantitatively. Here, when we think about coupling the bright state with the dark state through state $|A\rangle$ by off-resonance microwaves, we have a Λ-type system that effectively behaves like a two state system and can be analyzed via a procedure called adiabatic state elimination [68, 69]. Fig. 5.4.5 presents how the system can be viewed first in terms of dark and bright states and then after the adiabatic elimination. In general, a three-state hamiltonian:

$$H = \begin{array}{c} \begin{matrix} |G_1\rangle & |G_2\rangle & |A\rangle \end{matrix} \\ \begin{pmatrix} 0 & 0 & \frac{A\Omega}{2} \\ 0 & 0 & \frac{B\Omega}{2} \\ \frac{A\Omega}{2} & \frac{B\Omega}{2} & \delta \end{pmatrix} \end{array}$$

becomes effectively:

$$H_{\text{eff}} = \begin{array}{c} \begin{array}{cc} |G_1\rangle & |G_2\rangle \end{array} \\ \begin{pmatrix} A^2\frac{\Omega^2}{4\delta} & AB\frac{\Omega^2}{4\delta} \\ AB\frac{\Omega^2}{4\delta} & B^2\frac{\Omega^2}{4\delta} \end{pmatrix} \end{array}$$

In other words, we obtain two states with energies equal to their respective AC Stark shifts ($\Omega^2/4\delta$) that are coupled with an effective light field equal to a combined AC Stark shift. Such a system yields simply Rabi oscillations between two states. We can solve the time evolution of the density matrix driven by this hamiltonian (there is no dissipation in this system). Assuming that we have generic initial conditions:

$$\rho(0) = \begin{array}{c} \begin{array}{cc} |G_1\rangle & |G_2\rangle \end{array} \\ \begin{pmatrix} C & 0 \\ 0 & 1-C \end{pmatrix} \end{array},$$

we find that (assuming $\delta > 0$):

$$\begin{aligned} \rho_{|G_1\rangle}(t) &= C + \frac{4A^2B^2}{(A^2+B^2)^2}(1-2C)\sin^2\left(\frac{A^2+B^2}{8\delta}\Omega^2 t\right) \\ &= C\frac{(A^2-B^2)^2}{(A^2+B^2)^2} + \frac{4A^2B^2}{(A^2+B^2)^2}\left[C\cos^2\left(\frac{A^2+B^2}{8\delta}\Omega^2 t\right) + (1-C)\sin^2\left(\frac{A^2+B^2}{8\delta}\Omega^2 t\right)\right], \end{aligned} \tag{5.4.1}$$

where we can identify the angular frequency of the time evolution and show that it is equal to sum of AC Stark shifts:

$$\omega = \Delta^+_{\text{AC}} \equiv \Delta^{G_1}_{\text{AC}} + \Delta^{G_2}_{\text{AC}} = \frac{(A^2+B^2)\Omega^2}{4\delta},$$

which in fact appears there via combination of the remixing rate $R_{\text{AC}} \equiv AB\,\Omega^2/2\delta^2$ and the difference in energy levels (splitting) induced by the AC Stark shifts. Namely:

$$R^2_{\text{AC}} + \left(\Delta^{G_1}_{\text{AC}} - \Delta^{G_2}_{\text{AC}}\right)^2 = \left(4A^2B^2 + A^4 - 2A^2B^2 + B^4\right)\frac{\Omega^2}{4\delta} = \frac{(A^2+B^2)\Omega^2}{4\delta} = \Delta^+_{\text{AC}}.$$

For the simplest initial conditions of $C = 0$ we can simplify Eq. (5.4.1) to obtain:

$$\rho_{|G_1\rangle}(t) = \frac{4A^2B^2}{(A^2+B^2)^2}\sin^2\left(\frac{\Delta^+_{\text{AC}}t}{2}\right),$$

which shows that amplitude of the oscillation does not depend on the initial conditions. We can also rewrite the equation using the rate R_{AC}, AC Stark shifts and induced splitting, which we define as $\Delta^{-}_{\mathrm{AC}} \equiv |\Delta^{G_1}_{\mathrm{AC}} - \Delta^{G_2}_{\mathrm{AC}}|$:

$$\rho_{|G_1\rangle}(t) = \frac{R^2_{\mathrm{AC}}}{(\Delta^{+}_{\mathrm{AC}})^2} \sin^2\left(\frac{\Delta^{+}_{\mathrm{AC}} t}{2}\right) = \frac{R^2_{\mathrm{AC}}}{R^2_{\mathrm{AC}} + (\Delta^{-}_{\mathrm{AC}})^2} \sin^2\left(\frac{\sqrt{R^2_{\mathrm{AC}} + (\Delta^{-}_{\mathrm{AC}})^2}t}{2}\right),$$

where at the end we obtain form we are all familiar with - Rabi oscillations between two states coupled with rate R_{AC} with detuning Δ^{-}_{AC}.

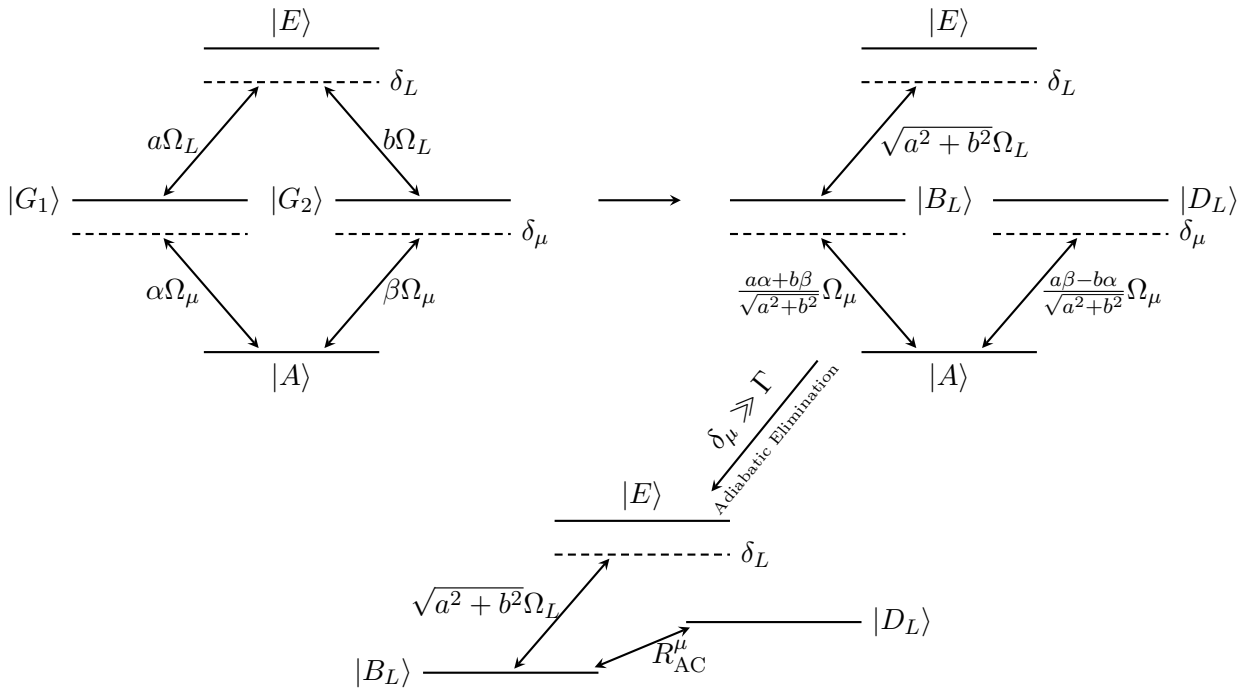

Figure 5.4.5: Diagram of the four-level system with microwave coupling with $\Delta = 0$ shown in basic basis, the basis with dark and bright states with respect to the laser transition, and its approximation as a 3-level system after adiabatic elimination process for large detunings δ_μ.

In our toy model $A = (a\beta - b\alpha)/\sqrt{a^2+b^2}$ and $B = -(a\alpha + b\beta)/\sqrt{a^2+b^2}$, so assuming that at the beginning of the microwave pulse population of the bright state is equal to 0, we can induce oscillations:

$$\rho_{|B\rangle}(t) = \frac{4(a\alpha + b\beta)^2(a\beta - b\alpha)^2}{(a^2+b^2)^2(\alpha^2+\beta^2)^2} \sin^2\left(\frac{\Delta^{+}_{\mathrm{AC}}}{2}t\right),$$

with $\Delta^{+}_{\mathrm{AC}} = (\alpha^2+\beta^2)\Omega^2_\mu/4\delta_\mu$. Before, we used $a = b = 1$ and $\alpha = 1/3$ and $\beta = 2/3$, which gives amplitude of oscillations equal to $9/25$ and their angular frequency of $5/9\,\Omega^2_\mu/4\delta_\mu \approx 0.26\,\Gamma$, which

shows that in order to obtain a π pulse (maximum population transfer between the bright and dark state) we need $t_p = \pi/\omega \approx 12.06\,\Gamma^{-1}$. Indeed, when we look at the graph in figure 5.4.4 we see populations of bright and dark states oscillating with exactly these parameters.

It is also worth noting that we can write the formula above as:

$$\rho_{|B\rangle}(t) \propto (a\alpha + b\beta)^2(a\beta - b\alpha)^2 = |\langle B_L|B_\mu\rangle|^2 |\langle B_L|D_\mu\rangle|^2,$$

which can be intuitively understood - the strength (amplitude) of the remixing between dark and bright state depends on orientation of two bases with respect to each other. If ϑ is the angle between $|B_L\rangle$ and $|B_\mu\rangle$, then $\rho_{|B\rangle}(t) \propto \cos\vartheta \sin\vartheta = 1/2 \sin 2\vartheta$, which is maximized for $\vartheta = \pi/4$.

However, if we look at the steady-state scattering rate in the system, the situation seems to be slightly more complicated. To obtain analytical results, we assume that $|B_L\rangle = |G_1\rangle$, which is equivalent to $a = 1$ and $b = 0$. Then, using the previously defined angle ϑ, we get $\alpha = \cos\vartheta$ and $\beta = \sin\vartheta$. First, in the high microwave detuning regime (and $\delta_L = 0$), where we apply the adiabatic approximation, the excited state population is:

$$\rho_{|E\rangle}(t) = \frac{2\varkappa^2 \sin^2\vartheta\cos^2\vartheta}{4\varkappa^4\sin^2\vartheta + \varkappa^2\left(4\sin^2\vartheta - 6\sin^4\vartheta + \frac{\Gamma^2}{\Omega_L^2}\right) + \frac{1}{4}}, \tag{5.4.2}$$

where $\varkappa \equiv \Delta^\mu_{\mathrm{AC}}/\Omega_L = \Omega_\mu^2/4\delta_\mu\Omega_L$. In the limit of $\Omega_L \gg \Gamma$ with $\varkappa \approx 1$, we can drop one of the terms and obtain:

$$\rho_{|E\rangle}(t) = \frac{2\varkappa^2 \sin^2\vartheta\cos^2\vartheta}{4\varkappa^4\sin^2\vartheta + 4\varkappa^2\left(\sin^2\vartheta - \frac{3}{2}\sin^4\vartheta\right) + \frac{1}{4}}.$$

The term above is maximal at $\varkappa \approx 0.5$ and can reach values higher than 0.25 obtained from a naive limit for a 4-level system. In the case of on-resonance microwaves ($\delta_\mu = 0$), we obtain:

$$\rho_{|E\rangle}(t) = \frac{2\xi^2 \sin^2\vartheta\cos^2\vartheta}{2\xi^4\sin^2\vartheta + 4\xi^2\left[\sin^2\vartheta - 2\sin^4\vartheta + \frac{1}{4}\frac{\Gamma^2}{\Omega_L^2}\left(1 + \sin^2\vartheta\right)\right] + 2\sin^2\vartheta}, \tag{5.4.3}$$

where now $\xi \equiv \Omega_\mu/\Omega_L$. In the limit of $\Omega_L \gg \Gamma$ with $\xi \approx 1$, this simplifies to:

$$\rho_{|E\rangle}(t) = \frac{\xi^2\cos^2\vartheta}{1 + 2\xi^2\left(1 - 2\sin^2\vartheta\right) + \xi^4},$$

which is equal to exactly 0.25 for any angle ϑ at $\xi = 1$. We can see that while in both Eq. (5.4.2) and Eq. (5.4.3) the numerator is proportional to $\sin 2\vartheta$, the optimal angle is not $\pi/4$, due to the fact that the denominators in both formulas are functions of $\sin\vartheta$ as well. In the end, the optimal

angle depends on the parameters $\varkappa$ and ξ, and the optimal scattering rate has to be obtained by looking at the whole parameter space. It is not surprising - as was shown before, the optimal scattering rate is obtained when remixing rate is comparable to the dark state re-population rate via the spontaneous decay; the latter is proportional to Ω_L, while the former depends on both Ω_μ and angle ϑ. We should also note that the analytical formulas found here are applicable for the chosen coupling parameters, but would be different for the ones we used before that, i.e. $a = b = 1$ and $\alpha = 1/3$, $\beta = 2/3$.

Finally, we solve the four level system with strong off-resonance microwaves continuously in the background and plot dependence of the excited state population on the Rabi rate, and the AC Stark shift for $a = 1$, $b = 0$ and $\alpha = \beta = 1/\sqrt{2}$. For such choice of parameters and $\varkappa = 1/2$, $R^\mu_{\mathrm{AC}} = 2\alpha\beta\Delta^\mu_{\mathrm{AC}}/4\delta_\mu = 2\alpha\beta\varkappa\Omega_L = \Omega_L/2$, which, as can be seen in Fig. 5.4.6, provides the highest excited state population, larger than the 1/4 limit.

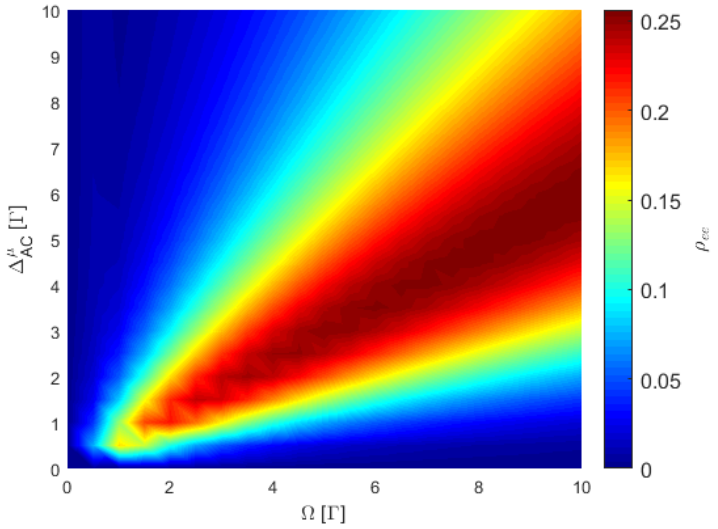

Figure 5.4.6: Excited state population in a 4-level system as a function of laser Rabi rate and induced AC Stark shift. Solution provided for $a = 1$, $b = 0$ and $\alpha = \beta = 1/\sqrt{2}$ with completely degenerate levels. The highest scattering rates are achieved at $\varkappa \approx 1/2$.

In conclusion, we see that the highest scattering rate can be achieved when we can adiabatically eliminate the auxiliary states, which is possible when we couple them with strong off-resonance microwaves. Such coupling should be acting continuously on the system together with the main (laser) coupling. What is problematic is matching the remixing and excitation rates, which for such

a small system like the one discussed can already be a challenge. We might also run into problem with feasibility - while high power microwaves can be obtained, there are still some reasonable limits on what we can actually use.

5.5 A Five-state System

Next, we will quickly look at a system where adding one microwave coupling will not allow us to completely get rid of the dark states. Fig. 5.5.1 shows the system considered - we just added an additional ground state $|G_3\rangle$ to the previously solved system.

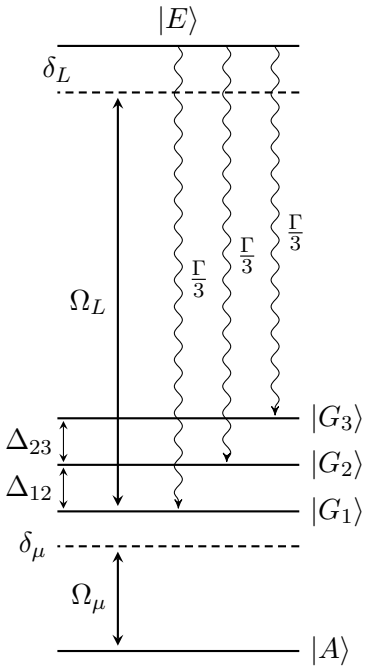

Figure 5.5.1: Diagram of a simplified five-level system with microwave coupling.

Now, the hamiltonian takes form:

$$H = \begin{array}{c} \begin{matrix} |A\rangle & |G_1\rangle & |G_2\rangle & |G_3\rangle & |E\rangle \end{matrix} \\ \begin{pmatrix} -\delta_L - \delta_\mu & -\frac{\alpha\Omega_\mu}{2} & -\frac{\beta\Omega_\mu}{2} & -\frac{\gamma\Omega_\mu}{2} & 0 \\ -\frac{\alpha\Omega_\mu}{2} & -\delta_L & 0 & 0 & -\frac{a\Omega_L}{2} \\ -\frac{\beta\Omega_\mu}{2} & 0 & \Delta_{12} - \delta_L & 0 & -\frac{b\Omega_L}{2} \\ -\frac{\gamma\Omega_\mu}{2} & 0 & 0 & \Delta_{23} + \Delta_{12} - \delta_L & -\frac{c\Omega_L}{2} \\ 0 & -\frac{a\Omega_L}{2} & -\frac{b\Omega_L}{2} & -\frac{c\Omega_L}{2} & 0 \end{pmatrix} \end{array}.$$

From the perspective of only the optical transition, the bright state will be given as $\mathbf{B_L} = (a, b, c)$ (in space spanned states $|G_1\rangle$, $|G_2\rangle$ and $|G_3\rangle$), and the dark state space can be defined as kernel of the bright state space, $\mathbf{D_L} = \ker \mathbf{B_L}$. In other words, if $\mathbf{V_G} \equiv \mathrm{span}\{|G_1\rangle, |G_2\rangle, |G_3\rangle\}$ then $\mathbf{V_G} = \mathbf{B_L} \oplus \mathbf{D_L}$. Similarly, for the microwave transition $\mathbf{B}_\mu = (\alpha, \beta, \gamma)$, $\mathbf{D}_\mu = \ker \mathbf{B}_\mu$ and $\mathbf{V_G} = \mathbf{B}_\mu \oplus \mathbf{D}_\mu$. Because we know that $\dim \mathbf{B_L} = \dim \mathbf{B}_\mu = 1$, we have $\dim \mathbf{D_L} = \dim \mathbf{D}_\mu = 2$. To avoid creation of dark states, we definitely need $\mathbf{B_L} \neq \mathbf{B}_\mu$ (they cannot be co-linear), and $\mathbf{B_L} \not\subset \mathbf{D}_\mu$ (because $|A\rangle$ state does not decay to $\mathbf{V_G}$). However, it is always true that $\dim \mathbf{D_L} \cap \mathbf{D}_\mu = 1$ (in our situation both are planes in a 3-dimensional space that go through the origin, i.e. they are vector, not affine planes). No matter how we set our system, it will always evolve into state that is an intersection of both dark state spaces. We can find that dark state by treating state $|A\rangle$ as an excited state. Then:

$$\mathbf{D_{L+\mu}} = \mathbf{D_L} \cap \mathbf{D}_\mu = \ker \mathbf{\Omega}^{\mathrm{T}} = \ker \begin{pmatrix} -\frac{\alpha\Omega_\mu}{2} & -\frac{\beta\Omega_\mu}{2} & -\frac{\gamma\Omega_\mu}{2} \\ -\frac{a\Omega_L}{2} & -\frac{b\Omega_L}{2} & -\frac{c\Omega_L}{2} \end{pmatrix}.$$

Eventually we find that:

$$|D_{L+\mu}\rangle = \begin{vmatrix} \alpha & \beta & \gamma \\ a & b & c \\ |G_1\rangle & |G_2\rangle & |G_3\rangle \end{vmatrix} = (\beta c - b\gamma)\,|G_1\rangle + (\gamma a - c\alpha)\,|G_2\rangle + (\alpha b - a\beta)\,|G_3\rangle\,.$$

To show this explicitly, we will transform the hamiltonian to basis:

$$
\begin{aligned}
|D_{L+\mu}\rangle &= \frac{1}{D}\left[(\beta c - b\gamma)\,|G_1\rangle + (\gamma a - c\alpha)\,|G_2\rangle + (\alpha b - a\beta)\,|G_3\rangle\right] \\
|B_L\rangle &= \frac{1}{B_L}\left(a\,|G_1\rangle + b\,|G_2\rangle + c\,|G_3\rangle\right) \\
|B_\mu\rangle &= \frac{1}{B_\mu}\left(\alpha\,|G_1\rangle + \beta\,|G_2\rangle + \gamma\,|G_3\rangle\right)
\end{aligned}
$$

which yields:

$$
H = \begin{array}{c}
\begin{array}{ccccc} |A\rangle & |B_\mu\rangle & |B_L\rangle & |D_{L+\mu}\rangle & |E\rangle \end{array} \\
\begin{pmatrix}
-\delta_L - \delta_\mu & -\Omega_\mu \frac{B_\mu}{2} & -\Omega_\mu \frac{a\alpha+b\beta+c\gamma}{2B_L} & 0 & 0 \\
-\Omega_\mu \frac{B_\mu}{2} & \frac{\beta^2\Delta_{12}+\gamma^2(\Delta_{12}+\Delta_{23})}{B_\mu^2} - \delta_L & \frac{\Delta_{12}(b\beta+c\gamma)+\Delta_{23}c\gamma}{B_L B_\mu} & \frac{\Delta_{12}\alpha(b\gamma-c\beta)+\Delta_{23}\gamma(b\alpha-a\beta)}{DB_\mu} & -\Omega_L \frac{a\alpha+b\beta+c\gamma}{2B_\mu} \\
-\Omega_\mu \frac{a\alpha+b\beta+c\gamma}{2B_L} & \frac{\Delta_{12}(b\beta+c\gamma)+\Delta_{23}c\gamma}{B_L B_\mu} & \frac{b^2\Delta_{12}+c^2(\Delta_{12}+\Delta_{23})}{B_L^2} - \delta_L & \frac{\Delta_{12}a(b\gamma-c\beta)+\Delta_{23}c(b\alpha-a\beta)}{DB_L} & -\Omega_L \frac{B_L}{2} \\
0 & \frac{\Delta_{12}\alpha(b\gamma-c\beta)+\Delta_{23}\gamma(b\alpha-a\beta)}{DB_\mu} & \frac{\Delta_{12}a(b\gamma-c\beta)+\Delta_{23}c(b\alpha-a\beta)}{DB_L} & \frac{(a\gamma-c\alpha)^2\Delta_{12}+(a\beta-b\alpha)^2(\Delta_{12}+\Delta_{23})}{D^2} - \delta_L & 0 \\
0 & -\Omega_L \frac{a\alpha+b\beta+c\gamma}{2B_\mu} & -\Omega_L \frac{B_L}{2} & 0 & 0
\end{pmatrix}
\end{array},
$$

where $D = |\langle D_{L+\mu}|D_{L+\mu}\rangle| = \sqrt{(\beta c - b\gamma)^2 + (\gamma a - c\alpha)^2 + (\alpha b - a\beta)^2}$ is dark state's norm, $B_L = |\langle B_L|B_L\rangle| = \sqrt{a^2+b^2+c^2}$ and $B_\mu = |\langle B_\mu|B_\mu\rangle| = \sqrt{\alpha^2+\beta^2+\gamma^2}$. We can clearly see that the dark state has no direct coupling to either $|A\rangle$ or $|E\rangle$ states and it evolves to other bright states with rate proportional to splittings. If both of them are zero, the state loses all of its couplings no matter what parameters we choose.

5.6 A Six-state System

An easy way to get rid of that one-dimensional dark state space in our toy models is to add an additional lower-lying auxiliary ground state $|A_2\rangle$ coupled to states $|G_1\rangle$, $|G_2\rangle$ and $|G_3\rangle$ as shown in diagram presented in Fig. 5.6.1.

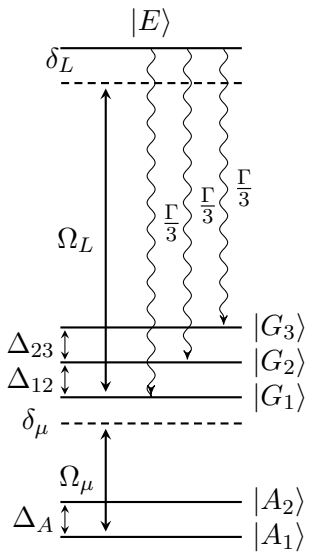

Figure 5.6.1: Diagram of a simplified six-level system with microwave coupling.

The hamiltonian looks very much the same as the previous one:

$$H = \begin{array}{c} \begin{array}{cccccc} |A_1\rangle & |A_2\rangle & |G_1\rangle & |G_2\rangle & |G_3\rangle & |E\rangle \end{array} \\ \begin{pmatrix} -\delta_L - \delta_\mu & 0 & -\frac{\alpha_1\Omega_\mu}{2} & -\frac{\beta_1\Omega_\mu}{2} & -\frac{\gamma_1\Omega_\mu}{2} & 0 \\ 0 & \Delta_A - \delta_L - \delta_\mu & -\frac{\alpha_2\Omega_\mu}{2} & -\frac{\beta_2\Omega_\mu}{2} & -\frac{\gamma_2\Omega_\mu}{2} & 0 \\ -\frac{\alpha_1\Omega_\mu}{2} & -\frac{\alpha_2\Omega_\mu}{2} & -\delta_L & 0 & 0 & -\frac{a\Omega_L}{2} \\ -\frac{\beta_1\Omega_\mu}{2} & -\frac{\beta_2\Omega_\mu}{2} & 0 & \Delta_{12} - \delta_L & 0 & -\frac{b\Omega_L}{2} \\ -\frac{\gamma_1\Omega_\mu}{2} & -\frac{\gamma_2\Omega_\mu}{2} & 0 & 0 & \Delta_{23} + \Delta_{12} - \delta_L & -\frac{c\Omega_L}{2} \\ 0 & 0 & -\frac{a\Omega_L}{2} & -\frac{b\Omega_L}{2} & -\frac{c\Omega_L}{2} & 0 \end{pmatrix} \end{array}.$$

We now have to ensure that matrix $\mathbf{\Omega}$ is full rank, that is (with normalized rows):

$$\det \mathbf{\Omega} = \det \begin{pmatrix} \frac{\alpha_1}{B_{\mu_1}} & \frac{\beta_1}{B_{\mu_1}} & \frac{\gamma_1}{B_{\mu_1}} \\ \frac{\alpha_2}{B_{\mu_2}} & \frac{\beta_2}{B_{\mu_2}} & \frac{\gamma_2}{B_{\mu_2}} \\ \frac{a}{B_L} & \frac{b}{B_L} & \frac{c}{B_L} \end{pmatrix} \neq 0,$$

where $B_L = |\langle B_L|B_L\rangle| = \sqrt{a^2+b^2+c^2}$ and $B_{\mu_i} = |\langle B_{\mu_i}|B_{\mu_i}\rangle| = \sqrt{\alpha_i^2+\beta_i^2+\gamma_i^2}$. Otherwise there exists a dark state. If we were using proper excited states, i.e. with non-zero decay rates,

this would be a sufficient condition. Given that auxiliary states $|A_1\rangle$ and $|A_2\rangle$ do not decay to ground states $|G_i\rangle$ in this toy model, just like in the 4-level system, there are some additional conditions on orthogonality of the bright states that have to be met. We definitely have to ensure that $\mathbf{B_{\mu_1}} \not\subset \ker \mathbf{B_L}$ or $\mathbf{B_{\mu_2}} \not\subset \ker \mathbf{B_L}$, that is bright states for either of microwave transitions cannot completely lie in the optical transition's dark state space, which is to say they cannot both be simultaneously perpendicular to $|B_L\rangle$. However, this condition is not sufficient. If both $\langle B_L|B_{\mu_1}\rangle \neq 0$ and $\langle B_L|B_{\mu_2}\rangle \neq 0$, then there is no further condition on both microwave transition's bright state spaces other than the condition stating that $|B_{\mu_1}\rangle \not\propto |B_{\mu_2}\rangle$ (they cannot be co-linear). But, if one of them is actually orthogonal to $|B_L\rangle$, then they cannot be orthogonal with respect to each other.

If we construct a matrix $\mathbf{O} = \mathbf{\Omega}^\dagger\mathbf{\Omega}$ (which is essentially a matrix of dot products between all bright states), that statement is equivalent to saying that at least two off-diagonal elements have to be non-zero (though such statement would not hold for larger systems) or, more generally, every bright state associated with transition to a non-decaying excited state has to have a connection to a bright state associated with transition to a proper decaying excited state. By connection we mean at least one non-zero dot product with a state that already is connected, where a bright state with respect to transition to a decaying excited state is already trivially connected to itself. In our system:

$$\mathbf{O} = \begin{pmatrix} 1 & \frac{\alpha_1\alpha_2+\beta_1\beta_2+\gamma_1\gamma_2}{B_{\mu_1}B_{\mu_2}} & \frac{\alpha_1 a+\beta_1 b+\gamma_1 c}{B_{\mu_1}B_L} \\ \frac{\alpha_1\alpha_2+\beta_1\beta_2+\gamma_1\gamma_2}{B_{\mu_1}B_{\mu_2}} & 1 & \frac{\alpha_2 a+\beta_2 b+\gamma_2 c}{B_{\mu_2}B_L} \\ \frac{\alpha_1 a+\beta_1 b+\gamma_1 c}{B_{\mu_1}B_L} & \frac{\alpha_2 a+\beta_2 b+\gamma_2 c}{B_{\mu_2}B_L} & 1 \end{pmatrix}$$

so the additional conditions we obtain are:

$$\begin{cases} \alpha_2 a + \beta_2 b + \gamma_2 c \neq 0 \\ \alpha_1 a + \beta_1 b + \gamma_1 c \neq 0 \end{cases} \quad \text{or} \quad \begin{cases} \alpha_1\alpha_2 + \beta_1\beta_2 + \gamma_1\gamma_2 \neq 0 \\ \alpha_1 a + \beta_1 b + \gamma_1 c \neq 0 \end{cases} \quad \text{or} \quad \begin{cases} \alpha_1\alpha_2 + \beta_1\beta_2 + \gamma_1\gamma_2 \neq 0 \\ \alpha_2 a + \beta_2 b + \gamma_2 c \neq 0 \end{cases}$$

One of them has to be true. Additionally, as mentioned before, bright states have to span the whole ground state space. This condition, in terms of this newly defined matrix, is equivalent to $\det \mathbf{O} = (\det \mathbf{\Omega})^2 \neq 0$. Here, we first show results for $a = b = c = 1$, $\beta_1 = 2\alpha_1 = 2\gamma_1 = 1$, $\alpha_2 = 4\beta_2 = 4\gamma_2 = 2$, $\Delta_{12} = \Delta_{23} = \Delta_G = 0$ and $\delta_L = \delta_\mu = 0$. For such choice of parameters we

have $\det \mathbf{\Omega} = 1/6$ and

$$\mathbf{O} = \begin{pmatrix} 1 & \frac{7}{6\sqrt{3}} & \frac{2\sqrt{2}}{3} \\ \frac{7}{6\sqrt{3}} & 1 & \frac{\sqrt{2}}{\sqrt{3}} \\ \frac{2\sqrt{2}}{3} & \frac{\sqrt{2}}{\sqrt{3}} & 1 \end{pmatrix},$$

so we expect that there will be no dark states. Indeed, the steady state reached for high Rabi rates for both laser and microwave fields leads to scattering rate close to the maximum scattering rate of $n_e/(n_e + n_g)\,\Gamma = 1/(1+5)\,\Gamma \approx 0.167\,\Gamma$. Fig. 5.6.2 depicts that behavior.

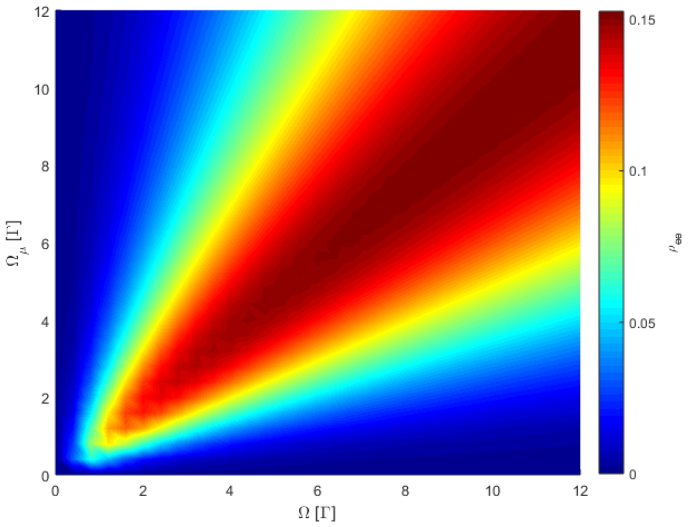

Figure 5.6.2: Steady state excited state population as a function of Rabi rates Ω_L and Ω_μ in a six-state toy model. For chosen parameters no dark states are created.

5.7 Polarization Switching

Now, using introduced mathematical methodology, we will look at polarization switching as a way to remix the dark states or, equivalently, effectively decrease the number of the dark states. For that purpose we will work with unknown dipole transition elements, just like in previous toy models. We will also begin with a simple Λ-type system to show how populations can be juggled between dark states following the diagram presented in Fig. 5.7.1.

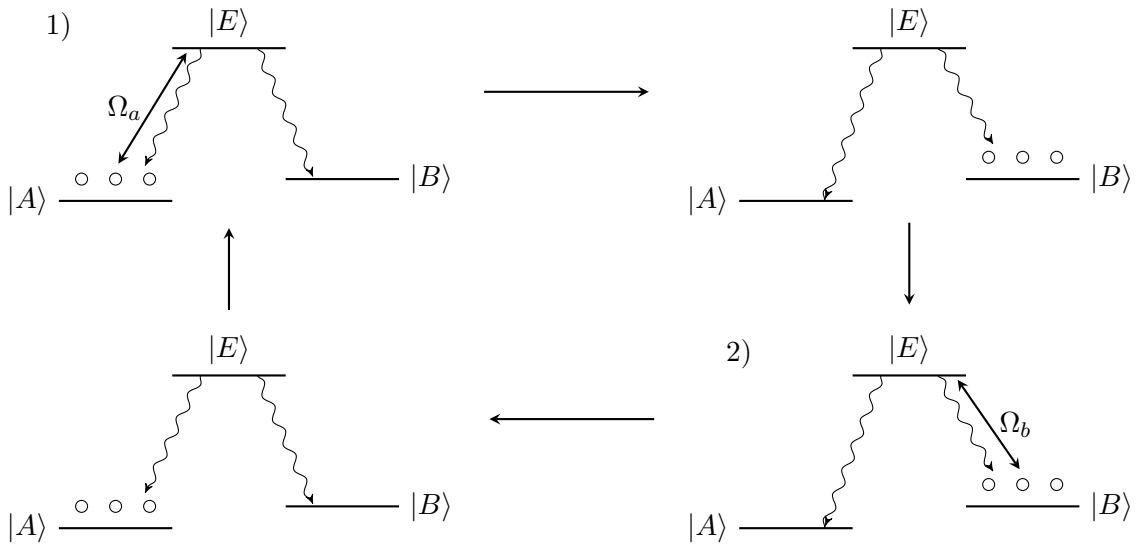

Figure 5.7.1: Juggling population in a three-level system in Λ configuration. In 1) state $|A\rangle$ is bright and $|B\rangle$ is trivially dark. In 2) both states change places.

In such scheme, we begin with population in state $|A\rangle$ and start with it being bright. Then, state $|B\rangle$ is trivially dark and population accumulates in it. Next, we flip the states, i.e. by coupling states $|B\rangle$ and $|E\rangle$ we make $|B\rangle$ a bright state and $|A\rangle$ becomes a dark state. After population finishes accumulating in current dark state $|A\rangle$, we restart the cycle. Thus, having only one excited state and two ground states that, in principle, can be degenerate, we avoid trapping population in dark states by juggling it between all of them.

If we define $\mathbf{V_G} \equiv \text{span}\{|A\rangle, |B\rangle\}$, we can write that in situation 1) the bright state is a $(1, 0)$ vector in this space, while in situation 2) it is a vector that is perpendicular to the previous bright state - a $(0, 1)$ vector. One way to obtain these results in a framework consistent with the one we used when describing our toy models is to artificially add an additional excited state. Then, we can draw an "effective" diagram shown in Fig. 5.7.2. For such a system we could write down the hamiltonian, followed by the matrix representing the couplings ($\mathbf{\Omega}$), which would be diagonal and, therefore, have a non-zero determinant. We would find that the bright states for both transitions span full space of the ground states. In fact, any schemes with switching the couplings would work as long as $\det \mathbf{\Omega} \neq 0$, i.e. bright states during different pulses constituting a scheme are not co-linear. For example, having both lasers on at the beginning and then switching one of them off would *not* yield a dark state, even though dark and bright states do not fully swap places.

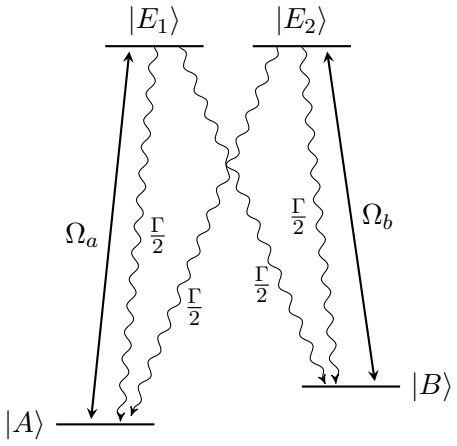

Figure 5.7.2: Diagram of an effective three-level system in Λ configuration with coupling switching.

It is also worth noting that dark state destabilization method based on phase modulation is nothing more then performing the above-described procedure in a continuous way. By suddenly changing phase of one of the lasers with respect to the other, we would simply obtain a discrete scheme we are showing here - bright and dark states spanning the space would shift, so that the two bright states (before and after phase difference change) would span the whole ground state space. In the continuous case, we constantly change the linear superposition of the instantaneous bright and dark states. As long as the changes are fast, i.e. non-adiabatic, population in the dark state will be continuously moved into a bright state (if we think of this process in terms of couplings of a well-defined linear dark state superposition, this process corresponds to continuously changing the coupling between bright and dark states with rate proportional to $\exp(i\varphi(t))$ as was shown before).

We can also generalize what we found here. For example, in a system with 1 excited state and 3 degenerate ground state, for a single pulse, that is for a single combination of light fields, the bright state space will be one-dimensional, while the dark state space will be two-dimensional. If we used a scheme with three different pulses, we would obtain three different bright states that could allow us to span the whole ground state space. By creating an "effective" diagram we can quickly find conditions that have to be imposed on the light fields at every pulse. In the end we want three different dark state spaces to have a zero intersection.

Now, let's assume we have N_e excited states and N_g degenerate ground states ($N_g > N_e$), where every ground state has a possibility to be coupled to any excited state, and it has at least

one excited state partially decaying to it (Fig. 5.7.3).

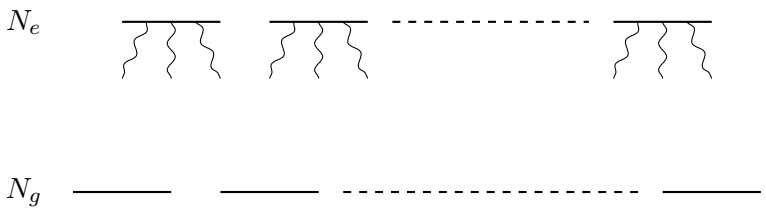

Figure 5.7.3: Diagram of a system with N_e excited and N_g ground states.

Now, for a single pulse i we can write a general hamiltonian:

$$H_i = \begin{pmatrix} \overbrace{\quad}^{N_g} & \overbrace{\quad}^{N_e} \\ \mathrm{G} & \Omega_i \\ \Omega_i^\dagger & \mathrm{E} \end{pmatrix},$$

where Ω_i is an N_g-by-N_e matrix representing coupling between ground and excited states. Let's assume that this matrix has rank $\mathbf{\Omega_i}^{\mathrm{T}} = N_e$, that is none of its rows representing bright states is co-linear, i.e. given:

$$\mathbf{\Omega_i}^{\mathrm{T}} = \begin{matrix} |B_{i,1}\rangle \\ \vdots \\ |B_{i,N_e}\rangle \end{matrix} \begin{pmatrix} b^i_{11} & \cdots & \cdots & b^i_{1,N_g} \\ \vdots & & \ddots & \vdots \\ b^i_{N_e,1} & \cdots & \cdots & b^i_{N_e,N_g} \end{pmatrix},$$

none of the states $|B_{i,j}\rangle$ are co-linear, which is to say that $\langle B_{i,j}|B_{i,k}\rangle \neq 0$ for all $1 \leq j,k \leq N_e$. This is equivalent to saying that the bright state space $\mathbf{B_i} \equiv \mathrm{span}\{|B_{i,1}\rangle, \ldots, |B_{i,N_e}\rangle\}$ is exactly N_e-dimensional. Because the ground state space $\mathbf{V_G} \equiv \mathrm{span}\{|G_1\rangle, \ldots, |G_{N_g}\rangle\}$ is N_g-dimensional, we can write that for every pulse i:

$$\dim \mathbf{B_i} = \mathrm{rank}\, \mathbf{\Omega_i} = N_e$$

$$\dim \mathbf{D_i} = \dim(\ker \mathbf{\Omega_i}) = N_g - N_e,$$

where $\mathbf{D_i}$ is the dark state space for pulse i. To cover the whole ground state space $\mathbf{V_G}$ with bright states, we need to ensure that the dimension of sum of all the bright state spaces is equal to the dimension of $\mathbf{V_G}$. If we assume that we have m pulses, then we can eliminate all the dark states, if:

$$\dim\left(\bigcup_{i=1}^{m}\mathbf{B_i}\right) = \dim\mathbf{V_G} = N_g \tag{5.7.1}$$

or, equivalently:

$$\dim\left[\ker\left(\bigcup_{i=1}^{m}\mathbf{B_i}\right)\right] = \dim\left(\bigcap_{i=1}^{m}\mathbf{D_i}\right) = 0. \tag{5.7.2}$$

In other words, we want the dark state space, understood as an intersection of all dark state spaces $\mathbf{D_i}$ with respect to pulses i, to be 0-dimensional. The best case scenario happens when all the bright state spaces for all-but-one of the pulses are disjoint, that is:

$$\forall_{i,j\leq m-1}\dim(\mathbf{B_i}\cap\mathbf{B_j}) = 0,$$

with the last bright state space having only to span the remaining dimensions of the ground state space. Then, if we follow the previously given assumption that for every pulse the dimension is maximal, i.e. $\dim B_i = N_g - N_e$, we can obtain a lower bound on the number of pulses required to eliminate all dark states:

$$m_{\min} = \left\lceil\frac{\dim\mathbf{V_G}}{\dim\mathbf{B_i}}\right\rceil = \left\lceil\frac{N_g}{N_g - N_e}\right\rceil.$$

The upper bound is simply N_g - if quantum system allows, we can couple all the states independently and cover the whole ground state space. Of course that may not be possible in a real system. Even in a simple TlF toy model discussed in the next chapter we cannot address all the states separately. In general, it might not be possible to find enough independent pulses to eliminate all dark states. To see how well we can do, we need to calculate dimensions of either the resulting bright state space or dark state space using Eq. (5.7.1) or Eq. (5.7.2). The easiest way to do that is to create a matrix with all the bright state vectors as rows and calculate either its rank or dimension of the kernel of such matrix. By keeping only the independent bright states and assuming pulse i has a

bright state space of dimension N_i we can write:

$$\mathbf{B} \equiv \bigcup_{i=1}^{m} \mathbf{B_i} = \left(\begin{array}{cccc} b^1_{1,1} & \cdots & \cdots & b^1_{1,N_g} \\ \vdots & & & \vdots \\ b^1_{N_1,1} & \cdots & \cdots & b^1_{N_1,N_g} \\ \hdashline b^2_{1,1} & \cdots & \cdots & b^2_{1,N_g} \\ \vdots & & & \vdots \\ b^2_{N_2,1} & \cdots & \cdots & b^2_{N_2,N_g} \\ \hdashline \vdots & & & \vdots \\ \hdashline b^m_{1,1} & \cdots & \cdots & b^m_{1,N_g} \\ \vdots & & & \vdots \\ b^m_{N_m,1} & \cdots & \cdots & b^m_{N_m,N_g} \end{array} \right) \begin{array}{l} \left. \begin{array}{l} \\ \\ \\ \end{array} \right\} \mathbf{B_1} \\ \left. \begin{array}{l} \\ \\ \\ \end{array} \right\} \mathbf{B_2} \\ \vdots \\ \left. \begin{array}{l} \\ \\ \\ \end{array} \right\} \mathbf{B_m} \end{array} \tag{5.7.3}$$

This matrix can be substituted if we create an "effective" system with m copies of N_e excited states, just like in the Λ-system that we showed. We then obtain hamiltonian:

$$H_{\text{eff}} = \left(\begin{array}{c:c} \overbrace{}^{N_g} & \overbrace{}^{mN_e} \\ \mathrm{G} & \Omega_{\text{eff}} \\ \hdashline \Omega^{\dagger}_{\text{eff}} & \mathrm{mE} \end{array} \right),$$

where $\mathbf{\Omega}^{\dagger}_{\text{eff}}$ is the same as matrix representation of $\mathbf{B}$ in Eq. (5.7.3), if for every pulse i the number of bright states N_i is equal to N_e. Regardless, the dimension of the resulting dark state space $\mathbf{D}$ can be calculated from:

$$\dim \mathbf{D} = \dim(\ker \mathbf{B}) = \dim \mathbf{V_g} - \operatorname{rank} \mathbf{B} = N_g - \operatorname{rank} \mathbf{\Omega}_{\text{eff}}, \tag{5.7.4}$$

where the last equality is true, because while $\mathbf{\Omega}_{\text{eff}}$ contains mN_e superpositions, only $\operatorname{rank} \mathbf{\Omega}_{\text{eff}}$ are independent and they are exactly the bright state vectors spanning $\mathbf{B}$ space. However, we cannot simply use $\ker \mathbf{\Omega}_{\text{eff}}$, unless for every pulse i, matrix $\mathbf{\Omega_i}$ consists of N_e independent bright state

vectors (then $\mathbf{\Omega}_{\text{eff}} = \mathbf{B}$). Finally, from the above, for full elimination of dark states we require $\operatorname{rank}\mathbf{\Omega}_{\text{eff}} = \operatorname{rank}\mathbf{B} = N_g$, and if matrix representation of $\mathbf{B}$ ends up being an $N_g \times N_g$ matrix, this is equivalent to condition $\det\mathbf{B} \neq 0$. In a general case when matrix $\mathbf{\Omega}_{\text{eff}}$ has multiple co-linear components, obtaining its rank is most easily done by using Singular Value Decomposition (SVD) algorithm.

5.8 Summary

At the end of such chapter it is prudent to provide a short summary of the analysis. First, it is important to once again emphasize when the dark states are created. As has been mentioned, perfect dark states are created when interaction part of the hamiltonian (following [67]) $\mathbf{\Omega} \equiv QHP$ has a zero determinant for a group of degenerate ground states, where P is a projection operator onto the excited state space, while Q is a projection operator onto a chosen subspace of the ground state space. In such case, system's eigenvectors (creating a dressed state picture) corresponding to the dark states will have no contribution from the excited state levels.

It has also been shown that when the states in the discussed ground state subspace are not fully degenerate, the resulting dark states are remixed into bright states with rates equal to the energy splittings between the states. This leads us to the first and most widely used method of remixing - lifting the degeneracy. By inducing a high energy difference, the remixing rate is increased. If remixing rate is then matched with rate with which dark states are re-populated via the spontaneous decay, the scattering rate reaches its maximum value.

Most common way of lifting degeneracy is based on the Zeeman effect. However, in TlF we will utilize a different method - we can split states' energies by creating an AC Stark shift by coupling the dark and bright states to an auxiliary state space via microwaves. The microwaves can also be used on resonance and induce remixing by moving the population from the dark to bright state by first moving the population to an intermediate state. Both of these methods can potentially remix all the dark states; eliminate them. Conditions imposed on light fields' parameters (like polarization or amplitudes) can obtained from matrices $\mathbf{\Omega}$ and $\mathbf{O}$.

Other method of destabilizing dark states is based on re-defining the bright and dark states, on changing the linear superpositions. Here, either discretely or continuously, we couple different part

of the ground state subspace to the excited state - if we pump population from bright to a dark state, we then make the dark state a new bright state. This can be achieved with multiple light fields and clever manipulation of their phases, by switching light fields on and off, by switching light fields' polarizations, etc.. The execution depends on the real physical constraints and the equipment at hand. In our experiment we will use this method by switching polarizations of both laser and microwaves.

Chapter 6

Optical Cycling Toy Models

6.1 Motivation and Potential Problems

Having understood how one can find dark states in a system, we would like to first apply this knowledge to a problem of optimizing the average scattering rate. High scattering rate is especially crucial in optical laser cooling. As shown in [38], in principle TlF has favorable Franck-Condon factors and one should be able to scatter approximately 10,000 photons per molecule with three additional vibrational repump lasers. However, for this to work we have to make sure that for single optical cycling transition the scattering rate can be close to its maximum value, which can be estimated to be $\widetilde{\Gamma} = n_e/(n_e + n_g)\,\Gamma$, where n_e and n_g are number of excited and ground states respectively [70]. High scattering rate is also important for our nuclear Schiff moment experiment - the final state will be projected onto different rotational levels, and population in those projections will be detected via laser-induced fluorescence.

Given the rotational branching ratios (table B.4) the best candidate for a cycling transition is transition from the $J = 1$ manifold in the ground $X^1\Sigma^+$ state to the f-parity $\widetilde{J}' = 1^+$ state in the excited electronic state $B^3\Pi_1$ - a so-called Q1 line already mentioned in the experimental overview. Such cycling transition should be limited only by the vibrational branching ratio $b_{\nu=0\to\nu=1} = 0.01$ (FCF_{00}=0.99) allowing to scatter $\sim$ 100 photons per molecule. However, there is a problem. The hyperfine splittings in the excited state disallow simultaneous coupling of multiple hyperfine manifolds with one light field - the smallest splitting is $\sim$ 300 MHz, which is more than enough to suppress coupling to neighboring hyperfine states. We are left with one hyperfine manifold of our

choice. Given the rotational branching ratios, the best candidate is the $\left|\widetilde{J}'=1^+,\widetilde{F}_1'=1/2,F'=1\right\rangle$ manifold with 3 sublevels. On the other hand, energy splittings in the ground state are order of magnitude smaller than the natural linewidth γ, so all the levels will be coupled simultaneously. With 3 excited states and 12 ground states, dark states are easily created.

The experiments trying to reach the highest possible average scattering rate have been performed in group of Larry Hunter at Amherst College. They estimate that despite all the measures undertaken to destabilize the dark states (polarization switching of the laser, microwaves coupling $J=0$ to $J=1$ levels and their polarization switching), the number of photons per molecule from the cycling transition is somewhere between 50 and 60, while their observed average scattering rate is approximately order of magnitude smaller than the estimated $\Gamma/5$ scattering rate. One then needs ask: why is the scattering rate and the number of photons per molecule so small?

In this chapter we will investigate what the best methods of maximizing scattering rate are. Various approaches will be looked at and their average scattering rate estimated from numerical simulations of the process. We will mostly concentrate on a simplified version of the real TlF molecule - we will only include thallium's nuclear spin.

6.2 Rabi Rates and Electric Field

Before we begin discussion of optical cycling we look at the relationship between Rabi rates and the electric field. The off-diagonal terms in the hamiltonian responsible for interaction with the electric field can be written using Eq. (2.5.1). For polarization p dipole matrix element in the Rabi rate $\langle f|T^1_p(\mathbf{d})|i\rangle$ is calculated using Eq. (2.5.4) with appropriate transition dipole depending on type of the transition: for optical transitions $\mu_{\text{eff}} = 0.81$ Debye $= 0.4095$ MHz/ V/cm and the permanent dipole moment $\mu_0 = 4.2282$ Debye $= 2.1285$ MHz/ V/cm for microwave transitions. The electric field amplitude $\mathcal{E}$, no matter what polarization (denoted by a vector $\vec{\varepsilon}$), will be assumed to have no spatial dependence. We will also use the rotating wave approximation, just like in the simple toy models, and consider only dipole transitions. Then, we can write that:

$$\boldsymbol{\mathcal{E}} = \boldsymbol{\mathcal{E}} e^{i\mathbf{k}\cdot\mathbf{r}} \cos\omega t \approx \frac{\mathcal{E}}{2} e^{i\omega t}\vec{\varepsilon}.$$

We will also assume that the field's intensity is uniform. We will consider a beam with power P

with cross-sectional diameter d. Then, the intensity is:

$$I = \frac{4P}{\pi d^2},$$

which is related to the amplitude of electric field via:

$$\mathcal{E} = \sqrt{\frac{2I}{c\varepsilon_0}} = \sqrt{\frac{8P}{\pi c\varepsilon_0 d^2}}. \tag{6.2.1}$$

Now, the electric field's amplitude calculated directly from beam's power can be in general a superposition of amplitudes of beams of different polarizations. While in this chapter some polarizations will be chosen arbitrarily, in general we will assume the following geometry[1] (Fig. 6.2.1): the molecular beam moves along the **y** direction; the **z** direction defines the quantization axis; the laser propagates along the **z** direction with one of two circular polarizations (assumed for simplicity; linear polarizations will be used in more realistic models); microwaves propagate along a direction **k** that creates an angle θ_μ with the **z**-axis; microwaves are in the **xz**-plane perpendicular to the molecular beam; microwaves are also linearly polarized with angle χ with respect to direction perpendicular to vector **k** and lying in the **xz**-plane. In that geometry, we can decompose the microwave electric field in following way:

$$\begin{aligned}
\mathcal{E}_{\mu,\sigma^+} &= -\mathcal{E}_\mu^{p=1} = \frac{\mathcal{E}_\mu}{\sqrt{2}}(\sin\chi + i\cos\theta_\mu\cos\chi) \\
\mathcal{E}_{\mu,\sigma^-} &= \mathcal{E}_\mu^{p=-1} = \frac{\mathcal{E}_\mu}{\sqrt{2}}(\sin\chi - i\cos\theta_\mu\cos\chi) \\
\mathcal{E}_{\mu,z} &= \mathcal{E}_\mu^{p=0} = \mathcal{E}_\mu\cos\chi\sin\theta_\mu.
\end{aligned} \tag{6.2.2}$$

To clarify, knowing the geometry, polarization and beam parameters, the off-diagonal element in the hamiltonian will be then calculated using following steps:

Step 1 - calculate total electric field amplitudes:

$$\mathcal{E}_\mu = \sqrt{\frac{8P_\mu}{\pi c\varepsilon_0 d_\mu^2}}$$

$$\mathcal{E}_L = \sqrt{\frac{8P_L}{\pi c\varepsilon_0 d_L^2}}$$

[1] Note that it slightly differs from the overall geometry assumed for CeNTREX.

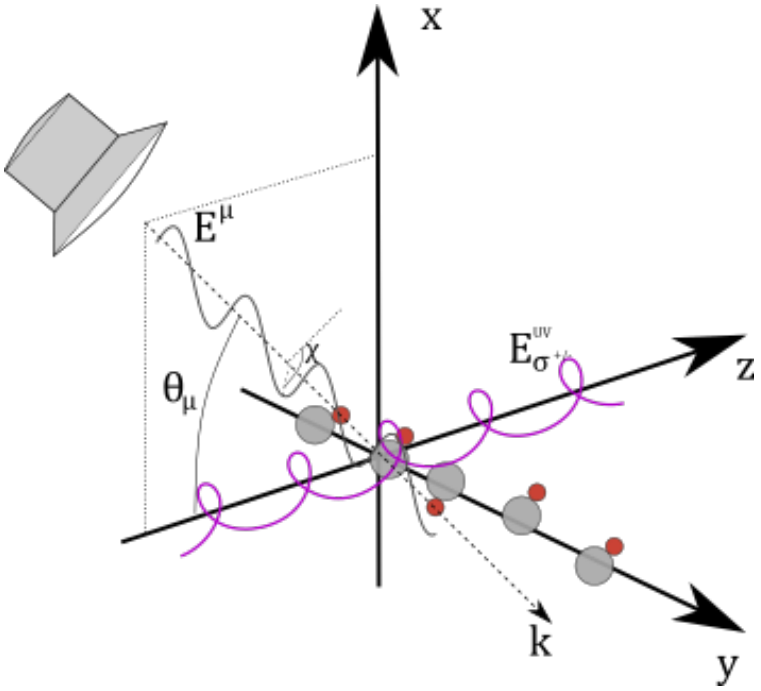

Figure 6.2.1: Geometry assumed in full system models.

Step 2 - obtain amplitudes of light in different polarizations. For microwaves we use Eq. (6.2.2), while for the optical field $\mathcal{E}_L$ is often assumed to be the amplitude of electric field in σ^+ or σ^- polarization.

Step 3 - calculate Rabi rates using previously calculated dipole transition elements from Eq. (2.5.2) and Eq. (2.5.4):

$$\Omega^{if}_{R,L} = \frac{\mu_{\text{eff}}\mathcal{E}_L}{\hbar}\langle f|T^1_{\pm 1}|i\rangle$$
$$\Omega^{if}_{R,\mu} = \frac{\mu_0}{\hbar}\left(\mathcal{E}_{\mu,z}\langle f|T^1_0|i\rangle - (-1)^1\mathcal{E}_{\mu,\sigma^+}\langle f|T^1_{-1}|i\rangle + (-1)^{(-1)}\mathcal{E}_{\mu,\sigma^-}\langle f|T^1_{+1}|i\rangle\right)$$

Step 4 - calculate off-diagonal elements in the hamiltonian using rotating wave approximation:

$$H_{if} = \overline{H}_{fi} = \frac{\Omega^{if}_{R,L}}{2}e^{i\omega_L t} + \frac{\Omega^{if}_{R,\mu}}{2}e^{i\omega_\mu t}$$

Realistically, the off-diagonal elements will have only contributions from either the laser's field or the microwaves. Both fields will not drive the same transitions. Also, in simpler toy models, we

will not worry about exact dipole transition matrix elements and polarizations.

6.3 Models with Thallium Nuclear Spin

The optical cycling models that we will use closely resemble the system in TlF molecule - we include thallium's nuclear spin of $I_1 = 1/2$, which results in creation of hyperfine states. We will use a simplified version of Eq. (2.5.4) to find transitions and decay rates in our system. Namely, a transition from state $\left|X^1\Sigma^+; J', \Omega', F', M_F', \mathcal{P}'\right\rangle$ to state $\left|B^3\Pi_1; J, \Omega, F, M_F, \mathcal{P}\right\rangle$ [2] can be calculated from:

$$\frac{1}{e\left\langle \mathbf{r}\right\rangle }\left\langle f|T_p^1(\mathbf{d})|i\right\rangle =(-1)^{F-M_F+F'+2J-\Omega+3/2}\sqrt{(2F+1)(2F'+1)(2J+1)(2J'+1)}$$

$$\begin{pmatrix} F & 1 & F' \\ -M_F & p & M_F' \end{pmatrix}\begin{Bmatrix} J' & F' & \frac{1}{2} \\ F & J & 1 \end{Bmatrix}\sum_{q=-1,0,1}\left[\begin{pmatrix} J & 1 & J' \\ -\Omega & q & \Omega' \end{pmatrix}+(-1)^{\mathcal{P}}\begin{pmatrix} J & 1 & J' \\ \Omega & q & \Omega' \end{pmatrix}+\right.$$

$$\left.+(-1)^{\mathcal{P}'}\begin{pmatrix} J & 1 & J' \\ -\Omega & q & -\Omega' \end{pmatrix}+(-1)^{\mathcal{P}+\mathcal{P}'}\begin{pmatrix} J & 1 & J' \\ \Omega & q & -\Omega' \end{pmatrix}\right]. \tag{6.3.1}$$

where $\mathcal{P}$ is the parity type of the state. Rabi rates will be defined in a similar way as before, although we will not pay much attention yet to how electric fields are propagating - we will arbitrarily choose their amplitudes and polarizations.

6.3.1 Model's Dipole Transitions

We begin with a simple system with two $J = 1$ states to try to understand any problems that might arise. The ground state is always of type e ($\mathcal{P} = 0$) and the excited state here is of parity type f ($\mathcal{P} = 1$). The formula Eq. (6.3.1) allows to evaluate branching ratios, which in this system are shown in table 6.3.1 (no hyperfine mixing is assumed).

Because hyperfine splitting due to interaction with thallium's nuclear spin is enormous in the $B^3\Pi_1$ state ($\sim$ 13.5 GHz), we will just concentrate on the $F' = 1/2$ manifold. For such system, given that we have 2 excited states and 6 ground states, we expect 4 dark states and 2 bright states. To confirm that, we can look at the hamiltonian in the same manner as we did in the previous

[2] Please note that to match the notation used in the formula, in the following line the *ground* state is primed.

$\lvert J,F,M_F\rangle$	$\lvert 1^+,\frac{1}{2},-\frac{1}{2}\rangle$	$\lvert 1^+,\frac{1}{2},\frac{1}{2}\rangle$	$\lvert 1^+,\frac{3}{2},-\frac{3}{2}\rangle$	$\lvert 1^+,\frac{3}{2},-\frac{1}{2}\rangle$	$\lvert 1^+,\frac{3}{2},\frac{1}{2}\rangle$	$\lvert 1^+,\frac{3}{2},\frac{3}{2}\rangle$
$\lvert 1^-,\frac{1}{2},-\frac{1}{2}\rangle$	2/9	4/9	1/6	1/9	1/18	0
$\lvert 1^-,\frac{1}{2},\frac{1}{2}\rangle$	4/9	2/9	0	1/18	1/9	1/6
$\lvert 1^-,\frac{3}{2},-\frac{3}{2}\rangle$	1/6	0	1/2	1/3	0	0
$\lvert 1^-,\frac{3}{2},-\frac{1}{2}\rangle$	1/9	1/18	1/3	1/18	4/9	0
$\lvert 1^-,\frac{3}{2},\frac{1}{2}\rangle$	1/18	1/9	0	4/9	1/18	1/3
$\lvert 1^-,\frac{3}{2},\frac{3}{2}\rangle$	0	1/6	0	0	1/3	1/2

Table 6.3.1: Branching ratios for decays from pure states $|J,F,M_F\rangle$ (columns) in $B^3\Pi_1$ to states in $X^1\Sigma^+$ (rows) in a simplified model of TlF.

chapter. We will assume that the coupling laser light field present is decomposed into following components: $\Omega_z = 0$, $\Omega_{\sigma^-} = \Omega_{\sigma^+} = \Omega/\sqrt{2}$, where Ω is assumed to be real. Fig. 6.3.1 depicts the system. In such a simplified situation we obtain:

$$H = \begin{array}{c} \begin{matrix} \lvert 1^-,\frac{1}{2},-\frac{1}{2}\rangle & \lvert 1^-,\frac{1}{2},\frac{1}{2}\rangle & \lvert 1^-,\frac{3}{2},-\frac{3}{2}\rangle & \lvert 1^-,\frac{3}{2},-\frac{1}{2}\rangle & \lvert 1^-,\frac{3}{2},\frac{1}{2}\rangle & \lvert 1^-,\frac{3}{2},\frac{3}{2}\rangle & \lvert 1^+,\frac{1}{2},-\frac{1}{2}\rangle & \lvert 1^+,\frac{1}{2},\frac{1}{2}\rangle \end{matrix} \\ \begin{pmatrix} -\delta_L & 0 & 0 & 0 & 0 & 0 & 0 & \frac{\Omega}{3\sqrt{2}} \\ 0 & -\delta_L & 0 & 0 & 0 & 0 & -\frac{\Omega}{3\sqrt{2}} & 0 \\ 0 & 0 & \Delta-\delta_L & 0 & 0 & 0 & \frac{\Omega}{4\sqrt{3}} & 0 \\ 0 & 0 & 0 & \Delta-\delta_L & 0 & 0 & 0 & \frac{\Omega}{12} \\ 0 & 0 & 0 & 0 & \Delta-\delta_L & 0 & \frac{\Omega}{12} & 0 \\ 0 & 0 & 0 & 0 & 0 & \Delta-\delta_L & 0 & \frac{\Omega}{4\sqrt{3}} \\ 0 & -\frac{\Omega}{3\sqrt{2}} & \frac{\Omega}{4\sqrt{3}} & 0 & \frac{\Omega}{12} & 0 & 0 & 0 \\ \frac{\Omega}{3\sqrt{2}} & 0 & 0 & \frac{\Omega}{12} & 0 & \frac{\Omega}{4\sqrt{3}} & 0 & 0 \end{pmatrix} \end{array},$$

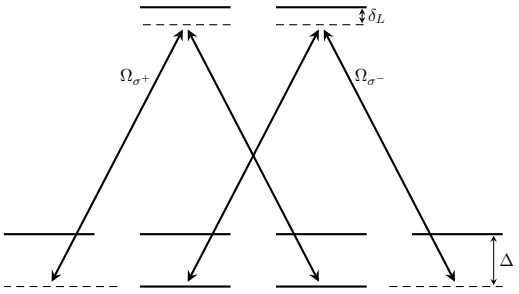

(a) Couplings.

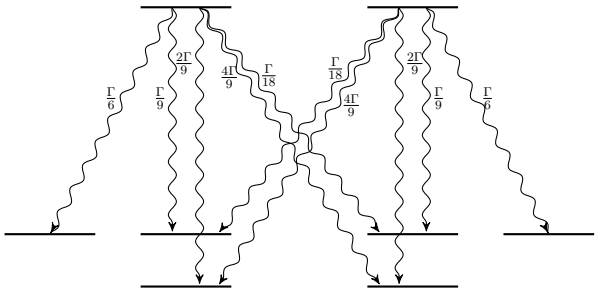

(b) Decays.

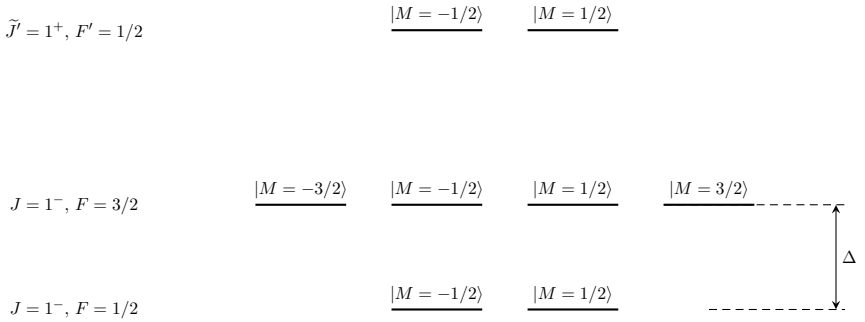

(c) Energy structure.

Figure 6.3.1: Structure for $J = 1^- \leftrightarrow \widetilde{J}' = 1^+$ transition in a simplified TlF system with coupling to thallium's nuclear spin only.

We can easily find that (after normalization):

$$\mathbf{\Omega}^{\mathrm{T}} = \begin{pmatrix} 0 & -\frac{\sqrt{2}}{\sqrt{3}} & \frac{1}{2} & 0 & \frac{1}{2\sqrt{3}} & 0 \\ \frac{\sqrt{2}}{\sqrt{3}} & 0 & 0 & \frac{1}{2\sqrt{3}} & 0 & \frac{1}{2} \end{pmatrix},$$

and clearly see that $\dim(\ker \mathbf{\Omega}^{\mathrm{T}}) = 4$. Bright state space will be spanned by vectors given in the matrix above, that is (where states are defined as $|J, F, M_F\rangle$ and from now on we drop the parity of the state):

$$|B_1\rangle = -\frac{\sqrt{2}}{\sqrt{3}} \left|1, \frac{1}{2}, \frac{1}{2}\right\rangle + \frac{1}{2} \left|1, \frac{3}{2}, -\frac{3}{2}\right\rangle + \frac{1}{2\sqrt{3}} \left|1, \frac{3}{2}, \frac{1}{2}\right\rangle$$

$$|B_2\rangle = \frac{\sqrt{2}}{\sqrt{3}} \left|1, \frac{1}{2}, -\frac{1}{2}\right\rangle + \frac{1}{2\sqrt{3}} \left|1, \frac{3}{2}, -\frac{1}{2}\right\rangle + \frac{1}{2} \left|1, \frac{3}{2}, \frac{3}{2}\right\rangle$$

Equally easily we could find the dark states. It is worth noting that the exact form of these bright and dark states depends on Rabi rates of transitions (just like in toy models from previous

chapter), and the most trivial cases are when we only have light of one polarization. For example, if we only had right-circularly polarized light, states $|1, 1/2, 1/2\rangle$, $|1, 3/2, 1/2\rangle$ and $|1, 3/2, 3/2\rangle$ would be trivially dark - they would not be coupled to any excited state whatsoever. The fourth dark state would be created from $|1, 1/2, -1/2\rangle$ and $|1, 3/2, -1/2\rangle$ states. In the specific system we chose, the dark states are less trivial superpositions of our states. We should also emphasize, just like in the previous chapter, that these states become dark once splitting Δ is equal to 0, though when the splitting is very small the dark states evolve with timescale much longer than interaction timescales of molecular beam experiments.

In order to couple the dark states to the excited states, we could lift the degeneracy by using different lasers for σ^+, σ^- and π transitions - energy of levels in the hamiltonian will be given by detunings, so a careful adjustment could lead to removal of most, if not all, dark states. Same could also be achieved with selective phase modulation of lasers associated with only certain type of transitions as was shown before. These methods also work on a model with $J = 1 \leftrightarrow J = 0$ transition [49].

However, in our system we will not use those tricks. The initial design shown here, i.e. with one light field coupling to all states and their complete degeneracy, is the most appropriate representation of our experimental reality. Therefore, to avoid population accumulation in the dark states, we will use other approaches shown in previous toy models. Given that we have 4 dark states, we need to find at least 4 non-decaying (or decaying) auxiliary "excited" states that we could couple to our ground state. The ground rotational state will not do - it only has 2 Zeeman sublevels. But coupling our ground state to the $J = 2^+$ rotational state, which has 10 Zeeman sublevels, should easily destabilize our dark states. Separately, we will also present a different method - by simply switching polarization of the laser we can effectively double the number of the excited states. In our case that will reduce the number of dark states to 2, which should allow us to destabilize them with coupling to $J = 0^+$ manifold.

To compare how effective various methods are in our system, we will find an average scattering rate $\widetilde{\Gamma}$, which we will calculate over the approximate interaction time for a cold molecular beam. We will use interaction time of $T \approx 70\,\mu s$ and evaluate the scattering rate using:

$$\widetilde{\Gamma} = \frac{\int_0^T \left(\rho_{|1,1/2,-1/2\rangle}(t) + \rho_{|1,1/2,1/2\rangle}(t)\right)\Gamma dt}{T}, \tag{6.3.2}$$

where both density matrix elements are taken from the diagonal and represent populations of the excited states.

6.3.2 Destabilization Using $J = 2^+$ Manifold

The $J = 2^+$ rotational level has 10 Zeeman sublevels: 6 with $F = 5/2$ and 4 with $F = 3/2$ (as shown in Fig. 6.3.2 depicting level structure in the ground electronic state). Given that we have 4 dark states in $J = 1^-$ rotational state we should easily destabilize them. There are several methods, as seen in toy models of the previous chapter, which can be used to achieve our goal: we can couple both rotational levels using on-resonance microwaves and cause population transfer from dark states to bright states via auxiliary states or we can couple both rotational levels with strong off-resonance microwaves causing AC Stark shift and hastening evolution of bright and dark states. Both of these methods can also be achieved utilizing light field pulses, where microwaves and laser are not simultaneously on (method was presented in the 4-level toy model), or by having microwaves and laser interacting with the system at the same time.

We start with the simplest case - coupling both rotational levels using on-resonance microwaves simultaneously with the laser. As was seen before, for high Rabi rates of both laser and microwaves such method should allow us to reach steady state with maximum allowed scattering rate. There are a few problems with this approach however. Firstly, just by counting multiplicities of our states, we have an upper limit on the scattering rate of $2/(2+6+10)\,\Gamma = \Gamma/9$. Secondly, this limit can only be reached if other parameters are chosen well. For instance, it can be seen in $J = 1 \leftrightarrow J = 0$ toy model [49], the maximum scattering rate occurs only if Rabi rates of Ω_z, Ω_{σ^+} and Ω_{σ^-} are the same (which occurs for polarization angle $\theta = \arccos 1/\sqrt{3}$). The same goes for detunings - they have to be chosen well. In an 18-state system accurately choosing the optimal parameters will not be easy. Finally, reaching the maximum scattering rate requires Rabi rates of couple Γ for the optical transition. Given that our optical transition is in the UV, we are limited by the available power - assuming, optimistically, 100 mW available power, we can get to Rabi rates $\lesssim 10\,\Gamma$.

Fig. 6.3.3a, depicting results of numerical simulations of discussed system, shows that we indeed can achieve non-zero scattering rates with the help of on-resonance microwaves, though slightly below the $\Gamma/9$ upper limit. We used splittings in $J = 1^-$ and $J = 2^+$ as in real TlF system, i.e.

$\Delta_1 = 176$ kHz and $\Delta_2 = 278$ kHz[3], $\delta_L = \delta_\mu = 0$. For the microwave Rabi rates we assumed $\Omega_{\mu,z} = \Omega_\mu/\sqrt{2}$, $\Omega_{\mu,\sigma^+} = \Omega_{\mu,\sigma^-} = \Omega_\mu/4$ and $\Omega_{L,z} = \Omega_L$, $\Omega_{L,\sigma^+} = \Omega_{L,\sigma^-} = 0$ for the laser, which were found to yield high scattering rates, although were chosen arbitrarily. For such parameters and $\Omega_L = 2.5\,\Gamma$, we obtain $\widetilde{\Gamma} \approx \Gamma/15.4$. Fig. 6.3.3b depicts evolution of bright and dark states (with respect to the optical transition) in $J = 1^-$ state, population in $J = 2^+$ state and population in both excited states.

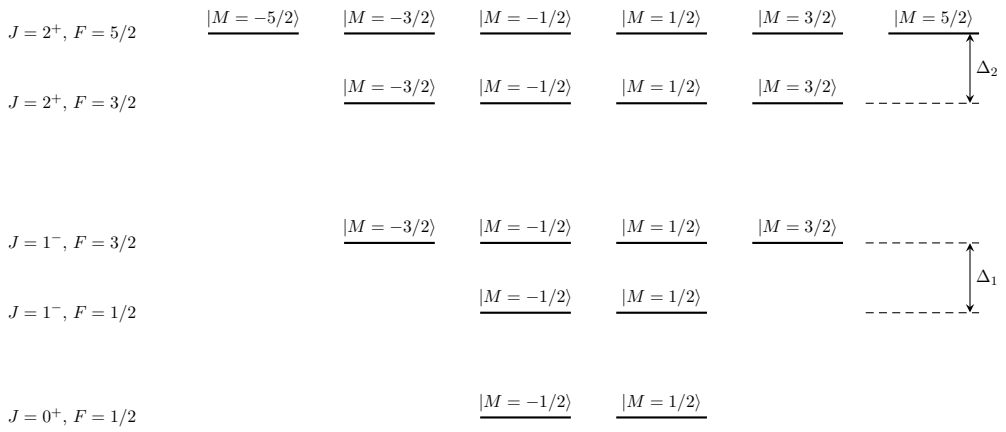

Figure 6.3.2: Level structure of the first three rotational states in TlF.

The results look quite promising - even for a more realistic UV power of 40 mW we can obtain average scattering rates $\widetilde{\Gamma} \approx \Gamma/17.5$. However, in this scheme with microwaves and laser being continuously on, the average scattering rate is quite sensitive to values of various couplings in the system. These depend on polarization of light and microwaves. For almost any combination we could achieve a non-zero steady-state scattering rate, but to reach high values the polarizations have to be correctly chosen, which experimentally is not always easy to achieve.

The second approach, with a strong off-resonance pulse of microwaves to induce a strong AC Stark shift in $J = 1^-$ states to quicken the dark state evolution, might bring better results. In this scheme, first we assume a $t_L = 1.6\,\mu s$ long pulse of laser light with Rabi rate of $\Omega_L = 1.58\,\Gamma$ (Rabi rate obtained for laser power of 40 mW focused to a 1 cm diameter beam), where we choose to use an equal superposition of right- and left-circular polarization (either way we will create 4 dark states), which is equivalent to a laser with polarization perpendicular to the quantization axis.

[3]In simulations we used angular frequency units, so the actual values were $2\pi \times 176$ kHz and $2\pi \times 278$ kHz.

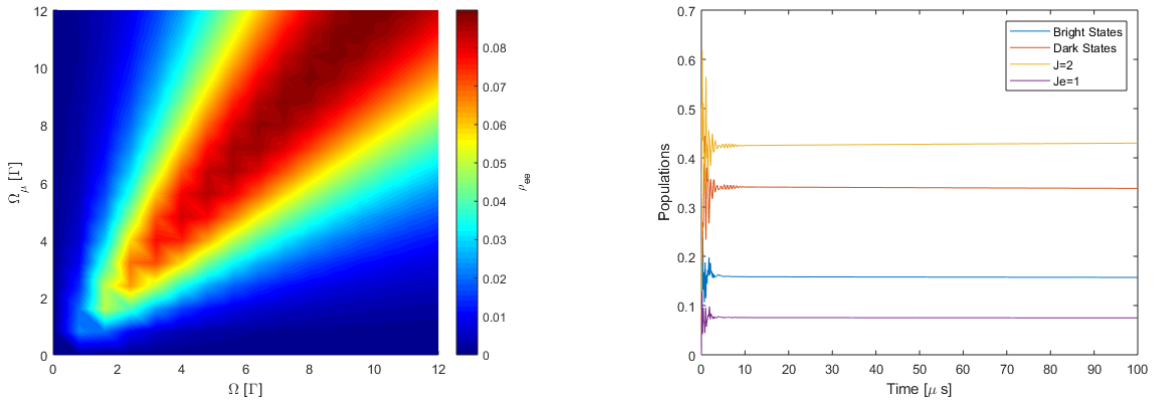

(a) Steady state excited state population as a function of Rabi rates Ω_L and Ω_μ.

(b) Time evolution of populations for $\Omega_L = 2.5\,\Gamma$ and $\Omega_\mu = 2.5\,\Gamma$.

Figure 6.3.3: Results for dark state destabilization utilizing continuous on-resonance microwave coupling to $J = 2^+$ rotational level. Parameters used: $\Delta_1 = 176$ kHz and $\Delta_2 = 278$ kHz, $\delta_L = \delta_\mu = 0$, as well as $\Omega_{\mu,z} = \Omega_\mu/\sqrt{2}$, $\Omega_{\mu,\sigma^+} = \Omega_{\mu,\sigma^-} = \Omega_\mu/2$ and $\Omega_{L,z} = \Omega_L$, $\Omega_{L,\sigma^+} = \Omega_{L,\sigma^-} = 0$ for the laser. Je in the figure marks excited state's total angular momentum quantum number.

For microwaves, like before, we assumed $\Omega_{\mu,z} = \Omega_\mu/\sqrt{2}$, $\Omega_{\mu,\sigma^+} = \Omega_{\mu,\sigma^-} = \Omega_\mu/2$. All the states in $J = 1^-$ will be coupled to $J = 2^+$ regardless of the polarization, because of state multiplicity of both manifolds. For this particular choice of polarizations, microwave power does not have to be enormous to yield desired results. Here, we used $P_\mu = 2\,\mathrm{W}$ focused to 3 cm, which is equivalent to $\Omega_\mu \approx 19.4\,\Gamma$, and $\delta_\mu = 180\,\Gamma$. Fig. 6.3.4 shows results obtained for this scheme. We clearly see that just like in simple toy models, the strong off-resonance microwave pulse neatly mixes bright and dark state populations while not causing any population transfer to and from the $J = 2^+$ rotational state. This method results in average scattering rate $\widetilde{\Gamma} \approx \Gamma/36$ for mentioned laser power, and $\widetilde{\Gamma} \approx \Gamma/34$ for $P_L = 100$ mW.

Performing the same pulsed procedure with on-resonance microwaves is expected to perform similarly, if not worse, given that the population is moved between dark and bright states through the auxiliary state. However, we should also look at off-resonance continuous beam of microwaves. In previous chapter we saw that in the simple 4-level system toy model the off-resonance microwaves should provide high scattering rate when $\varkappa \equiv \Delta^\mu_{AC}/\Omega_L = \Omega^2_\mu/4\delta_\mu\Omega_L \approx 1$. For previously used $\Omega_L \approx 1.58\,\Gamma$, we should use $\Omega_\mu \approx 57.5\,\Gamma$ and $\delta_\mu = 522\,\Gamma$ in order to keep the population transfer

ratio as low as before (Ω_μ/δ_μ ratio has to be the same). Indeed, solving the system with such parameters gives a non-zero average scattering rate of $\widetilde{\Gamma} = \Gamma/31$, which is decent, although obtaining such large Rabi rates with microwaves would pose a significant technical challenge.

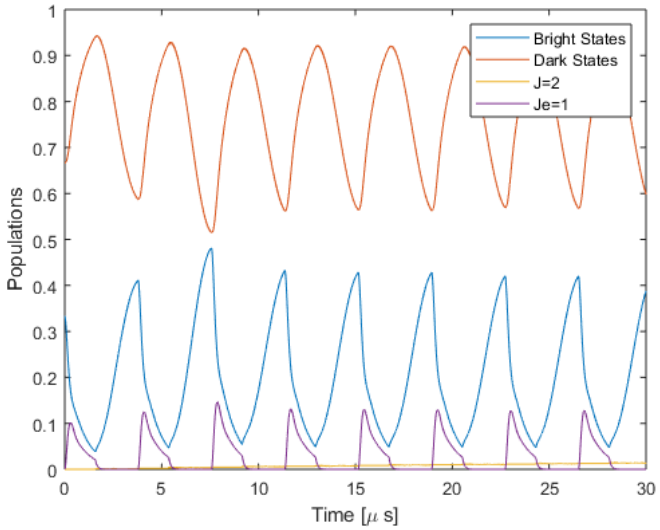

Figure 6.3.4: Time evolution of populations for a scheme with switching between optical and microwave transitions driven by strong off-resonance pulses. Je in the figure marks excited state's total angular momentum quantum number.

6.3.3 Effects of Polarization Switching

We would now like to look at our system using the approach to polarization switching described in the previous chapter. First thing we would like to explore is the effect of simply switching between two circular polarizations, instead of applying them simultaneously to the system. By doing so, we can create an "effective" system and diagram shown previously in Fig. 6.3.1 will be changed into the one of Fig. 6.3.5. In it we not only added those additional effective excited states, but also transferred to a basis with bright and dark states with respect to either right- or left-circularly

polarized light. These superpositions are (in $|J, F, M_F\rangle$ basis with parity not shown):

$$|B_{1+}\rangle = \left|1, \frac{3}{2}, -\frac{3}{2}\right\rangle \qquad |B_{1-}\rangle = -\frac{2\sqrt{2}}{3}\left|1, \frac{1}{2}, \frac{1}{2}\right\rangle + \frac{1}{3}\left|1, \frac{3}{2}, \frac{1}{2}\right\rangle$$

$$|B_{2+}\rangle = \frac{2\sqrt{2}}{3}\left|1, \frac{1}{2}, -\frac{1}{2}\right\rangle + \frac{1}{3}\left|1, \frac{3}{2}, -\frac{1}{2}\right\rangle \qquad |B_{2-}\rangle = \left|1, \frac{3}{2}, \frac{3}{2}\right\rangle$$

$$|D_{+}\rangle = \frac{1}{3}\left|1, \frac{1}{2}, -\frac{1}{2}\right\rangle - \frac{2\sqrt{2}}{3}\left|1, \frac{3}{2}, -\frac{1}{2}\right\rangle \qquad |D_{-}\rangle = \frac{1}{3}\left|1, \frac{1}{2}, \frac{1}{2}\right\rangle + \frac{2\sqrt{2}}{3}\left|1, \frac{3}{2}, \frac{1}{2}\right\rangle.$$

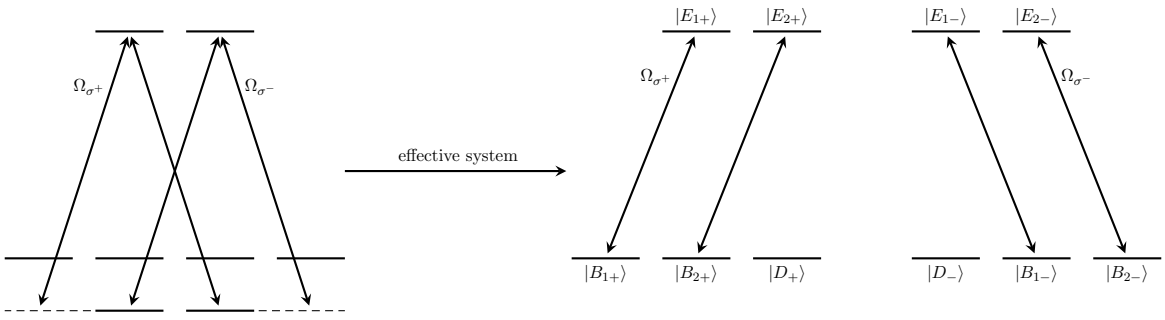

Figure 6.3.5: Diagram of an "effective" simplified $J = 1^- \leftrightarrow \widetilde{J}' = 1^+$ TlF system with switching between two circular polarizations.

It is worth noting that the decays behave just like in Fig. 6.3.1, i.e. state $|E_{1+}\rangle$ and state $|E_{1-}\rangle$ decay exactly like the $\left|\widetilde{J}' = 1, F' = 1/2, M'_F = -1/2\right\rangle$ state, while states $|E_{2+}\rangle$ and $|E_{2-}\rangle$ decay analogically to the other excited state, $\left|\widetilde{J}' = 1, F' = 1/2, M'_F = 1/2\right\rangle$. In this case, we will juggle the population between bright states, just like in Λ-type system. Fig. 6.3.6 shows schematically the process.

Because with only 4 effective excited states we can at most obtain 4 bright states, in the presented scheme we always end up with population trapped in two dark states. In order to completely eliminate them, we need to find a light field that would increase dimension of the bright state space to 6 ($\dim \mathbf{V_g}$ in this system). We could simply try to add an additional light field pulse (switch) with π polarization. Of course, while switching between two circular polarization is possible for one beam only, in order to obtain an additional π polarization pulse we would need an additional laser, which may not be feasible in our experiment, although in general it does not have to be a problem. Having 3 pulses (switches) we can write down an effective hamiltonian and from it obtain the effective coupling matrix (with normalized vectors as rows), which in this case is the

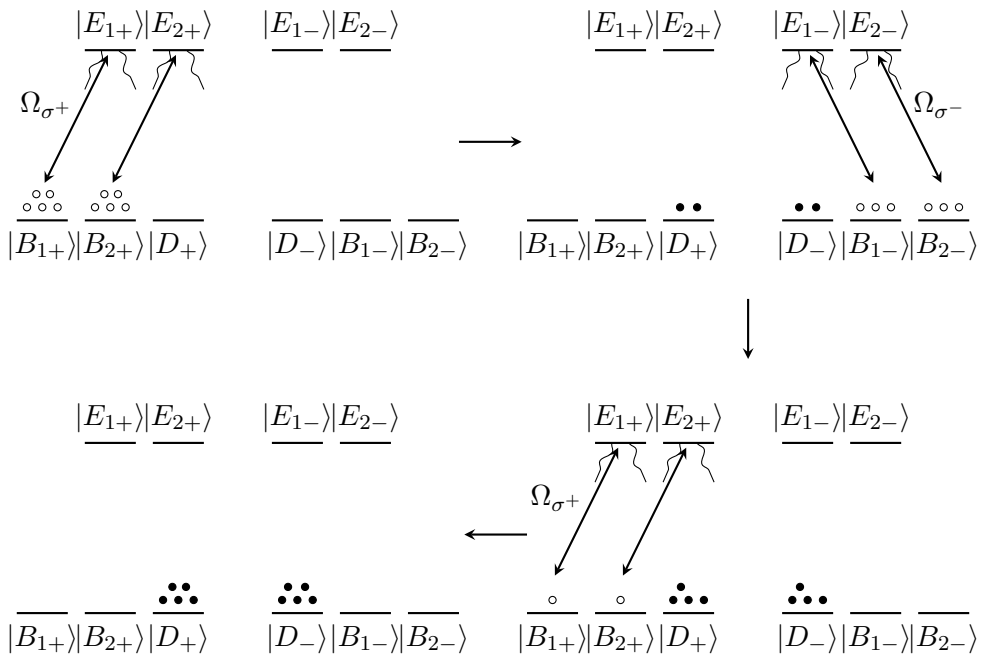

Figure 6.3.6: Juggling population in an "effective" simplified $J = 1^- \leftrightarrow \widetilde{J} = 1^+$ TlF system. When switching only between two circular polarizations we inevitably end up with population trapped in dark states.

same as matrix representation of the bright state space:

$$\mathbf{B} = \mathbf{\Omega}_{\text{eff}}^{\text{T}} = \begin{array}{c} \\ |B_{1+}\rangle \\ |B_{2+}\rangle \\ |B_{1-}\rangle \\ |B_{2-}\rangle \\ |B_{1,\pi}\rangle \\ |B_{2,\pi}\rangle \end{array} \begin{array}{c} \begin{array}{cccccc} \left|1,\tfrac{1}{2},-\tfrac{1}{2}\right\rangle & \left|1,\tfrac{1}{2},\tfrac{1}{2}\right\rangle & \left|1,\tfrac{3}{2},-\tfrac{3}{2}\right\rangle & \left|1,\tfrac{3}{2},-\tfrac{1}{2}\right\rangle & \left|1,\tfrac{3}{2},\tfrac{1}{2}\right\rangle & \left|1,\tfrac{3}{2},\tfrac{3}{2}\right\rangle \end{array} \\ \begin{pmatrix} 0 & 0 & 1 & 0 & 0 & 0 \\ \frac{2\sqrt{2}}{3} & 0 & 0 & \frac{1}{3} & 0 & 0 \\ 0 & -\frac{2\sqrt{2}}{3} & 0 & 0 & \frac{1}{3} & 0 \\ 0 & 0 & 0 & 0 & 0 & 1 \\ -\sqrt{\frac{2}{3}} & 0 & 0 & \frac{1}{\sqrt{3}} & 0 & 0 \\ 0 & \sqrt{\frac{2}{3}} & 0 & 0 & \frac{1}{\sqrt{3}} & 0 \end{pmatrix} \end{array}.$$

The matrix $\mathbf{\Omega}_{\text{eff}}$ is $N_g \times N_g$ in size, so we just need to check its determinant to see if the scheme will work. As it happens, $\det \mathbf{\Omega}_{\text{eff}} = -2/3$, so the whole ground state space can be covered by

bright states. To test the result, we once again solve the Liouville - von Neumann equation in Lindblad form (Chapter 4) for parameters used previously, when we looked at dark destabilization using the $J = 2^+$ rotational state: $P_L = 40$ mW focused to 1 cm corresponding to $\Omega_L \approx 1.58\,\Gamma$, detuning $\delta_L = 0$, there are no microwaves and all three pulses are of equal lengths of $t_p \approx 0.7\ \mu s$. As a result we obtain average scattering rate $\widetilde{\Gamma} \approx \Gamma/11$. Time evolution is plotted in Fig. 6.3.7, where we can nicely see that first 2 pulses (left- and right-circular polarizations) remove population from respective bright states, while the third removes population from a dark states common to those transitions and re-populates the bright states through the decay from the excited state. In the end we obtain a periodic quasi-steady state with a non-zero average excited state population.

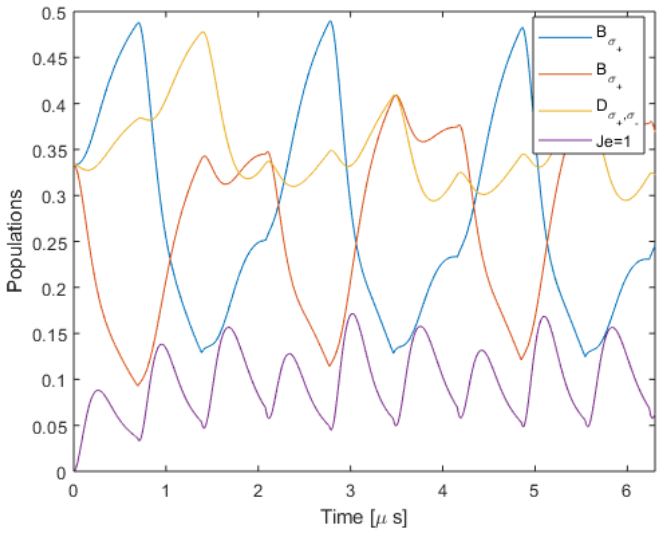

Figure 6.3.7: Time evolution of populations for a scheme with switching between three different light polarizations - σ_+, σ_- and π. States $|B_{\sigma_+}\rangle$ and $|B_{\sigma_-}\rangle$ are bright states with respect to σ_+- and σ_--polarized laser induced transitions respectively, while $|D_{\sigma_+,\sigma_-}\rangle$ represents all dark states with respect to these transitions. It can be seen that indeed the third pulse, having π polarization, properly remixes the indicated dark and bright states. Je in the figure marks excited state's total angular momentum quantum number.

6.3.4 Destabilization Using $J = 0^+$ Manifold

In reality using a second laser to obtain the third pulse might be challenging. However, microwave technology allows for easy manipulation of the pulses. That is why instead of using a π-polarized

pulse, we can instead couple the ground rotational state with π-polarized microwaves. Having two sublevels in the $J = 0^+$ state (diagram in Fig. 6.3.2), we should be able to address both of the dark states. In a general system with (normalized) couplings $a_{+/-}$, $b_{+/-}$ and $c_{+/-}$ for $\sigma_{+/-}$ polarizations and couplings $\alpha_{i,\pi}$ and $\beta_{i,\pi}$ for the microwave transition, we will obtain the following coupling matrix:

$$\mathbf{\Omega}_{\text{eff}}^{\text{T}} = \begin{array}{c} \\ |B_{1+}\rangle \\ |B_{2+}\rangle \\ |B_{1-}\rangle \\ |B_{2-}\rangle \\ \left|B_{1,\pi}^{\mu}\right\rangle \\ \left|B_{2,\pi}^{\mu}\right\rangle \end{array} \begin{array}{c} \begin{array}{cccccc} \left|1,\frac{1}{2},-\frac{1}{2}\right\rangle & \left|1,\frac{1}{2},\frac{1}{2}\right\rangle & \left|1,\frac{3}{2},-\frac{3}{2}\right\rangle & \left|1,\frac{3}{2},-\frac{1}{2}\right\rangle & \left|1,\frac{3}{2},\frac{1}{2}\right\rangle & \left|1,\frac{3}{2},\frac{3}{2}\right\rangle \end{array} \\ \begin{pmatrix} 0 & 0 & c_+ & 0 & 0 & 0 \\ a_+ & 0 & 0 & b_+ & 0 & 0 \\ 0 & a_- & 0 & 0 & b_- & 0 \\ 0 & 0 & 0 & 0 & 0 & c_- \\ \alpha_{1,\pi} & 0 & 0 & \beta_{1,\pi} & 0 & 0 \\ 0 & \alpha_{2,\pi} & 0 & 0 & \beta_{2,\pi} & 0 \end{pmatrix} \end{array}.$$

For such a matrix one obtains the full-rank condition of:

$$\det \mathbf{\Omega}_{\text{eff}}^{\text{T}} = c_+c_-(a_-\beta_{2,\pi} - b_-\alpha_{2,\pi})(a_+\beta_{1,\pi} - b_+\alpha_{1,\pi}) \neq 0,$$

which is true in our system. Because the ground rotational state is treated here as a special non-decaying excited state, we also have additional orthogonality conditions. We can see that:

$$\mathbf{O} = \mathbf{\Omega}_{\text{eff}}^{\dagger}\mathbf{\Omega}_{\text{eff}} = \begin{pmatrix} 1 & 0 & 0 & a_+\alpha_{1,\pi} + b_+\beta_{1,\pi} & 0 & 0 \\ 0 & 1 & 0 & 0 & a_-\alpha_{2,\pi} + b_-\beta_{2,\pi} & 0 \\ 0 & 0 & 1 & 0 & 0 & 0 \\ a_+\alpha_{1,\pi} + b_+\beta_{1,\pi} & 0 & 0 & 1 & 0 & 0 \\ 0 & a_-\alpha_{2,\pi} + b_-\beta_{2,\pi} & 0 & 0 & 1 & 0 \\ 0 & 0 & 0 & 0 & 0 & 1 \end{pmatrix},$$

from which we obtain conditions:

$$\begin{cases} a_+\alpha_{1,\pi} + b_+\beta_{1,\pi} \neq 0 \\ a_-\alpha_{2,\pi} + b_-\beta_{2,\pi} \neq 0 \end{cases}$$

which hold in our system. Just like before, we test our scheme with the same parameters. Here, like before, $\Omega_\mu = 19.4\,\Gamma$, $\delta_\mu = 180\,\Gamma$ and $\Omega_L = 2.5\,\Gamma$ although the microwave pulse time is longer than the laser pulse time - $t_\mu \approx 1.6\ \mu s$. In the end, for such parameters we obtain $\widetilde{\Gamma} \approx \Gamma/21$. Fig. 6.3.8 depicts time evolution of states in this quantum system.

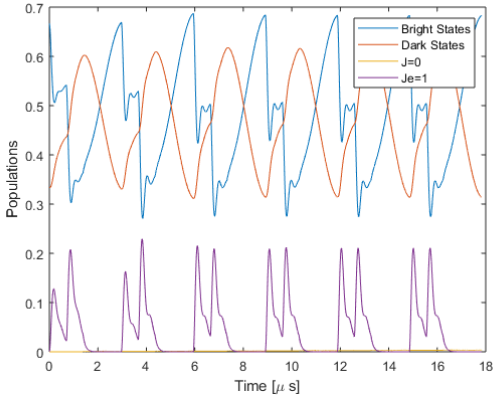

(a) Time evolution of populations for a scheme with switching between microwaves and σ_+ and σ_- polarization of light.

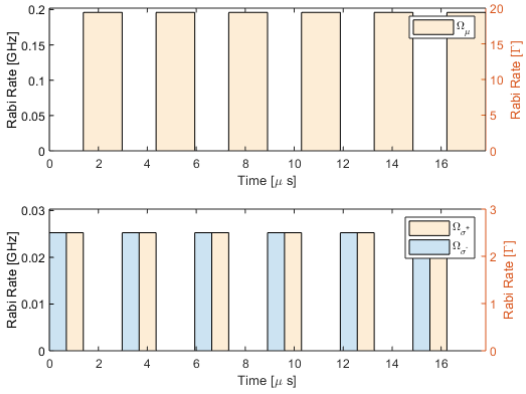

(b) Rabi rates of pulses used.

Figure 6.3.8: Results for dark state destabilization utilizing continuous microwave coupling to $J = 0^+$ rotational level. Here $\Omega_\mu = 19.4\,\Gamma$, $\delta_\mu = 180\,\Gamma$ and $\Omega_L = 2.5\,\Gamma$ and $\delta_L = 0$. Je in the figure marks excited state's total angular momentum quantum number.

The result can be improved upon by noticing that in fact we do not need to switch microwaves on and off - we can keep them constantly on. Such a change improves our average scattering rate to $\widetilde{\Gamma} \approx \Gamma/12.5$ for the same parameters. The time evolution is shown in Fig. 6.3.9. We also tried matching the microwave-induced AC Stark shift with the laser Rabi rate by simply assuming $\Delta^\mu_{AC}/\Omega_L = \Omega^2_\mu/4\delta_\mu\Omega_L \approx 1$ for $\Omega_L = 1.58\,\Gamma$, which gave us $\widetilde{\Gamma} \approx \Gamma/14$. Presumably, such matching for $\Omega_L = 2.5\,\Gamma$ would lead to average scattering rates higher than $\Gamma/12.5$.

Finally, in this system as well the microwaves can actually stay on-resonance. Before, we kept them off-resonance to avoid any population transfer between rotational states. The quasi-steady

state that is generated with on-resonance microwaves leads to a very comparable scattering rate. For $\Omega_\mu = \Omega_L = 2.5\,\Gamma$ we obtain $\widetilde{\Gamma} \approx \Gamma/9$. Time evolution is shown in Fig. 6.3.10.

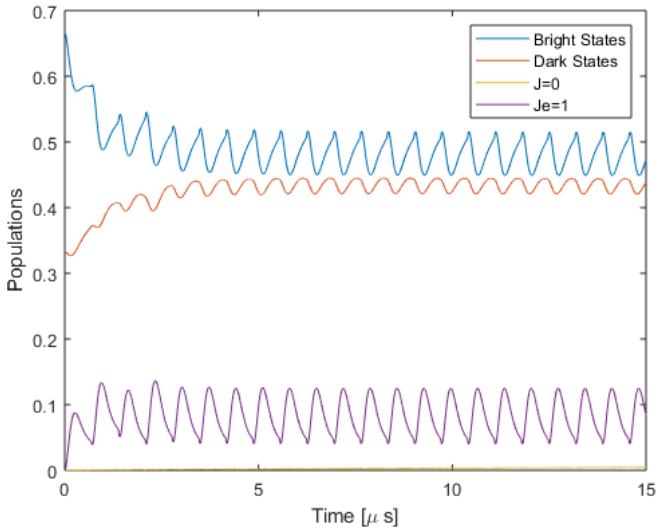

Figure 6.3.9: Time evolution of populations for a scheme with switching between σ_+ and σ_- polarization of light with strong off-resonance coupling to $J = 0^+$ state constantly on. Bright states and dark states drawn are with respect to both laser transitions. Parameters used were $\Omega_\mu = 19.4\,\Gamma$, $\delta_\mu = 180\,\Gamma$ and $\Omega_L = 2.5\,\Gamma$ and $\delta_L = 0$. Je in the figure marks excited state's total angular momentum quantum number.

6.3.5 Comparison of Different Methods

We have analyzed several different methods of destabilizing dark states in this toy model. Table 6.3.2 lists methods, parameters and results for all the schemes. The angles are defined in such a way that:

$$\Omega_{\sigma^+} = \frac{\Omega}{\sqrt{2}} \sin\theta$$
$$\Omega_{\sigma^-} = \frac{\Omega}{\sqrt{2}} \sin\theta$$
$$\Omega_\pi = \Omega \cos\theta,$$

which is to say that θ is polarization angle with respect to the quantization axis for a linearly polarized light. All the results shown below were chosen to yield decent results, while also keeping parameters consistent between schemes to allow for a better comparison. These are not, however,

the global optima. For instance, in schemes with switching, pulse times can be optimized to obtain better results than the ones shown here.

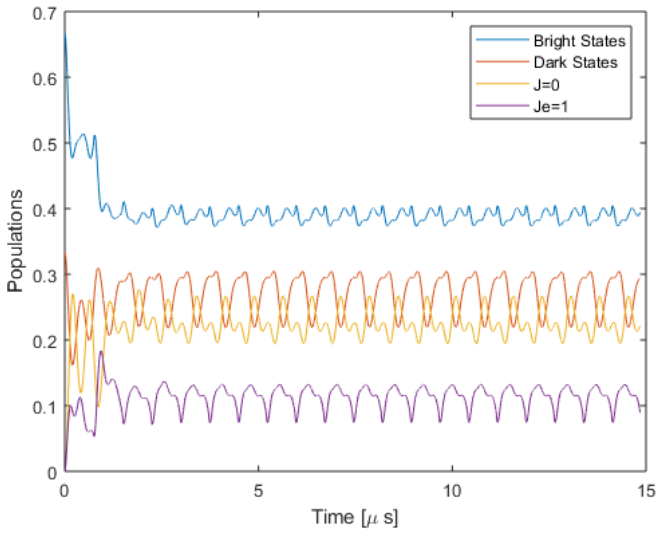

Figure 6.3.10: Time evolution of populations for a scheme with switching between σ_+ and σ_- polarization of light with strong on-resonance coupling to $J = 0^+$ state constantly on. Bright states and dark states drawn are with respect to both laser transitions. Here $\Omega_\mu = 2.5\,\Gamma$, $\delta_\mu = 0$, $\Omega_L = 2.5\,\Gamma$ and $\delta_L = 0$. Je in the figure marks excited state's total angular momentum quantum number.

We wanted to discuss different methods and choose the one that is yields the best results and is easy to realize experimentally. We started with the simplest scheme with on-resonance laser and on-resonance microwaves coupling $J = 1^-$ state to $J = 2^+$. This method allows to quickly reach a steady state with quite high scattering rate. It also is insensitive to laser and microwave powers once a threshold is reached, although that threshold is slightly beyond the maximal UV power we can obtain. The issues with this scheme are, firstly, that the result depends quite strongly on the laser-to-microwave ratio of Rabi rates and that it also depends on coupling strengths for different transitions, and therefore on polarization angles, as is expected from the simple toy models discussed in the previous chapter. While keeping the ratio of Rabi rates seems straight forward to achieve, obtaining proper directionality of the electric field interacting with molecules would require a careful design of the geometry of the setup. Angles chosen here were found to yield good results, but many different combinations result in scattering rate that is order of magnitude lower.

Additional state	Switching type	Parameters										$\widetilde{\Gamma}$
		$P_L[mW]$	$\Omega_L[\Gamma]$	$P_\mu[W]$	$\Omega_\mu[\Gamma]$	$\delta_L[\Gamma]$	$\delta_\mu[\Gamma]$	θ_L	θ_μ	$t_L[\mu s]$	$t_\mu[\mu s]$	
$J = 2^+$	None	40	1.58	0.013	1.58	0	0	0	$\frac{\pi}{4}$	-	-	$\frac{\Gamma}{18}$
		100	2.5	0.033	2.5							$\frac{\Gamma}{15}$
	μ-waves $\leftrightarrow$ laser	40	1.58	2	19.4	0	180	0	$\frac{\pi}{4}$	1.6	2.2	$\frac{\Gamma}{36}$
		100	2.5							0.9		$\frac{\Gamma}{34}$
	None	40	1.58	17.6	57.5	0	522	0	$\frac{\pi}{4}$	-	-	$\frac{\Gamma}{31}$
$J = 0^+$	μ-waves $\leftrightarrow \sigma_+ \leftrightarrow \sigma_-$	40	1.58	2	19.4	0	180	σ_+/σ_-	0	1/1	1.6	$\frac{\Gamma}{24}$
		100	2.5							0.7/0.7		$\frac{\Gamma}{21}$
	$\sigma_+ \leftrightarrow \sigma_-$	40	1.58	17.6	57.5	0	522	σ_+/σ_-	0	1/1	-	$\frac{\Gamma}{14}$
	$\sigma_+ \leftrightarrow \sigma_-$	40	1.58	0.013	1.58	0	0	σ_+/σ_-	0	1/1	-	$\frac{\Gamma}{12}$
		100	2.5	0.033	2.5					0.7/0.7		$\frac{\Gamma}{9}$
None	$\sigma_+ \leftrightarrow \sigma_- \leftrightarrow \pi$	40	1.58	-	-	0	-	$\sigma_+/\sigma_-/\pi$	-	0.6/0.6/0.6	-	$\frac{\Gamma}{10}$

Table 6.3.2: Comparison of different methods of dark state destabilization in the toy model. All values for the average scattering rate are approximate and calculate using Eq. (6.3.2) for integration time of $T = 70$ μs.

Second possibility is to use strong off-resonance microwaves, either with pulses, although this method yields quite small scattering rates and is limited by quite long required microwave pulse times, or without. Given large multiplicity of states in $J = 2^+$ manifold, to quickly remix bright and dark state, we require high microwave Rabi rates and very high detuning. In the table above we show solutions for the same microwave power and detuning to allow a more direct comparison of methods, although increasing the microwave power to about 5 W and detuning to $300\,\Gamma$ would allow us to reach better results. As proof of principle, we show that keeping such strong off-resonance microwaves continuously on, therefore matching remixing and excitation rates, can lead to reasonable results as well. However, changing the polarizations away from these somewhat optimal values would put even bigger requirements on the microwaves beyond what is perhaps feasible.

Next, we took a look at schemes utilizing microwaves coupling $J = 1^-$ to the ground rotational

state. As was mentioned before, all the schemes using this coupling require polarization switching of the laser field in order to effectively eliminate 2 dark states. By using off-resonance strong microwave pulses we obtain results that are better than the ones obtained when coupling $J = 1^-$ to $J = 2^+$. Additionally, this scheme is not very sensitive to polarization angle of the microwaves and the required pulse time scale much better with increasing power.

A different, more appealing option that was explored before is to continue remixing dark and bright states in the background, i.e. we can keep the off-resonance microwaves continuously on. This method gives even higher average scattering rate, because we do not need to waste time on microwave pulses, while having all the advantages of the previous scheme. Very similar results are obtained with on-resonance microwaves, which have an advantage of having smaller requirements on microwave power, though ratio of laser and microwave Rabi rates must be kept close to 1.

Finally, we also find scheme with short laser pulses of three different polarization yielding quite high scattering rates. However, even though we do not need any microwaves, we would definitely need an additional laser. Using two lasers, we would also have to turn both of them on and off. Given that the microwaves and their manipulation is easier and cheaper, the previous method seems to be more approachable and, when optimized, should allow us to obtain a similar average scattering rate.

6.4 A Full Model of Q1 Transition

The natural next step is to extend our discussion to a full model with both nuclear spins. The relevant structure of this Q1 transition that is used in detection region to measure population in one of the projections of the final superposition state is shown in Fig. 6.4.1. We see that now we have three excited state, but as many as 12 ground states! Naturally, we will obtain 9 dark states that require taking care of. We can quickly get rid off 3 dark states by switching between two circular polarizations (one can check that easily by looking at kernel of the effective coupling matrix $\mathbf{\Omega}_{\text{eff}}$ that includes both pulses). In order to get rid of the remaining 6 dark states, we need to either couple the ground state to the $J = 2^+$ manifold or use a clever scheme utilizing the ground rotational state, which, as we saw previously, should provide better results. However, we need to be careful.

6.4.1 Disjoint Dark States

Coupling the $J = 1^-$ state to the ground rotational state with microwaves at any polarization can help with eliminating at most 4 additional dark states. In fact, coupling with π-polarized microwaves eliminates only 3 of them and leaves 3. However, we can try switching between two circular polarization of microwaves as well. We find the coupling matrix to be (in the $|F_1, F, M_F\rangle$ basis, where $J = 1^-$ is implied):

$$\mathbf{\Omega}_{\text{eff}}^{\text{T}} = \begin{array}{c} \\ |B_{1+}\rangle \\ |B_{2+}\rangle \\ |B_{3+}\rangle \\ |B_{1-}\rangle \\ |B_{2-}\rangle \\ |B_{3-}\rangle \\ |B_{1+}^{\mu}\rangle \\ |B_{2+}^{\mu}\rangle \\ |B_{3+}^{\mu}\rangle \\ |B_{4+}^{\mu}\rangle \\ |B_{1-}^{\mu}\rangle \\ |B_{2-}^{\mu}\rangle \\ |B_{3-}^{\mu}\rangle \\ |B_{4-}^{\mu}\rangle \end{array} \begin{array}{c} \begin{array}{cccccccccccc} |\frac{1}{2},0,0\rangle & |\frac{1}{2},1,-1\rangle & |\frac{1}{2},1,0\rangle & |\frac{1}{2},1,1\rangle & |\frac{3}{2},1,-1\rangle & |\frac{3}{2},1,1\rangle & |\frac{3}{2},1,1\rangle & |\frac{3}{2},2,-2\rangle & |\frac{3}{2},2,-1\rangle & |\frac{3}{2},2,0\rangle & |\frac{3}{2},2,1\rangle & |\frac{3}{2},2,2\rangle \end{array} \\ \begin{pmatrix} 0 & 0 & 0 & 0 & 0 & 0 & 0 & 1 & 0 & 0 & 0 & 0 \\ 0 & \sqrt{\frac{2}{3}} & 0 & 0 & -\frac{1}{2\sqrt{3}} & 0 & 0 & 0 & \frac{1}{2} & 0 & 0 & 0 \\ -\frac{2}{3} & 0 & \frac{2}{3} & 0 & 0 & -\frac{1}{3\sqrt{2}} & 0 & 0 & 0 & \frac{1}{3\sqrt{2}} & 0 & 0 \\ -\frac{2}{3} & 0 & -\frac{2}{3} & 0 & 0 & \frac{1}{3\sqrt{2}} & 0 & 0 & 0 & \frac{1}{3\sqrt{2}} & 0 & 0 \\ 0 & 0 & 0 & -\sqrt{\frac{2}{3}} & 0 & 0 & \frac{1}{2\sqrt{3}} & 0 & 0 & 0 & \frac{1}{2} & 0 \\ 0 & 0 & 0 & 0 & 0 & 0 & 0 & 0 & 0 & 0 & 0 & 1 \\ 0 & 0 & 0 & -\frac{1}{\sqrt{3}} & 0 & 0 & \sqrt{\frac{2}{3}} & 0 & 0 & 0 & 0 & 0 \\ \frac{1}{\sqrt{3}} & 0 & \frac{1}{\sqrt{3}} & 0 & 0 & \frac{1}{\sqrt{6}} & 0 & 0 & 0 & \frac{1}{\sqrt{6}} & 0 & 0 \\ 0 & 0 & 0 & \frac{1}{\sqrt{3}} & 0 & 0 & \frac{1}{\sqrt{6}} & 0 & 0 & 0 & \frac{1}{\sqrt{2}} & 0 \\ 0 & 0 & 0 & 0 & 0 & 0 & 0 & 0 & 0 & 0 & 0 & 1 \\ 0 & -\frac{1}{\sqrt{3}} & 0 & 0 & \sqrt{\frac{2}{3}} & 0 & 0 & 0 & 0 & 0 & 0 & 0 \\ 0 & 0 & 0 & 0 & 0 & 0 & 0 & 1 & 0 & 0 & 0 & 0 \\ 0 & -\frac{1}{\sqrt{3}} & 0 & 0 & -\frac{1}{\sqrt{6}} & 0 & 0 & 0 & \frac{1}{\sqrt{2}} & 0 & 0 & 0 \\ \frac{1}{\sqrt{3}} & 0 & -\frac{1}{\sqrt{3}} & 0 & 0 & -\frac{1}{\sqrt{6}} & 0 & 0 & 0 & -\frac{1}{\sqrt{6}} & 0 & 0 \end{pmatrix} \end{array},$$

where, as before, rows are the (normalized) bright state superpositions of ground states. Rows 1-3 correspond to laser σ_+ transition, rows 4-6 to laser σ_- transition, while rows 7-10 show bright state superposition for microwave σ_+ transition, and rows 11-14 represent superpositions for microwave σ_- transition. Having a matrix of dimensions 14×12 with only 12 ground states, we expect to find at least two linearly dependent superpositions. Indeed row 1 and 12 (states $|B_{1+}\rangle$ and $\left|B_{2-}^{\mu}\right\rangle$), as well as row 6 and 10 (states $|B_{3-}\rangle$ and $\left|B_{4+}^{\mu}\right\rangle$) are exactly the same vectors. After eliminating one copies of each, we are left with a 12×12 matrix. As was mentioned previously, a necessary condition is that the rank of the effective coupling matrix must be equal to dimension of the ground state space, and in case of a square matrix this boils down to a non-zero determinant. Here, we

find that $\det \mathbf{\Omega}_{\text{eff}} = 1/3$ (after making it a square matrix) and so $\operatorname{rank} \mathbf{\Omega}_{\text{eff}} = 12$.

Because we're using non-decaying states, we also need to check non-orthogonality of some of the bright states by looking at the matrix $\mathbf{O} = \mathbf{\Omega}_{\text{eff}}^{\dagger} \mathbf{\Omega}_{\text{eff}}$. Unfortunately, we realize that two states, namely $\left|B_{3+}^{\mu}\right\rangle$ and $\left|B_{3-}^{\mu}\right\rangle$, create their own disjoint subspace, i.e. they are not connected to any of the bright states with respect to optical transition. In other words, these two state states lie in dark state space (with respect to optical transition), and even though they are bright states with respect to the microwave transitions, the population trapped in these states cannot be moved to any of the other 10 states in the $J = 1^-$ manifold.

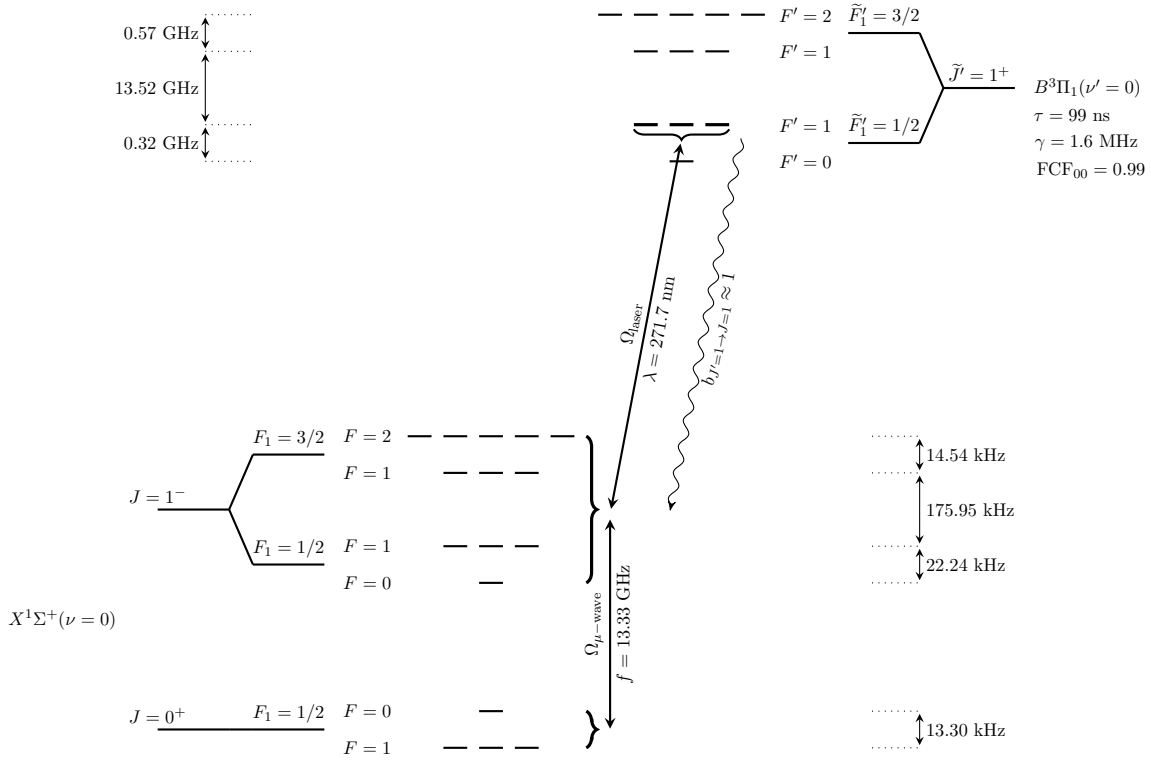

Figure 6.4.1: Diagram of the Q1 optical cycling transition in a real TlF system. We use it to measure population of one of the projections of the final superposition state.

To prove that the conclusion is correct, we solve the equations for density matrix time evolution with all splittings equal to 0 (to avoid any evolution of dark states that could obscure the result) and in a scheme with 4 distinct pulses: laser with σ_+ polarization, laser with σ_- polarization, microwaves with σ_+ polarization and finally microwaves with σ_- polarization. The solution was obtained for $\Omega_L = 1.58\,\Gamma$, $\delta_L = 0$, $\Omega_\mu = 19.4\,\Gamma$ and $\delta_\mu = 200\,\Gamma$ and pulse times: $t_{L,+} = t_{L,-} = 1\ \mu s$

and $t_{\mu,+} = t_{\mu,-} = 2\ \mu s$. Plot in Fig. 6.4.2 shows time evolution of: bright states with respect to optical transitions (both polarizations; sum of 6 states), all dark states collectively, the two disjoint dark states $\left|B^{\mu}_{3+}\right\rangle$ and $\left|B^{\mu}_{3-}\right\rangle$, the ground rotational state and the excited state. It can be seen quite clearly that even though the main principles of the scheme work as they should, that is that microwaves remix dark and bright states, through the decay the population slowly accumulates in the disjoint dark states, which are not remixed, and that eventually causes the scattering rate to drop to zero.

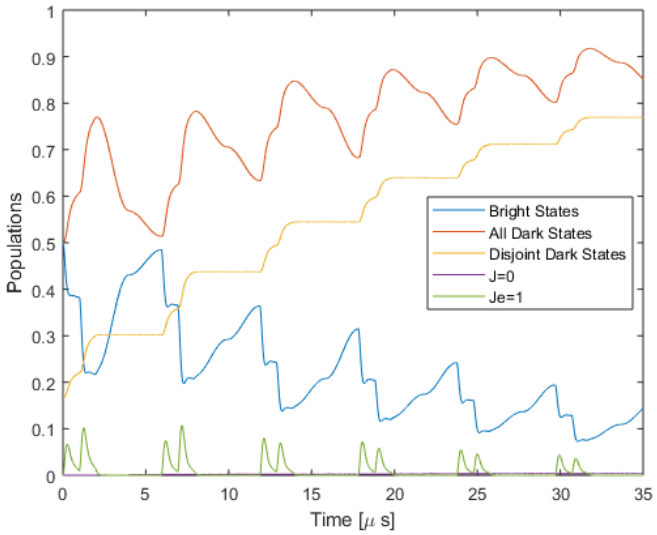

Figure 6.4.2: Time evolution of populations in a real TlF system for a scheme with switching between σ_+ and σ_- polarization of light and between strong off-resonance pulses of σ_+- and σ_--polarized microwaves coupling to $J = 0^+$ state. We used $\Omega_L = 1.58\,\Gamma$, $\delta_L = 0$, $\Omega_\mu = 19.4\,\Gamma$ and $\delta_\mu = 200\,\Gamma$ while keeping splittings $\Delta_0 = \Delta_1 = \Delta_{11} = \Delta_{12} = 0$. Je in the figure marks excited state's total angular momentum quantum number.

This method in our system might be viable to a certain extent. If the splitting-induced evolution of the disjoint dark states is moderately fast or if we want to maximize scattering rate over a rather short interaction time, this scheme will not result in a zero scattering rate - there simply will not be enough time for that to happen. However, in general this method will not destabilize all the dark states. For that we will have to add a different coupling. One of the options would be to couple the states with additional laser beam to $\left|\widetilde{J}' = 1, \widetilde{F}'_1 = 3/2, F' = 2\right\rangle$ excited state and switch its polarization. Indeed one can check that the resulting effective coupling matrix has a

non-zero determinant, and these being normal decaying excited states, we can be sure the scheme would work. However, in a real system this state is problematic and that is why this scheme was not explored in the previous toy model. Namely, the real $\left|\widetilde{J}'=1,\widetilde{F}_1'=3/2,F'=2\right\rangle$ has strong admixtures of higher rotational states and it causes it to decay to $J=3^-$ rotational state as can be seen in table B.4. Therefore, we should destabilize the dark state with the help of $J=2^+$ state or find different spatial and polarization configurations of laser and microwaves in the described scheme.

6.4.2 Experimentally Achievable Optical Cycling

As it happens, a slightly different configuration of microwaves and lasers actually allows for a complete removal of the dark states by using the $J=0^+$ rotational manifold as the source of auxiliary states (diagram in Fig. 6.4.1 depicts details of the Q1 transition). This configuration was used by L. Hunter's group at Amherst College. There, laser polarization was switched between two orthogonal linear polarizations: π and $x\equiv(\sigma_+ + \sigma_-)/\sqrt{2}$. Microwaves, being at an angle of 45° from the laser in the plane perpendicular to the quantization axis were also switched between two orthogonal linear polarizations with phase offset of $\pi/2$ with respect to laser's polarization switching. The real setup is presented in Fig. 6.4.3.

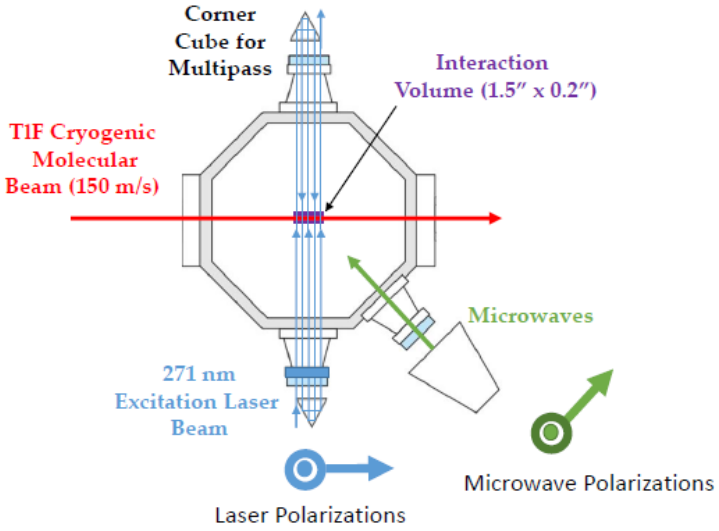

Figure 6.4.3: Experimental setup of TlF optical cycling experiment performed at Amherst College in group of L. Hunter. Courtesy of Nathan Clayburn.

In such configuration and for a system with real transition dipoles, i.e. with excited state mixing of hyperfine states included (for considered $\left|\widetilde{J}'=1^+,\widetilde{F}_1'=1/2,F'=1\right\rangle$ state the mixing is almost negligible), all the dark states are expected to be remixed, unlike in the example with disjoint dark states shown before. The conclusion from the previously described models is also that the most effective and feasible method for reaching high scattering rates is keeping the microwaves on-resonance and balancing its Rabi rate with respect to the laser Rabi rate.

Simulating the process gives results shown in Fig. 6.4.4. It can be seen in Fig. 6.4.4a that, as expected, proper balancing of Rabi rates is crucial in obtaining high scattering rates. In Fig. 6.4.4b we show time evolution for $\Omega_L = 10\,\Gamma$ and $\Omega_\mu = 9\,\Gamma$ that gives an average scattering rate of $\widetilde{\Gamma} \approx \Gamma/8.3$, which already is pretty close to the limit of $\Gamma/6.3$ for this system. Such Rabi rates should also be quite reasonable to obtain in an experimental setting and can be utilized in the detection region of our experiment, where we will have to scatter as many photons as possible from the $J = 1$ manifold.

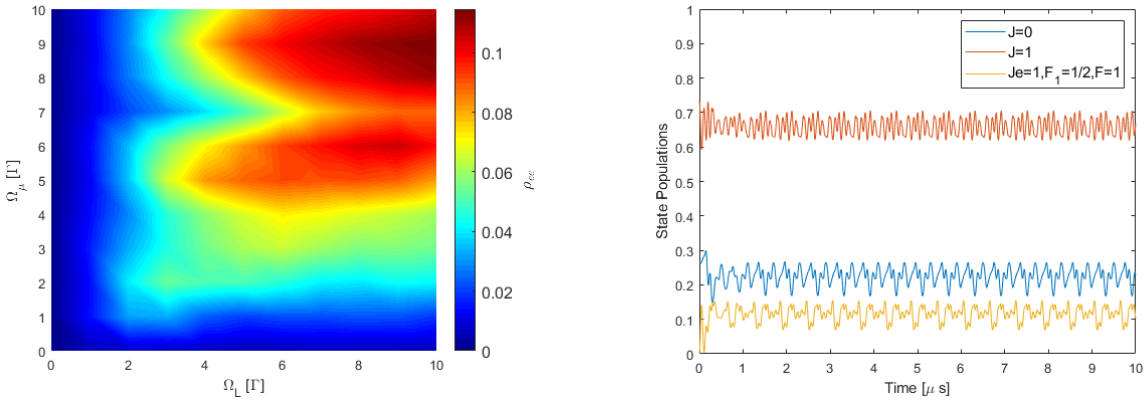

(a) Total excited state population versus microwave and laser Rabi rates.

(b) Time evolution of populations for $\Omega_L = 10\,\Gamma$ and $\Omega_\mu = 9\,\Gamma$.

Figure 6.4.4: Results of optical cycling simulation in a real system with $J = 0^+$ and $J = 1^-$ rotational manifolds in the $X^1\Sigma^+$ state and mixed $\left|\widetilde{J}'=1^+,\widetilde{F}_1'=1/2,F'=1\right\rangle$ excited state. Assumed geometry was that of Fig. 6.4.3 and both lasers and microwaves had their polarization switched with frequency of 1.67 MHz.

6.5 Q23 Transition

As was mentioned in Chapter 3, the final post-precession state has to have both of its projections measured in order to calculate the asymmetry $\mathcal{A}$ parameter. While one of the projection's population can be simply measured efficiently by using the Q1 transition (as was just shown), the second projection is more challenging to measure. This projection has to be in a rotational state $J > 1$ to allow for a proper detection of the other projection via the Q1 transition. Out of the choices available, simply projecting onto $J = 2$ rotational level seems to be our best option. The main reason behind this, other than potential technical difficulties and inefficiencies of projecting onto higher rotational states, is the fact that the Q-line transitions for $J > 1$ begin to overlap due to similar rotational constants in $X^1\Sigma^+$ and $B^3\Pi_1$ states [39].

A reasonable choice of the detection transition is the Q23 line shown in Fig. 6.5.1. All Q-line transitions for $J = 2$ overlap with other Q-lines, but the transition coupling to the excited state $\left|\widetilde{J}' = 2^-, \widetilde{F}_1' = 5/2, F' = 3\right\rangle$ is especially good comparing to other Q2 transitions. The reasons are following: assuming full dark state remixing, this transition should scatter almost 17 photons before the population is lost to a different rotational state; most of the hyperfine states in ground $J = 2$ rotational states are coupled (all except $F = 1$); and it is overlapped with a Q3 line coupling $J = 3$ ground state manifold with the $\left|\widetilde{J}' = 3^+, \widetilde{F}_1' = 7/2, F' = 3\right\rangle$ excited state that by itself can scatter up to about 30 photons. This overlap with a Q3 line also allows to kill two birds with one stone, namely remixing of the dark states in both $J = 2$ and $J = 3$ rotational manifolds can be done simultaneously by coupling them with microwaves at ~ 40 GHz.

Unlike in the case of the Q1 transition, here we are not limited by the vibrational branching ratios, so in the best case scenario we will be able to scatter between 17 and 30 photons per molecule. The exact number will depend on laser and microwave powers and behavior of their polarizations - the number of photons in the end will be decided by the average time a molecule spends in Q3 versus Q2 transition. In Fig. 6.5.2 we show populations of different rotational states that take part in the process over the first 50 μs of the interaction. In this calculation, used as an example to show that a decent number of photons can indeed be scattered through this transition, we assumed experimentally realistic $\Omega_L \approx 5.3\,\Gamma$ and $\Omega_\mu \approx 5.2\,\Gamma$, with both laser and microwaves polarization-switched with pulse time of 500 ns (1 MHz modulation frequency), a $\pi/2$ phase shift between both modulations, and geometry of the previously discussed Q1 transition (Fig. 6.4.3).

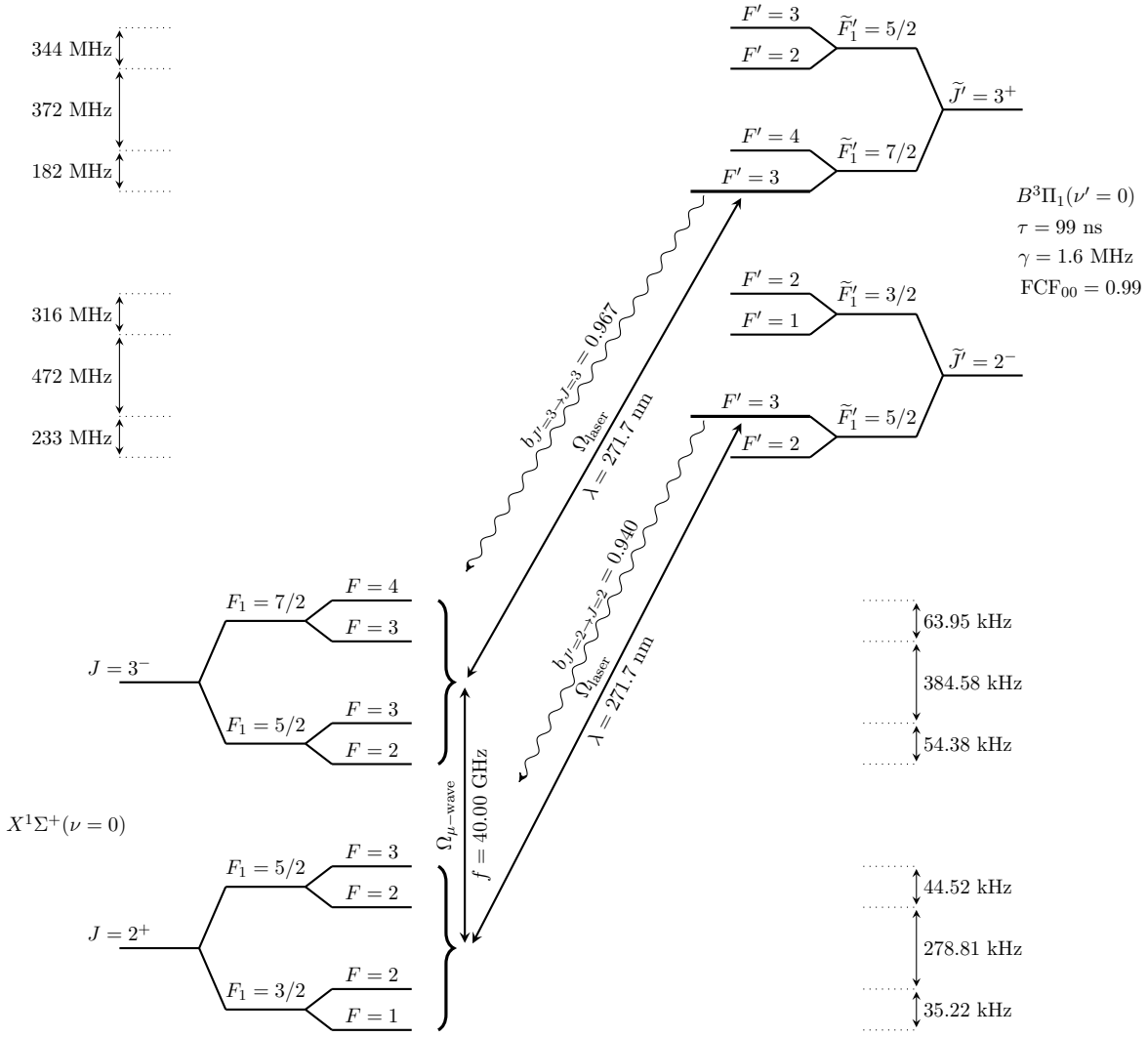

Figure 6.5.1: Diagram of the Q23 transition (overlapped Q2 and Q3 transitions) used to measure population in the other projection of the final superposition state.

The total number of photons scattered per molecule within the interaction time was calculated to be $n_\gamma = 22$, a number higher than the 17 photons we would expect from a pure Q2 transition. Fig. 6.5.2 also clearly shows that the scattering process cannot be sustained and the population inevitably accumulates in higher rotational states due to lack of rotational closure in the Q2 and Q3 lines, and therefore an average scattering rate $\widetilde{\Gamma}$ is not a good unit of measure to describe efficiency of this process. Nevertheless, this transition should still provide a strong signal that can be used for final state's projection detection.

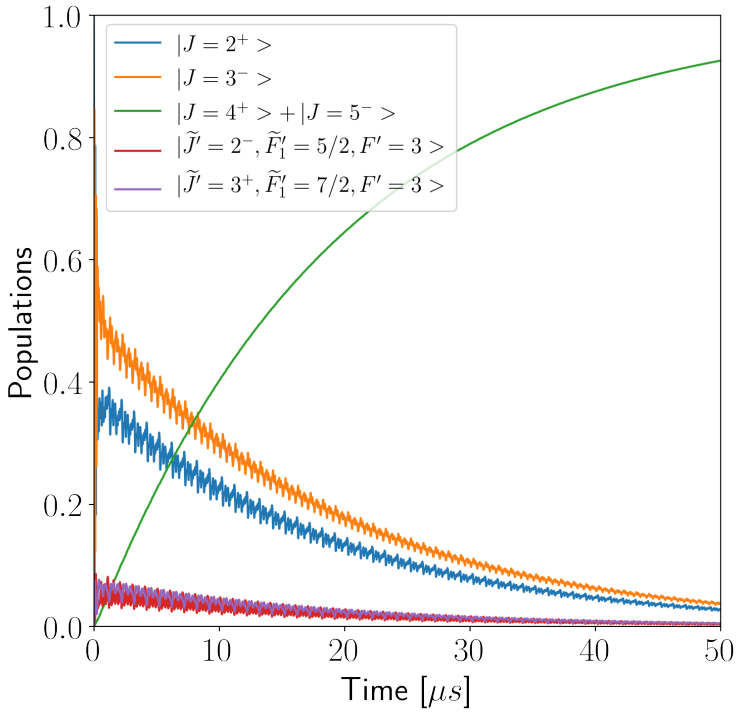

Figure 6.5.2: Time evolution of populations in different rotational states in an example of an overlapped Q23 transition. Solution was obtained for $\Omega_L \approx 5.3\,\Gamma$ and $\Omega_\mu \approx 5.2\,\Gamma$ with 1 MHz polarization switching applied to both the laser and the microwaves. In this simulation 22 photons are scattered per interacting molecule proving viability of using this transition for final state's projection detection.

Chapter 7

Rotational Cooling Models

7.1 Models for Rotational Cooling

One of the major parts of the experiment is rotational cooling, where we want to bring the molecules to the ground rotational state $J = 0$. Task seems pretty straight-forward: by coupling rotational states other than $J = 0$ to $J = 2$ rotational state, and by simultaneously coupling the $J = 2$ state to the excited electronic state, the spontaneous decay process should eventually bring most of the molecules to the $J = 0$ state. Simple models show that this is of course true, such method will work. However, we require the molecules not only to be in the ground rotational state, but also to be in the single $F = 0$ hyperfine state. How can this be achieved most efficiently? Should we rely only on spontaneous decay or couple other hyperfine states in $J = 0$ with microwaves? Can we create a system where the desired final state is completely dark, and so the whole population ends up in it at the end of the process?

7.1.1 Various Parameters

In this chapter's simulation we are assuming that the interaction time is limited by the transit time through the laser beam, for which we will assume $d = 1 - 2$ cm. Because molecules in the experiment move with speeds approaching 200 m/s, the assumed interaction time will be 50-100 μs depending on the analyzed scheme. We will assume that all of the molecules move with the same speed, so no Doppler broadening will be present and interaction time will be the same for all of them. Also, as mentioned earlier, $\Gamma \approx 2\pi \times 1.6$ MHz, and the spontaneous emission will be the only

cause of decoherence in the system. All the fields are assumed to be phase-coherent, i.e. phases of all the fields interacting with molecules stay constant with regards to each other over the course of interaction. Rabi rates and electric fields will be defined as in Chapter 6. Finally, the energy splittings between states will be those of diagram shown in Fig. 2.2.1 and no external fields will be assumed.

7.1.2 Initial Distribution

We will assume that the populations in different rotational states are distributed according to Boltzmann distribution:

$$n_J = \frac{g_J e^{-2\pi\hbar B_{\rm rot} J(J+1)/k_B T}}{\sum_J g_J e^{-2\pi\hbar B_{\rm rot} J(J+1)/k_B T}}, \tag{7.1.1}$$

where $B_{\rm rot} = 6.668$ GHz is the effective rotational constant for $X^1\Sigma^+$, and $g_J = 4(2J+1)$ are degeneracy factors in TlF system. At $T = 7$ K, which is approximately rotational temperature we measure in our beam (measured distribution is shown in Fig. 3.2.2) and what we used in numerical simulations, the population is concentrated at low J's: $n_{J=0} = 0.0451$, $n_{J=1} = 0.1235$, $n_{J=2} = 0.1714$, $n_{J=3} = 0.1822$, $n_{J>3} = 0.4778$. When used as initial conditions in our equations the populations will be normalized to 1. In more realistic models, population in given rotational state will be evenly divided into hyperfine states given that our hyperfine splittings are on the order of hundreds of kHz ($\sim 5\mu$K).

7.2 Optical Pumping and Polarization Switching

The basis of the rotational cooling process is optical pumping. We would like to move population from $J = 2$ rotational manifold to $J = 0$. First, we need to choose an appropriate excited state. Unlike in the case of optical cycling, here we will be using excited states of e-parity. Given the rotational branching ratios (table B.3), the state that would suit our needs the most is $\left|\widetilde{J}' = 1^-, \widetilde{F}_1' = 3/2, F' = 1\right\rangle$, which preferentially decays into $|J = 0, F_1 = 1/2, F = 0, M_F = 0\rangle$ state. Simplified diagram in Fig. 7.2.1 shows these branching ratios together with the transition used in this optical pumping process. This transition, using spectroscopic terms, is a P2 transition (P-branch corresponds to transitions for which $J' = J - 1$). Because it will be mentioned very often in this and following chapters, we will abbreviate it by calling it a P2F1 transition (F1 referring to

the excited hyperfine state).

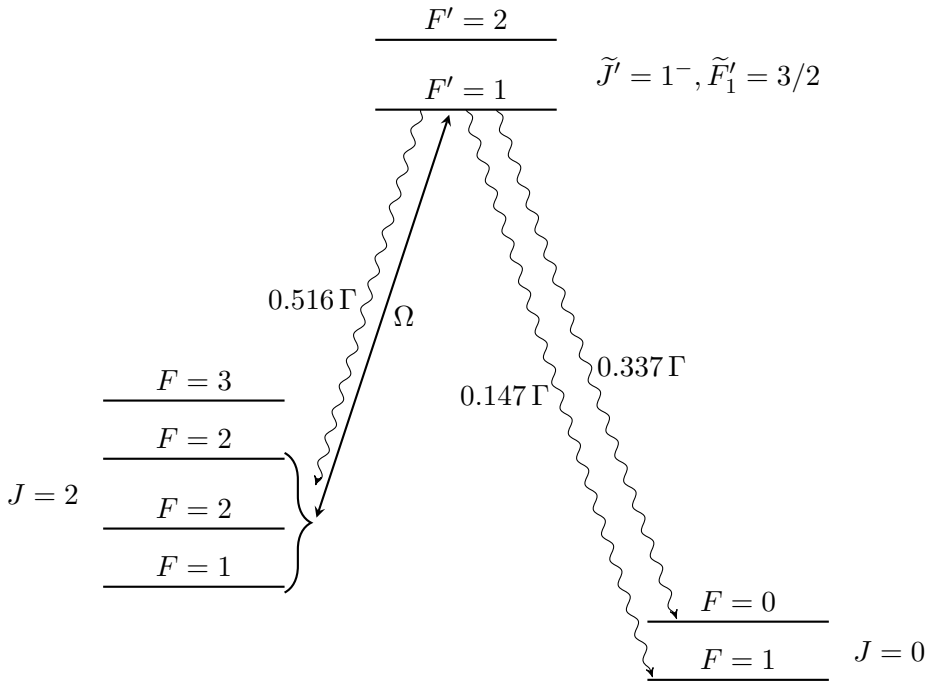

Figure 7.2.1: Diagram of P2F1 transition together with real rotational branching ratios.

This transition couples 20 ground states to 3 excited states creating 17 dark states, from which the population cannot be removed if dark state destabilization methods are not used. Out of the dark states involved, the whole hyperfine $F = 3$ manifold is trivially dark, i.e. the selection rules $\Delta F = 0, \pm 1$ forbid this transition to occur. This already points towards the necessity of utilizing microwaves for dark state destabilization and population removal that would couple this hyperfine manifold to an auxiliary set of states. However, first we will simply concentrate on the dark states in the remaining 15 sublevels of $J = 2$ rotational manifold, and discuss the role of microwaves in next sections.

The number of remaining dark states can be reduced from 12 to 9, if we employ laser polarization switching. Given the limited interaction time, we need to ask what is the most optimal switching frequency that will allow us to remove most population from the existing bright states given the Rabi rate of our laser. In the previous section, the pulse times and, equivalently, switching frequencies were chosen by trial and error which yielded results good enough to act as proof of principle for our methods. Here, we would like to obtain a more precise numerical value.

In order to find the switching frequency, we need to look at the population removal time. The easiest way to do it is to setup a Λ-type system analyzed before and shown here in Fig. 7.2.2. For such system one can show that the populations in considered states behave like:

$$\begin{aligned}
\rho_{|B\rangle}(t) &= A_{|B\rangle}e^{-r_0 t}\left[1 + B_{|B\rangle}e^{-r_1 t}\cos\left(\omega_{|B\rangle}t + \delta_{|B\rangle}\right)\right] \\
\rho_{|E\rangle}(t) &= A_{|E\rangle}e^{-r_0 t}\left[1 - B_{|E\rangle}e^{-r_1 t}\cos\left(\omega_{|E\rangle}t + \delta_{|E\rangle}\right)\right] \\
\rho_{|D\rangle}(t) &= 1 - A_{|D\rangle}(t)e^{-r_0 t}\left[1 - B_{|D\rangle}e^{-r_1 t}\cos\left(\omega_{|D\rangle}t + \delta_{|D\rangle}\right)\right],
\end{aligned}$$

where all parameters $A_i, B_i, r_0, r_1, \omega_i, \delta_i$ are functions of Γ, Ω and α assuming that we are on resonance. In such situation, all of these parameters are also directly functions of roots of a 3rd degree polynomial $P(x)$:

$$P(x) = x^3 + \frac{3\Gamma}{2}x^2 + \frac{1}{2}\left(2\Omega^2 + \Gamma^2\right)x + \frac{1}{2}\alpha\Omega^2\Gamma = 0.$$

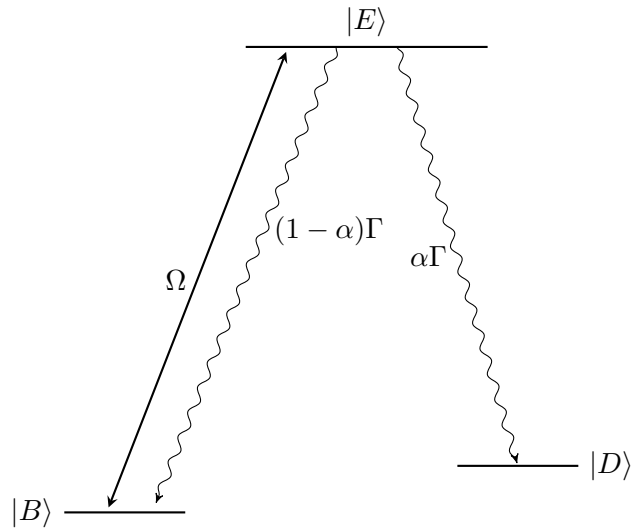

Figure 7.2.2: Diagram of a three-level system in Λ configuration with explicit dark and bright states. Decay to the dark state occurs with rate $\alpha\Gamma$.

We can see that the population in the bright state decays within an exponential envelope - any oscillations that appear due to the existence of the cosine term, and that become visible when $\Omega \gg \Gamma$, have exponentially decaying amplitude. We can then use the r_0 rate to determine time t_0 it takes the initial population to drop to $1/e$ of its initial value:

$$t_{1/e} = \frac{1}{r_0} \xrightarrow{\Omega \gg \Gamma} \frac{2}{\alpha\Gamma} = \frac{2\tau}{\alpha}, \tag{7.2.1}$$

where τ is excited state's lifetime.

Similarly, we can look at the total number of photons scattered in the process per molecule in the initial state (1 in this toy model). We can define it using the excited state population function:

$$n_\gamma(T) = \frac{1}{\rho_{|B\rangle}(t=0)} \int_0^T \Gamma \rho_{|E\rangle}(t) dt = \Gamma \int_0^T \rho_{|E\rangle}(t) dt.$$

As it happens, for $\Omega \gg \Gamma$:

$$n_\gamma(T) \xrightarrow{\Omega \gg \Gamma} \frac{1}{\alpha} - \frac{e^{-\alpha \Gamma T/2}}{\alpha}, \tag{7.2.2}$$

which, as expected, for sufficient long interaction time goes to $1/\alpha$. This long interaction time limit holds for any Rabi rate Ω and is consistent with a result obtained from a discrete model of optical pumping in system described here, where every time system gets into the excited state, it has α probability to decay into the dark state and $1-\alpha$ probability to decay back into the bright state. Such a process, where we can treat decay into the dark state as "success" is described by a geometric distribution, which tells us that the expected number of decays to obtain a "success" event is simply $1/\alpha$, which is also the number of scattered photons.

The above can also be easily understood if we simply consider the excited state decaying with constant rate R. For large Rabi rates we can simply model the process as a typical first-order decay. Percentage of population that underwent the decay until time t under this model is simply $1-\exp(-Rt)$, and because for every such decay n_γ photons is scattered, the number of photons scattered until time t is $n_\gamma(1-\exp(-Rt))$. For $n_\gamma = 1/\alpha$ we obtain the result shown in Eq. (7.2.2) with $R = \alpha\Gamma/2$.

From Eq. (7.2.2) we can also obtain the characteristic time $t_{1/e}$ after which we will have already scattered $(1-1/e)/\alpha$ photons. This will lead to the same result as in Eq. (7.2.1). In the real TlF system in our P2F1 rotational cooling transition $\alpha \approx 0.484$ and $\tau \approx 99$ ns, which gives us $t_{1/e} = 409.1$ ns. In case of polarization switching, this should be interpreted as the pulse time at every polarization. Hence, switching frequency should be $f_{\text{sw}} = 1/2t_{1/e} \approx 1.22$ MHz. If we used pure states instead, we would obtain $f_{\text{sw}} \approx 1.67$ MHz. True experimental optimal value can be expected to be somewhere around value estimated here. One could also argue that it might be even more beneficial to not wait for population to drop to $1/e$ of its initial value, but instead look at its half-life. Then, $t_{1/2} = t_{1/e} \ln 2 \approx 283$ ns and $f_{\text{sw}} \approx 1.76$ MHz. In numerical simulations we decided to use switching frequency of 1.67 MHz corresponding to 300 ns pulse times.

7.3 Selective Hyperfine State Coupling in $J = 0^+$

Before we move to the actual models we eventually considered for rotational cooling, we will quickly explore a seemingly good idea that in our particular molecular level structure cannot efficiently work. In principle, we could try to selectively move population from the $|J = 0, F = 1\rangle$ state leaving population in $|J = 0, F = 0\rangle$ untouched (effectively the latter would be a dark state). This could be done by a microwave coupling to $J = 1$ rotational manifold. However, given the very small hyperfine splittings in the ground electronic states, this process might be challenging to realize. Diagram in Fig. 7.3.1 depicts the system that we considered.

We designed the system in such a way that only relevant hyperfine states are included and other states are represented as one level. Zeeman sublevels were not included, so there is also no polarization dependence in the system. We decided to assume the following couplings: $|J = 2\rangle$ to $\left|\widetilde{J}' = 1\right\rangle$ via laser Ω_L representing the P2F1 rotational cooling transition; $|J = 1, F = 1, 2\rangle$ to $|J = 2\rangle$ via microwaves Ω_{μ_2}, which in real system not only remixes dark states in $J = 2$, but also brings population from $J = 1$ to $J = 2$; $|J = 0, F = 0\rangle$ to $|J = 1, F_1 = 3/2, F = 1\rangle$ via microwaves Ω_{μ_1} ($F = 0$ to $F = 2$ dipole transition is forbidden) and $|J = 0, F = 1\rangle$ to both $|J = 1, F_1 = 3/2, F = 1, 2\rangle$ via the same microwaves. The last transition is the one we investigated. Splitting the $J = 0$ and $J = 1$ rotational states into to two hyperfine states allowed us to see how selective this transition can be, and the states we chose represent the best-case scenario due to one transition being forbidden. Optical pumping from $J = 2$ and moving population from $J = 1$ to $J = 2$ in this system was not a cause of any unforeseen problems.

Couplings are determined only by the respective Rabi rates related to driving field strengths. No additional parameters were added, e.g. coupling between states $|J = 1, F = 1, 2\rangle$ and $|J = 2\rangle$ is the same and is equal to $\Omega_{\mu_2}/2$. Laser was assumed to be always on, while both microwaves are never on simultaneously. The change occurs after t_p time has elapsed. This allowed us to observe more clearly how populations in different states are affected by the light couplings. Finally, decays from the excited state go to the $J = 2$ rotational state with rate $\Gamma/2$ and to states $F = 0, 1$ in $J = 0$ with rates $\Gamma/4$, where $\Gamma \approx 2\pi \times 1.6$ MHz. These branching ratios are *not* the real ones and were chosen not to decay preferentially into any of the states.

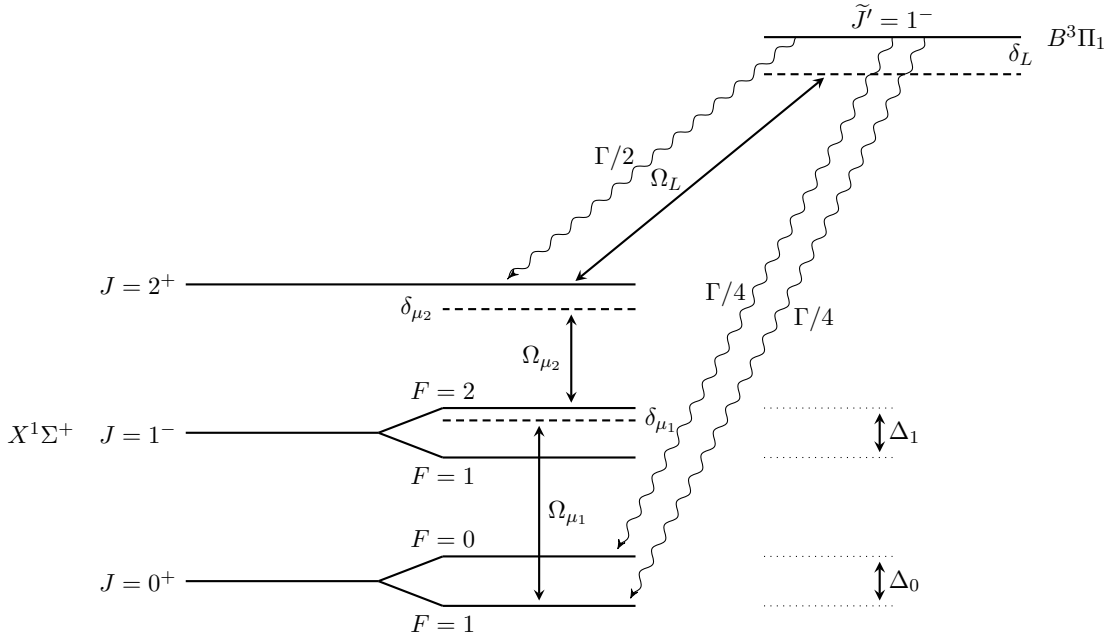

Figure 7.3.1: Simplified system of thallium fluoride designed to investigate efficiency of selective coupling to specific hyperfine levels.

In such a system the hamiltonian after eliminating its time dependence with a unitary transformation (and assuming real Rabi rates) takes form:

$$H = \begin{array}{c} \begin{array}{cccccc} |J=0,F=1\rangle & |J=0,F=0\rangle & |J=1,F=1\rangle & |J=1,F=2\rangle & |J=2\rangle & |\widetilde{J}'=1\rangle \end{array} \\ \begin{pmatrix} 0 & 0 & -\frac{\Omega_{\mu_1}}{2} & -\frac{\Omega_{\mu_1}}{2} & 0 & 0 \\ 0 & \Delta_0 & -\frac{\Omega_{\mu_1}}{2} & 0 & 0 & 0 \\ -\frac{\Omega_{\mu_1}}{2} & -\frac{\Omega_{\mu_1}}{2} & \delta_{\mu_1}-\Delta_1 & 0 & -\frac{\Omega_{\mu_2}}{2} & 0 \\ -\frac{\Omega_{\mu_1}}{2} & 0 & 0 & \delta_{\mu_1} & -\frac{\Omega_{\mu_2}}{2} & 0 \\ 0 & 0 & -\frac{\Omega_{\mu_2}}{2} & -\frac{\Omega_{\mu_2}}{2} & \delta_{\mu_1}+\delta_{\mu_2} & -\frac{\Omega_L}{2} \\ 0 & 0 & 0 & 0 & -\frac{\Omega_L}{2} & \delta_L+\delta_{\mu_1}+\delta_{\mu_2} \end{pmatrix} \end{array}.$$

For simplicity, we also assumed $\delta_{\mu_2} = \delta_L = 0$. The goal of this toy model was to find such combination of Rabi rates and detuning δ_{μ_1} for given splittings Δ_0 and Δ_1 that in $t \approx 100\ \mu s$ we obtain maximal population in the $|J=0,F=0\rangle$ state. In principle, we could expect that the most sensible solution involves having the microwave transition from $J = 0$ on resonance with the $|J=0,F=1\rangle \leftrightarrow |J=1,F=2\rangle$ transition, so that the molecules in the $|J=0,F=0\rangle$ are not strongly affected (they would be detuned by $\Delta_0 + \Delta_1$ for the resonance). At the same time we

would need $\Omega_{\mu_1} < \Delta_0 + \Delta_1$ to avoid power broadening, and Ω_L and Ω_{μ_2} to be rather larger (on the order of Γ).

To get a sense of what would be the best pulse time t_p, we can think of a situation when both ground states $|J = 0, F = 0, 1\rangle$ are coupled separately to an excited state. Then, over a course of one pulse we would want to transfer all the population away from $|J = 0, F = 1\rangle$, which corresponds to a $(2n + 1)\pi$ pulse, and have the population in state $|J = 0, F = 0\rangle$ to go back from the excited state, corresponding to a $2k\pi$ pulse. Then, we get following conditions:

$$\Omega_{\mu_1} t_p = (2n + 1)\pi$$
$$\sqrt{\Omega_{\mu_1}^2 + (\Delta_0 + \Delta_1)^2}\, t_p = 2k\pi,$$

for $k, n \in \mathbb{N}$, where $\Delta_0 + \Delta_1$ is the effective detuning from resonance for one of the transitions ($\delta_{\mu_1} = 0$ in such case) and should be provided in angular frequency units. Then:

$$t_p = \frac{\pi}{\Delta_0 + \Delta_1} \sqrt{4k^2 - (2n + 1)^2}$$

$$\Omega_{\mu_1} = (\Delta_0 + \Delta_1) \frac{2n + 1}{\sqrt{4k^2 - (2n + 1)^2}}.$$

Ideally, we would want the shortest pulse time for given detuning, which one can find for $n = 0$ and $k = 1$ (so a π and a 2π pulse). However, for such a choice of n and k the obtained Rabi rate affects the $|J = 0, F = 0\rangle$ quite strongly. Hence, we tried using $n = 0$ and $k = 2$ instead in order to minimize that effect. We should also note that this is of course an approximation that would require the $|J = 0, F = 1\rangle$ state to not "talk" at all to the $|J = 1, F = 1\rangle$ state, which is simply not true. However, the mentioned coupling is weaker due to effective detuning of Δ_1, which causes the population transfer to be suppressed.

To test if the idea can in principle work in our system, we considerws splittings that are 10 times bigger than in the real molecule, namely (in angular frequency units) $\Delta_0 = 2\pi \times 133$ kHz and $\Delta_1 = 2\pi \times 145$ kHz. For such splittings, $n = 0$ and $k = 2$ we calculated $t_p \approx 6.96$ μs and $\Omega_{\mu_1} = 2\pi \times 72$ kHz. We also tried to compare results obtained for these calculated parameters with numerically found optimal solution with the identical pulse time and number of pulses. Optimization yielded microwave Rabi rate $\Omega_{\mu_1} = 2\pi \times 57$ kHz, quite close to the estimated one. We also used $\Omega_L = \Omega_{\mu_2} = \Gamma$ and $\delta_{\mu_2} = \delta_L = 0$ for which optical pumping from $J = 1$ and $J = 2$ was efficient enough given the

pulse time. Fig. 7.3.2 depicts evolution of population in states $|J=0,F=0\rangle$ and $|J=0,F=1\rangle$ for the optimal set of parameters.

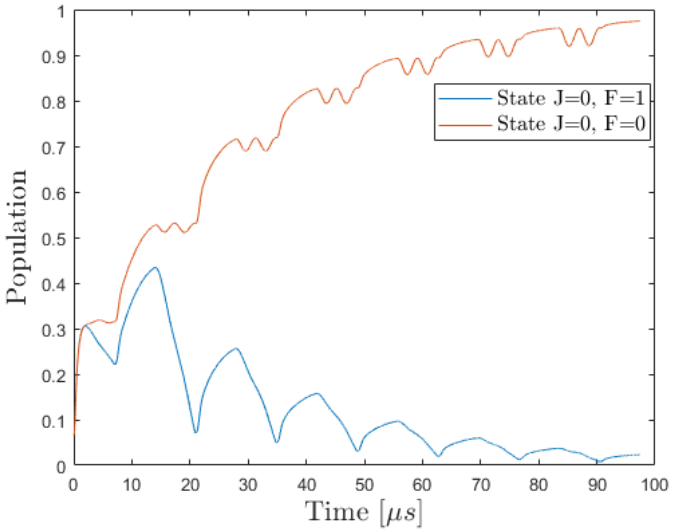

Figure 7.3.2: Evolution of states $|J=0,F=0\rangle$ and $|J=0,F=1\rangle$ for TlF hyperfine splittings order of magnitude larger than in the real system. Shown solution was obtained for 14 pulses of $t_p \approx 6.96$ μs length, $\Omega_L = 2\pi \times 1.6$ MHz, $\Omega_{\mu_1} = 2\pi \times 57.3$ kHz, $\Omega_{\mu_2} = 2\pi \times 1.6$ MHz and $\delta_{\mu_1} = \delta_{\mu_2} = \delta_L = 0$.

We can clearly see that for obtained parameters and chosen interaction time of 100 μs we obtain more population in the $|J=0,F=0\rangle$ state. Indeed, within one pulse time population in $|J=0,F=1\rangle$ is slowly removed in a π-like transition, while population in $|J=0,F=0\rangle$ state moves back and forth eventually stopping at local maximum of oscillations at the end of the pulse (here, 2 full oscillation occurred, which we can call a 4π-like transition). This simple model shows us that in 100 μs we can obtain approximately 97% of the molecules in the ground rotational state and the $F=0$ hyperfine state.

The question is if the same approach will work in the real TlF system. The procedure itself should work, after all in reality simply the hyperfine splittings are smaller. However, $t_p \sim (\Delta_0 + \Delta_1)$ and $\Omega_{\mu_1} \sim (\Delta_0 + \Delta_1)^{-1}$, which means that in the real system the Rabi rate would have to be much smaller if it is to just barely couple to the $F=0$ state, and that the pulse time would have to be order of magnitude higher. Fig. 7.3.3a shows the solution for $\Omega_{\mu_1} = 2\pi \times 5.73$ kHz and $t_p \approx 69.6$ μs and 14 pulses clearly proving that the method works just as well, although now the total interaction time would have to be increased by the same order of magnitude, which is not possible

experimentally. Even changing the duty cycle of microwave pulses (the optical pumping process here is much faster than the Rabi oscillations), which would allow us to cut the total interaction time almost in half, would not be enough.

Of course, we could try larger Rabi rates giving larger number of oscillations per pulse (larger k and n), which should provide a similar result. Fig. 7.3.3b shows results for interaction time of 100 μs, 14 pulses and $\Omega_{\mu_1} = 2\pi \times 668$ kHz found through numerical optimization. Indeed, correctly matched oscillations still allow for selective population removal. However, these oscillations have much larger amplitude than before and, because of their frequency, their result strongly depends on the exact pulse time. We can imagine that in realistic experimental setting where we interact with an imperfect molecular beam, such precision and control is not achievable.

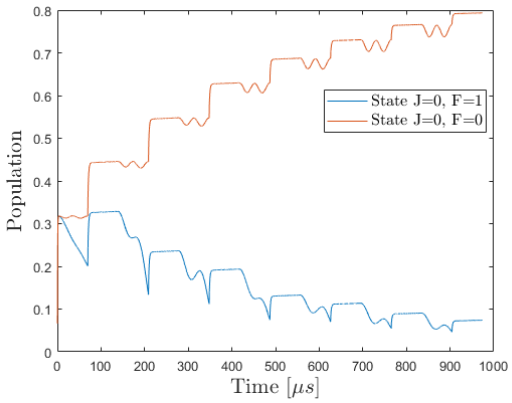

(a) Solution for estimated $\Omega_{\mu_1} = 2\pi \times 5.73$ kHz and 14 pulses with duration of $t_p \approx 69.6$ μs resulting in ~ 1 ms total interaction time.

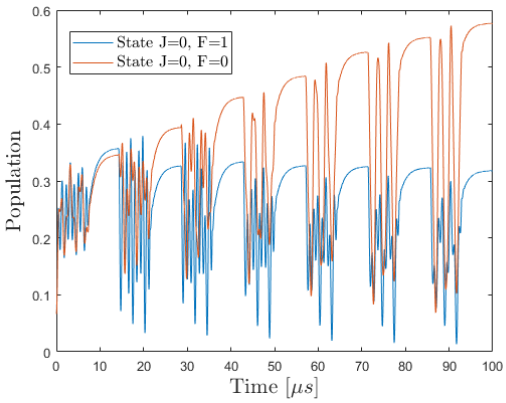

(b) Solution for $\Omega_{\mu_1} = 2\pi \times 668$ kHz obtained through numerical optimization and 14 pulses with duration of $t_p \approx 7.14$ μs resulting in ~ 100 μs total interaction time.

Figure 7.3.3: Evolution of states $|J = 0, F = 0\rangle$ and $|J = 0, F = 1\rangle$ for real TlF hyperfine splittings. Both solutions used $\Omega_L = 2\pi \times 1.6$ MHz, $\Omega_{\mu_2} = 2\pi \times 1.6$ MHz and $\delta_{\mu_1} = \delta_{\mu_2} = \delta_L = 0$.

7.4 Investigated Schemes

Having understood how quickly a process of removing population from the bright states occurs and having realized that a tempting method of selective population removal would not work for

states of our choice in TlF molecule, we investigate three different experimentally feasible schemes by performing numerical simulations on the full quantum system. The first one is a benchmark scheme where we simply use P2F1 rotational cooling transition and two additional microwaves to optically pump the desired state. In this scheme it is the rotational branching ratios that do the work of selectively choosing our final state. The next two schemes use an additional laser beam that allows us to create one specific dark state of our choice in our TlF system. Naturally, the population accumulates in that dark state and rotational cooling process becomes very efficient. The second scheme shows a configuration where the specific dark state superposition depends on polarization of the auxiliary laser, while the final scheme is thought of in such a way, that the dark state is polarization-independent. To compare the schemes, we included only the $J = 1 \leftrightarrow J = 2$ microwave coupling, which simplifies the calculations. The chosen scheme was then also evaluated with the second set of microwaves included.

7.4.1 Benchmark Scheme

We begin with a scheme that is based solely on the P2F1 transition and is depicted in Fig. 7.4.1. We call this a benchmark scheme, because two other methods that are investigated are built on top of this one. Here, the chosen excited state preferentially decays into the $|J = 0, F = 0\rangle$ hyperfine state, and for this reason we treat it as our final desired state in this scheme. Population from the $J = 2$ rotational manifold is then optically pumped into it. In order to remove the population from other rotational states, we couple them via microwaves to the $J = 2$ manifold.

Dark states, just as was mentioned previously, being an ever-present problem, decrease efficiency of this process as well. To alleviate that we switch laser's polarization between two orthogonal linear polarizations - one defining the quantization axis $\hat{\mathbf{z}}$ and one along the $\hat{\mathbf{x}}$ direction. The remaining dark states in $J = 2$ are then remixed by the microwave coupling, which, as we saw in the previous chapter, is quite efficient at this job. Additionally, the microwaves are here also assumed to have their polarization switched between two orthogonal linear polarizations following the geometry first shown in Fig. 6.2.1. Rabi rates are then constructed using the equations provided in previous chapter such as Eq. (6.2.2). Microwave polarization switching is offset in phase from the laser polarization switching by $\pi/2$, and both are switched with frequency of ~ 1.67 MHz (so closer to the excited state's decay half-time described at the beginning of this chapter).

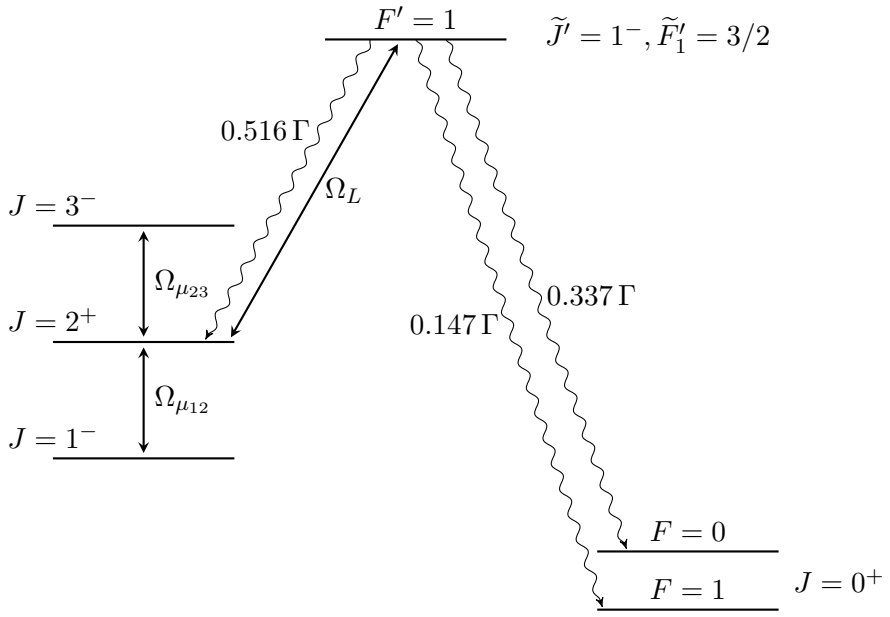

Figure 7.4.1: Benchmark rotational cooling scheme based on P2F1 transition and utilizing uneven rotational branching ratios to accumulate population in the $|J = 0, F_1 = 1/2, F = 0\rangle$ state. Populations in $J = 1^-$ and $J = 3^-$ rotational manifolds are coupled to $J = 2^+$ state via microwaves.

In this scheme we used a 50 μs interaction time, the base Rabi rate given by Eq. (6.2.1) for both the laser and microwaves was assumed to be around $5.8\,\Gamma$, which for the laser corresponds to 50 mW of power uniformly distributed in a beam of 3 mm diameter. We should note that such parameters are what we expect to achieve experimentally and obtaining such interaction time with such narrow beam can be done using multipassing. In case of microwaves such Rabi rate corresponds to ~ 125 mW of power in a beam of ~ 2.5 cm diameter. Laser is assumed to be on resonance with the $|J = 2, F_1 = 3/2, F = 2\rangle$ manifold, although small hyperfine splittings ($\Delta \ll \Omega \approx \Gamma$) are not "visible" from laser's point of view - the power broadening will be much higher than the splittings. The microwaves were on resonance with the $|J = 1, F = 1/2, F = 0\rangle \leftrightarrow |J = 2, F_1 = 3/2, F = 1\rangle$ transition, but again it is pretty irrelevant - not only the power broadening is higher than any splitting, the energy differences between hyperfine levels in $J = 1$ and $J = 2$ manifold are very similar. They were also assumed to propagate an angle of $45°$ with respect to the quantization axis. When $J = 2 \leftrightarrow J = 3$ microwaves were used, they propagated at an angle of $-45°$.

In figure 7.4.2 we present graphs showing time evolution of populations in different states that were used in the numerical simulation. We notice that, as expected, the population accumulates

in the $F = 0$ hyperfine state of the ground rotational state. It reaches value of approximately 0.63, meaning that 63% of all the molecules that started in $J = 0 - 2$ rotational states ends up in that final state. Simultaneously, we obtain about 99% of molecules in the ground rotational state. The accumulation happens quite quickly for given parameters and then after about 30 μs reaches a plateau. The population does not linger in any dark state subspace, although we can observe that population in $J = 2$ seems to be removed the slowest. However, it is probably not the case - the rate with which the removal occurs is the same, but given the higher initial population more time is required to complete the process. If it is the case, it is the population in the $F = 3$ hyperfine level, which is not directly coupled to the excited state, that takes the longest to be optically pumped as it has to first be transferred to the $J = 1$ rotational state, where it only couples to the $F = 2$ manifold. We expect that adding $J = 2 \leftrightarrow J = 3$ microwaves might quicken this process.

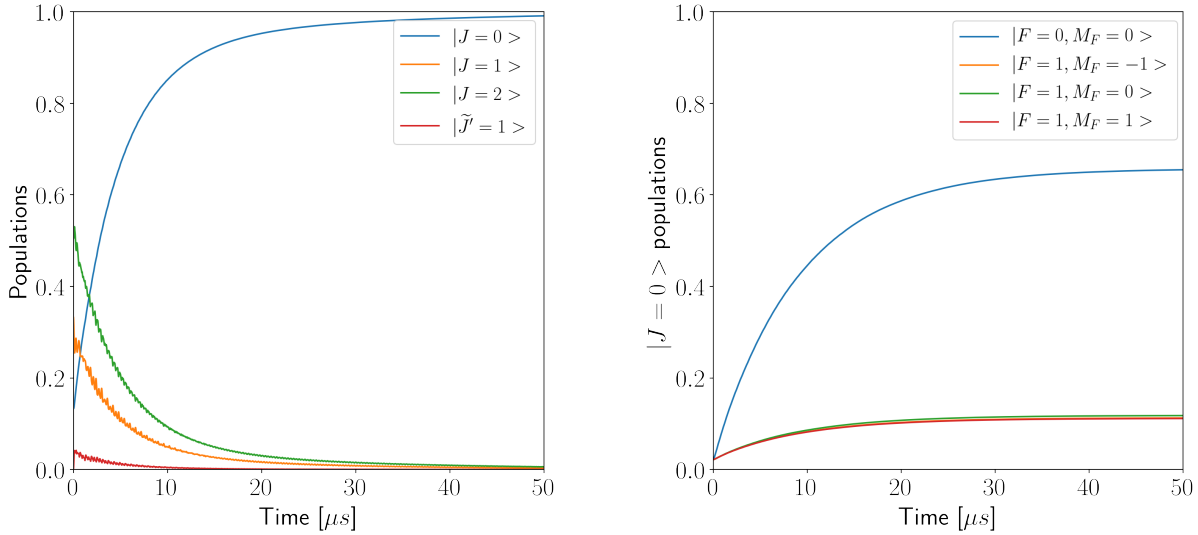

(a) Time evolution of populations in $J = 0 - 2$ rotational manifolds in the $X^1\Sigma^+$ ground electronic state and $\left|\widetilde{J}' = 1^-, \widetilde{F}_1' = 3/2, F' = 1\right\rangle$ hyperfine state in the $B^3\Pi_1$ excited electronic state.

(b) Time evolution of populations in the $J = 0$ rotational manifold in the $X^1\Sigma^+$ ground electronic state.

Figure 7.4.2: Time evolution of states in the benchmark rotational cooling scheme. The population clearly accumulates in the $|J = 0, F_1 = 1/2, F = 0\rangle$ state and reaches population of ~ 0.63 after 50 μs interaction time.

7.4.2 Polarization-dependent Engineered Dark State

As was shown in the previous section, selective coupling or selective creation of a dark state in the $J = 0$ rotational ground state is not feasible using microwaves. Instead, we can think of solutions utilizing an additional laser. With its help we can engineer a dark state and make it our final state into which we accumulate population. The first such idea is depicted in Fig. 7.4.3 showing couplings in this scheme, and it includes an addition of an auxiliary laser inducing a R0F1 transition ($J \leftrightarrow J' + 1$ transition for $J = 0$ state and $F = 1$ hyperfine excited state).

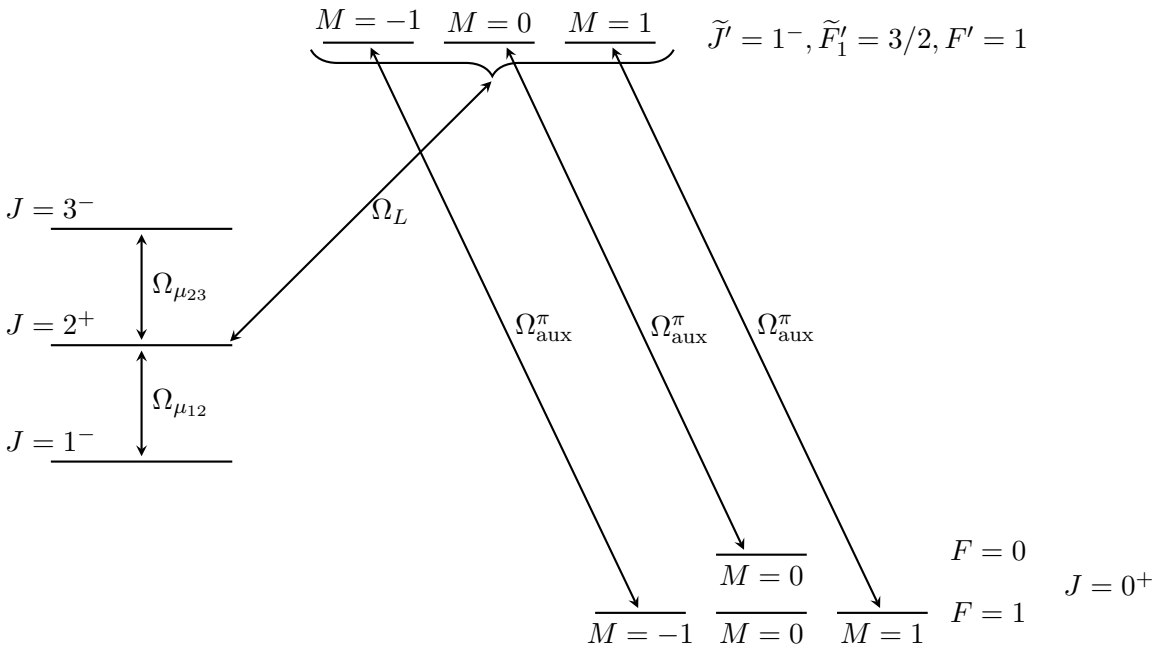

Figure 7.4.3: Rotational cooling scheme based on the P2F1 transition accumulating population in the hyperfine Zeeman sublevel $|J = 0, F_1 = 1/2, F = 1, M_F = 0\rangle$ by making it a polarization-dependent dark state with the help of second π-polarized R0F1 laser transition. Populations in $J = 1^-$ and $J = 3^-$ rotational manifolds are coupled to $J = 2^+$ state via microwaves. For clarity, decays paths were not shown.

By coupling the $J = 0$ manifold to the same hyperfine state we are using for the main rotational cooling transition, we are creating a single dark state. This dark state depends on polarization of the additional laser. In the simulations we assumed a π-polarized light which makes $|J = 0, F = 1, M_F = 0\rangle$ state dark. However, for other polarizations it would be different, e.g. for light polarized along the $\hat{\mathbf{x}}$ direction we would obtain a dark state that is a superposition of two stretched states, namely $(|J = 0, F = 1, M_F = -1\rangle - |J = 0, F = 1, M_F = 1\rangle)/\sqrt{2}$. This dependence

of the final state on the auxiliary laser's polarization is the main drawback of this scheme.

It also seems that this accumulation process is slower than in the benchmark case, and so we used 100 μs interaction time instead of 50 μs like before. Rabi rates of the P2F1 transition laser and microwaves were identical as in the previously investigated scheme, and so were the switching frequencies and phases, and detunings. We did not include the $J = 3$ rotational state either and potential problems related to that and appearing in the benchmark scheme persisted. The auxiliary laser had a Rabi rate of $4\,\Gamma$, was on resonance with the $|J = 0, F = 1\rangle$ manifold and, just to emphasize, the it had a *constant* π-polarization (along the chosen quantization axis $\hat{\mathbf{z}}$).

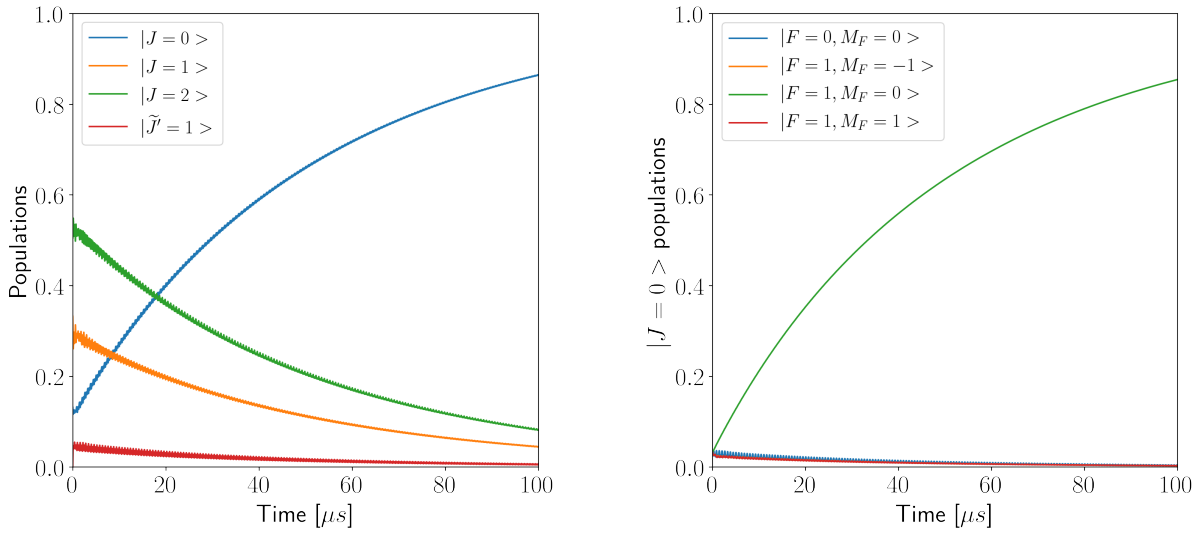

(a) Time evolution of populations in $J = 0 - 2$ rotational manifolds in the $X^1\Sigma^+$ ground electronic state and $\left|\widetilde{J}' = 1^-, \widetilde{F}_1' = 3/2, F' = 1\right\rangle$ hyperfine state in the $B^3\Pi_1$ excited electronic state.

(b) Time evolution of populations in the $J = 0$ rotational manifold in the $X^1\Sigma^+$ ground electronic state.

Figure 7.4.4: Time evolution of states in the benchmark rotational cooling scheme with an auxiliary laser creating a polarization-dependent dark state by coupling $J = 0^+$ ground rotational state to the $F' = 1$ hyperfine state (R0F1 transition). The population clearly accumulates in one final state $|J = 0, F = 1, M_F = 0\rangle$ and reaches population of ~ 0.63 after 50 μs of interaction time and ~ 0.85 after 100 μs.

In Fig. 7.4.4 we show results of the numerical calculation. As expected, the chosen engineered dark state is populated correctly, although, as mentioned, this process is quite slow. After the interaction time of 100 μs used in this simulation, we obtain as much as 85% of molecules in

the final state and almost none in the other Zeeman sublevels of the ground rotational manifold. However, if we consider only the first 50 μs we observe no gain comparing to the benchmark case. The slowness of this process can be attributed to the fact that we use the same excited state manifold for both main and auxiliary transitions.

7.4.3 Polarization-independent Engineered Dark State

A natural correction to the previous scheme would be to instead engineer a polarization-independent dark state and preferably also create it by adding a coupling to a different hyperfine state. We can achieve this by using a R0F2 transition instead of R0F1. Fig. 7.4.5 depicts this scheme and emphasizes the large hyperfine splitting in the excited electronic state.

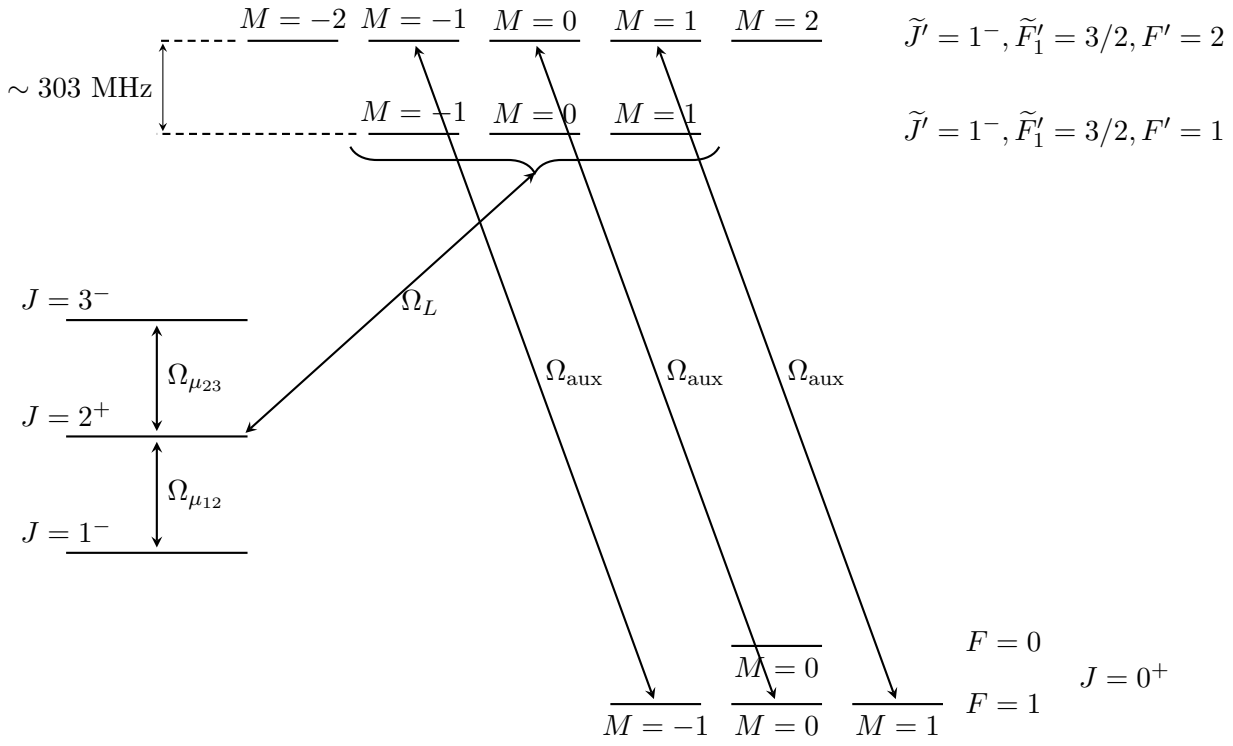

Figure 7.4.5: Rotational cooling scheme based on the P2F1 laser transition accumulating population in the $|J=0, F=0\rangle$ state by making it a polarization-independent dark state with the help of the second, R0F2 laser transition (π polarization shown for simplicity). Populations in $J=1^-$ and $J=3^-$ rotational manifolds are coupled to the $J=2^+$ state via microwaves. While for clarity the decays paths were not shown, we should note that the hyperfine state $F'=2$ in the excited electronic state decays into $|J=0, F=1\rangle$ state and all hyperfine states in the $J=2^+$ rotational manifold.

Because the $F' = 2$ hyperfine manifold is approximately 300 MHz "away" from the the $F' = 1$ state we are using for rotational cooling, any laser with Rabi rates on the order of $\sim \Gamma$ will selectively couple to it without interfering with other transitions. Coupling the $J = 0$ rotational state to the $F' = 2$ hyperfine state with an auxiliary laser brings with itself a huge advantage. Namely, the $F = 0 \leftrightarrow F' = 2$ transition is (dipole) forbidden. Therefore, such coupling will only interact with the $|J = 0, F = 1\rangle$ state and selectively remove that population regardless of laser's polarization. The excited $F' = 2$ state has similar decay paths and rotational branching ratios as the $F' = 1$ state we are using for the main rotational cooling transition despite somewhat stronger hyperfine mixing (see table B.3 for details), and so we still expect to be rotationally closed.

Here, we used interaction time of 50 μs like in the benchmark case. Analogically, the parameters of the P2F1 and microwave transitions, and lack of the $J = 3$ state in the numerical simulations were identical with the benchmark scheme. The auxiliary laser had a Rabi rate of $1\,\Gamma$, was on resonance with the $|J = 0, F = 1\rangle$ manifold and, for simplicity, was assumed to be linearly polarized along the quantization axis.

Fig. 7.4.6 shows time evolution of populations in different states. Population accumulates almost exclusively in the $|J = 0, F = 0\rangle$ state with rate similar to the benchmark case. After 50 μs we obtain about 98% of molecules in that state and almost none in the other sublevels of the ground rotational manifold.

7.4.4 Summary

In table 7.4.1 we present comparison of three schemes we investigated. Using simply the benchmark scheme based on preferential decay to one of the sublevels already leads, for parameters used, to a 7-fold increase in the population in the ground rotational state and a 19-fold increase in the population in the $|J = 0, F_1 = 1/2, F = 0, M_F = 0\rangle$ state. For a beam of molecules with rotational temperature of about 7 K that means that after the rotational cooling process, about 21% of all the molecules will be in that state.

The scheme with an auxiliary R0F1 transition that creates a polarization-dependent dark state leads to very similar results for interaction time of 50 μs. However, whereas in the benchmark scheme population transfer already plateaus after this interaction time, here the population keeps on increasing leaving the possibility of much higher cooling efficiency for longer interaction times. The

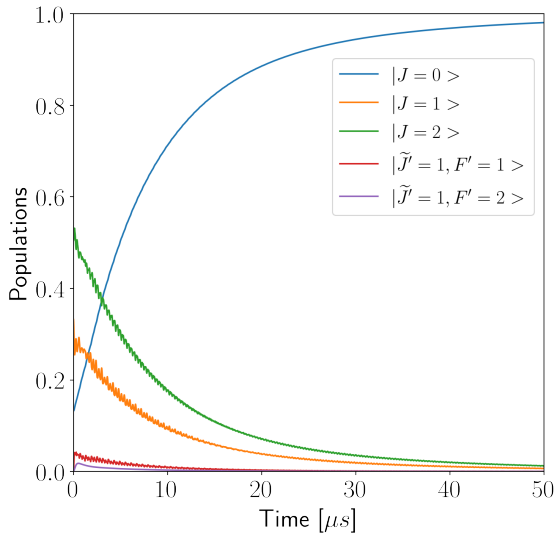

(a) Time evolution of populations in $J = 0 - 2$ rotational manifolds in the $X^1\Sigma^+$ ground electronic state and $\left|\widetilde{J}' = 1^-, \widetilde{F}_1' = 3/2, F' = 1, 2\right\rangle$ hyperfine states in the $B^3\Pi_1$ excited electronic state.

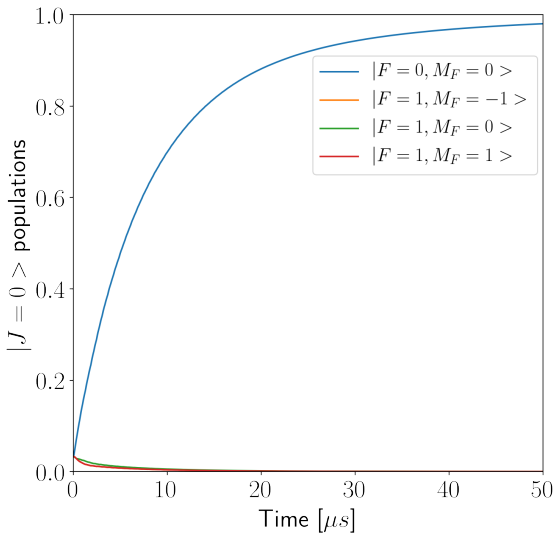

(b) Time evolution of populations in the $J = 0$ rotational manifold in the $X^1\Sigma^+$ ground electronic state.

Figure 7.4.6: Time evolution of states in the benchmark rotational cooling scheme with an auxiliary laser creating a polarization-independent dark state by coupling $J = 0^+$ ground rotational state to the $F' = 2$ hyperfine state (R0F2 transition). The population clearly accumulates in the $|J = 0, F_1 = 1/2, F = 0\rangle$ state and reaches population of ~ 0.98 after 50 μs of interaction time.

main drawbacks of this scheme are final state's strong dependence on auxiliary laser's polarization and its slow rate of population transfer.

Auxiliary R0F2 transition fixes the problems encountered in the previous scheme. The final state is again $|J = 0, F_1 = 1/2, F = 0, M_F = 0\rangle$ and it does not depend on laser's polarization. The population transfer rate is much faster as well - 50 μs is more than enough to reach a plateau even for modest auxiliary laser's Rabi rates. While the population in the ground rotational state increases by a factor of ~ 7.4, so slightly smaller than in the benchmark scheme, the high selectivity leads to a ~ 29.5-fold increase in population in the final state. In the end we obtain about 33% of all molecules in the desired state.

Scheme	Auxiliary transition	Final state $\|f\rangle$	Parameters				$\rho_{\|J=0\rangle}(T)$	$\rho_{\|f\rangle}(T)$	$\frac{\rho_{\|J=0\rangle}(T)}{\rho_{\|J=0\rangle}(0)}$	$\frac{\rho_{\|f\rangle}(T)}{\rho_{\|f\rangle}(0)}$	% at 7 K
			$\Omega_{\text{aux}}[\Gamma]$	$\Omega_L[\Gamma]$	$\Omega_{\mu_{12}}[\Gamma]$	$\Omega_{\mu_{23}}[\Gamma]$					
Bench.	None	$\|F=0, M_F=0\rangle$	-	5.88	5.82	-	0.9910	0.6304	7.47	19.00	21.45
Pol-dep.	R0F1	$\|F=1, M_F=0\rangle$	4.00	5.88	5.82	-	0.6620	0.6348	4.99	19.13	21.60
Pol-ind.	R0F2	$\|F=0, M_F=0\rangle$	1.00	5.88	5.82	-	0.9806	0.9803	7.39	29.55	33.37
Bench. - full	None	$\|F=0, M_F=0\rangle$	-	5.88	5.82	5.82	0.9963	0.6547	11.53	30.32	34.19

Table 7.4.1: Comparison of three different rotational cooling schemes. All results are given after interaction time of $T = 50\ \mu s$. We assumed that the total initial population is equal to 1 and is distributed between three lowest rotational states. The rightmost column shows the population in the final state as percentage of *all* the molecules at 7 K, not only those beginning in the lowest rotational states used in the numerical simulation. The last row shows results for the benchmark scheme with $J = 3$ included, for which initial population in four lowest rotational states sums to 1. The final state is implied to be in the $|J = 0, F_1 = 1/2\rangle$ manifold.

Unequivocally, engineering a polarization-independent dark state leads to the best results. Using population in the final state as our metric, it is almost 50% better than the benchmark scheme. Unfortunately, this comes at a cost. It requires an additional UV laser which would add a lot of complexity and cost to our laser system. Possibility of adding an acousto-optic modulator to the rotational cooling laser system, even at its IR or green stage, is excluded - frequency difference between two lasers is ~ 40 GHz. Ultimately, we decided to use the simplest scheme present - the benchmark.

Having chosen the benchmark scheme as the final one, we performed numerical simulation with inclusion of the $J = 3$ rotational state and the $J = 2 \leftrightarrow J = 3$ microwave coupling. The bottom row in table 7.4.1 shows the parameters used and the results obtained after 50 μs of interaction. To avoid any problematic dark states in the $J = 3$ manifold (there potentially can be $28 - 20 = 8$ such states) these microwaves were assumed to switch between two orthogonal linear polarization at the same switching frequency as the laser and the other set of microwaves, while their switching phase was offset by $\pi/4$ from laser's (and therefore by $-\pi/4$ from the $J = 1 \leftrightarrow J = 2$ microwaves). Fig. 7.4.7 shows time evolution of relevant states, from which we can conclude that the behavior is

that, which we observed in the previous benchmark scheme. Finally, comparing numbers from the last column, we see that coupling $J = 3$ rotational state leads to an overall increase in the final state population of about 60% with respect to the benchmark scheme with $J = 0 - 2$ only.

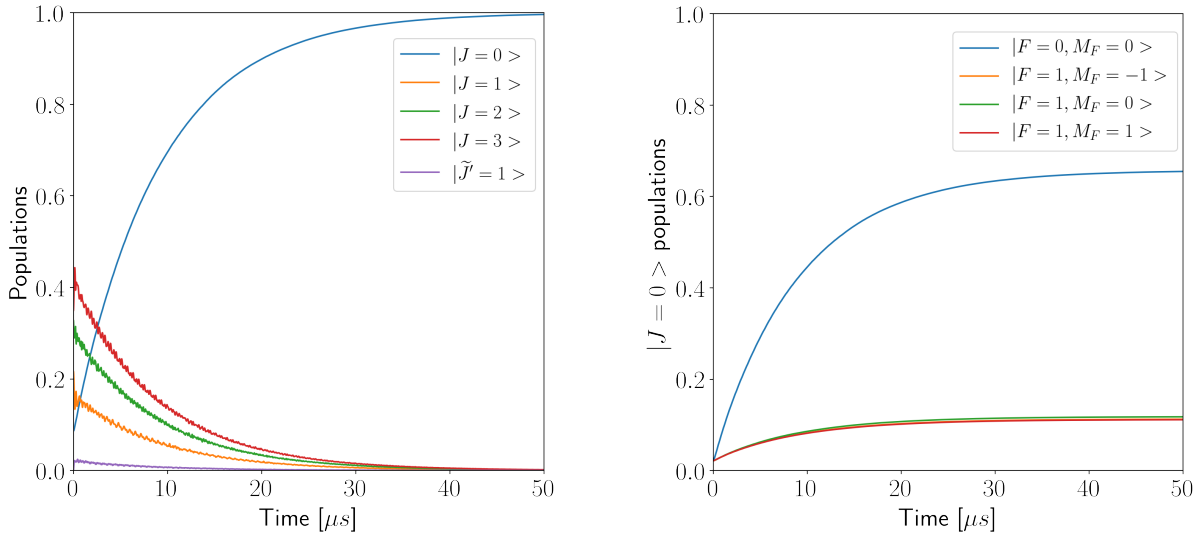

(a) Time evolution of populations in $J = 0 - 3$ rotational manifolds in the $X^1\Sigma^+$ ground electronic state and $\left|\widetilde{J}' = 1^-, \widetilde{F}_1' = 3/2, F' = 1\right\rangle$ hyperfine state in the $B^3\Pi_1$ excited electronic state.

(b) Time evolution of populations in the $J = 0$ rotational manifold in the $X^1\Sigma^+$ ground electronic state.

Figure 7.4.7: Time evolution of states in the benchmark rotational cooling scheme with coupled $J = 3^-$ manifold. The population accumulates in the $|J = 0, F_1 = 1/2, F = 0\rangle$ state and reaches population of ~ 0.65 after 50 μs of interaction time.

7.5 Effects of Doppler Broadening

All previously explored schemes assumed that the transverse velocity of interacting molecules is 0 and so that there is no Doppler shift in the UV laser's frequency. In a real-world setting this might play an important role - the process might work efficiently for only a narrow range of velocity classes. From beam characterization experiments we know that the transverse velocity spread is about $\sigma_{v_t} \approx 39$ m/s. Of course, most of the molecules with extreme velocities will never even reach the rotational cooling interaction region. However, we should consider all molecules that we expect

to collimate with the quadrupole lens and use in our experiment.

From the geometry of our setup and by assuming a point source we could expect that molecules with transverse velocities smaller than $|v_{t,\mathrm{lim}}| \approx 6.1\,\mathrm{m/s} \approx 14\,\Gamma/k$ (for wavenumber k related to the P2F1 transition frequency) will enter the quadrupole lens. To understand how this could affect our rotational cooling schemes, we first look at efficiency of the process for different velocity classes. We obtained population time evolutions for velocities $v \in [-14, 13, \ldots, 14]\,\Gamma/k$ (figure 7.5.1), which effectively cause a Doppler shift and change detuning of the laser transition yielding $\delta_L = -kv$. Otherwise, in every simulation we repeated the benchmark scheme with the exact same parameters. Using the velocity distributions we created a weighted average of resulting time evolutions, from which we were able to obtain average efficiency of the rotational cooling process in that investigated section of velocity classes. We should also note that we *did not* include the longitudinal velocity spread, which would additionally result in molecule-dependent interaction times. Finally, please note that this is the worst-case scenario - the true acceptance radius of the lens is smaller then its physical, geometric radius (Chapter 3). Realistically, we expect $|v_{t,\mathrm{lim}}| \approx 2 - 3$ m/s.

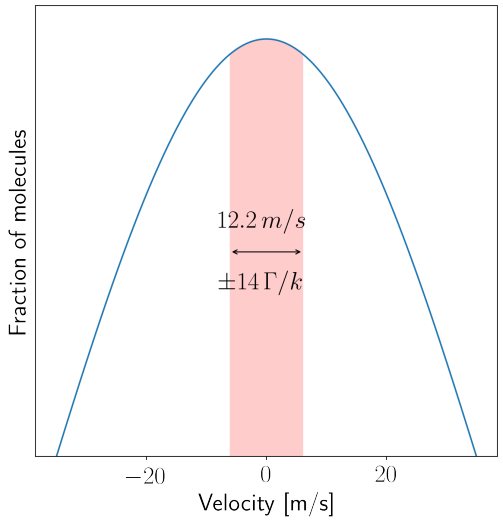

Figure 7.5.1: Part of the measured transverse velocity distribution with $\sigma = 39$ m/s. The shaded part corresponds to velocity range of ±6.1 m/s.

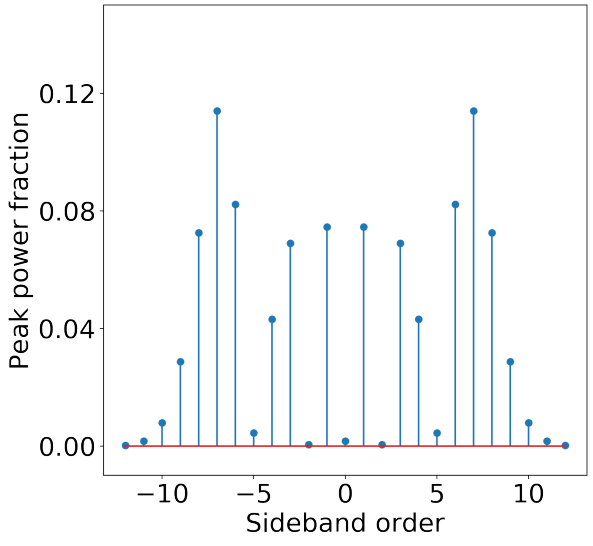

Figure 7.5.2: Power spectrum of sidebands obtained by phase modulation with depth $\beta = 8.5$ rad. In the simulation, the phase modulation frequency was $f_{\mathrm{mod}} = 1\,\gamma$.

Numerical simulations show that including a realistic transverse velocity distribution and suggested worse limits placed on the transverse velocities does decrease the average efficiency of the process quite substantially - by almost 50%. Despite the power broadening of the laser ($\sim 6\,\Gamma$), many of the molecules barely interact with it - they are too far from resonance. And because we are truncating a much wider distribution, the distribution of transverse velocities in the range considered is almost uniform, and so the percentage of molecules not interacting with the laser is quite substantial.

A possible solution to that problem is to distribute the total power into sidebands that would cover most, if not all, of the velocity classes. A natural choice is to consider a phase-modulating electro-optic modulator resonant at $\gamma \approx 1.6$ MHz creating sidebands spaced by γ (Γ in the angular frequency units). In Fig. 7.5.2 we present distribution of power fractions in different sidebands for modulation depth $\beta = 8.5$ rad, which should still be achievable by commercial resonant modulators. As can be seen, such modulation depth creates sidebands with non-zero power at $\pm 10\,\gamma$ and overall they should cover most of our $\pm 14\,\Gamma$ range of Doppler shifts. In table 7.5.1 comparing the results we observe that the efficiency of rotational cooling improves by 50% once phase modulation is included, although the average efficiency is still smaller than what is possible for a single velocity class.

Scheme	Velocity distribution	Phase modulation	$\rho_{\|J=0\rangle}(T)$	$\rho_{\|f\rangle}(T)$	$\frac{\rho_{\|J=0\rangle}(T)}{\rho_{\|J=0\rangle}(0)}$	$\frac{\rho_{\|f\rangle}(T)}{\rho_{\|f\rangle}(0)}$	% at $7\,K$
Benchmark	No	No	0.9910	0.6304	7.47	19.00	21.45
Benchmark	Yes	No	0.5866	0.3474	4.42	10.46	11.82
Benchmark	Yes	Yes	0.7994	0.4954	6.02	14.92	16.84

Table 7.5.1: Comparison of benchmark scheme results. The first row shows results obtained in the previous section, where no transverse velocity spread was included. The second row shows result averaged over the worst expected velocity spread - we observe almost a 50% drop in rotational cooling efficiency. Finally, results for the benchmark scheme with velocity distribution and laser phase modulation with depth $\beta = 8.5$ rad and $f_{\mathrm{mod}} = 1\,\gamma$ are included leading to increase in efficiency by a factor of 50%.

Chapter 8

The Laser System

8.1 System Overview

In thallium fluoride the main transition we needed to address is at an ultraviolet wavelength of approximately 271.7 nm. As it was shown, to scatter photons efficiently we will require a continuous-wave (CW) laser with powers up to 50 mW at the desired frequency. Unfortunately, we are only getting close to CW lasers operating in that regime [71, 72]. Therefore, our best option was to create a frequency quadrupling system. The fundamental wavelength of about 1087 nm is perfect from a technical stand point - stable and narrow-line sources are available, and so are the amplifiers. Frequency doubling stages can also be either obtained from commercial vendors or built following well-known techniques [73, 74, 75, 76].

To conduct the rotational cooling experiments, we built two such frequency quadrupling systems schematic of which is shown in Fig. 8.1.1. Both of them used NKT Photnics Koheras BASIK Y10 fiber lasers as the source. These lasers are tunable with a tuning range of about 800 GHz centered at 1086.78 nm, have narrow linewidths (< 20 kHz), low phase noise and allow for external frequency modulation within an 8 GHz range via the piezoelectric transducer. They are controlled by a USB connection to a computer with either the company-provided software or a home-built solution using provided SDK (software development kit). Their output is coupled to a polarization-maintaining (PM) fiber and was designed to be around 10 mW, although it decreased over time (currently, after 3 years of almost-everyday usage, it is ~ 7.5 mW).

Output of those so-called seed lasers is then coupled through Thorlabs ADAFC3 mating sleeve

to the input fiber of the NKT Photonics Koheras BOOSTIK Y80 Ytterbium-doped fiber amplifier. These amplifiers produce a stable < 2.5 W output and can be controlled either directly through the control panel on one of the amplifier's faces or via a Serial connection from a computer. Their output is coupled to a PM fiber terminated with a Thorlabs F220APC-1064 FC/APC fiber collimation package providing a Guassian beam of 2.4 mm diameter and divergence of 0.032°.

The infrared (IR) output of the the fiber amplifier has to be then split three ways: towards the frequency quadrupling system, the wavemeter and the frequency stabilization system, which we will describe later in this chapter. As shown in Fig. 8.1.1, the linearly polarized output is split using a standard Thorlabs PBS103 polarizing beam splitter cube. The remainder of about ~ 20 mW for a 2 W amplifier output, appearing due to an imperfect extinction ratio of the beam splitter, is directed towards a single-mode (SM) 90:10 Fiber Splitter (Thorlabs TN1064R2A1B). Low-power part of the fiber splitter is directed to the Agiltron LBSC-0160X1003 16-channel fiber switcher, which then is connected to the Bristol Instruments 671A wavemeter, while the high-power part is directed towards the frequency stabilization system.

After passing through the polarizing beam splitter (PBS), the beam is directed through multiple optical beam-shaping lenses, a Thorlabs WPH05M-1064 zero-order half-wave plate and a home-built electro-optical modulator (EOM) into the first second-harmonic generation cavity (details presented in the next section). Frequency-doubled light (wavelength of approximately 543.5 nm) leaves the cavity through a collimating plano-convex spherical lens with $f = 100$ mm. This beam is then coupled to a PM fiber bringing it to the commercial UV doubling stage built by Toptica, where UV light at ~ 271.7 nm is generated. The UV stage of the laser system is described in Chapter 9.

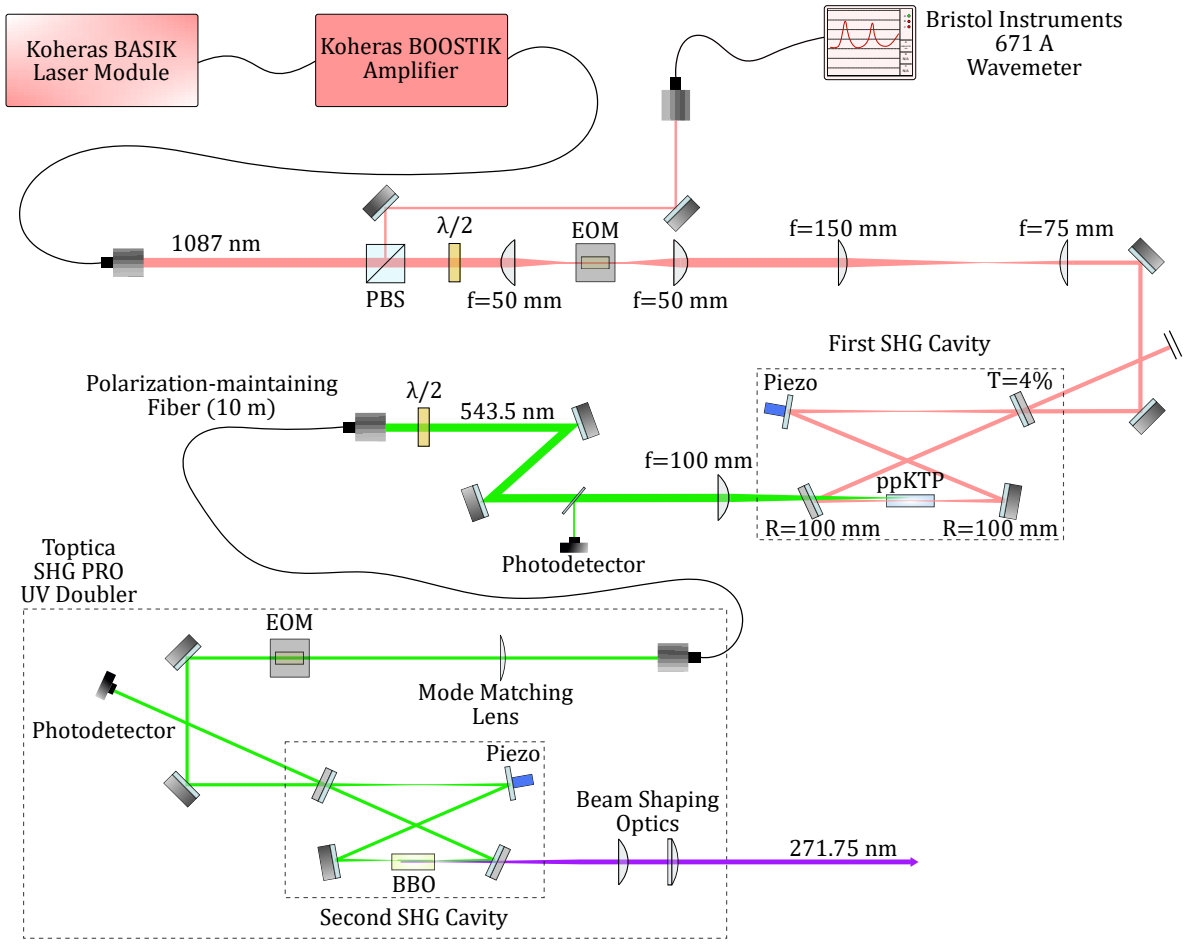

Figure 8.1.1: Schematic of the laser quadrupling system. Abbreviations used: PBS - polarizing beam splitter, $\lambda/2$ - half-wave plate, EOM - electro-optic modulator. ppKTP and BBO are the nonlinear crystals used for second harmonic generation (SHG).

8.2 Frequency Doubling

One of the most important parts of the laser system is the second-harmonic generation stage converting IR laser into laser at green wavelengths of about 543 nm. The frequency doubling process is a special case of sum-frequency generation and was first described and observed in the early sixties [77, 78]. It is by nature a nonlinear optical process that occurs in media with

no inversion symmetry, for example, in some birefringent crystals. In this process a nonlinear polarization wave is generated with double the frequency, and the efficiency of this process depends on the nonlinear susceptibility tensor $\chi^{(2)}$ via $P(2\omega) = \epsilon_0 \chi^{(2)} E^2(\omega)$ for low conversion rates (without power depletion at the fundamental frequency ω) [79, 80]. One can then show that in an extended nonlinear medium giving an interaction length l light intensity at the second harmonic (2ω) is given by:

$$I(2\omega, l) = \frac{2\omega^2 d_{\text{eff}}^2 l^2}{n_{2\omega} n_\omega^2 c^3 \epsilon_0} \text{sinc}^2\left(\frac{\Delta k l}{2}\right) I^2(\omega), \tag{8.2.1}$$

where d_{eff} is an effective coefficient depending on components of the $\chi^{(2)}$ tensor, n_ω is refraction index at the fundamental frequency, $n_{2\omega}$ at doubled frequency and $\Delta k \equiv k_{2\omega} - 2k_\omega$ is difference between the wavevectors at both frequencies.

The relation of Eq. (8.2.1) shows that the conversion is maximized for $\Delta k = 0$, the so-called phase matching criterion - the second-harmonic electromagnetic waves have to constructively interfere at medium's exit placing a condition on waves' phases along the propagation direction. Otherwise, energy transfer between both frequency components changes direction often within the medium. Experimentally, the phase matching is usually performed by adjusting crystal's angle with respect to the beam's propagation direction ("critical phase matching"). However, we chose to utilize a periodically-poled crystal allowing quasi-phase-matching to take place.

Quasi-phase-matching is a clever way of ensuring that efficient energy transfer between the pump (fundamental) frequency and signal (doubled) frequency can occur. In this process the phase matching criterion is met by adding an additional contribution corresponding to the wavevector of the periodic structure of the material [81, 82]. This leads to a slightly modified version of Eq. (8.2.1), namely $I(2\omega) \propto \text{sinc}^2(\Delta k \Lambda/2)$ with period of the structure Λ.

In practice, the periodically-poled crystals are grown in layers of alternating orientation of ordinary and extraordinary axes (crystal domains). The period of those domains is chosen for a particular wavelength, and because of the thermal expansion, the crystal has to be kept at a particular temperature. For our purposes we chose an AR-coated 1mm × 2mm × 20mm ppKTP (periodically-poled potassium titanyl phosphate $KTiOPO_4$) crystal grown for us by Raicol Crystals with a 9.5 μm period. One of the first tests we performed was observing single-pass frequency doubling efficiency and its temperature dependence - the former should be quadratic for small conversion rates, while the latter should behave like a sinc-squared function. Indeed, in Fig. 8.2.1

we can see that the doubled frequency's power grows quadratically with our input power (the relationship holds for low conversion rates, i.e. low loss of power in the fundamental frequency, so these input powers are not large in this context). Similarly, in Fig. 8.2.2, as expected, the output power follows a sinc^2 dependence of Eq. (8.2.1) - changing the temperature changes the distance between the domains (poles) in the crystal.

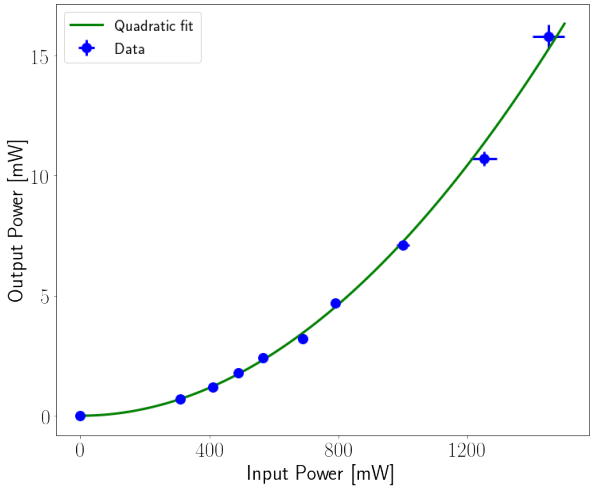

Figure 8.2.1: Output power of the second-harmonic frequency generated in the ppKTP crystal as a function of input power of the coupled CW laser light at 1087 nm. The data follows a simple quadratic relationship $f(x) = ax^2$ expected for low conversion efficiencies and represented here by the fitted curve.

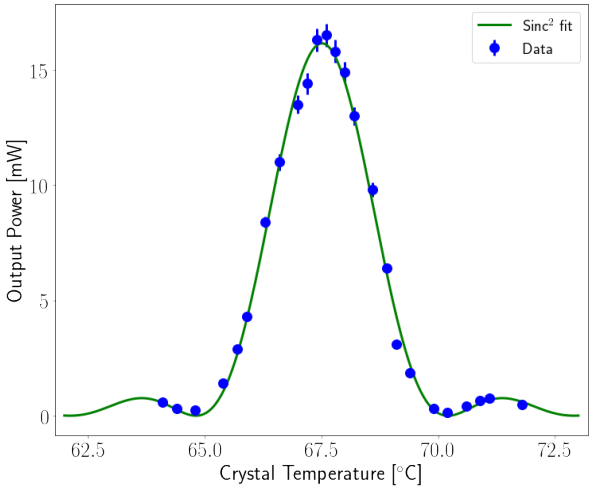

Figure 8.2.2: Output power of the second-harmonic frequency generated in the ppKTP crystal as a function crystal's temperature for a 1.45 W continuous-wave laser input at 1087 nm. As expected, power of the doubled light follows a relationship proportional to $\text{sinc}^2 T$

8.2.1 Second-harmonic Generation Cavity

As shown in Fig. 8.2.1, conversion efficiency for input powers of even a couple of watts is unfortunately not very high ($\sim 1\%$ for 1.45 W). To generate enough green laser light for the next stage of frequency conversion we have two choices: we can use a much stronger amplifier and obtain input powers of tens of watts or we can build a resonant cavity. Given the amplifier's power limits we chose the latter and decided to build it in a bow tie configuration. If designed correctly, the total

circulating power within such cavity can reach ~ 100 W for our input powers.

To design a resonant cavity for second harmonic generation, we first need to know parameters of a Gaussian beam passing through the nonlinear crystal that optimize the conversion efficiency. For a given crystal length l, one can find [83] that the optimal focusing condition for an incidence angle of 0 is:

$$\xi \equiv \frac{l}{b} \approx 2.84,$$

where ξ is the so-called focusing parameter and b is the confocal parameter equal to two Rayleigh ranges z_R defined as:

$$z_R = \frac{\pi \omega_0^2 n}{\lambda},$$

with beam's waist at the focus ω_0, crystal's refraction index n and light's wavelength λ. Putting both together, we obtain a condition for beam's waist inside the crystal:

$$\omega_0 = \sqrt{\frac{\lambda l}{2.84 \times 2\pi n}}. \tag{8.2.2}$$

Solving Eq. (8.2.2) for our problem's parameters, i.e. $\lambda = 1087$ nm, $n(\lambda) \approx 1.747$ (SHG in our crystal is of Type I, and the relevant index of refraction is n_y) and $l = 20$ mm leads to waist of $\omega_0 \approx 26.4\ \mu m$. Given this beam waist, one can then use software such as SNLO to find appropriate physical parameters for different components of the bow tie cavity.

In such a cavity (Fig. 8.2.3) the light entering through mirror M1 (input coupler) travels in a loop. The exact length of the loop is controlled by position of one of the mirrors, usually a high-reflectivity mirror M2, which can be finely adjusted by a piezoelectric transducer (a "piezo"). The beam is then focused into a crystal located between spherical concave mirrors M3 and M4, with the latter being a dichroic letting light of double the frequency through. The power build-up in the cavity occurs when the total optical path length $k_0 l_0 + k_{\mathrm{KTP}} l_{\mathrm{KTP}} = 2m\pi$ for any integer m allowing constructive interference. However, because the beam is Gaussian by nature, it diverges, and so together with a previously obtained condition on beam's waist inside the crystal ω_0, a condition on M3 and M4 mirrors' radius curvature and their distance from each other, as well as the beam's waist ω_1 between M1 and M2 mirrors has to be found in addition to the total path length to make the resonator stable for the TEM_{00} mode. Finally, the total circulating power inside the resonator (cavity) is also determined by the total losses at the entry mirror M1 and inside the cavity. It can be found that the circulating power is maximized when M1 mirror's transmittance matches all the

intracavity losses [84] (impedance matching), e.g. on other mirrors' faces, inside the crystal, on crystal's faces etc..

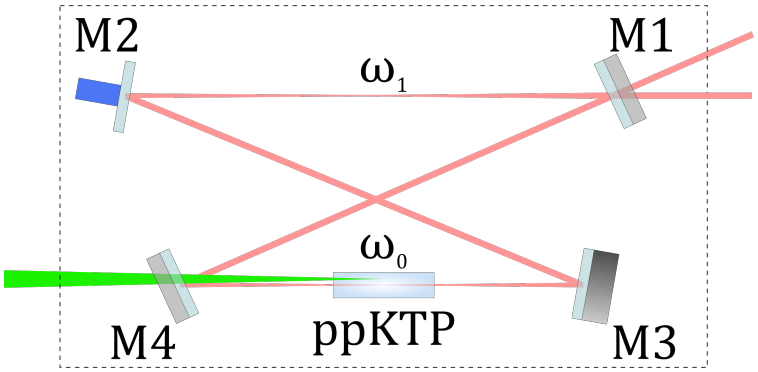

Figure 8.2.3: A generic bow tie resonant cavity.

We determined that the cavity will work best with M3 and M4 mirrors of $R = 100$ mm curvature separated by 110 mm, and a total length of approximately 520 mm giving an FSR of about 575 MHz. Given these parameters and waist inside the crystal, we were able to determine waist ω_1 between M1 and M2 mirrors. Knowing that number, we can determine what optical elements to use to shape the beam appropriately - one can use Gaussian optics formula:

$$\omega(z) = \omega_0 \sqrt{1 + \left(\frac{z}{z_R}\right)^2},$$

to find the beam waist at distance z from the focal point. In the first SHG system, shown in Fig. 8.1.1, we created a telescope with one lens of $f = 150$ mm focal length and one with $f = 75$ mm, while in the other SHG system the lenses had focal lengths of 160 mm and 40 mm respectively (the difference comes from the fact that in the first system $f = 50$ mm lenses were used to focus the beam passing through the EOM).

Having estimated the losses inside the cavity, input coupler M1 was chosen to have transmittance $T \approx 4\%$. Together with other losses, this led to a cavity with finesse $\mathcal{F} \approx 70$. While initially the cavity was built on a breadboard using single clamped posts, then it was designed in SolidWorks as monolithic structure and machined in a block of aluminum. Two versions were built (machine drawings are showng in Appendix C) designed to accomodate slightly different commercially available components. In the first version, shown in Fig. 8.2.4, the input coupler M1 had 1" diameter and was placed in a Thorlabs Polaris Line mount. Mirror M2 was 0.5" in diameter and glued onto a

round Thorlabs PA44RK piezo ring which was in turn glued onto a 1"-diameter 2"-long aluminum cylinder placed inside another Polaris mount. M3 and M4 mirrors were both 0.5" in diameter and held by Newport HVM-05i top-adjust mirror mounts, while the crystal holder was placed onto a Newport 9081 five-axis alignment stage. In the second version of the cavity, M1 and M2 mirrors were also held by Newport HVM-05i mirror mounts, with M1 having a diameter of 0.5" and M2 being glued onto a smaller, 0.5"-diameter cylinder. The crystal alignment was performed with the help of the Thorlabs PY005 five-axis stage. In both cases all the mirrors were custom-made by Layertec.

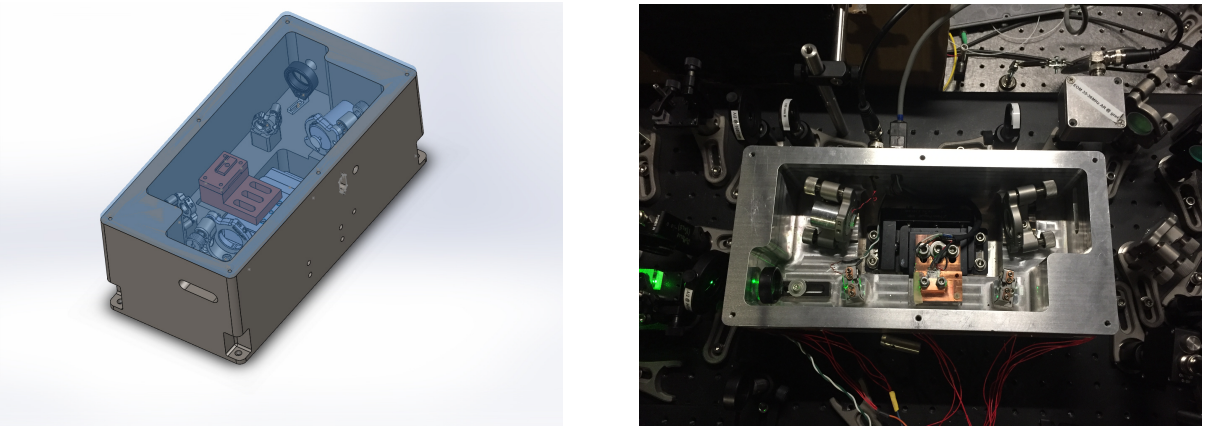

(a) SolidWorks design of the cavity.

(b) Top-view picture of the cavity.

Figure 8.2.4: Design and top-view of the first home-built second-harmonic generation resonant cavity.

In both cavities, the ppKTP crystal had to be kept at $T \approx 67°C$. We achieved that by using Thorlabs TECD2S thermoelectric (TEC) elements operated by Thorlabs TED200C temperature controllers reading the temperature through a Thorlabs TH10K thermistor. The crystal itself was first wrapped in indium foil and placed into a copper crystal holder and delicately clamped. The crystal holder was then placed onto the TEC element after applying thermal paste to its TEC-touching surface, and clamped to a copper heat sink, touching the other side of the TEC element, with plastic screws. Designs for both the crystal holder and the heat sink for the second cavity are shown in Fig. C.5 and Fig. C.6. The thermistor was placed inside a small hole drilled into the crystal holder.

Once built, performance of both cavities was measured. Because the power circulating inside

the cavity is much bigger than the input power ($P_{\text{circ}} \approx \mathcal{F} P_{\text{input}}/\pi$ when impedances are matched), we cannot use Eq. (8.2.1) to correctly describe the output power in the doubled frequency. Once power depletion at the fundamental frequency is taken into account and phase matching $\Delta k = 0$ is assumed, one obtains a relationship [85] :

$$I(2\omega, l) = I(\omega, 0) \tanh^2 \left(\frac{\omega d_{\text{eff}} l}{n_\omega c} \mathcal{E}(\omega, 0) \right), \tag{8.2.3}$$

where $\mathcal{E}(\omega, 0)$ is electric field amplitude at the crystal's input face at the fundamental frequency. We therefore expect that the relationship between the output power in the doubled frequency and the input power in the fundamental frequency will behave as $P(2\omega) = aP(\omega) \tanh^2 \left(b\sqrt{P(\omega)}\right)$ for some constants a and b. In Fig. 8.2.5 we can see that data obtained from the first second-harmonic generation cavity fits the model well.

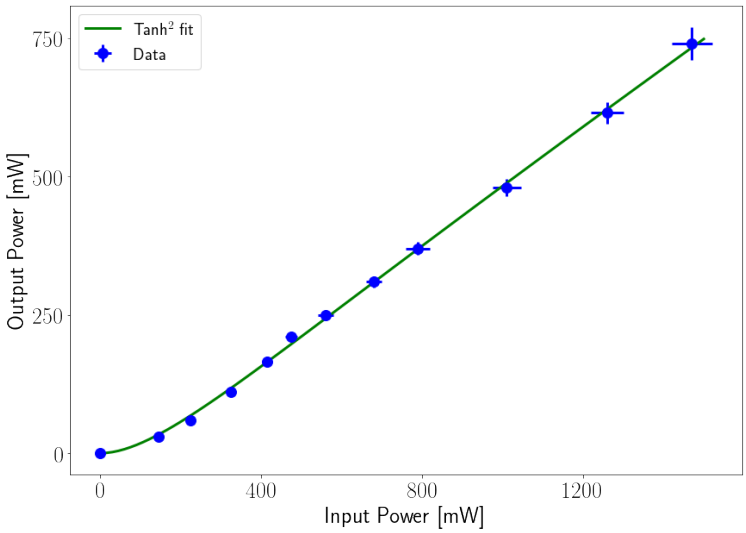

Figure 8.2.5: Cavity's output power at the doubled frequency generated in the ppKTP crystal as a function of power of the coupled CW laser light at 1087 nm at cavity's input mirror. The data follows an expected $f(x) = ax \tanh^2 \left(b\sqrt{x}\right)$ relationship for high input powers and shown as the fitted curve.

8.2.2 Cavity Locking and Alignment

One important aspect of building an SHG system is making the cavity stable. The total path length inside the cavity has to be stabilized to allow for build-up of the circulating power. A standard and most widely used method of cavity locking is the so-called Pound-Drever-Hall (PDH)

technique [86, 87]. It is quite easy to set up and allows for a strong and zero-crossing locking with high bandwidth. Its simplest realization takes signal from frequency-modulated or phase-modulated input light reflected off the cavity's input coupler and mixes it with the modulation signal. The low-frequency component of mixer's output has a characteristic shape with a steep linear part crossing the zero line. In the first iteration of the doubling cavity this technique was used and provided a robust and stable lock. However, because the intensity of light reflected off the input coupler is very high, its attenuation and photodetector's sensitivity created some problems. The main one was related to cavity's re-locking process. While the lock itself was stable, on rare occasions the lock was lost. The analog servo controller in those cases looks for the next zero-crossing. Unfortunately, the obtained signal consisted of more points to lock to than was desired, because even small cavity misalignment imperfections were imprinted onto it, albeit with smaller amplitudes. To alleviate the problem we had two choices: create an amplitude discriminator circuit or use the transmitted frequency-doubled light, which should be less sensitive to these imperfections. We chose the latter.

In this locking scheme, presented in Fig. 8.2.6, we pick off some of the frequency-doubled light using a thin AR-coated window (Thorlabs WG41010-A) and detect it using Thorlabs Si amplified photodetector (PDA36A or PDA10A2). Output of the photodetector is directed into a standard frequency mixer (Mini-Circuits ZAD-1+), where it is mixed with the modulation signal. In our setup, because the NKT Photonics fiber lasers do not support external modulation in megahertz frequencies required by the PDH locking technique, we decided to use an EOM to modulate the phase of our laser.

The resonant EOM was initially built following instructions provided in Eric Norrgard's thesis [88]. We used AR-coated Y-cut 3mm × 3mm × 40mm lithium tantalate ($LiTaO_3$) crystals that we obtained from Almaz Optics as our nonlinear crystal, Hammond 1590LB aluminum boxes as our EOM case and SPI 05063-AB silver paste. The inductor in the EOM's RLC circuit was an iron powder toroid obtained from Amidon. Because the PDH lock does not require the modulation to be deep, we do not need an RLC circuit with high Q-factor (the resonance can be weak and so we do not need to be impedance-matched). Because of that, we used a universal 16:1 chip transformer RFMW XFA-0101-16UH, with which we reached ~ -20 dB resonances at approximately 17 MHz. Unfortunately, we ran into problems with this design. Namely, after putting 2 W of laser power through this home-built EOM, we observed unexpected changes to polarization, modulation depth

and some residual amplitude modulation due to heating and EOM's temperature instability. To fix that problem, we designed a new case (Fig. C.7, Fig. C.8, Fig. C.9) that allowed us to stabilize the temperature of the EOM with TEC elements. Additionally, that case makes it easier to clamp the copper wire to one of the crystal's faces, as well as provides necessary space for the transformer and the toroidal inductor. Once we moved all the components to the new case, previously observed problems disappeared.

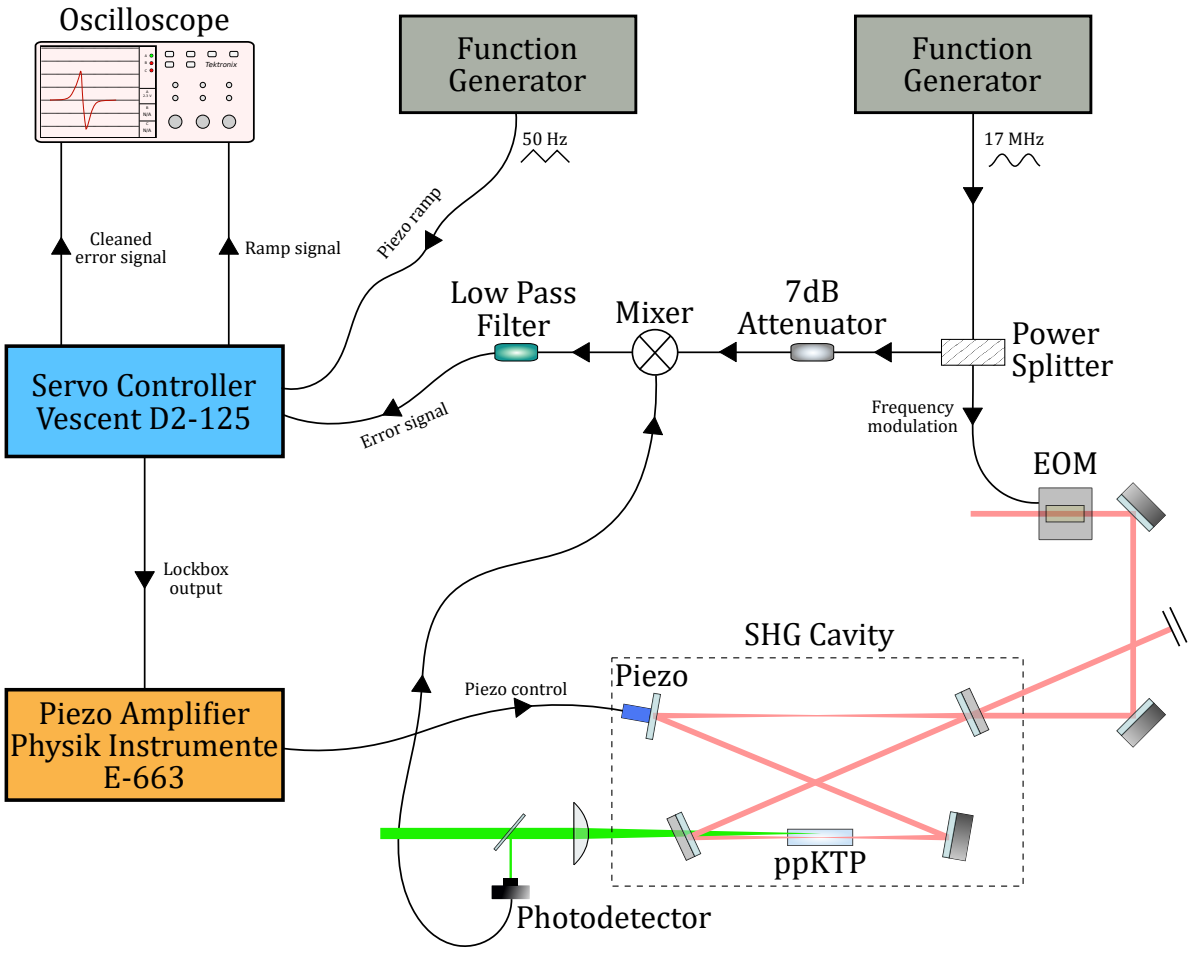

Figure 8.2.6: Schematic of cavity locking setup that uses transmitted frequency-doubled light to create the error signal necessary for locking.

The modulation signal was provided by a generic function generator (such as B&K Precision 4043) and split using a Mini-Circuits ZSC-2-1+ power splitter. Mixer's low-frequency output was

then directed to the servo controller (Vescent Photonics D2-125). We operated the controller in the slave mode, where the triangular piezo ramp signal was provided by a function generator (signals used were between 30 Hz and 50 Hz), and both the ramp signal and a cleaned error signal were observed on an oscilloscope during cavity's alignment. In our case, the error signal was simply a derivative of Lorentzian peaks representing cavity's frequency-doubled transmission obtained when ramping the piezo, providing clear zero-crossings that were used for locking by the servo controller. Servo's output, between -10 V and 10 V, was then directed to Physik Instrumente E-663 piezo amplifier where it was amplified and biased in order to obtain signals within the 0-150 V range accepted by the piezo.

Because the locking setup is completely analog, we came across some typical problems, like existence of 60 Hz (and its higher harmonics) noise in the error signal, which we traced to servo's malfunctioning power supply. However, one of the issues had to be addressed by building an additional circuit. Namely, automatic re-locking, where the servo increases or decreases output voltage until it finds a new zero-crossing lock point in the error signal, eventually causes the voltage to rail beyond servo's maximum or minimum output or beyond maximum or minimum voltage accepted by the piezo. Fortunately, one of controller's inputs automatically resets its voltage back to 0 when supplied with ~ 5 V input. Circuit shown in Fig. 8.2.7 activates this reset function at appropriate moments by taking servo's output as its input. Circuit's input is directed to two operational amplifiers which output 15 V, when the input goes above (under) the upper (lower) limit set by the potentiometers. This output is then decreased to 6 V by a voltage divider, and a $2\,\mu F$ capacitor is added to filter high frequency signals and therefore prevent the circuit from resetting the servo controller too often.

Finally, cavity's alignment was performed using the following procedure. First, with M1 and M4 mirrors, and the crystal removed, we used the two mirrors preceding the cavity to place IR laser's spot in the center of M2 mirror, and then proceeded to using M2 and M3 mirrors to direct the IR light through the center of cavity's output hole. Then, the ppKTP crystal was placed in the holder and single-pass SHG was optimized. We did that by mostly adjusting crystal's position via the 5-axis stage, and sometimes by *slightly* changing M2 and M3 mirrors' angles, as well as changing crystal's temperature. It was also useful to already place M4 mirror after the crystal, which allowed to filter the transmitted IR light. Once single-pass doubling was maximized, M1 mirror was placed

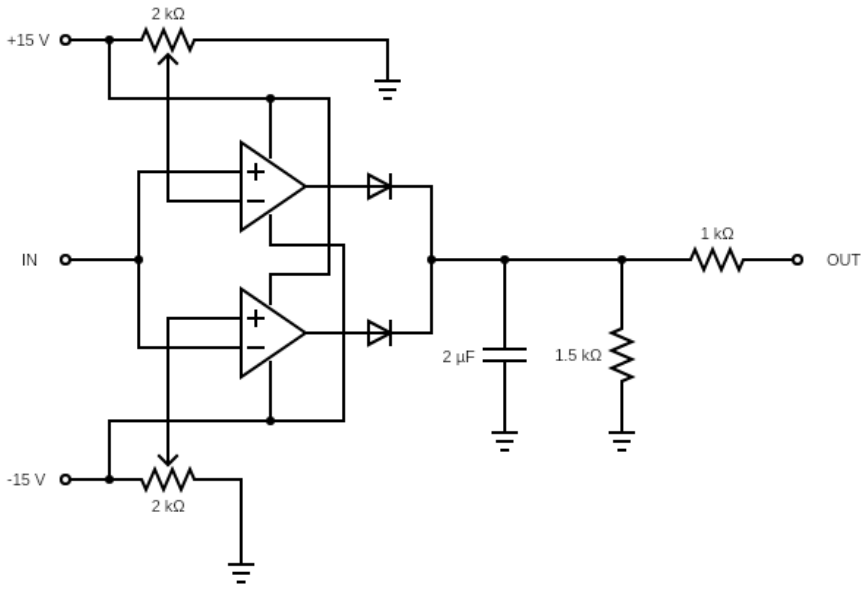

Figure 8.2.7: Electronic circuit used for automatic cavity re-locking and protecting against voltage rails in the servo. By adjusting voltage limits on the operational amplifiers, the circuit works as a comparator - if the input voltage is below the lower limit or above the upper limit, it provides a 6 V output that is connected to the servo controller. Otherwise, there is 0 V on the output.

inside the cavity, and IR light reflecting off the M4 mirror was directed at the same spot on the M1 mirror where the input light is transmitted. Next, M1 mirror was adjusted until the second order spot (from light making 1 loop inside the cavity) was aligned with the first order spot (from light just entering the cavity) on the M2 mirror. At this point, spots of higher orders could already be seen and mirrors M4 and M1 were simultaneously used to align all of the visible spots close to crystal's input face after mirror M3 (the light is focused tightly there, so many spots can be seen). Once this was done, usually it was possible to observe the cavity's frequency-doubled output on a photodetector while scanning cavity's loop distance by ramping the piezo, and several peaks were observed representing different Gaussian modes. On rare occasions when this was not the case, cavity's output would itself consist of closely overlapping spots that were used for the initial alignment using M4 and M1 mirrors, and once the piezo scan was engaged, one could notice with naked eye different modes and interference patterns of the output light when it was directed onto a screen (for example a piece of paper).

Once peaks were seen by the photodetector, further adjustment of M4 and M1 mirrors emphasized the TEM_{00} mode, although other peaks still remained. Initially, their elimination was performed by successive adjustments of two pairs of mirrors - two mirrors preceding the M1 mirror and the M4 + M1 pair - together with small changes to crystal's position. In general, it should not be necessary to touch M2 and M3 mirrors and it is not advised to do so, because they decide not only how the light is directed through the crystal, which can be changed by changing crystal's position, but also modify whole cavity's alignment. At the very end, it was also useful to check once again crystal's optimal temperature, as well as PID locking parameters that, by determining the actual lock point and lock's quality, influence output's power.

8.3 Reference Laser

All the "science" UV lasers will eventually have to consistently target one of the TlF transitions of interest, which all have a natural linewidth of $\gamma \approx 1.6$ MHz. While the fiber lasers we are using are narrow, their center frequency can drift over time and, in general, is not stable. Therefore, in such situation it is necessary to build a frequency-stabilizing system with stability (usually calculated as the root-mean-square of the error) comparable to the natural linewidth. One way of doing it is transferring stability through an additional cavity from a reference laser that is stabilized by being always on resonance with a particular transition in an atom or molecule of our choice. We decided to use cesium's so-called D_2 line [89], which corresponds to a transition between its $6\,^2S_{1/2}$ and $6\,^2P_{3/2}$ states and occurs at approximately 852.347 nm (351.725 THz).

In order to stabilize laser's frequency to one of its lines we decided use a well-known Doppler-free technique called Modulation Transfer Spectroscopy (MTS) [90, 91, 92] that produces sub-Doppler lineshapes. This technique, in analogy to the saturation absorption spectroscopy, requires two counter-propagating beams (the pump and the probe beams), albeit of approximately equal power. In it a single-frequency pump beam is phase-modulated by an EOM, and thus acquires sidebands, and directed through a vapor cell. Unmodulated single-frequency probe beam is then passed through the same vapor cell aligned with the probe beam in the opposing direction, and directed onto a photodetector afterwards. Due to existence of nonlinear effects in the atomic vapor, frequency components of both beams combine and a four-wave mixing process occurs effectively

adding sidebands to the probe beam [93].

The MTS method of laser stabilization is popular due to several features of the resulting signal. The major advantage is that its lineshape baseline is not sensitive to changes in absorption within the cell that can potentially result from temperature, laser intensity or polarization fluctuations. The resulting signal has then a flat zero background. This lack of signal's dependence on absorption happens, because the process of transferring modulation can occur only when the sub-Doppler resonance takes place. In turn, this leads to the zero-crossing of the demodulated error signal to always be at the center of this resonance.

Our experimental realization of the MTS technique is shown on the left side of Fig. 8.3.1. As the light source we used Toptica DLC PRO diode laser, and the beam was shaped by a pair of anamorphic prisms not shown in the figure. By using a broadband PBS (Thorlabs PBS102) and a half-wave plate (Thorlabs WPH05M-850) we then divided the beam into part that is directed towards the wavemeter and the transfer cavity, and a part that is required for the MTS laser locking method. The latter was split into pump and probe beams by using Gouch&Housego AOMO 3080-122 830NM acousto-optic modulator (AOM) driven by $\sim$ 1 W of 80 MHz radio-frequency signal. We split the beam using an AOM instead of a PBS to avoid parasitic interferences [94] that might appear due creation of etalons on different pairs of optical elements. This frequency shift of 80 MHz means that the modulation transfer resonance will occur for atoms that have equal, but opposite Doppler shifts for the probe and the pump beams, i.e. $\pm\,40$ MHz, which in turn means that the laser itself will be locked 40 MHz away from the zero-velocity resonance.

The pump beam was then directed through a 3 MHz resonant EOM (custom made Thorlabs EO-PM-R-3-C1). The modulation frequency was chosen to be close to $\sim 0.3-0.6\,\gamma_{\mathrm{Cs}}$, with natural linewidth $\gamma_{\mathrm{Cs}} \approx 5.22$ MHz, for which the resulting error signal has the steepest zero-crossing [92]. Both probe and pump beams were expanded using two plano-convex lenses with focal lengths of 50 mm and 100 mm. The beams were counter-propagated through the Cs vapor cell placed inside a mu-metal cylindrical magnetic shield obtained from Magnetic Shield Corporation. The magnetic shielding of the vapor cell is necessary due to $\sim$ 0.5 MHz/G effective g-factors of the hyperfine states we are addressing in the D_2 line and that could cause locked laser's frequency to change with changing ambient magnetic field. Finally the probe beam was directed onto a standard Thorlabs Si amplified photodetector. The error signal was obtained by first amplifying the photodetector's

signal (Mini-Circuits ZFL-2AD+ 9 dB amplifier) and demodulating it using a combination of a mixer and a low-pass filter, just like it was done in the PDH technique for the doubling cavity. The resulting error signal was then connected to one of the input channels of the laser control box provided by Toptica, which allowed us to use their built-in laser locking module.

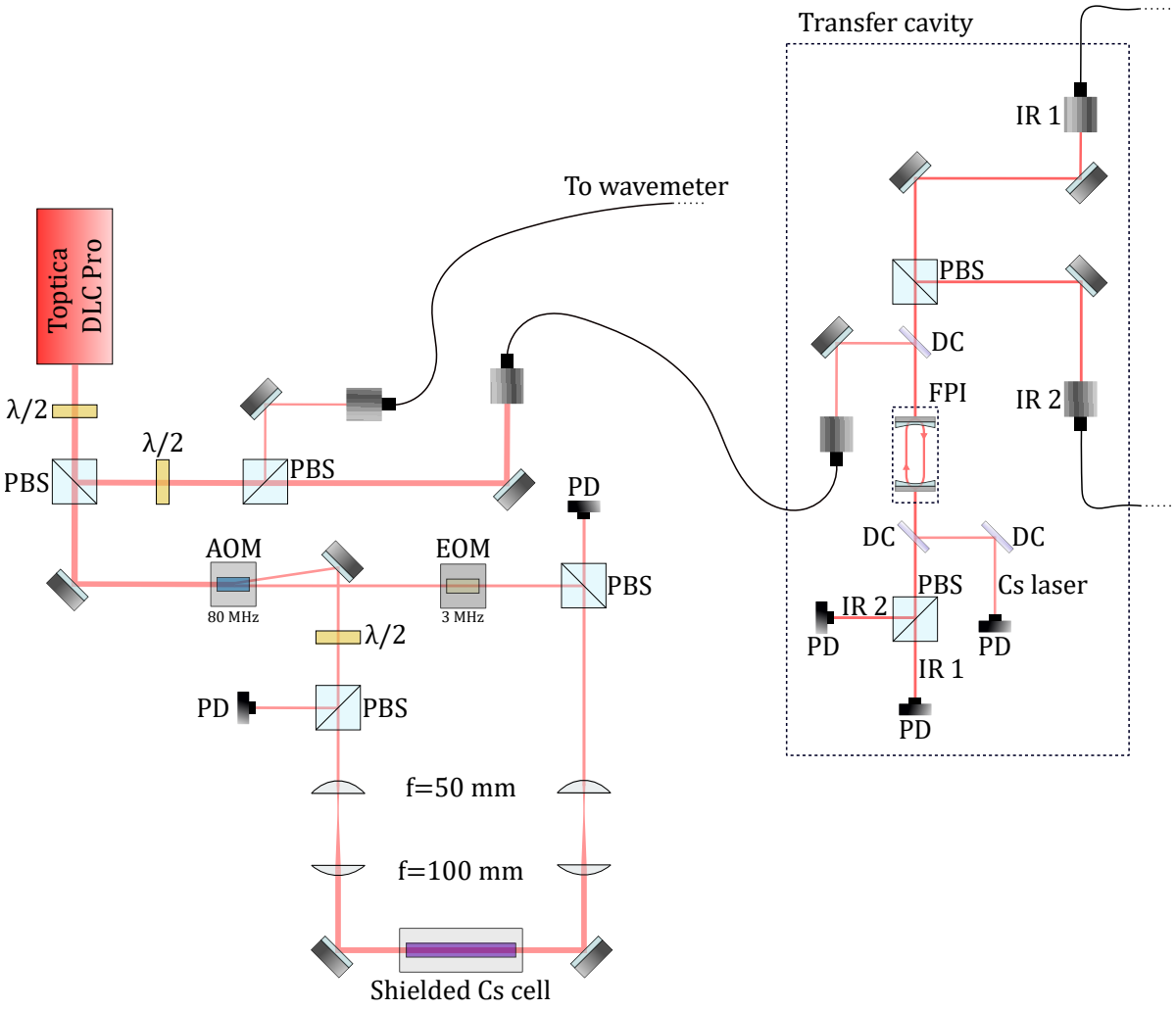

Figure 8.3.1: Schematic of the Cesium reference setup and the transfer cavity system. Abbreviations used: PD - photodetector, DC - dichroic mirror, FPI - Fabry-Perot interferometer, PBS - polarizing beam splitter, $\lambda/2$ - half-wave plate, EOM - electro-optic modulator, AOM - acousto-optic modulator, IR 1 and IR 2 - the first and the second infrared lasers used in the frequency quadrupling system.

Stability of frequency locking was finally tested by beating the laser against its sister system built simultaneously for a different experiment. The measurement was taken over a span of 12 hours and its results are presented in Fig. 8.3.2 showing an approximately 14 kHz RMS error, well below the ~ 1.6 MHz requirement imposed by thallium fluoride's natural linewidth. Reaching this level of stability was not initially easy and one crucial element (not shown in the diagram) was added to improve system's performance. Namely, we added a combination of a half-wave plate and a polarizer (Thorlabs LPNIRB050-MP2) along the pump beam's beamline just before the EOM. This increased polarization purity inside the EOM and allowed us to eliminate polarization fluctuations and unwanted EOM effects, such as residual amplitude modulation, that somewhat influenced the quality of the error signal.

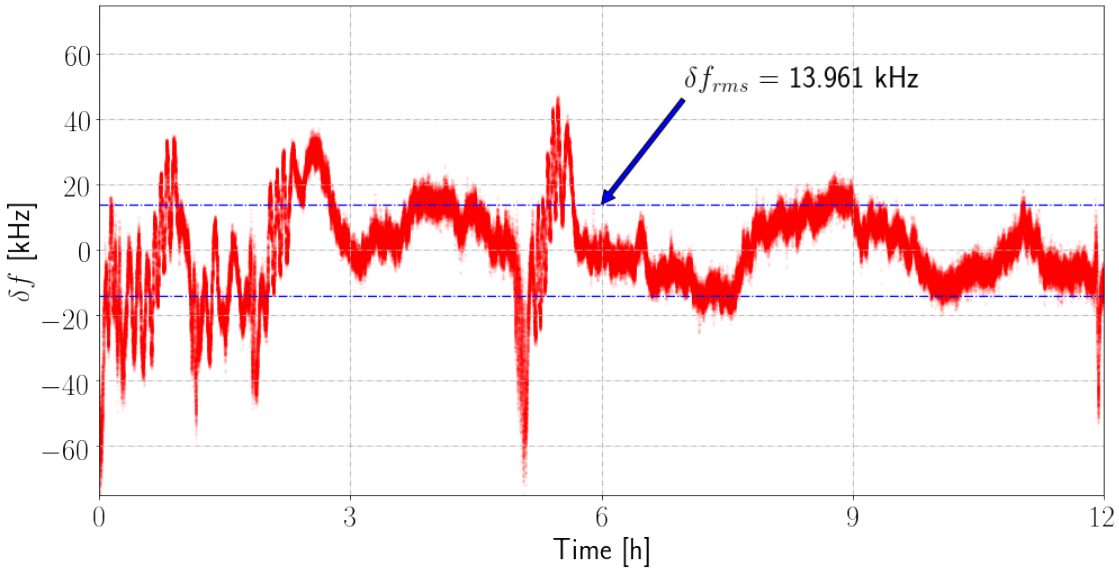

Figure 8.3.2: Cesium frequency lock stability beat-note measurement data obtained by beating the laser's frequency against another one coming from an analogical system stabilized to the same spectral line. The measurement was taken over a period of 12 hours and resulted in a 14 kHz RMS error.

8.4 Transferring Stability

The final step is transferring stability of the Cesium frequency locking system to our science lasers. One of the most commonly used techniques is based on utilizing a Fabry-Perot Interferometer (FPI) [86, 95], where the path length inside the cavity is stabilized to a transmission or reflection peak of

the reference laser, just like in the case of the doubling cavity, and then the science laser's frequency is stabilized to "fit" locked cavity's length. To gain flexibility in controlling science laser's frequency (one can lock it to an already locked cavity only at frequencies spaced by cavity's free spectral range) one adds an AOM to create an easily controllable frequency offset. However, we decided to choose a different approach and to implement the so-called scanning cavity lock [96, 97, 98].

In this approach the cavity is constantly scanned, and we lock it to the reference laser by locking transmission peak's *position* since the beginning of the scan, e.g. we always want to detect the peak 4 ms after the scan started. The feedback loop then adjusts piezo scan's offset voltage accordingly. Science lasers can then be locked by locking position of their transmission peaks, which are controlled by adjusting voltage on lasers' piezos, with regards to the reference laser peak. The feedback loop can also be easily implemented digitally, although such approach leads to lower (sub-kilohertz) bandwidths, which, fortunately, are sufficient for us.

Experimental realization of this scanning cavity lock is shown on the right side of Fig. 8.3.1. As the FPI we used Toptica's FPI 100-0980-3V0 scanning Fabry-Perot confocal cavity with 1 GHz FSR, finesse of about 500 and 2 MHz resolution. The reference laser was transferred to this laser system via a single-mode patchcord (e.g. Thorlabs P3-830A-FC-2) and coupled to the FPI using two mirrors - one standard broadband mirror and Thorlabs DMLP950 longpass dichroic mirror with cutoff wavelength of 950 nm. The reference laser light that is transmitted through the cavity was placed onto a photodetector and separated from science IR lasers by an identical dichroic mirror. Science lasers' light was brought by polarization-maintaining fibers with lasers having linear polarization perpendicular with respect to each other. In principle, we can lock any number of lasers using this cavity, as long as the cavity mirrors have appropriate coating and lasers are separable. In our case, both science lasers have roughly the same wavelength, so we can separate them only by adjusting their polarization. It means we can at most couple two science lasers to our cavity.

Before the science lasers reached the FPI, they were combined on a PBS. In addition to what is already shown in Fig. 8.3.1, we also placed half-wave plates before the PBS to make it possible to adjust intensity of light reaching the FPI. After the lasers were combined, they went through the dichroic mirror and were both coupled to the cavity. Transferred light of both lasers went through the second dichroic mirror and was separated by another PBS afterwards. Finally, light from both

science lasers reached their respective photodetectors.

As was mentioned, the lock itself is digital. Signals from all the photodiodes are collected by a computer, analyzed on-line, and then generated feedback signals are sent to both science lasers and FPI's piezo. To send and receive analog signals we used National Instruments PCIe-6353 data acquisition card with 4 analog outputs and allowing 1 MS/s multichannel data collection, and two National Instruments BNC-2110 boards. Using SDKs provided by national instruments and NKT Photonics, we built multithreading software (together with a graphical user interface) in Python that controls the science lasers and the FPI used as a transfer cavity. It is responsible for data collection, analysis, plotting and feedback control[1]. This program enabled us to not only lock the science lasers to chosen frequencies, but also to scan their frequencies in multiple ways. It also communicates with our wavemeter, as well as with another experiment data collection software we built. Screenshot of the GUI is shown in Fig. 8.4.2

The lock itself is based on finding peak positions when scanning the FPI. In order to quickly and reliably determine positions of those peaks, the software first applies a peak-emphasizing filter to the obtained photodetector data. This filter replaces a data point from an array A (our data is simply a time-series represented by an array of numbers) at position i by using a formula:

$$A[i] \leftarrow A[i]^2 - A[i-k]A[i+k],$$

for window size k. This simple filter is fast and greatly enhances signal-to-noise ratio. Afterwards, the signal is passed through a Savitzky-Golay derivative filter, and zero-crossings, representing peak positions, are found. To showcase how the process works on noisy Lorentzian peaks, we plotted simulated signals at every filtering stage and present them in Fig. 8.4.1.

Once the peak positions are obtained, we use a so-called velocity algorithm to create the feedback signal. It is simply a different way of looking at a PID loop. Namely, assuming E is the error signal (peak position minus desired peak position), then the feedback signal FS would normally be calculated using:

$$FS = K_P E + K_I \int E dt + K_D \frac{dE}{dt},$$

where K_P, K_I and K_D are proportional, integral and differential gain respectively. We can look at

[1]The program is available at https://github.com/kwenz/Transfer-Cavity-Lock-Control

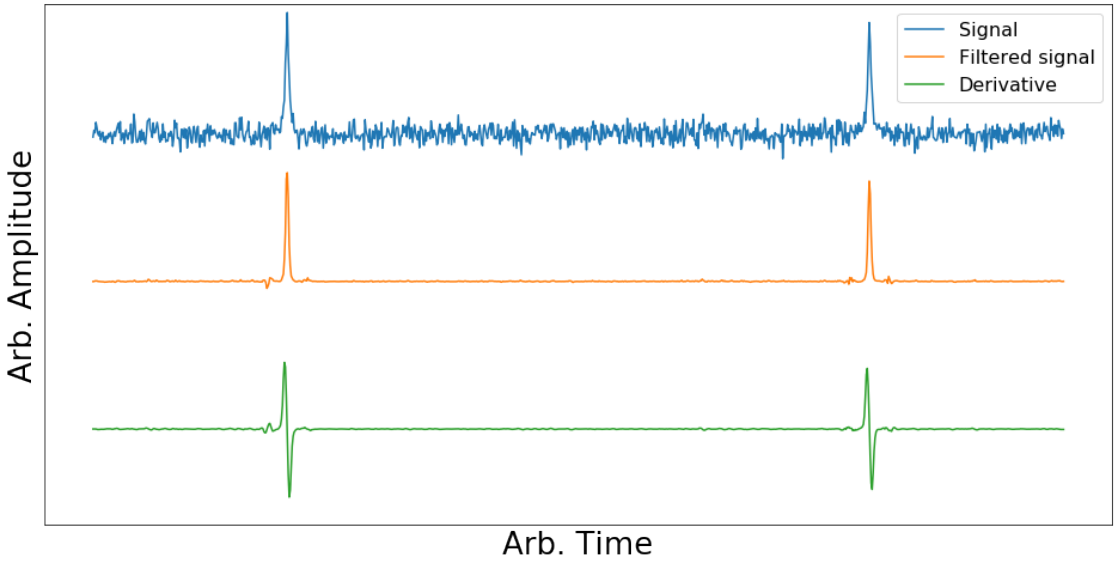

Figure 8.4.1: Simulated photodetector signal passed through a peak-enhancing filter and a Savitzky-Golay derivative filter. Zero-crossings in the derivative signal correspond to peak positions needed for the scanning cavity lock.

this formula from another angle and see how the feedback signal changes:

$$\frac{d}{dt}FS = K_P\frac{dE}{dt} + K_I E + K_D\frac{d^2E}{dt^2}. \tag{8.4.1}$$

Now the proportional term becomes a "velocity" term proportional to changes in the error signal in time, integral term is a "positional" term, and derivative term is an "acceleration" term. In our software we use only proportional and integral gains, and update the feedback signal iteratively. Assuming time interval between consecutive feedback-generating iterations is T (in reality it is simply time between two data inputs from the photodetector), we can write Eq. (8.4.1) at iteration j as:

$$FS(j) = FS(j-1) + K_P\left[E(j) - E(j-1)\right] + K_I T E(j).$$

The software uses the above formula for every feedback loop engaged separately, and simply assumes $FS = 0$ and $E = 0$ at the 0-th iteration. In the end, the RMS error of the cavity lock is about ~ 0.15 MHz and ~ 0.2 MHz for both laser at their IR frequency, which provides a total 1 MHz RMS error at laser's UV frequency. The cavity is scanned with frequency of approximately 30-33 Hz and is limited by Python's multithreading implementation. Putting the data acquisition and

signal-sending processes operated via the PCIe on a separate process than the GUI (via Python's multiprocessing) can increase this frequency to about 100 Hz.

Figure 8.4.2: Screenshot of our home-built scanning cavity locking software. White peaks correspond to Cs reference laser signals, green ones are created by the rotational cooling seed laser and magenta by the detection seed laser.

Chapter 9

Apparatus for Rotational Cooling

9.1 Overview

Having chosen the best scheme for the rotational cooling process we designed and built an experimental setup allowing us to test and validate methods and predictions discussed in previous chapters. The apparatus is shown in figure Fig. 9.1.1 and is, basically, a shortened version of the planned final setup - in the future, both the beam source and rotational cooling chambers will be in the same positions, while in place of the detection chamber, a pre-lens state-selection region will be moved. The overall idea behind such experimental configuration is simple:

- First, we ablate the TlF target with a pulsed Nd-YAG laser. The molecules thermalize with cold Ne atoms present in the chamber and undergo expansion into vacuum once they leave the chamber creating a cold molecular beam (described in Chapter 3).

- Just after the beam source, we placed a gate valve and wide 6" bellows. Gate valve allows us to perform changes to downstream chambers, while keeping the beam source under vacuum, and the bellows gives us some flexibility with molecular beam alignment.

- Bellows are connected to the rotational cooling chamber. There, ultraviolet laser propagates perpendicularly to the molecular beam and drives the main rotational cooling transition (P2F1). On both sides of the chamber, we also placed two sets of microwave horns producing beams that drive rotational transitions in the molecule.

- Finally, the rotational cooling chamber is connected to a rather large detection chamber. There, perpendicularly to the molecular beam, another ultraviolet laser is propagated. It drives a chosen detection transition. Underneath the chamber, we placed a photomultiplier tube sensitive to ultraviolat light emitted by the molecule. It is kept outside the vacuum, so the fluorescent light is transported via a light pipe.

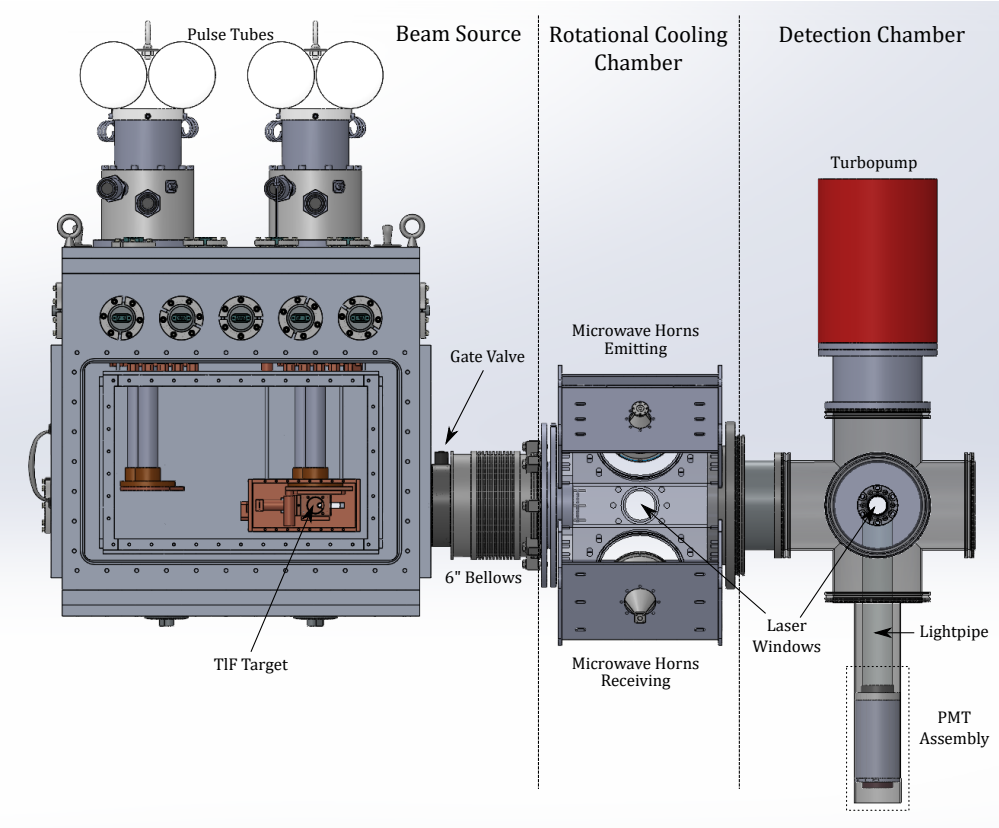

Figure 9.1.1: Side-view of the whole experimental apparatus. The setup consists of three main parts: the beam source, where we ablate the TlF target in a neon-filled chamber, the rotational cooling chamber, where we interrogate the molecules with the help of polarization-switched laser and microwaves, and the detection chamber, where we perform fluorescence spectroscopy measurements.

The whole system is kept under a vacuum of about 10^{-9} Torr, if there's no neon flow, and under approximately 10^{-6} Torr once the gas is flowing. The pressure is measured by InstruTech Hornet IGM 401 vacuum gauges placed on the beam source and the detection chamber. The vacuum is created by two turbopumps: one, a very small one, is placed on the beam source, while the main one, the Pfeiffer Vacuum HiPace 700M, is placed on top of the detection chamber.

We found that good results are obtained with neon flowing at a rate of at least 25 sccm and no more than 50 sccm, and with cell temperature kept at about $16 - 20$ K. As described in Chapter 3, we obtain a molecular beam with a longitudinal velocity of $\bar{v}_z = 184 \pm 17$ m/s with spread of $\sigma_{v_z} = 16.1 \pm 0.8$ m/s corresponding to longitudinal temperature of $T_{\rm tr} = 7.0 \pm 0.7$ K. Beam's transverse velocity is distributed around $\bar{v}_t = 0$ with $\sigma_{v_t} = 39 \pm 3$ m/s. Rotational temperature we are working with is estimated to be $T_{\rm rot} = 6.3 \pm 0.2$ K.

As was shown in the previous chapter, molecules' transverse velocity spread negatively affects rotational cooling results. Hence, as depicted in Fig. 9.2.1, we installed circular apertures of 4 mm radius along the beam line, which drastically reduces the velocity spread in the detection region, though at a cost of much smaller signal. However, the apertures have also drastically helped with removing noise coming from the rotational cooling lasers.

9.2 Rotational Cooling Laser System

The main part of the laser system used in our experiment was already described in Chapter 8. In this section, we will describe the last part of the optical setup. Fig. 9.2.1 shows the layout used in the rotational cooling experiment. In total we used three lasers: Nd-YAG pulsed laser ablating the target, and two frequency-stabilized UV lasers created through two frequency doubling stages.

9.2.1 Ablation

In order to produce the molecular beam, we ablate a solid TlF target made of pressed TlF powder. The ablation laser is a Litron Lasers Nano LG 130-50 solid-state, water-cooled Nd-YAG nanosecond free-space laser. Its pulse energy can be adjusted between 2 and 130 mJ with repetition rate up to 50 Hz. Apart from the main 1064 nm harmonic, it also emits doubled 532 nm light, which, while useful for alignment, is redirected into a beam dump.

We direct the ablation light through 2" optics into the beam source chamber. We use a set of lenses to focus the beam onto the target, and two mirrors to point the laser at the right spot. The mirror closest to the beam chamber is placed on Zaber T-MM2 motorized mirror mount, which we control via RS-232 serial interface. We use a motorized mirror in order to be able to easily change the ablated spot once signal becomes smaller. Signal decay usually occurs after $\sim 500 - 1000$ shots,

which for often-used repetition rates of 5-10 Hz means that at most we have to move the mirror every minute or so. Moreover, the software control of the motorized mirror mount allows us to continuously move the spot as well.

The ablation laser and supporting optics are kept on separate vibration-isolated optical table to prevent random changes to the ablated spot's position. Despite the fact that most of the light is either directed towards the TlF target (1st harmonic) or towards the beam dump (2nd harmonic), the amount of scattered light is big enough to be caught by photodetectors responsible for frequency stabilization. To ameliorate this problem, we keep the system under an enclosure.

9.2.2 UV Lasers

Ultraviolet light at approximately 271.7 nm is obtained through a frequency doubling process. In the doubling system described in Chapter 8, we produce 500-1000 mW of green linearly-polarized laser light, which we couple to 10 m long single-mode polarization-maintaining fibers. These fibers are then coupled to a commercial doubling cavity.

9.2.2.1 Optical Fibers

The fibers we use are Thorlabs P3-488PM-FC-10 PANDA-style patch cables with angled FC/APC connectors. These fibers, while specified to operate with powers under 100 mW, perform very well with powers we coupled. We did not observe any visible damage. We achieved coupling efficiencies of 60% and did not observe any decline in the transmitted power. However, given high light intensities it is crucial to keep fibers clean and well coupled. Otherwise, the glue and face of fiber's ferrule might melt. The 10 m length of fibers is determined by physical constraints of our laboratory space. The doubling system producing the green light is on a separate optical table, while the UV laser system is close to the main apparatus to allow free space coupling of the UV light into the vacuum chamber. The 10 m fiber length does cause some rather annoying problems.

In polarization-maintaining fibers, the polarization is stabilized by tension inside the fiber created by rods placed inside the patch cable. Any changes of this tension can cause changes in polarization. Polarization stability is very important in the frequency doubling process, if we desire to keep the light intensity relatively constant. When we first coupled the light through the 10 m fibers, we observed modulation of polarization on the time scale of tens of seconds. Because the

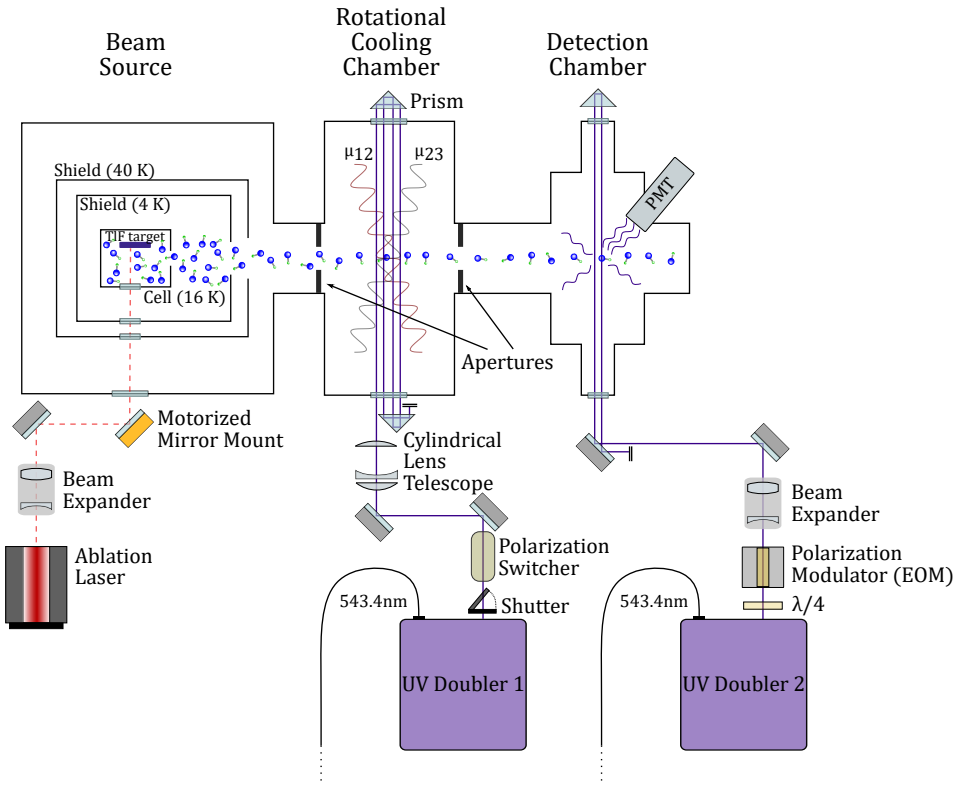

Figure 9.2.1: Schematic of the laser system used in rotational cooling experiment. Both commercial UV doublers use a green laser input described in chapter 8. One of the lasers drives the main rotational cooling transition, while the other the detection transition of choice. Both are multipassed through their respective chambers with the help of right-angle prisms.

fiber cables were placed close to the ceiling on racks above the optical tables, we attributed this modulation to temperature changes and air flow caused by lab's temperature and humidity stabilization system. To fix the problem, we first placed both fibers in separate 9 m long plastic tubes that we placed inside a silicone foam pipe providing temperature isolation.

Another important fix was precision of the laser coupling. We launched the light coming out of the fiber through a polarization beam-splitting cube into two photodetectors (such as Thorlabs PDA10A2 fixed gain Si amplified photodetector), which allowed us to look at light intensity of both polarizations simultaneously. To adjust the fiber coupling, we placed an additional zero-order half-wave plate (Thorlabs WPH05M-546) upstream from the fiber coupler and rotated it until signal from one of the linear polarizations is maximized and stabilized while simultaneously scanning

laser's frequency over a range of several GHz. Eventually, we got rid of most of polarization-modulating effects. They still occur on time scales of minutes, albeit with a very small amplitude. Fig. 9.2.2 shows polarization stability before and after the adjustments were made.

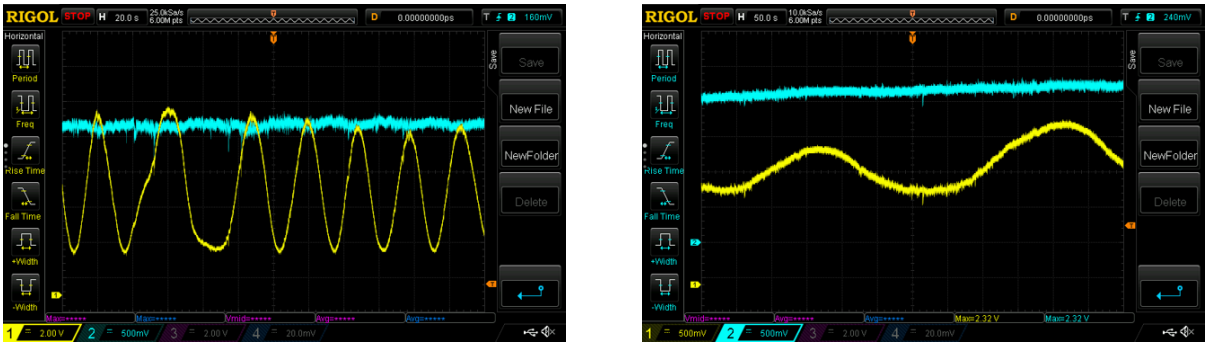

(a) Before adjustments.

(b) After adjustments.

Figure 9.2.2: Photodiode signal traces taken from the oscilloscope. The cyan trace corresponds to high-power beam of polarization accepted by the doubling cavity, while the yellow trace corresponds to the low-power beam of rejected polarization. Before adjustments were made, oscillation period was about 1 min (one box corresponds to 50 s), while after it is as long as 6 min. The amplitude decreased by a factor of 2.

9.2.2.2 Doubling Cavity

The doubling cavity we use is fiber-coupled Toptica's SHG Pro. It is a stand-alone system that requires only the input light. Light coupled into the system is first directed through a mode-matching lens, which can be moved along the beam path, then through an EOM already provided by the company, and is finally coupled into the doubling cavity via two steering 1" mirrors (Fig. 9.2.3).

The doubling resonator is of a standard bow tie configuration and uses an AR-coated BBO (BaB_2O_4) crystal as its nonlinear medium. The cavities are stabilized using PDH locking procedure, where the error signal is generated from the light reflected from cavity's in-coupling mirror. The locking system has a built-in re-locking mechanism as well, which very quickly stabilizes the cavity in case the lock is lost. The output of the beam is directed through beam-shaping optics creating an almost-Gaussian beam shape (Fig. 9.2.4) of approximately 3 mm diameter.

Both doubling cavities in use are specified to provide 30 mW of output light. We managed to obtain more light from both. The UV doubler on the rotational cooling laser beam line provides up

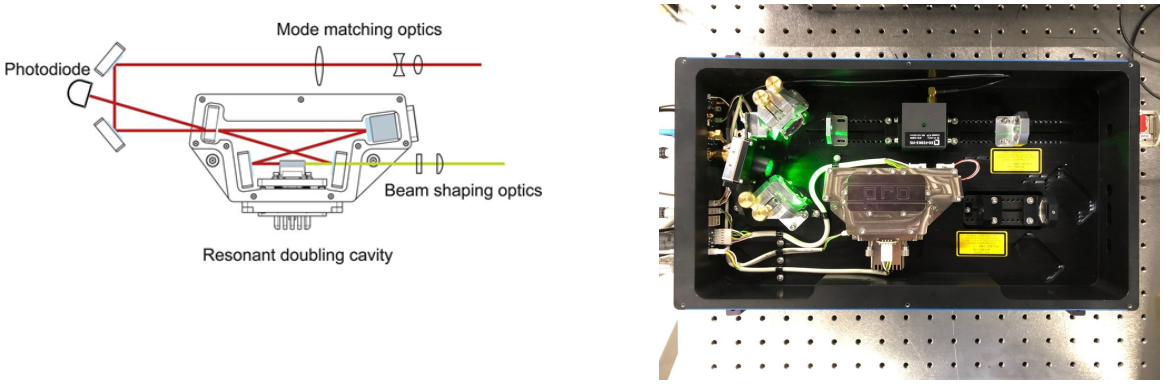

(a) Doubler's schematic.

(b) Picture of the doubler with lid removed.

Figure 9.2.3: Schematic and real picture of Toptica's frequency doubler. Fine adjustments and cavity alignments can be performed using set screws and knobs on cavity's walls. However, simplicity and robustness of this system requires such actions to be taken very rarely.

to 90 mW of UV light given a 500 mW linearly polarized input, while the doubler on the detection laser line can reach powers of 45 mW with 280 mW input. Usually, we operate the rotational cooling laser at 80 mW output power (providing $\sim 40-50$ mW of laser power inside the rotational cooling chamber), and the detection laser was always set to provide 30 mW.

9.2.2.3 Polarization Modulation and Switching

Once the laser beam leaves the UV doubling system it goes through a polarization modulation or polarization switching stage (in Fig. 9.2.1 the rotational cooling laser beam also goes through a shutter first, which we will discuss later). As was shown in Chapter 7, character of the main rotational cooling P2F1 transition necessitates polarization switching of the laser light; polarization switching is a feature of the benchmark scheme we chose. The detection transition might or might not require any manipulation of polarization - it depends on transition that is chosen. Details are provided in Chapter 10.

Polarization switching of the rotational cooling laser is performed by a non-resonant electro-optic modulator. We use Conoptics 370-LA-DUV EOM specified to work in deep UV wavelengths. Despite the wavelength specification, we observe laser power transmission losses as high as 35%. The

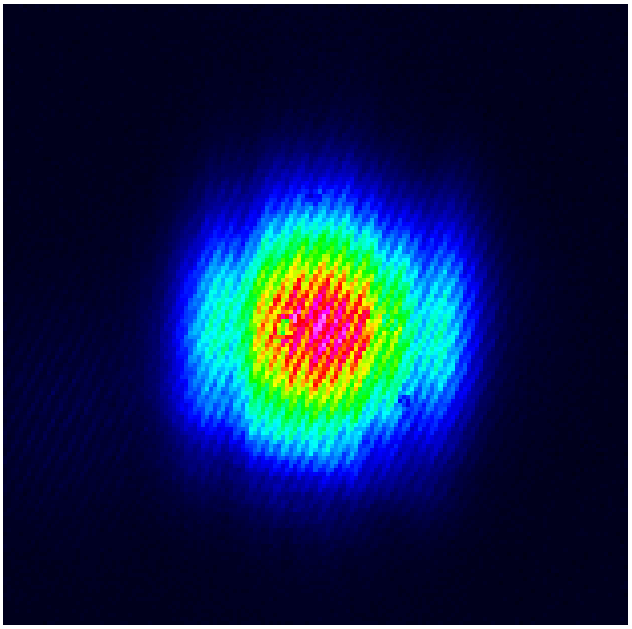

Figure 9.2.4: Beam profile of the output of one of the Toptica doubling cavities taken using Thorlabs BC106N-UV beam profiler. The beam has a nearly-Gaussian shape with discernible vertical bands on both sided. These bands do not contain much power, and so do not cause any unexpected problems with either rotational cooling or detection.

EOM is driven by Conoptics 25D high-voltage driver. By adjusting bias voltage and amplitude of modulating signal, modulation of full π rad depth is achievable (90° polarization rotation). In order to find proper bias voltage and laser alignment, we placed a polarizing beam-splitter cube after the EOM and directed both polarization components to their respective photodetectors. When the laser is aligned, and bias voltage chosen correctly, the polarization extinction ratio reaches maximum. We adjusted the EOM's alignment by placing it on a 4-axis stage, such as Newport's NewFocus 9071, and provide stability by mounting it in a V-shaped mount.

To find appropriate modulation amplitude, we connect the TTL input of our high-voltage EOM driver to a function generator, such as BK Precision 4063, which we run at desired modulation frequency. As was shown in the previous chapter, modulation frequencies of $\sim$ 1 MHz are most suitable. We set the TTL input to be a square wave of 3.3 V amplitude and aforementioned frequency. Photodiodes are fast enough (nanosecond rise time) to capture power changes occurring with such frequency. Therefore, we simply adjust the drive amplitude until we reach exactly modulation depth of π radians shown in Fig. 9.2.5a.

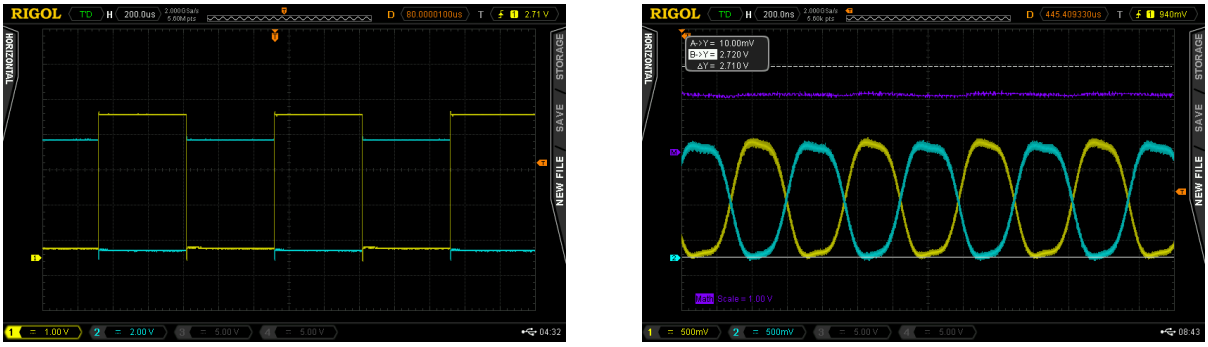

(a) Polarization switching.

(b) Polarization modulation.

Figure 9.2.5: Oscilloscope screenshots depicting polarization switching and modulation. Both show a perfect π rad modulation (90° polarization rotation). Traces show light intensity of orthogonal linear polarizations hitting the photodiode. **a)** Switching was performed at 100 kHz frequency due to limited photodiode bandwidth. Measured photodiode voltages were different due to imperfect alignments. **b)** Modulation was performed at 1.56 MHz. The purple trace is sum of both photodiode signals and is constant over time.

On the detection laser, polarization is sinusoidally modulated by a resonant Qubig AM6-UV polarization modulator showing very high laser power transmission of around 98%. It is driven by sinusoidal signal of another arbitrary function generator at resonant frequency of about 1.56 MHz. Before reaching the modulator, output of the function generator is first amplified by about 20 dB by an off-the-shelf RF amplifier - the EOM requires sufficiently high drive amplitude in order to provide π rad modulation depths. In order to reach desired modulation depth, we need to place a quarter-wave plate before the modulator and properly align the laser as well.

The UV laser beam, just after leaving the UV doubler, was passed through Thorlabs WPQ05M-266 quarter-wave plate before going through the EOM, which was mounted on Thorlabs PY005 5-axis stage that provided stability and ability of fine position adjustment. Like before, we placed a polarizing beam-splitter cube together with two photodiodes downstream from the modulator. The first step in the optimization process was quarter wave-plate rotation angle adjustment - we moved it until light intensity on both photodiodes was identical in the presence of no modulation (due to making the polarization nearly circular). Next, we started adjusting both frequency and amplitude of modulating signal until we observed two 180° out-of-phase sinusoidal signals of same amplitude and minimum of ~ 0 V on our photodiodes shown in Fig. 9.2.5b. Reaching that point

required slight adjustment of EOM's position and quarter-wave plate's rotation angle as well.

9.2.2.4 Multipassing

After the polarization is switched on the rotational cooling laser, we asymmetrically expand it using a cylindrical lens telescope with adjustable magnification. We create an elongated beam of an approximately ellipsoidal shape of $\sim 2.4 \times 7.4$ mm. This beam is then passed through a vacuum UV window AR coated at laser's wavelength in order to minimize transmission losses. On the other side of the rotational cooling chamber, on a linear translation stage we placed UV AR-coated CVI P180-100-266-UV 90° angle prism. The laser beam undergoes internal reflection inside the prism and then propagates through the rotational cooling chamber in the opposite direction. Identical prism is placed on the side of UV doublers, just in front of the vacuum window. Using these two prisms, we manage to multipass the laser beam through the rotational cooling chamber $17 - 19$ times (Fig. 9.2.6).

Even though every pass incurs a power loss, this method creates an interaction region of decently uniform laser intensity that is about 7 mm tall and 25 mm long. The height of the interaction region allows us to be certain that we talk to the molecules that end up being detected downstream, while the length leads to approximate interaction time of $\sim 250\ \mu s$. In Chapter 7 we showed that 50 μs should be more than enough to fully perform the cooling with the caveat that we have sufficiently intense laser. While we work with a beam of smaller intensities than assumed in simulations (our real Rabi rate can be estimated to be on the order of $3\,\Gamma$ for the first beam entering the chamber with total power in the beam of about 50 mW), we have ample interaction time, and, therefore, expect to realize the cooling process in its entirety.

In the case of the detection laser, the beam is first expanded using Thorlabs BE03-266 UV beam expander with $3\times$ magnification and then passed through the UV AR-coated vacuum chamber windows. Here, we also placed an identical prism on the other side of the chamber, but not on the side of UV doublers, so the laser beam passes the detection chamber twice. Because the detection transitions do not require very high intensities or interaction times to scatter maximum possible number of photons, as will be soon explained, this setup is sufficient. This configuration creates an interaction region ~ 1 cm long (interaction time of $\sim 50\,\mu s$) and ~ 6 mm tall with estimated Rabi rates of $\sim 1\,\Gamma$. Finally, we should note that while in the previous section we discussed how

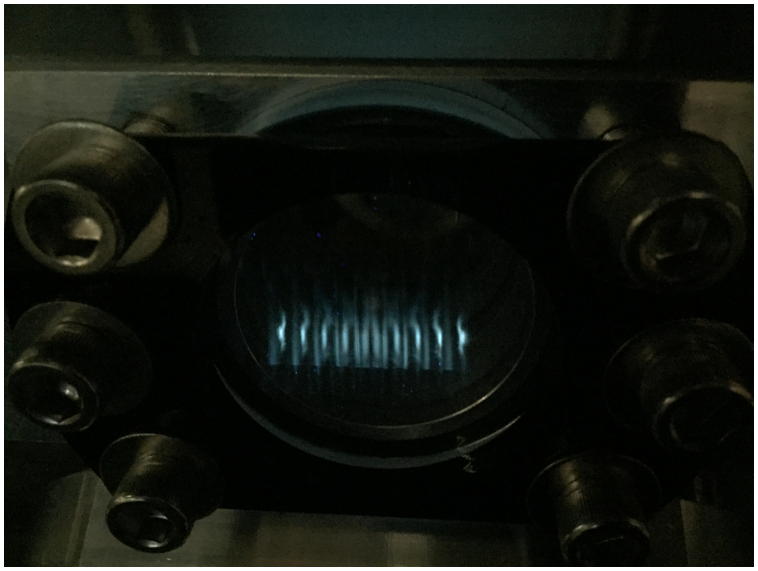

Figure 9.2.6: Picture of rotational cooling chamber's UV window showing the multipassed elongated laser beam.

the velocity spread affects the observed signal, and sidebands placement as a way of increasing the number of molecules we talk to, in this experiment our goal was to simply observe the process occurring, and so we performed it *without* laser phase modulation.

9.3 Microwave Sources

In the rotational cooling process, apart from the laser, microwaves play an important role. As was shown in Chapter 7, we require two sets of microwaves: one coupling $J = 1$ with $J = 2$, and one coupling $J = 2$ with $J = 3$. The rotational cooling chamber is designed in such a way, that these microwaves can propagate at an angle of $\pm 45^\circ$ with respect to the laser beam in the plane perpendicular to the molecular beam (Fig. 9.3.1). They are emitted by microwave horns with microwave lenses attached to them. These lenses ensure that the microwave beam is Gaussian and focused exactly where molecules interact with the laser. The horns are just outside of the vacuum chamber behind a special large vacuum window. Its thickness and index of refraction are such, that the transmitted microwaves of frequencies 26.6 GHz and 40 GHz constructively interfere (the window creates a small Fabry-Perot cavity) resulting in high power transmission.

The microwave-generating setup for $J = 1 \leftrightarrow J = 2$ is depicted in Fig. 9.3.2 with major compo-

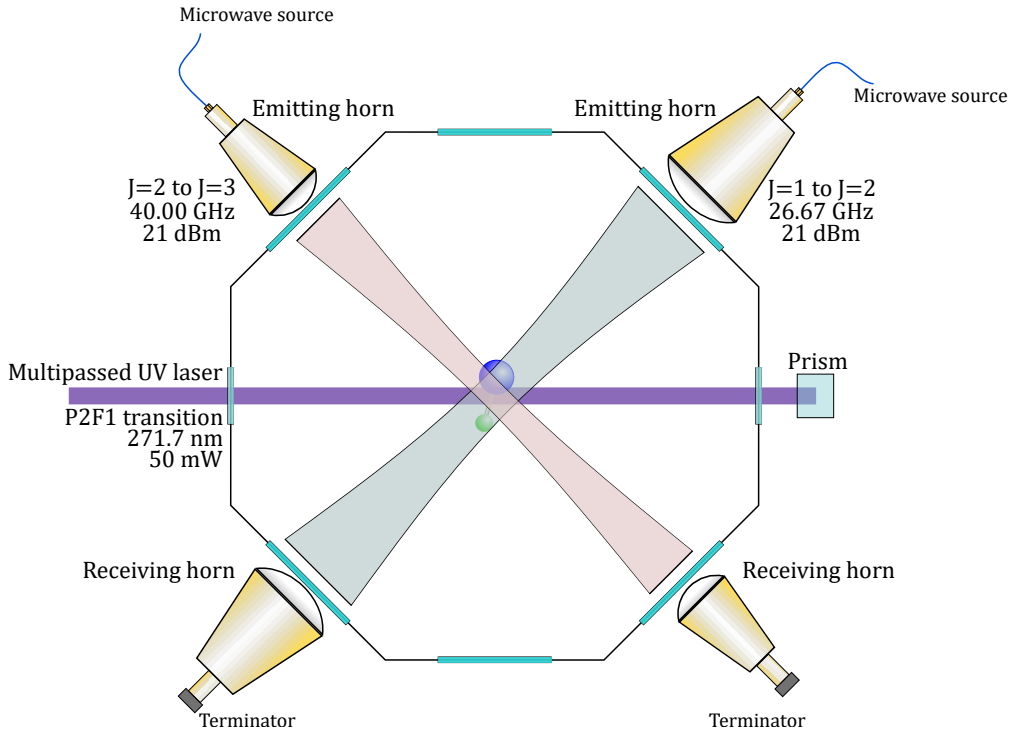

Figure 9.3.1: Schematic of the rotational cooling chamber with laser and microwave beams included. Both microwave beams propagate at $\pm 45°$ angle with respect to the laser beam in the plane perpendicular to the molecular beam.

nents included ($J = 2 \leftrightarrow J = 3$ system has the same architecture, but with components designed for different frequency). All of our microwaves are generated by a computer-controlled Windfreak Technologies SynthHD microwave synthesizer. It allows external modulation and attaching an external 10 GHz reference. We tested accuracy of generated microwaves with and without an external reference, for which we used SRS FS740 Rubidium clock, with a spectrum analyzer and observed that connecting external frequency reference does not cause any discernible change in accuracy. The synthesizer can generate microwaves with powers up to 10 dBm and frequencies up to 20 GHz. We generated microwaves with frequencies 10.001 GHz and 13.334 GHz, and output power of up to 5 dBm.

Microwaves of sub-20 GHz frequencies can be transmitted using SM cables with standard SMA termination, while microwaves in the $20 - 40$ GHz range require KM cables. Both, incur quite high transmission losses in power, so it was important to keep the connectors as short as possible. We therefore connected the synthesizer output with a short SM cable to an active doubler (Marki

Microwave ADA 1020) in case of the 26.6 GHz microwaves, and to an active quadrupler (Norden Millimeter NQ3350G10P10) in case of the 40 GHz microwaves. Both components amplify the signal by several dBm, which is then put into a KM cable.

The next major component is a so-called SPDT (single pole double throw) switch, which depending on voltage applied to its TTL pin, sends the signal through one of its two outputs. We do this to be able to modulate microwaves' polarization. These distinct outputs, controlled by an external modulation signal, can then be directed to different inputs of an orthomode transducer, which results in emission of linearly polarized microwaves with polarizations perpendicular to one another. We use Pasternack Enterprises PE71S6215 SPDT switch in the case of 26.6 GHz microwaves, and Eravant (previously known as Sage Millimeter) SKD-2734034560-KFKF-A3 switch for 40 GHz ones.

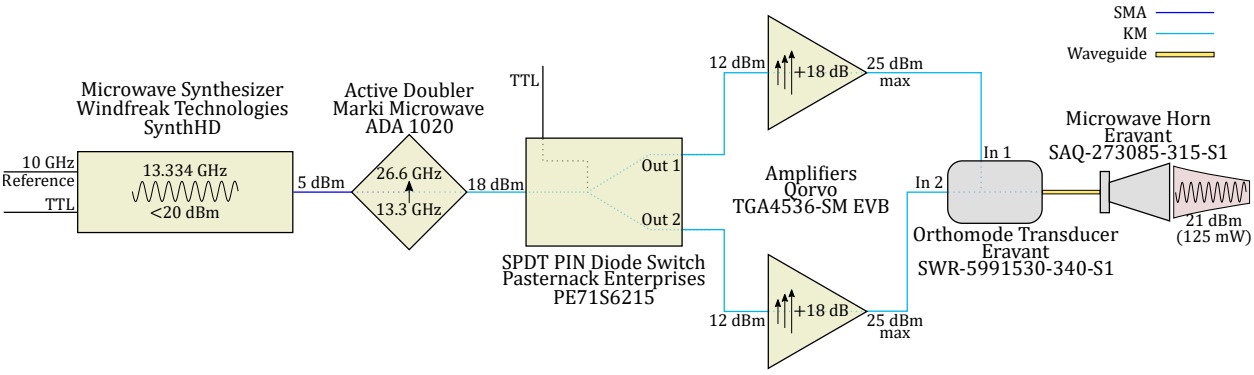

Figure 9.3.2: Schematic of the 26.6 GHz-generating $J = 2 \leftrightarrow J = 3$ microwave system with major components included. We modulate their polarization by directing the signal to different inputs of an orthomode transducer by using an SPDT switch. Power measurements were taken with Rhode&Schwarz NRP50S power meter. The 40 GHz $J = 2 \leftrightarrow J = 3$ system has identical architecture.

Before reaching the transducer, the microwaves need to be amplified. Given the beam waists of a couple centimeters, we need approximately 100-150 mW of microwaves in the beam interacting with the molecules. That corresponds to about 20-22 dBm output horn output power. Given all the losses, an active frequency multiplier is not enough. Because the SPDT switch is responsible for significant losses, we place amplifiers after both of its outputs. For 26.6 GHz microwaves we use Qorvo TGA4536-SM EVB amplifiers, and Spacek Labs SP394-30-30 for 40 GHz microwaves. The Qorvo amplifiers, while specified to amplify the signal by 18 dBm, have a maximum output of

$25 - 27$ dBm. Because of that, we can operate the microwave synthesizer at powers as low as -5 dBm and obtain the same power output from the amplifiers.

Amplified 26.6 GHz signals are finally directed to Eravant SWR-5991530-340-S1 orthomode transducer, and 40 GHz towards Eravant SAT-FQ-22422-S1 transducer. These are then connected via a waveguide to a microwave horn. The $J = 1 \leftrightarrow J = 2$ setup uses Eravant SAQ-273085-315-S1 horn, while Eravant SAQ-403085-219-S1 horn is used by in the $J = 2 \leftrightarrow J = 3$ setup. In both cases we can easily obtain 21 dBm of output power. In general, power budget for both setups is very similar. Values shown in Fig. 9.3.2 were obtained by connecting the outputs to directional couplers, such as Eravant SCD-0632732912-SF-SA for 26.6 GHz and SCD-1834032012-KF-SA for 40 GHz, and directing the auxiliary output (decreased by 20 or 30 dBm) to a power meter such as Rhode&Schwarz NRP50S. Finally, on the side opposite to the emitting horn, we placed identical receiving horns (Fig. 9.3.1) connected to a terminator. These horns can also be connected directly to the power meter, which allowed us to measure power transmitted through the chamber.

Initially, the frequency modulation signal for $J = 1 \leftrightarrow J = 2$ microwaves, connected to the TTL port on the SPDT switch, was generated by the same function generator that creates modulation signal for laser's polarization switching EOM. The microwave-modulating signal is a square wave with the same modulation frequency and a $\pi/2$ phase offset with respect to the laser's polarization-modulating signal. The third modulating signal (for the 40 GHz microwaves) was identical, but the phase offsets were changed to $\pi/3$ and $2\pi/3$.

9.4 Detection System

The detection chamber is directly connected to the rotational cooling chamber and the distance between both interaction regions is about 60 cm. The connection between these chambers was initially 6" in diameter, which led to light scattered from the rotational cooling UV windows to reach the detection setup. To ameliorate that problem, we installed a beam collimator with a 1 cm diameter (in addition to the 4 mm apertures mentioned earlier). To further reduced the light scatter inside the detection chamber, its interior walls were painted with Alion Quart MH2200 black paint. Finally, we installed additional 6"-long 2"-diameter nipples on both sides of the detection chamber through which the detection laser propagates. They minimize the amount of light scattered from

the UV windows reaching the detection region.

The fluorescent light is detected by a head-on Hamamatsu P375 photomultiplier tube with quantum efficiency at 271.7 nm of about $20 - 25\%$ and a circular active area of 46 mm diameter. We keep the PMT outside the vacuum chamber, as is shown in Fig. 9.4.1, and collect the light directly via a fused silica polished lightpipe. The lightpipe is 1' long and has a 2" diameter. It is placed about 1 cm below the interaction region and its outer cylindrical surface inside the vacuum chamber is shielded by 2"-diameter lens tubes made of blackened aluminum.

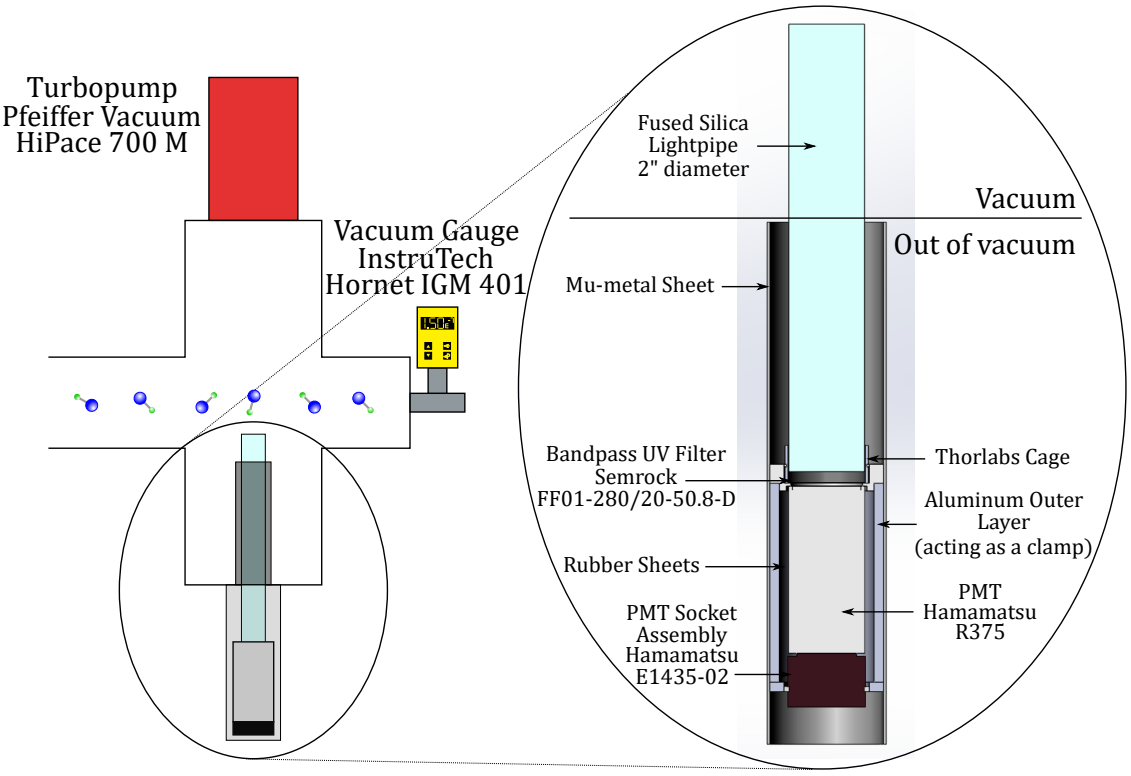

Figure 9.4.1: Schematic of the detection chamber with a magnified view of the cross-section of the PMT assembly.

The lightpipe leaves the vacuum chamber through a special flange and connects to the PMT assembly. Placed between the lightpipe and the PMT active area is a Semrock FF01-280/20-50.8-D UV bandpass filter, which is placed inside a Thorlabs cage (lens tube). PMT's output is connected to Hamamatsu E1435-02 socket and both are wrapped in a rubber sheet and placed in a clamping aluminum cover. That cover, together with lens tube and the out-of-vacuum part of the light pipe are then wrapped in a mu-metal sheet providing some magnetic field shielding. Finally, a clamp

(not shown in the figure) touching the mu-metal sheet is placed around the PMT, and attached via 4 rods to the bottom of the vacuum chamber.

The PMT was at the beginning operated at an input voltage of -1 kV. Initially, big amount of scattered light reaching the PMT and chosen PMT voltage caused it to operate in the nonlinear regime, i.e. the output signal voltage was no longer depending linearly on the incident light's intensity. This caused unusual problems - we observed a stronger signal (higher gain) when the amount of background light was higher. Placing a beam collimator fixed the issue by substantially reducing the amount of scattered light. Additionally, out of caution, we lowered the voltage to -850 V. The output signal of the PMT is directed towards SRS SR445A 350 MHz pre-amplifier, where it undergoes three amplification processes, each increasing the signal by a factor of 5. The output then goes through a 1 kHz low-pass filter, and the filtered and amplified signal is eventually connected to the data-collecting oscilloscope.

9.4.1 Data Collection

Rotational cooling data collection has to be performed in a way that would allow to measure accumulation in desired states. Theoretical details on how this can be achieved are shown in the next chapter. Here, we just mention that this requires performing fluorescence spectroscopy at various transitions and comparing the signals with and without rotational cooling. We achieve that by installing a shutter at the output of the P2F1 transition-driving laser's UV doubler (Fig. 9.2.1) and interchangeably collect appropriate data.

The data collection is performed by National Instruments PXIe-5171 8-channel 250 MHz oscilloscope that is interfaced with a computer with the help of National Instruments PCIe-8381 card allowing a 3.2 GB/s data transfer. One of the oscilloscopes inputs is connected to the output of the PMT amplifier, while another one obtains a TTL signal that initiates a single data collection event resulting in a time series with PMT voltage on the y-axis. The signal is collected for a total time of 20 ms in 10 μs steps resulting in 2000 data points (with an exception of the final data collection run, where we increased the number of data points to 2500 and total time to 25 ms). Each time series (time-of-flight data), together with additional information such as instantaneous frequency of rotational cooling and detection lasers, their lock status or status of the shutter, are recorded as separate datasets and attributes in an hdf5 file.

We control the data collection sequence by programming the Spincore PBESR-PRO-250-USB-RM programmable pulse generator. It controls the exact timing of ablation, shutter opening and closing, and data collection initialization. In most of the experimental runs, the ablation laser was sent a 10 Hz TTL signal. Identical TTL signal was directed to the PXIe oscilloscope in order to initialize the data collection. Another signal, with frequency of 5 Hz was sent to the shutter. The shutter we use is SRS475 laser shutter and it requires a typical 3.3 V TTL signal that is provided by the pulse generator. This signal was delayed with respect to the ablation-controlling signal by about 30 ms - we want the shutter to open or close after the 20 ms-long data collection shot, but before the next one. Given a 10 Hz ablation frequency, time between the shots is 100 ms, so a 30 ms delay should work well - 70 ms is enough for this shutter to open or close.

We collect one time-of-flight data instance with rotational laser going through the chamber and interacting with the molecules, and then one without. Comparing both allows us to deduce the sought-after values. Such approach allows us to estimate effects of rotational cooling by minimizing the shot-to-shot signal variance - while we scan the motorized mirror controlling the location of ablation, the scan is slow enough to allow for high degree of similarity between consecutive shots. However, as we will discuss in the next chapter, the number of shots with or without rotational cooling laser that is used for analysis is chosen to be higher than 1 in order to be able to average several results, which helps to improve signal-to-noise ratio and further average out the shot-to-shot variation.

Chapter 10

Rotational Cooling Results

10.1 Theoretical Predictions

Before we move on to presenting results of the experiment, we would first like to investigate how the rotational cooling process and its efficiency can be measured experimentally and what its signatures are. First, we will look at the detection transitions that can be used to deduce the accumulation of population in the desired state.

Next, we will show how the detection line strength change depending on the details of the rotational cooling process. We would like to see what results we expect if we simply perform optical pumping on the rotational cooling transition with or without the help of microwaves, or with or without polarization switching.

10.1.1 Accumulation Detection Lines

In order to perform measurements on the ground rotational state and see the effects of rotational cooling we need measure line strengths of transitions, which would be sensitive to the population in all Zeeman sublevels. Using two transitions, which we will call, using spectroscopic notation, R0F2 and R0F1, we were able to estimate the population in the final $|J = 0, F_1 = 1/2, F = 0\rangle$ state. Fig. 10.1.1 shows these transitions.

The line strength of both transitions depends on the populations in different sublevels in the ground rotational manifold. In the case of the R0F2 transition, regardless of laser's polarization, due to selection rules we have 3 ground state sublevels in the $|J = 0, F = 1\rangle$ hyperfine state and

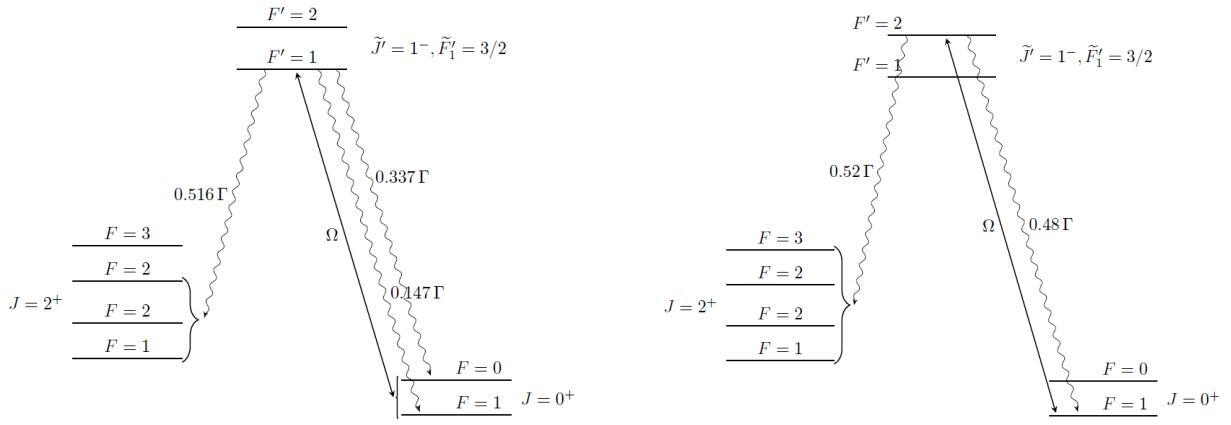

(a) R0F1. (b) R0F2.

Figure 10.1.1: Detection transitions. **a)** R0F1 transition is sensitive to total population in the whole ground rotational state, while **b)** the R0F2 transition is sensitive only to population in the $F = 1$ hyperfine state.

5 available excited state sublevels (this line is separated from the R0F1 line by about 300 MHz), which means no dark states will be created. The line strength of this transition is proportional to total number of photons scattered, which in turn depends on the number of interacting molecules and number of photons per molecule we can obtain from this process. Because in our experiment the number of all molecules that can interact with the detection laser is on average constant, the total number of photons will depend on the *percentage* of all molecules that do interact with the detection laser, which in our calculations is represented by the populations appearing in the density matrix. Assuming L_{R0F2} is the line strength of the transition and that we completely remove the population from the interacting states, we have:

$$L_{\mathrm{R0F2}} = \alpha \rho_{|J=0,F=1\rangle} = \alpha \left(\rho_{1,-1} + \rho_{1,0} + \rho_{1,1}\right),$$

where ρ_{F,m_F} represent populations in Zeeman sublevels of the hyperfine state F in the ground rotational manifold $J = 0$, and α is a proportionality constant. We should note that while the exact number of photons we obtain per interacting molecule from this transition depends simply on the rotational branching ratios and is $n_\gamma \approx 1.92$, it is not relevant to our calculations - this number is already included in the constant α.

In the case of the R0F1 transition, the situation is slightly more complicated. This transition couples to all 4 sublevels (ground state splitting is only on the order of 10 kHz as shown in Fig. 2.2.1)

in the $J = 0$ manifold, while in the excited $F' = 1$ state it couples to 3 sublevels - a dark state will be created and it will depend on laser's polarization. Fortunately, a simple polarization modulation or switching procedure will destabilize it. Like in the case of the R0F2 transition, if we assume that we completely remove population from the interacting states, we can write:

$$L_{\mathrm{R0F1}} = \beta \rho_{|J=0\rangle} = \beta \left(\rho_{0,0} + \rho_{1,-1} + \rho_{1,0} + \rho_{1,1} \right),$$

with a different proportionality constant (in this case number of photons per molecule is very similar, $n_\gamma \approx 1.94$).

If we define L^{RC} as line strengths after the rotational cooling process, we can easily find ratios:

$$k_{\mathrm{R0F1}} \equiv \frac{L^{\mathrm{RC}}_{\mathrm{R0F1}}}{L_{\mathrm{R0F1}}} \qquad\qquad k_{\mathrm{R0F2}} \equiv \frac{L^{\mathrm{RC}}_{\mathrm{R0F2}}}{L_{\mathrm{R0F2}}}. \tag{10.1.1}$$

If we assume that the initial populations before a rotational cooling process in all Zeeman sublevels of $J = 0$ manifold are equal, i.e. $\rho_{0,0} = \rho_{1,-1} = \rho_{1,0} = \rho_{1,1}$, then one can show that the factor by which the population has increased in the final $|J = 0, F_1 = 1/2, F = 0\rangle$ state is:

$$r_f \equiv \frac{\rho^{\mathrm{RC}}_{0,0}}{\rho_{0,0}} = 4k_{\mathrm{R0F1}} - 3k_{\mathrm{R0F2}}. \tag{10.1.2}$$

In the experiment, by measuring line strengths of both R0F1 and R0F2 transitions before and after rotational cooling, we will be able to use Eq. (10.1.1) and Eq. (10.1.2) to estimate how big the gain we achieve is and compare it to predictions obtained from numerical simulations.

10.1.2 Effects of Rotational Cooling on Detection

To make experimental predictions, we simulated both R0F1 and R0F2 transitions that we have just described. In the simulations we tried to emulate real experimental values of various parameters. In them, we assumed a conservative $T_{\mathrm{det}} = 25\ \mu s$ interaction time, laser with uniform intensity, beam diameter of $d_{\mathrm{det}} = 4.5$ mm and total power $P_{\mathrm{det}} = 32$ mW ($\Omega_{\mathrm{det}} \approx 3.1\,\Gamma$). For the R0F1 transition we also assumed polarization modulation with $f_{\mathrm{mod}} = \gamma \approx 1.6$ MHz and depth of $\beta_{\mathrm{mod}} \approx \pi$ rad. For such parameters the whole ground rotational manifold becomes depopulated.

In order to properly measure the line strength, we used procedure similar to the one, when we were discussing optical cycling and average scattering rates. Namely, the total number of photons scattered, and so the line strength, can be written as $N_\gamma = \widetilde{\Gamma}\, T_{\mathrm{det}}$ with $\widetilde{\Gamma}$ defined analogically to

Eq. (6.3.2). Because decay rate Γ is the same for all the excited states we are using, for simplicity we can define the line strength as:

$$L \equiv \sum_i \int_0^{T_{\text{det}}} \rho_{e_i,e_i} dt, \tag{10.1.3}$$

where the sum is over all excited states.

Having chosen detection transitions, parameters and a measuring method, we simulated the detection transitions for various initial populations, where each one was a final population of a rotational cooling process. To obtain those populations we simulated the chosen benchmark scheme with previously used parameters. We chose to simulate the process without the microwaves (simple optical pumping) first, with and without polarization switching, in order to have a guideline prediction with the simplest experimental realization. The benchmark scheme with microwaves was also simulated with and without microwave polarization switching. In figure Fig. 10.1.2 we compare evolution of populations in different rotational states for the aforementioned processes.

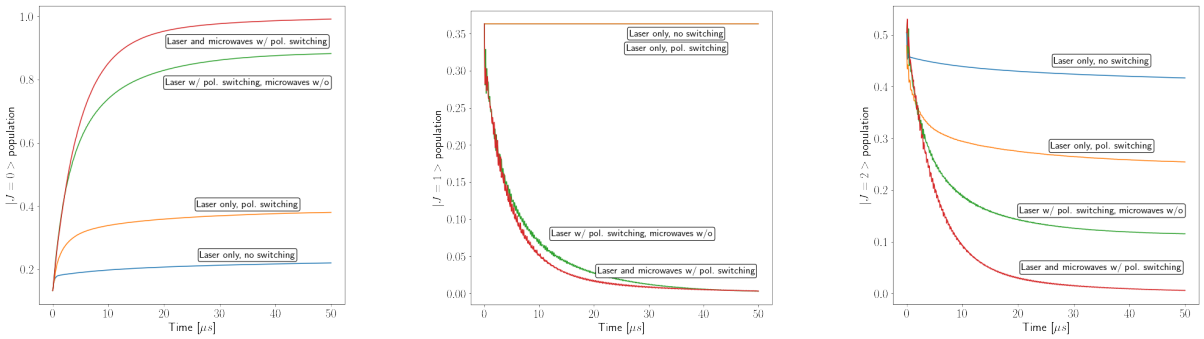

(a) $J = 0$. (b) $J = 1$. (c) $J = 2$.

Figure 10.1.2: Evolution of populations in first three rotational states in the benchmark rotational cooling process with: laser only and no polarization switching, laser with polarization switching only, laser with polarization switching and microwaves without, both laser and microwaves with polarization switching.

To show how the line strengths are expected to change, we also plotted the first 5 μs of time evolution of excited state populations in both detection transition. Fig. 10.1.3 shows these for: initial populations with no rotational cooling process, and after the optical pumping processes with and without polarization switching (P2F1 transition without the $J = 1 \leftrightarrow J = 2$ microwaves).

Finally, in table 10.1.1 we included predictions for all the variations of the rotational cooling

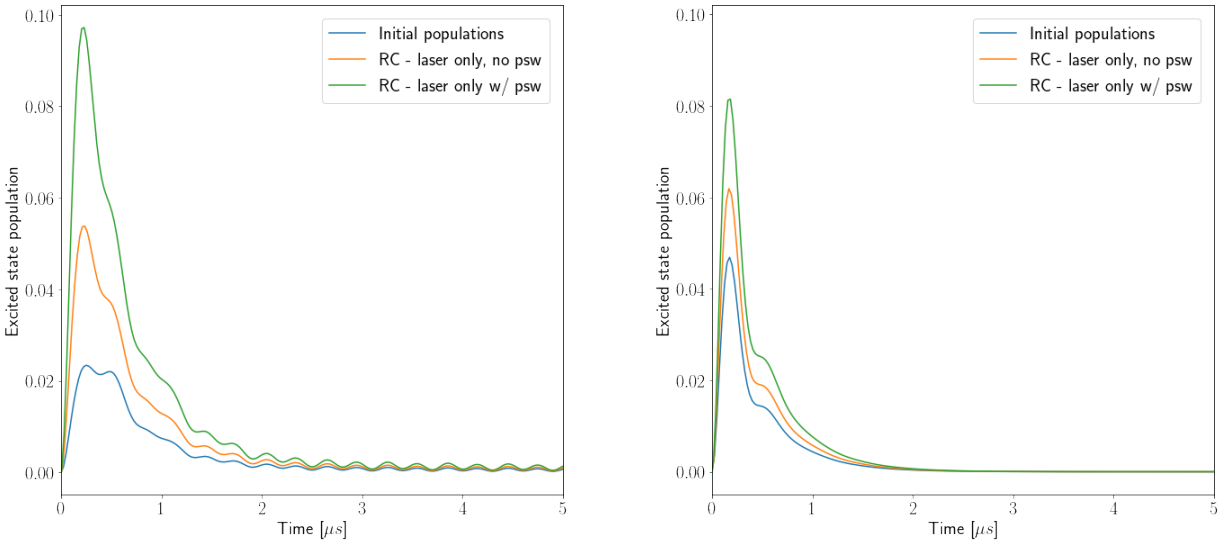

(a) R0F1.

(b) R0F2.

Figure 10.1.3: Time evolution of excited states' populations for both detection transitions for initial populations without a preceding rotational cooling process, and with preceding optical pumping on the P2F1 rotational cooling transition.

benchmark scheme. We calculated the predicted increase in the final state's population directly from populations obtained in numerical simulations, and by using Eq. (10.1.2) with the ratios that are presented in the table. The ratios were obtained from rounded line strengths that are shown in the table and were calculated using Eq. (10.1.3). We can see that the predicted factors r_f agree well (up to rounding errors) with the direct results of our numerical simulations.

Scheme	Rotational Cooling Details				$\rho_{0,0}$	$\rho_{1,-1}$	$\rho_{1,0}$	$\rho_{1,1}$	L_{R0F1}	L_{R0F2}	k_{R0F1}	k_{R0F2}	$\frac{\rho_{0,0}^{\mathrm{RC}}}{\rho_{0,0}}$	r_f
	Ω_L	f_L^{psw}	$\Omega_{\mu_{12}}$	f_μ^{psw}										
Initial	-	-	-	-	0.033	0.033	0.033	0.033	25.00	18.94	1	1	1	1
Benchmark	Yes	No	No	No	0.095	0.042	0.043	0.042	41.39	23.84	1.65	1.26	2.88	2.85
Benchmark	Yes	Yes	No	No	0.208	0.058	0.061	0.058	71.89	33.54	2.89	1.78	6.30	6.19
Benchmark	Yes	Yes	Yes	No	0.555	0.106	0.115	0.106	167.27	62.31	6.69	3.29	16.80	16.89
Benchmark	Yes	Yes	Yes	Yes	0.630	0.117	0.126	0.118	188.01	68.57	7.52	3.62	19.10	19.22
Initial	-	-	-	-	0.022	0.022	0.022	0.022	16.55	12.32	1	1	1	1
Benchmark - full	Yes	Yes	Yes	Yes	0.655	0.112	0.118	0.111	190.94	64.92	11.54	5.27	30.32	30.35

Table 10.1.1: Summary of predicted line strengths and population increase in the desired final state. All results are based on the benchmark scheme described in Chapter 7 and use the same parameters. Columns 2 through 5 represent information about the scheme used - columns labeled "Ω" show whether or not transition was used, while f^{psw} say if the corresponding light field had its polarization switched. The second-to-last column was calculated directly from the estimated populations, while the last column was evaluated using Eq. (10.1.2). We see that the estimates are quite accurate.

In the table we also included results for a full benchmark rotational cooling process that includes the $J = 3$ rotational manifold and $J = 2 \leftrightarrow J = 3$ microwaves. Because the numerical values of populations represent the percentage of molecules in given state, in the full simulations we begin with a smaller number molecules in the ground $J = 0$ rotational state relative to population in the first four rotational states $J = 0 - 3$.

It is also worth noting that results for incomplete rotational cooling, that is either without any microwaves or with one pair of microwaves, but without polarization switching, are only as good as the parameters used. Change of interaction time or Rabi rates would lead to factors k_{R0F1} and k_{R0F2} different than shown in the table above, and so we expected presented numbers to be only ballpark estimates of what we will actually see in the experiment. In the case of full rotational cooling, because we are removing population from $J = 1 - 3$ states completely, parameters other than used in simulations should lead to very comparable results as long as they lead to full removal of aforementioned populations. In the experiment, we expect the interaction time to be long enough

for the process to finish even for Rabi rates smaller than assumed in calculations presented here. Therefore, these predictions should be more accurate.

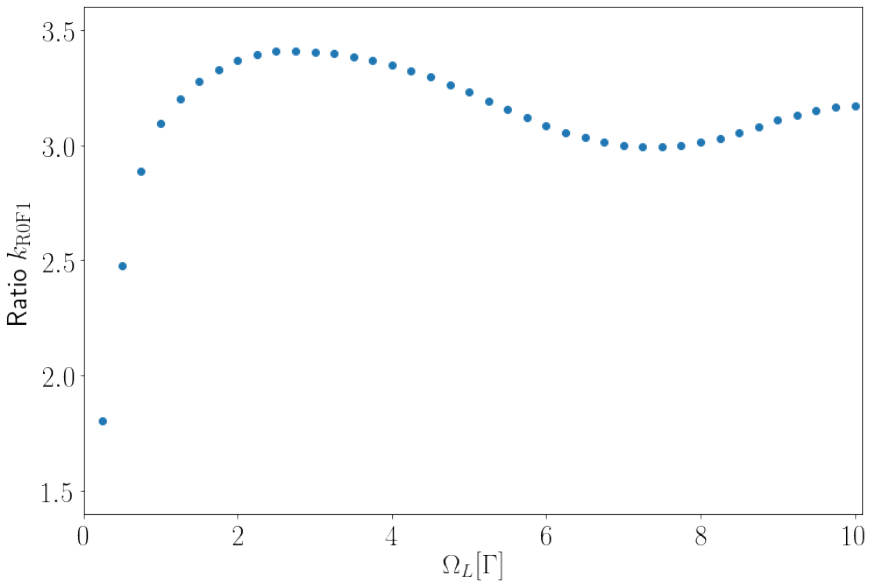

Figure 10.1.4: Ratios of R0F1 transition's signal strengths with and without the rotational cooling process including only the P2F1 transition's laser for different values of laser's Rabi rate.

To further emphasize this point, in Fig. 10.1.4 we show k_{R0F1} ratios as a function of rotational cooling's P2F1 laser's Rabi rate Ω_L in the benchmark scheme without microwaves and with laser's polarization switching (the third row of table 10.1.1). We can clearly see that depending on the laser's power, the sought-after ratio might vary and the maximum is reached when true Rabi rates, that is including the dipole transition matrix elements, are comparable to naturally occurring remixing rate related to energy splittings, as was discussed in Chapter 5. In reality, the beam is not only multipassed through the rotational cooling chamber, but it also has an elliptical Gaussian profile, which means that molecules see a spatially varying Rabi rate as they move.

Additionally, the non-zero transverse velocity spread creating Doppler shifts in the rotational cooling molecule-laser interaction causes the efficiency (and so the ratio as well) of this process to decrease. With the apertures that we installed at the entrance and exit of the rotational cooling chamber, $\sim 90\%$ of the molecules that reach the detection chamber and interact with the laser have transverse velocities $|v_t| \lesssim 2$ m/s limiting the Doppler shifts to at most $\sim 5\,\Gamma$. While for the R0F1 and R0F2 detection lines this makes little difference (50 μs interaction time, 30 mW laser

power and required scattering of only 2 photons per molecule ensures scattering to completion), this spread will still influence the final result. Finally, a small percentage of those molecules might not talk to the rotational cooling laser - trajectories going above or below the multipassed laser, and yet reaching the detection region are possible. Full Monte Carlo trajectory simulations with realistic laser beam shapes and experiment's geometry show that we should expect the k_{R0F1} ratio, in the discussed case of laser-only interaction, to be around 3.

10.2 Results

Having made predictions we are now interested in comparing them to the experimental results. First, however, we need to address some of the issues that come up during the data analysis and choose one and consistent method of approaching the experimental data.

10.2.1 Data Analysis

Analyzing the experimental data seems, on the face of it, rather easy. We simply need to look at signal strengths, i.e. integrals of the PMT signals, with and without the rotational cooling process taking place, and compare both. However, there are some complications, some stemming from the experimental imperfections themselves, but some because we need to look at ratios of two random numbers.

If we assume that we collected the experimental signals and their integrals are normally distributed around their respective means (and, for simplicity, the same variances), i.e. $X_1 = \mathcal{N}(\mu_1, \sigma)$, $X_2 = \mathcal{N}(\mu_2, \sigma)$ shown in Fig. 10.2.1a, estimating the true ratio of their means μ_1/μ_2 from the distribution of their ratios X_1/X_2 is not straight-forward. The ratio distribution, shown in Fig. 10.2.1b, does not have any well-defined moments such as the mean, although empirical estimators can still be obtained. It is also a heavy-tailed distribution with many potential outliers. For this reason the empirical mean does not provide a good estimate of normal distributions' means' ratio (in our case it overestimates them). The median value, on the other hand, seems to be pretty accurate in this estimation. However, that is the case if the ratio distribution can be constructed - we need enough ratio data points and the variances of both normal distributions cannot be unreasonably large. Empirically, what helps is filtering the data by removing the outliers, even just the

last percentile, and by keeping the ratios above 0.

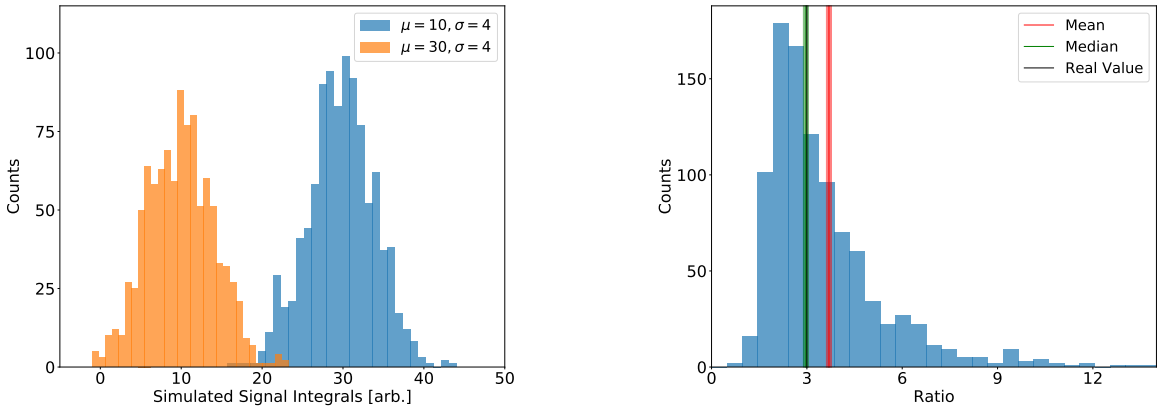

(a) Normal distributions.

(b) Ratio distribution.

Figure 10.2.1: Simulated distribution of signals' integrals. The ratio distribution obtained from two normal distributions is heavy-tailed and does not have well-defined moments. Its median provides the best estimate of the ratio of normal distributions' means.

Of course, one could ask why not just obtain the means of the normal distributions first, and then calculate the ratio. Unfortunately, due to experimental imperfections this method does not provide good and consistent results. The problem is the shot-to-shot noise created by the necessity of moving ablation spots on the target. Otherwise, we could expect the signal to perform a kind of symmetric random walk leading to a normal distribution of its integrals. However, because the signal decays quite quickly, and after putting the apertures the number of molecules reaching the detection region is severely limited, we must move between different location on the target. That causes sudden random changes of signal's strength akin to a jump process. Averaging the integrals of signals with and without the rotational cooling process over the whole data run results then in incorrectly estimated ratios.

The problem can be somewhat ameliorated by ablating a spot on the TlF target 50 times - 25 with the shutter open (with the P2F1 laser reaching the rotational cooling chamber) and 25 with it being closed. The signal was found to be quite stable over this many shots. Then, we can move to another spot and repeat the process. When analyzing the data, we could then bunch 25 signals together and obtain a good estimate of the ratio for every ablated spot, and next combine all ratios

into one ratio distribution. Given the total number of shots of, usually, 4000, this method might not provide enough data to obtain a good estimator. Hence, instead we decided to bunch 2 signals together obtaining in the end 1000 ratios creating a robust distribution.

The whole data analysis process was performed in following steps. First, we subtracted the background mean from obtained PMT signals by looking at the first 3 ms of the time-of-flight data[1]. Then, we averaged two consecutive signals with the shutter open and two with shutter closed, and calculated integrals of both average signals. On most occasions we did not perform any filtering of the signals, but when we did, for example by removing signals resulting in negative or very small integrals, we did it in pairs - if either of the consecutive signals, with the shutter open or closed, had to be removed, both of them were, and so the overall number of signals with shutter open or closed stayed the same.

Once all the integral ratios were obtained, we first removed the last percentile (we kept the lowest 99% of values), and removed ratios smaller than 0. In vast majority of cases the data was robust and this filtering process did not affect the estimate in any way. Finally, we estimated the sought-after ratios by taking median of the remaining integral ratios. As the error of the estimate we chose to use error of the empirical mean, i.e. $\bar{s}/\sqrt{n}$, where $\bar{s}$ is empirical standard deviation and n is number of averaged data points.

10.2.2 Line Searches

One of the first experimental data was taken before the full rotational cooling setup was constructed. We first needed to identify spectral lines of TlF and find their approximate frequencies, and results for a couple of them are depicted in Fig. 10.2.2. In the experiment the most crucial were frequencies of: the P2F1 rotational cooling line, R0F1 and R0F2 detection lines, and Q1 and Q23 quasi-cycling lines that were used for depletion measurements. Once these were found, before every data run we would center the lasers close to the measured frequencies by looking at the wavemeter, locking them to the Cesium reference laser, and then narrowly scanning their frequencies in a 20 MHz range in IR (80 MHz in UV). After the scans were performed, center of their lines were dictating the choice of the frequency lockpoint that the software had to be set to.

Even though the effective rotational constant is known to a good precision, and so should be

[1]To be more precise, we used points from the interval between 1.25 ms and 2.5 ms.

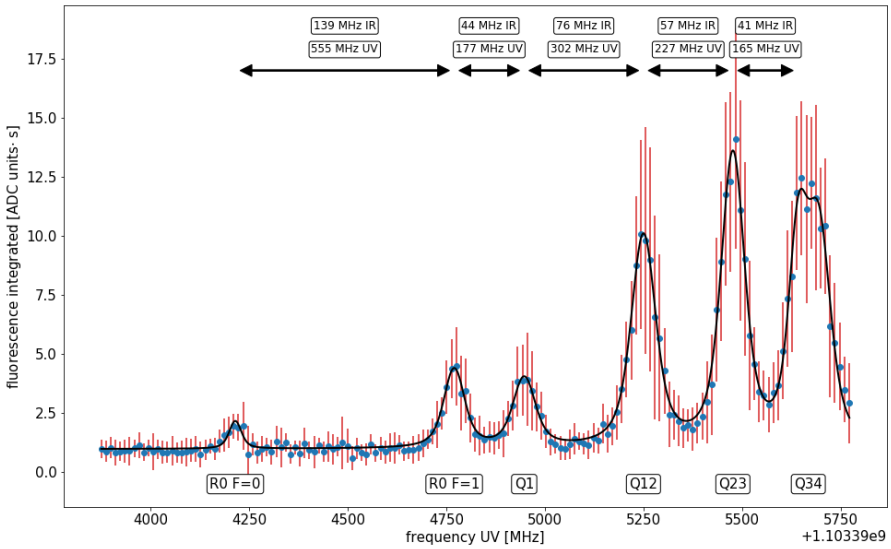

Figure 10.2.2: Spectral lines of TlF obtained through a frequency scan of the detection laser.

the $J = 1 \leftrightarrow J = 2$ and $J = 2 \leftrightarrow J = 3$ transition frequencies, we scanned microwave frequencies to confirm our prediction. In the case of the 26.6 GHz transition, we performed the scan by looking at population depletion in the $J = 1$ rotational state, which can be measured by looking at the Q1 line. Of course, by solely including the microwave interaction, populations of $J = 1$ and $J = 2$ states would simply mix - it would be a coherent population transfer process. This would not result in strong signal changes. Instead, we performed a rotational cooling measurement with both the P2F1 laser and the microwaves. By looking at the Q1 line in the detection region, we would expect the signal to drop drastically after the population in $J = 1$ is removed via the rotational cooling process. Indeed, in Fig. 10.2.3a we see a clear signature of depletion at a particular frequency with a Lorentzian lineshape fitted to the data. The obtained frequency matches the expectation - the transition occurs at 26.669 GHz.

The other microwave transition could potentially be measured using a similar procedure by looking at the Q23 line, which is sensitive to population in both $J = 2$ and $J = 3$ rotational state. However, to perform this scan we instead decided to see if the resonance signature can be seen by looking at the accumulation in the $J = 0$ state measured through the R0F1 detection line. As

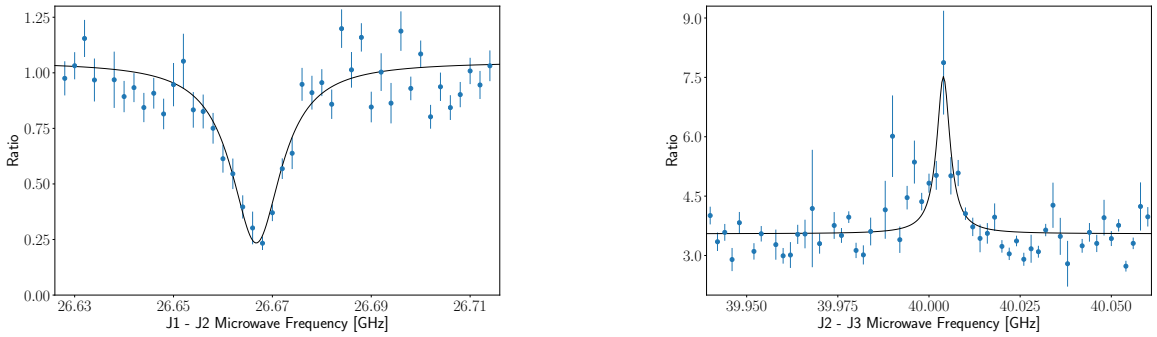

(a) $J = 1 \leftrightarrow J = 2$ microwave frequency scan.

(b) $J = 2 \leftrightarrow J = 3$ microwave frequency scan.

Figure 10.2.3: Microwave frequency scans using the rotational cooling process and detection centered on: **a)** Q1 line which measures depletion in the $J = 1$ rotational state; **b)** R0F1 line measuring accumulation in the $J = 0$ rotational state. We fitted Lorentzian lineshapes to both datasets to find center of every line.

shown in Fig. 10.2.3b, the resonance can be found and it is centered at 40.004 GHz.

10.2.3 Optical Pumping as Proof of Principle

The first measurement that we performed did not include any microwaves, and so it was strictly a optical pumping process removing population from the $J = 2$ rotational state and accumulating it in the ground rotational state. In this measurement, polarization of the P2F1 transition laser was switched with frequency of 1.5 MHz, which was slightly less than the frequency used in numerical simulations (and for which we obtained reasonably good results), but slightly more than the 1.22 MHz estimated at the beginning of Chapter 7 to be related to characteristic time of the spontaneous decay. Even though in the end we are interested in the r_f ratio representing population accumulation in the final $|J = 0, F_1 = 1/2, F = 0\rangle$ hyperfine state, initially, we checked how the k_{R0F1} ratio, measuring changes in total population in $J = 0$, behaves with changing rotational cooling laser power. In this and all other measurements presented the power of the detection laser was always around 30 mW.

The obtained ratios are shown in Fig. 10.2.4 and show an improvement with higher laser power. If we were to believe ratios acquired through numerical simulations and presented in Fig. 10.1.4, it seems that we are in the regime on the far left part of the plot, and observe a quick increase

in the accumulation in $J = 0$ with increasing power. The last three points would then point to a slight decrease in the ratio following the predictions. However, the predictions were created for an idealized experiment, and the last three data points are rather inconclusive when it comes to estimating how the data fits the predictions. In the end, it is not of high importance - a full rotational cooling process for our 250 μs interaction time should work quite efficiently for a rather large range of powers.

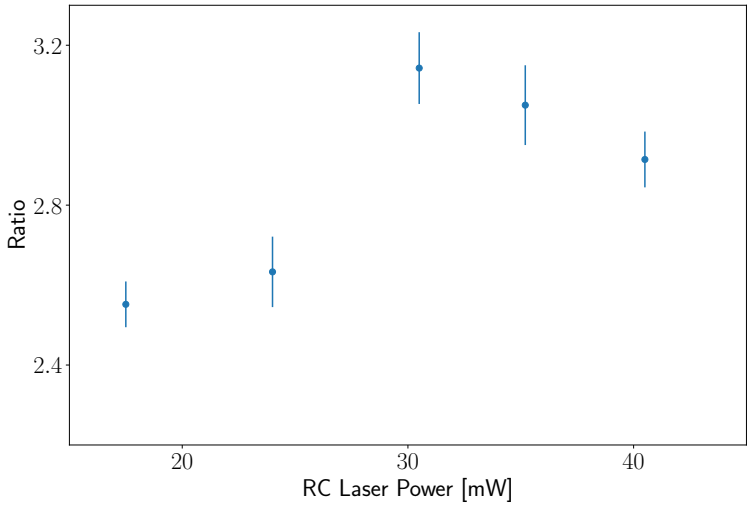

Figure 10.2.4: Measured R0F1 line strength ratios for different powers of the rotational cooling laser addressing the P2F1 transition.

Next, to follow the conditions for which results in table 10.1.1 were obtained, we measured both the k_{R0F1} and k_{R0F2} ratios with the rotational cooling laser's power of 45 mW. In Fig. 10.2.5 we present average PMT signals (after mean subtraction) with the shutter open and closed (so with and without the rotational cooling process, or simply optical pumping in this case, taking place). For clarity, both signals were plotted after applying a moving average filter with a very short window. The rotational cooling process results in the integral of the R0F1 signal increasing by a factor of 3.000 ± 0.083, and the R0F2 signal by 1.739 ± 0.029, as calculated using procedure described in the previous section. These ratios are very close to the ones predicted in simulations. Using Eq. (10.1.2), we can calculate that through this optical pumping process the population of the $|J = 0, F_1 = 1/2, F = 0\rangle$ hyperfine state increases by a factor of $r_f = 6.78 \pm 0.34$.

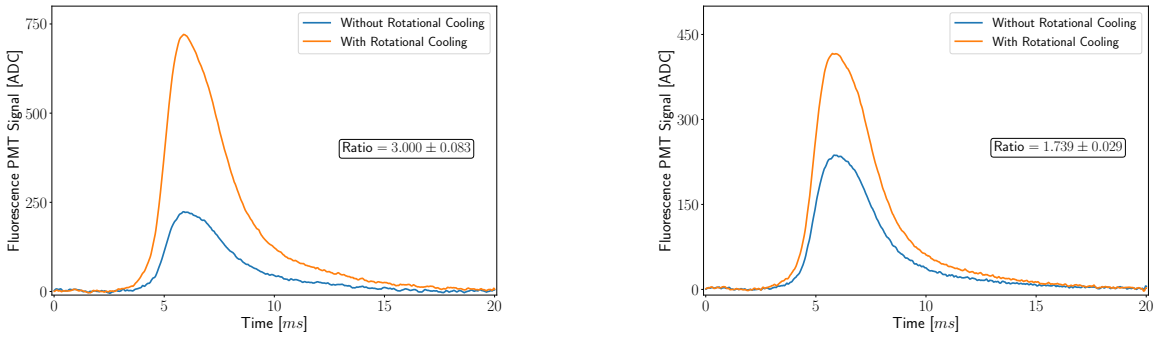

(a) R0F1 line.

(b) R0F2 line.

Figure 10.2.5: Average time-of-flight PMT signals with and without rotational cooling process taking place. **a)** The R0F1 transition resulting in a ratio $k_{\mathrm{R0F1}} = 3.000 \pm 0.083$ and **b)** the R0F2 transition leading to a $k_{\mathrm{R0F2}} = 1.739 \pm 0.029$ ratio. The rotational cooling process only included interaction with the P2F1 laser. The y-axis is provided in data acquisition hardware's internal analog-to-digital conversion (ADC) units.

This measurement was also performed to show that our data analysis method argumentation is sound. To do that, we plotted histograms of different filtered ratios obtained from measuring effects of rotational cooling on both detection lines. These are presented in Fig. 10.2.6 and both show skewed and heavy-tailed distributions very similar to the simulated one depicted in Fig. 10.2.1b. We also placed calculated mean and median on the plots - the mean is larger due to the outliers.

10.2.4 Rotational Cooling with $J = 1 \leftrightarrow J = 2$ Microwaves

Next, we turned on the 26.6 GHz microwaves and performed a proper rotational cooling measurement following the "benchmark" scheme discussed before. While keeping the P2F1 transition laser at a power of about 45 mW, we performed two scans: first, we scanned power of used microwaves, and then, we looked at how the effects of rotational cooling change with changing polarization switching frequency. The former was performed with a previously-used 1.5 MHz polarization switching frequency and the power was measured through a receiver horn on the other side of the rotational cooling vacuum chamber. The real power in the chamber was estimated to be about 1.5 dBm higher. Like in the previous power scan, we looked at the accumulation in $J = 0$ represented by strength of the R0F1 line. Results of this scan are shown in Fig. 10.2.7a. As

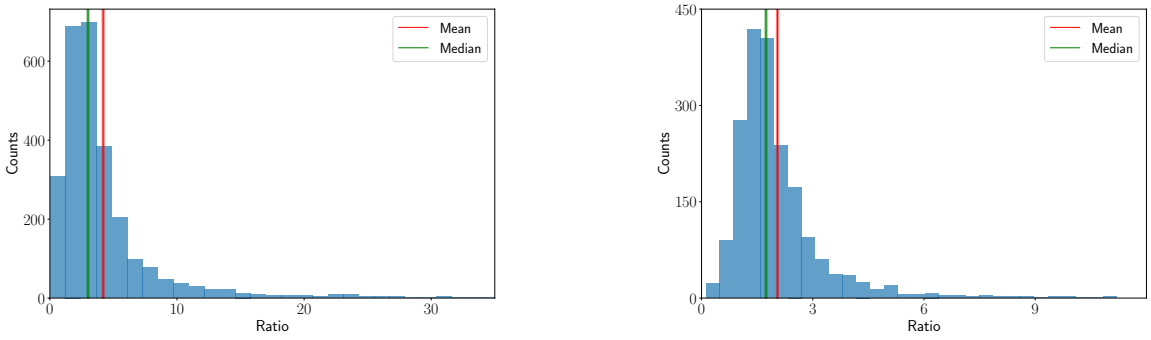

(a) R0F1 line.

(b) R0F2 line.

Figure 10.2.6: Histograms of filtered ratios obtained from a rotational cooling measurement representing their observed distributions, which follow a predicted skewed and heavy-tailed ratio distribution obtained from a ratio of two normal random variables.

expected, the scan reveals that once the microwaves reach certain power, the efficiency plateaus and the signal stops growing.

For the next measurement, and all the subsequent ones, we kept the microwaves at about 20 dBm power as measured by the receiver horn (corresponding to about 140 mW of microwave power inside the chamber). The polarization switching frequency was the same for both the laser and the microwaves, but with a $\pi/2$ phase offset assumed in the simulations. Experimentally, this can be set up by simply using a coupling function between two channels of a function generator. The scan, presented in Fig. 10.2.7b, reveals that in this regime, i.e. between 0.2 MHz and 2 MHz, the frequency does not play a major role. That is to be expected given our rather long interaction time and reasonably high Rabi rates. At the high end of the scan, that is at 2 MHz, the signal enhancement seems to get slightly lower, as it should, although we would require more data to reach a proper conclusion.

Having set the polarization switching frequency to 1.5 MHz as before, we again performed measurement of the ratios required to calculate the r_f factor we were looking for. Average signals of those measurements are depicted in Fig. 10.2.8, and the ratios obtained were $k_{\mathrm{R0F1}} = 6.422 \pm 0.174$ and $k_{\mathrm{R0F2}} = 2.888 \pm 0.033$, which lead to the population enhancement factor of $r_f = 17.02 \pm 0.70$, quite close to the predictions. It is worth noting that the difference between the obtained ratio

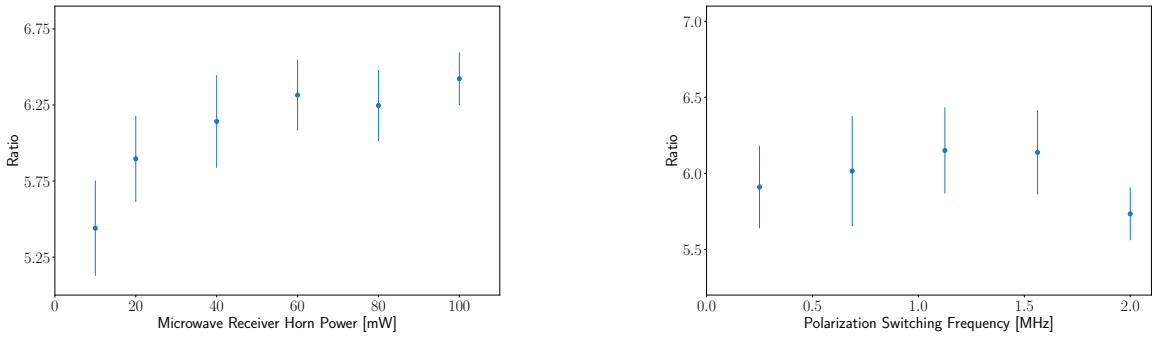

(a) Microwave power scan.

(b) Polarization switching frequency scan.

Figure 10.2.7: k_{R0F1} ratios for a rotational cooling process with the $J = 1 \leftrightarrow J = 2$ microwaves included obtained for different values of **a)** microwave power and **b)** polarization switching frequency of both the rotational cooling laser and the microwaves.

and the predicted value of ~ 19 is equal to about 10%, which could be taken as an estimate the number of molecule that are either outside of desired transverse velocity range obtained by placing two apertures, or that do not completely go through the multipassed rotational cooling laser.

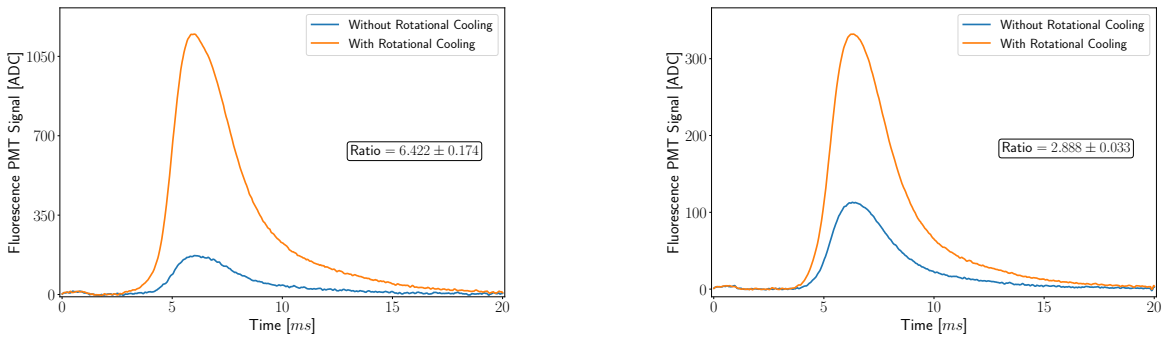

(a) R0F1 line.

(b) R0F2 line.

Figure 10.2.8: Average time-of-flight PMT signals with and without rotational cooling process taking place, which included both the P2F1 laser transition and the $J = 1 \leftrightarrow J = 2$ microwave coupling. **a)** The R0F1 transition resulting in a ratio $k_{\mathrm{R0F1}} = 6.422 \pm 0.174$ and **b)** the R0F2 transition leading to a $k_{\mathrm{R0F2}} = 2.888 \pm 0.033$ ratio. The y-axis is provided in data acquisition hardware's internal analog-to-digital conversion (ADC) units.

One additional measurement that can be performed is measurement of population removal (depletion) from the $J = 1$ rotational state. That can be easily achieved by looking at the cycling Q1 transition (Fig. 6.4.1) detailed in Chapter 6. This transition, while detected without full dark state remixing (there are no $J = 0 \leftrightarrow J = 1$ microwaves in our detection region), should be a good measure of remaining population, and should provide a strong clear signal. Ideally, after the rotational cooling takes place, this signal should average to zero. However, as can be seen in Fig. 10.2.9, there still is a non-zero residual signal. The actual ratio obtained on this transition was $k_{\mathrm{Q1}} = 0.100 \pm 0.001$ again confirming that we were left with approximately 10% of our molecules in their original states.

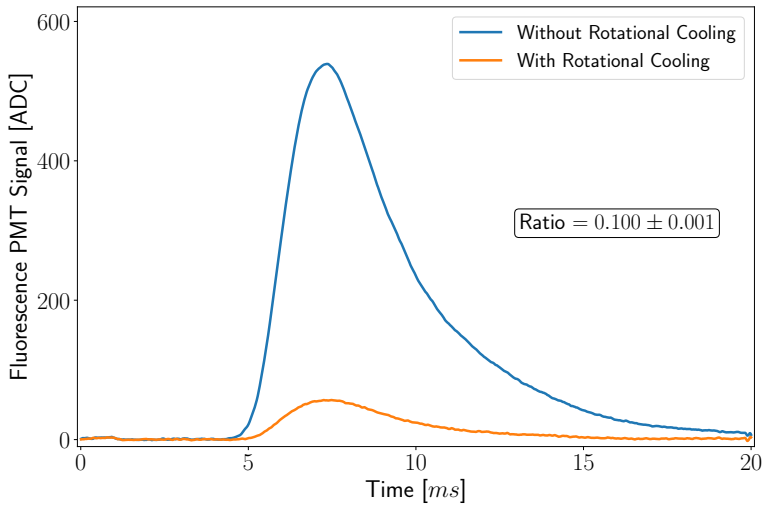

Figure 10.2.9: Average time-of-flight PMT signal with and without rotational cooling process taking place, which included both the P2F1 laser transition and the $J = 1 \leftrightarrow J = 2$ microwave coupling for the Q1 transition measuring population depletion in the $J = 1$ state. The measured ratio is $k_{\mathrm{Q1}} = 0.100 \pm 0.001$. The y-axis is provided in data acquisition hardware's internal analog-to-digital conversion (ADC) units.

10.2.5 Full Rotational Cooling

Finally, we added the last set of microwaves coupling $J = 2$ and $J = 3$ rotational states. Just like when we added the first set of microwaves, we performed a power scan and polarization switching frequency scan by measuring the k_{R0F1} ratio. The former was performed by adjusting current drawn

by microwave amplifiers, in contrast to the previous set of microwaves where we could adjust the power by adjusting the power at the source, and the emitted power was estimated by taking into account predicted losses on components downstream from the amplifiers. Polarization switching was set to 1.5 MHz and phase offsets between the laser and the other set of microwaves were $2\pi/3$ and $\pi/3$ respectively (in simulations we assumed $\pi/2$ and $\pi/4$ offsets) providing the most optimal combination of different fields' polarizations. Setting precise phase offsets between three different channels required us to connect two separate 2-channel function generators and synchronize them. The first channel of the first function generator provided the TTL signal to one of the polarization switching components, while the second channel was connected to a trigger input of the other function generator. Once the trigger was obtained, an infinite "burst" of a square TTL signal was initiated after an appropriately set delay. The delay was different for both channels and it determined the exact phase offset between all the signals. For these measurements, given that the signals were expected to be larger than before, the data was collect over 25 ms, not 20 ms.

The power scan of Fig. 10.2.10a is, rather surprisingly, consistent with a straight line. The data, however, was really noisy mostly due to vary large spot-to-spot variations of the signals and difficulty in finding a good place on the target to perform the ablation. Notwithstanding, we chose to subsequently operate this set of microwaves at about 325 mW of emitted power. The effects of changing polarization switching frequency were measured for a wider range than previously. This time the data more clearly shows that after reaching frequencies $\gtrsim 1.5$ MHz the ratio slightly drops matching our expectations.

For the final k_{R0F1} and k_{R0F2} ratio measurements we set the polarization switching frequency to 1 MHz. Average signals from these measurements are shown in Fig. 10.2.11 and show ratios of $k_{\mathrm{R0F1}} = 8.746 \pm 0.267$ and $k_{\mathrm{R0F2}} = 3.763 \pm 0.120$. These are below the predictions of table 10.1.1 by a wider margin than before, and so is the enhancement r_f in the final hyperfine state - we can calculate that $r_f = 23.70 \pm 1.13$, about 20% lower than the factor of 30 predicted for perfect rotational cooling.

Like before, we then performed a depletion measurement, this time on the quasi-cycling Q23 transition line (Fig. 6.5.1) being also one of the most prominent lines in TlF at our rotational temperature. This transition is a proxy for combined populations of $J = 2, 3$ rotational states, with the same caveat as before - without the microwave remixing some population inevitably ends

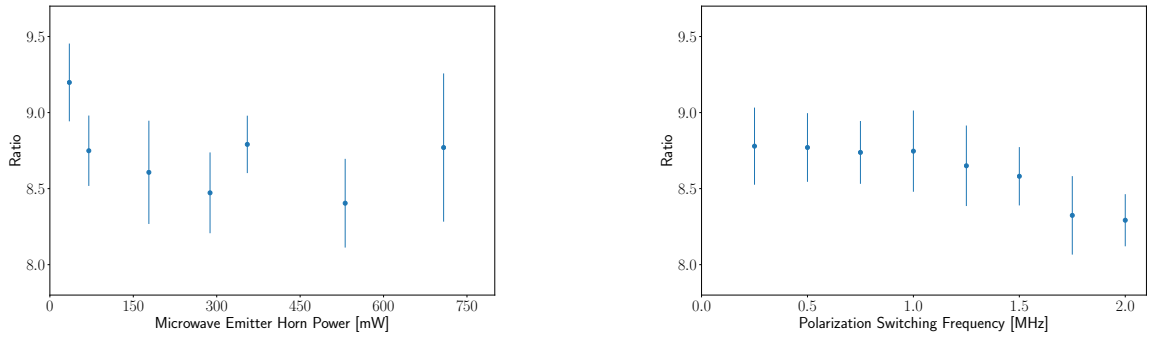

(a) Microwave power scan.

(b) Polarization switching frequency scan.

Figure 10.2.10: k_{R0F1} ratios for a rotational cooling process with both the $J = 1 \leftrightarrow J = 2$ and $J = 2 \leftrightarrow J = 3$ microwaves included obtained for different values of **a)** $J = 2 \leftrightarrow J = 3$ microwave power and **b)** polarization switching frequency of the rotational cooling laser and both sets of microwaves.

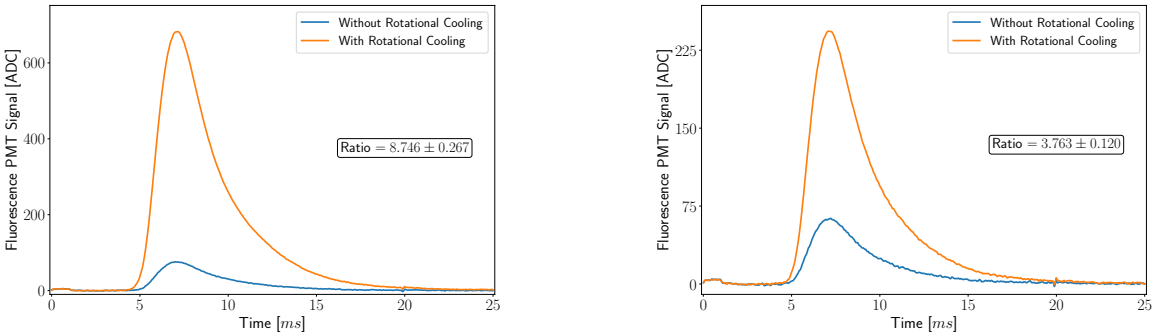

(a) R0F1 line.

(b) R0F2 line.

Figure 10.2.11: Average time-of-flight PMT signals with and without rotational cooling process taking place, which included both the P2F1 laser transition, the $J = 1 \leftrightarrow J = 2$ microwave coupling, as well as the last set of microwaves coupling $J = 2$ and $J = 3$ rotational states. **a)** The R0F1 transition resulting in a ratio $k_{\mathrm{R0F1}} = 8.746 \pm 0.267$ and **b)** the R0F2 transition leading to a $k_{\mathrm{R0F2}} = 3.763 \pm 0.120$ ratio. The y-axis is provided in data acquisition hardware's internal analog-to-digital conversion (ADC) units.

up in the dark state subspace. However, the obtained ratio, ideally 0 for complete state population depletion, should have still provided valuable information telling us what percentage of the initial population remained in the $J = 2, 3$ states after rotational cooling. As shown in Fig. 10.2.12, the

ratio, just like in the case of the Q1 depletion measurement, is equal to 0.101 ± 0.001. The depletion measurements while pointing to a 10% drop in efficiency comparing to the idealized situation, can be interpreted as such if the population is removed from hyperfine states within the $J = 1, 2, 3$ rotational manifolds uniformly. The depletion measurements without a proper remixing procedure look at population changes in the bright states with respect to these transitions. It is possible, however unlikely, that the dark state population had not been removed through the rotational cooling process with the same efficiency.

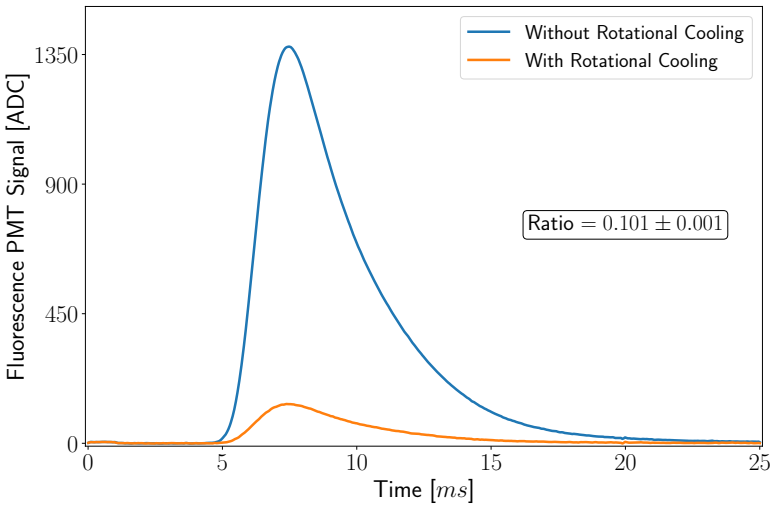

Figure 10.2.12: Average time-of-flight PMT signal with and without rotational cooling process taking place, which included both the P2F1 laser transition, the $J = 1 \leftrightarrow J = 2$ microwave coupling, as well as the last set of microwaves coupling $J = 2$ and $J = 3$ rotational states, for the Q23 transition measuring population depletion in both $J = 2$ and $J = 3$ states. The measured ratio is $k_{Q23} = 0.101 \pm 0.001$. The y-axis is provided in data acquisition hardware's internal analog-to-digital conversion (ADC) units.

10.3 Limitations and Possible Improvements

All in all, the observed increase in the $|J = 0, F_1 = 1/2, F = 0\rangle$ population is substantial - a factor of ~ 24. Comparison of growing average PMT fluorescence signals for the R0F1 line obtained for the "benchmark" scheme of rotational cooling with different light fields included is presented in Fig. 10.3.1. It shows a quite staggering improvement in signal's strength. The results are also with

a rather good agreement with theoretical predictions.

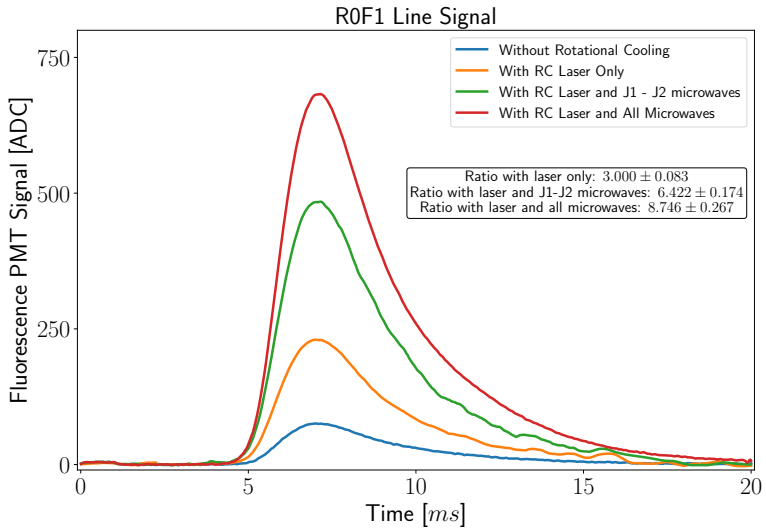

Figure 10.3.1: Average time-of-flight PMT signals for the R0F1 detection transition: without the rotational cooling, only with the optical pumping process, with both the P2F1 laser transition and the $J = 1 \leftrightarrow J = 2$ microwave coupling, and with the laser transition and both microwave couplings. The signal grows significantly, albeit the ratios do not reach the maximum value possible to obtain in an idealized situation. The y-axis is provided in data acquisition hardware's internal analog-to-digital conversion (ADC) units.

The discrepancies can be mostly explained by the fact that not all molecules that are detected undergo a full cooling process. As was mentioned before, not only does some portion of the detected molecules not talk to the high-intensity parts of the multipassed P2F1 transition laser beam, but also those that do can have quite large transverse velocities, and thus Doppler shifts, thereby limiting the efficiency of the process. We estimated the percentage of such molecules to be about 10%. However, even out of the remaining 90% not all of the TlF molecules might get transferred to the ground rotational manifold. A full Monte Carlo simulation with accurate depiction of all the light fields and real molecular trajectories is necessary to fully compare theory to the experiment.

If the results are indeed limited by the transverse velocity spread we have two solutions - we can either power broaden the P2F1 transition laser beam, i.e. increase its power, or add sidebands through phase modulation. Adding more power is the simpler option. Currently, the polarization-switching EOM incurs a $\sim 35 - 40\%$ loss in the UV laser power. Replacing it with a resonant

polarization-modulating EOM (a sine-wave modulation would work just as well) with losses no larger than $\sim 3\%$ would greatly increase available power. On the other hand, if we are limited by size of the beam, we can simply try expanding it further.

A less likely explanation points towards a rotational temperature of the beam being slightly higher than expected from the previous measurements. This would lead to population being more concentrated in higher rotational states, which would decrease the percentage of molecules accessible via rotational cooling inside the beam. One reason for that might be Ne flow lower than when the initial measurement was performed, although this is probably not the case. Our flow is only about 10 sccm smaller and we believe that we provide more than enough neon for the ablated TlF to quickly thermalize.

The performed experiment was also limited in its precision due to various imperfections. One of the major issues we experienced was the inconsistency of the molecular beam intensity, and therefore strength of our signal. The fluctuations were caused by randomness in the TlF target ablation efficiency and highly depended on the ablated spot, as well as ablation laser parameters such as its power and focus. One of the possible solutions to this problem would be placing a new target, preemptively scanning it for good spots and using only these for the actual measurement.

Another issue lowering our signal's SNR was the noise coming from the detection laser's scattered light. While the beam was going through 6"-long nipples on both sides of the detection chamber, both of which had an installed blackened aluminum honeycomb mesh on its inner walls, the chamber's walls were covered with a light-absorbing paint, and the lightpipe sticking inside the vacuum chamber was inside a blackened aluminum tube, the SNR of our R0 transition signals was around 2 for a single shot. We reckon that adding baffles inside the nipples could help us with reducing this noise. Better coated AR windows would also be provide a non-negligible improvement.

The laser systems we used were not always stable either. Any fluctuations coming from the seed lasers, amplifiers or any of the doubling cavities would then automatically be observed as a non-random noise on the PMT and potentially change the calculated ratios quite drastically. The simplest change is to go away with home-built systems altogether. There are currently sold sets of high-power amplifiers connected to single-stage frequency doubling components for a price that is comparable to a price of building a full frequency-doubling apparatus. We actually obtained one such part (MPB Communcations 2RU-VYFA-P-10000-543), which requires us to simply connect

the output of our seed laser to the input fiber of this amplifier-doubler combo. The output at $\sim$ 543.5 nm is already fiber coupled and can be directly connected to Toptica's UV cavity. The green output is also linearly polarized and power-stabilized with maximum power of 1.1 W.

Finally, our reference laser locked to Cesium's D2 line, while very stable on short timescales, experiences slow frequency drifts. These are rather tiny ($\sim$ 2 MHz), but given that we lock our science lasers at the IR frequency, the drift in the UV frequency increases to 8 MHz, or about 5 natural linewidths. Despite the fact that the P2F1 and both R0 detection transitions are quite broad, such drifts might cause a drop in measured rotational cooling efficiency. We plan to further stabilize the system by adding temperature stabilization of the Cs vapor cell and degaussing the magnetic shield it is in.

Chapter 11

Conclusions and Prospects

11.1 Effects of Rotational Cooling

As we have seen in the previous chapter, experimentally obtained enhancement ratio r_f is ~ 24. This is what we achieve for transverse velocities $|v_t| \lesssim 2$ m/s. In CeNTREX, what is of importance is the efficiency of this process for all the molecules that are accepted by the EQL. In Chapter 7 we saw that in the worst-case scenario of maximum Doppler shifts of $\pm 14\,\Gamma$ the r_f factor drops by about 50% compared to an ideal system. However, we can conclude from Monte Carlo trajectory simulations with realistic apparatus geometry that the electrostatic lens should accept molecules with $|v_t| \lesssim 2$ m/s along the **X** direction (laser beam propagation direction) and $|v_t| \lesssim 3$ m/s in the **Y** direction (perpendicular to the laser beam and the molecular beam), leading to the same Doppler shifts of at most $\pm 5\,\Gamma$ that we worked with in our experiment. Therefore, we can expect that the enhancement ratio in full beam experiment will be very close to the one we obtained.

Differences might potentially come from higher velocities along the **Y** direction, which could lead to fewer molecules flying through the rotational cooling interaction region and limiting the overall efficiency. However, small improvements to our experiment described at the end of the previous chapter, such as swapping the polarization-switching EOM for a polarization-modulating one and hence drastically increasing available laser power or further expanding the beam along the **Y** direction, would probably bring the ratio back to the observed value. Adding sidebands to the laser through phase modulation should also help with increasing the r_f factor. All in all, it is reasonable to assume that in CeNTREX we will be working with $r_f \approx 24$.

11.2 Anticipated Sensitivity

As was already briefly mentioned in the introduction and shown in Eq. (1.4.1), in molecular beam searches for EDMs utilizing spin precession experimental precision is dictated by the total precession time and the number of interrogated molecules. To be more specific, in CeNTREX, where we plan to perform a SOF frequency measurement, the molecule-shot-noise limited sensitivity to frequency changes induced by the NSM can be written as:

$$\delta\nu_{\mathrm{SNL}} = \frac{1}{2\pi T}\frac{1}{C_{\mathrm{SOF}}}\frac{1}{\sqrt{N_d N_p}}Z. \tag{11.2.1}$$

In this equation, just like in the general case, T is the total interaction time, which here occurs in the MI region, equal to $L_{\mathrm{SOF}}/\bar{v}_Z$, C_{SOF} is the SOF fringe contrast (slope of the curve around the RF transition resonance that determines sensitivity to changes in frequency ν [36]), and the total number of molecules detected N is divided into N_p - the number of pulses used in the measurement, and N_d - average number of molecules detected per pulse. We hope to obtain fringe contrast $C_{\mathrm{SOF}} \approx 1$, just like it was done in the ACME electron EDM measurement [61]. Finally, because the detection transitions we will be using, i.e. Q1 and Q23, are quasi-cycling transitions, which are not completely closed, an additional factor Z, taking values $1 < Z < \sqrt{2}$ has to be added in order to take into account an excess of noise [99]. To be conservative, we will assume $Z = \sqrt{2}$.

In order to estimate the N_d parameter, we start with the observed time-averaged beam intensity of 5×10^{12} molecules/state/sr/s, corresponding to 1×10^{11} molecules/state/sr/pulse. While the molecules within every pulse are initially distributed according to the Boltzmann distribution, rotational cooling is expected to increase the number of molecules in the $|J = 0, F_1 = 1/2, F = 0\rangle$ hyperfine state by a factor of 24. Then, all three state transfer procedures: SPA, SPB and SPC, are predicted to have efficiencies of 99%, 96% and 96% respectively, giving a combined 91% state transfer efficiency. Next, by assuming the transverse area of the fluorescence detection region to be 18 mm $\times$ 30 mm, and by using true apparatus geometry, we can expect the solid angle subtended by the detection region to be 1.3×10^{-5} sr. Finally, the electrostatic quadrupole lens is predicted to increase the number of molecules reaching the detection region (effectively increasing the detection region's solid angle) 24-fold. Given the currently designed fluorescence collection apparatus and the average number of photons scattered through Q1 and Q23 transitions, the detection efficiency should reach 90%. In the end, we anticipate $N_d \approx 6.1 \times 10^8$ molecules/pulse.

Given the measured average transverse velocity $\bar{v}_Z = 184$ m/s and $L_{\mathrm{SOF}} \approx 2.5$ m, we estimate that CeNTREX sensitivity to frequency shifts should be:

$$\delta\nu_{\mathrm{SNL}} \approx \frac{0.7}{\sqrt{N_p}}\,\mathrm{mHz}. \tag{11.2.2}$$

Assuming a total measurement time typical for molecular beam searches of about 300 hours, and a 50 Hz repetition rate gives $N_p \approx 5.4 \times 10^7$. By plugging this value into Eq. (11.2.2) we obtain $\delta\nu_{\mathrm{SNL}} \approx 90$ nHz, which is equivalent to sensitivity to CP-violating energy shifts of $\delta\Delta_{\mathrm{CPV}} \approx 45$ nHz. For comparison, the previous best limit achieved was $\delta\Delta_{\mathrm{CPV}} \approx 120$ μHz [34], showing that we anticipate to achieve a 2500-fold statistical improvement over the past limits.

11.2.1 Extracting the Energy Shift

The sought-after energy shift Δ_{CPV} can be extracted from the data following schemes similar to the ones used in previous experiments [36, 53, 61, 100]. The asymmetry parameter described in Chapter 3 is given by $\mathcal{A} = \mathrm{sgn}\,(\phi_{\mathrm{SOF}}) \sin\phi_{\mathrm{CPV}}$ if there are no experimental imperfections. However, in reality an additional contribution ϕ' to the accumulated precession phase must be taken into account, and that might appear due to various unwanted effects, e.g. deviations from RF resonance frequencies. Then $\mathcal{A} = \mathrm{sgn}\,(\phi_{\mathrm{SOF}}) \sin(\phi_{\mathrm{CPV}} + \phi')$ and in order to only obtain the phase term related to CP-violating interactions we will need to measure $\mathcal{A}$ under two different conditions where the energy shift Δ_{CPV} reverses its sign. One of such changes in conditions occurs when the direction of the MI electric field $\boldsymbol{\mathcal{E}}_{\mathrm{MI}}$ is reversed. We obtain:

$$\mathcal{A}_{+\mathcal{E}_{\mathrm{MI}}} - \mathcal{A}_{-\mathcal{E}_{\mathrm{MI}}} \approx \pm 2\phi_{\mathrm{CPV}},$$

independent of ϕ' so long as $\phi' \ll 1$. Following [34] we refer to this reversal as E-modulation. It is also possible to reverse the sign Δ_{CPV} in several other ways as well. For example, simultaneously reversing the magnetic fields in state preparation regions B and C, $\mathbf{B}_{\mathrm{SPB}}$ and $\mathbf{B}_{\mathrm{SPC}}$, reverses the signs of all the angular momenta relative to the fixed laboratory $\mathbf{z}$-axis, which corresponds to changing the signs of M_{I_1}, M_{I_2}, and M_J, and hence also the sign of Δ_{CPV}. Other possible ways of changing sign of the energy shift are described in detail in [34], and we plan to use most of them for in-situ diagnostics and independent extraction of the energy shifts.

11.3 Systematic Errors

Most of the EDM searches are also plagued by a myriad of systematic errors. It is important to bring them to values comparable to estimated statistical errors, and here we note a couple most important systematic errors that we anticipate to encounter. The first important contribution comes from non-reversing parts of the $\boldsymbol{\mathcal{E}}_{\mathrm{MI}}$ fields, e.g. stray DC fields. These non-reversing fields will cause the separation between the spin-up and spin-down states of thallium in the $|J=1, M_J=\pm 1\rangle$ science state to change slightly due to the higher-order spin-spin and spin-rotation couplings to distant $\left|\widetilde{J}, M_J\right\rangle$ states, which might then lead to changes in frequencies of the NMR transitions with changing orientation of the MI electric field. This systematic effect can be determined and suppressed by a proper combination of field reversals [34], and accounted for by adding small non-reversing DC offsets, as well as increasing precision of **B**-field reversals.

Another systematic effect, and perhaps the most obvious, comes from stray magnetic fields in the interaction region creating spurious contributions to the measured energy shift. Nominally, the free precession should occur with no magnetic field present. However, in spite of significant effort we will undertake to shield the MI region, some **B**-fields will persist. They can come from many sources, e.g. leakage currents, leakage of ambient magnetic fields through the magnetic shields or residual magnetization of the shield itself. All the these stray fields can act in two ways: by directly creating the energy shifts, or by acting together with motional-field effects.

If we consider the static fields only, for the pair of states used in the SOF measurement, that is pairs e+j and h+k, a **B**-field along $\boldsymbol{\mathcal{E}}_{\mathrm{MI}}$, i.e. B_z, generates a direct frequency shift of ± 2.5 mHz/μG, where the sign applies for the e$\leftrightarrow$j and h$\leftrightarrow$k transition respectively. CeNTREX hopes to obtain residual B-fields below 10 μG, which alone should shift the transition frequency by about ± 25 mHz. However, these stray static field, depending on their origin, will not change under certain combinations of field reversals and modulations. Hence, these effects can be measured and suppressed in the same way the aforementioned ϕ' contribution to the accumulated phase can by suppressed via E-modulation. However, the stray fields originating in leakage currents are more difficult to deal with and none of the modulations can be used to distinguish these shifts from the true NSM signal, since both the leakage currents and the real shift reverse when we flip the $\boldsymbol{\mathcal{E}}_{\mathrm{MI}}$ direction. It is therefore crucial to keep the leakage currents as small as possible - even as low as 1 nA to ensure that this effect is smaller than the predicted statistical sensitivity.

The motional magnetic field appears in the reference frame of moving molecules, that is:

$$\mathbf{B}_{\mathrm{mot}} = \mathbf{v} \times \frac{\boldsymbol{\mathcal{E}}}{c^2}.$$

It is always perpendicular to both $\mathbf{v}$ and $\boldsymbol{\mathcal{E}}$, i.e. nominally in the $\mathbf{y}$ direction. However, if there is any static magnetic field with a non-zero $\mathbf{y}$-component, the total magnetic field magnitude will be $B_{\mathrm{tot}} = \sqrt{B_{\mathrm{int}}^2 + (B_{\mathrm{mot}} + B_{\mathrm{st}})^2}$, where B_{int} is the intra-molecular static magnetic field. The total field B_{tot} will then change in magnitude when $\boldsymbol{\mathcal{E}}_{\mathrm{MI}}$ is reversed, which will cause frequency shift between the spin-up and spin-down states, because their Zeeman splitting is proportional to B_{tot}. Assuming we are able to reach our target level of residual magnetic field, $B_{\mathrm{st}} \lesssim 10\,\mu$G, a shift of 0.5 μHz is expected. Fortunately, this shift can also be suppressed by a one of the modulations - the M modulation, which, instead of reversing the field, changes the science state and the transitions used, i.e. e↔j and h↔k. This is possible due to unequal Zeeman shifts of both pairs of states due to the motional magnetic field. The resulting difference in transition frequencies for anticipated magnitude of static fields in the MI region is roughly the same as the estimated statistical sensitivity we hope to achieve.

Finally, we should mention one more known source of systematic errors which was taken into account in previous searches for NSM in TlF. Namely, the energy shifts can also be caused by the so-called Millman effect [101], which in turn is caused by misalignment of the NMR RF field coils. However, good construction techniques are predicted to limit this residual effect below our anticipated sensitivity. Furthermore, it can be quantified experimentally [34].

11.3.1 Internal Co-magnetometry in CeNTREX

The stray magnetic fields in EDM searches cause a lot of headache and are quite often the main factor ultimately limiting experimental sensitivity. The newest searches started using a new approach, co-magnetometry, allowing to measure magnetic fields located in the same place in space and time as the EDM-sensitive systems. One of the ways this has already been achieved was by using a different species that were, nominally, sharing the same volume [13, 100]. However, one can potentially use different internal states of utilized systems (upon which EDM measurements are performed) that have different sensitivity to EDM and/or magnetic fields [61, 102]. This so-called internal co-magnetometer approach guarantees spatial overlap between the two systems, and thereby reduces experimental complexity [103].

In CeNTREX, we hope to utilize different internal states of TlF. While for the NSM measurements we plan to use the discussed e↔j and h↔k transitions which both flip thallium's spin and simultaneously keep all other quantum numbers the same, it is possible to employ other pairs of states where the spin of fluorine's nucleus changes direction, i.e. the pairs e↔g and f↔h (Fig. 3.7.1). These pairs should be 2 to 3 times more susceptible to any effects caused by the magnetic fields, and at the same time their sensitivity to CP-violating effects is nearly negligible due to low atomic and charge numbers A and Z of the ^{19}F nucleus. Therefore, these pairs behave like classic co-magnetometers. A big advantage of utilizing this scheme is a miniscule change in experimental configuration that is required - we simply need to lower the NMR resonance frequency to about 10.6 kHz from 119.5 kHz used for the e↔j and h↔k transitions. This should provide a novel diagnostic method for systematic errors and stray fields in CeNTREX.

11.4 Prospects

As we have discussed, the predicted statistical sensitivity to the energy shifts induced by CP-violating effects is $\delta\Delta_{\mathrm{CPV}} \approx 50$ nHz, which roughly constitutes a 2500-fold improvement over the current best measurements of the nuclear Schiff moment in ^{205}Tl nucleus. We can then use Eq. (1.2.6) to translate this into limits that we can potentially place on the parameters of fundamental physics. Obtained sensitivities should be significantly better than the ones achieved in previous experiments. To give a few examples, CeNTREX is estimated to greatly improve the limit on the QCD $\bar{\theta}$ parameter: $\bar{\theta} \lesssim 1 \times 10^{-12}$, a factor of ~ 100 smaller than current bounds [11, 13]; and on the proton EDM: $d_p \lesssim 6 \times 10^{-27}\ e\,\mathrm{cm}$, a factor of ~ 30 smaller than the current best limit [11].

Now, that the rotational cooling measurements have been completed and proven to lead to 24-fold signal enhancement, the SPA region and then the EQL region will be attached to the apparatus for testing and optimization. The MI region is currently under construction, and the remaining regions are under design. After assembling the entire experimental setup, optimizing it and thoroughly testing, we will begin the main measurement process aiming to reach the target sensitivity $\delta\Delta_{\mathrm{CPV}} \lesssim 50\,\mathrm{nHz}$.

In the future, next generations of CeNTREX are planned. We plan to, for instance, implement

transverse laser cooling to collimate the TlF beam [39, 44], and to use a continuous cryogenic buffer gas beam source [104, 105, 106, 107] loaded by a thermal TlF beam. We estimate that with these improvements CeNTREX could increase the detected number of molecules by a factor of 30-100. It may also be possible to slow, cool, and optically trap the TlF molecules, which would drastically increase the interaction time per molecule further increasing the sensitivity.

Nonetheless, our experimental approach has the potential to yield greatly improved sensitivity to flavor-neutral CP-violating physics in the hadronic sector. Additionally, CeNTREX could potentially also be used to search for axions. This could be achieved by either measuring the oscillating Schiff moment produced by the interaction with an axion dark matter particle [108] or by searching for virtual axions mediating CP-violation and producing a Schiff moment in the Tl nucleus [109, 110].

Bibliography

[1] Lev Landau. On the conservation laws for weak interactions. *Nuclear Physics*, 3(1):127–131, 1957.

[2] James H Christenson, Jeremiah W Cronin, Val L Fitch, and René Turlay. Evidence for the 2π decay of the K_2^0 meson. *Physical Review Letters*, 13(4):138, 1964.

[3] M. Tanabashi et al. Review of particle physics. *Phys. Rev. D*, 98(3):030001, 2018.

[4] R. D. Peccei. CP violation: A theoretical review, 1995.

[5] Matthew D. Schwartz. *Quantum Field Theory and the Standard Model*. Cambridge University Press, 2013.

[6] Makoto Kobayashi and Toshihide Maskawa. CP-violation in the renormalizable theory of weak interaction. *Progress of Theoretical Physics*, 49(2):652–657, 1973.

[7] T. E. Chupp, P. Fierlinger, M. J. Ramsey-Musolf, and J. T. Singh. Electric dipole moments of atoms, molecules, nuclei, and particles. *Rev. Mod. Phys.*, 91:015001, Jan 2019.

[8] Laurent Canetti, Marco Drewes, and Mikhail Shaposhnikov. Matter and antimatter in the universe. *New J. Phys. 14 (2012) 095012*, 2012.

[9] Andrei D Sakharov. Violation of CP invariance, C asymmetry, and baryon asymmetry of the universe. *Soviet Physics Uspekhi*, 34(5):392, 1991.

[10] Maxim Pospelov and Adam Ritz. The theta term in QCD sum rules and the electric dipole moment of the vector meson. *Nuclear physics B*, 558(1-2):243–258, 1999.

[11] Brent Graner, Y Chen, EG Lindahl, BR Heckel, et al. Reduced limit on the permanent electric dipole moment of ^{199}Hg. *Physical review letters*, 116(16):161601, 2016.

[12] CA Baker, DD Doyle, P Geltenbort, K Green, MGD Van der Grinten, PG Harris, P Iaydjiev, SN Ivanov, DJR May, JM Pendlebury, et al. Improved experimental limit on the electric dipole moment of the neutron. *Physical Review Letters*, 97(13):131801, 2006.

[13] Christopher Abel, Samer Afach, Nicholas J Ayres, Colin A Baker, Gilles Ban, Georg Bison, Kazimierz Bodek, V Bondar, M Burghoff, E Chanel, et al. Measurement of the permanent electric dipole moment of the neutron. *Physical Review Letters*, 124(8):081803, 2020.

[14] R. D. Peccei and Helen R. Quinn. CP conservation in the presence of pseudoparticles. *Phys. Rev. Lett.*, 38(25):1440–1443, 1977.

[15] John Preskill, Mark B. Wise, and Frank Wilczek. Cosmology of the invisible axion. *Physics Letters B*, 120(1):127 – 132, 1983.

[16] J. Ipser and P. Sikivie. Can galactic halos be made of axions? *Phys. Rev. Lett.*, 50(12):925–927, 1983.

[17] Peter W Graham, Igor G Irastorza, Steven K Lamoreaux, Axel Lindner, and Karl A van Bibber. Experimental searches for the axion and axion-like particles. *Annual Review of Nuclear and Particle Science*, 65:485–514, 2015.

[18] T. Braine, R. Cervantes, N. Crisosto, N. Du, S. Kimes, L. J. Rosenberg, G. Rybka, J. Yang, D. Bowring, A. S. Chou, R. Khatiwada, A. Sonnenschein, W. Wester, G. Carosi, N. Woollett, L. D. Duffy, R. Bradley, C. Boutan, M. Jones, B. H. LaRoque, N. S. Oblath, M. S. Taubman, J. Clarke, A. Dove, A. Eddins, S. R. O'Kelley, S. Nawaz, I. Siddiqi, N. Stevenson, A. Agrawal, A. V. Dixit, J. R. Gleason, S. Jois, P. Sikivie, J. A. Solomon, N. S. Sullivan, D. B. Tanner, E. Lentz, E. J. Daw, J. H. Buckley, P. M. Harrington, E. A. Henriksen, and K. W. Murch. Extended search for the invisible axion with the axion dark matter experiment. *Phys. Rev. Lett.*, 124(10):101303, 2020.

[19] LI Schiff. Measurability of nuclear electric dipole moments. *Physical Review*, 132(5):2194, 1963.

[20] Maxim Pospelov and Adam Ritz. Electric dipole moments as probes of new physics. *Annals of physics*, 318(1):119–169, 2005.

[21] M Eh Pospelov and IB Khriplovich. Electric dipole moment of the W boson and the electron in the Kobayashi-Maskawa model. *Yadernaya Fizika*, 53(4):1030–1033, 1991.

[22] Daniel Ng and John N. Ng. A note on majorana neutrinos, leptonic ckm and electron electric dipole moment. *Modern Physics Letters A*, 11(03):211–216, 1996.

[23] M.B. Gavela, A. Le Yaouanc, L. Oliver, O. PĂ¨ne, J.-C. RaynaL, and T.N. Pham. Cp violation induced by penguin diagrams and the neutron electric dipole moment. *Physics Letters B*, 109(3):215 – 220, 1982.

[24] Timothy Chupp and Michael Ramsey-Musolf. Electric dipole moments: A global analysis. *Physical Review C - Nuclear Physics*, 91(3):1–11, 2015.

[25] V. V. Flambaum and V. A. Dzuba. Electric dipole moments of atoms and molecules produced by enhanced nuclear Schiff moments. *Phys. Rev. A*, 101(4):042504, Apr 2020.

[26] MS Safronova, D Budker, D DeMille, Derek F Jackson Kimball, A Derevianko, and Charles W Clark. Search for new physics with atoms and molecules. *Reviews of Modern Physics*, 90(2):025008, 2018.

[27] V. V. Flambaum, V. A. Dzuba, and H. B. Tran Tan. Time- and parity-violating effects of the nuclear Schiff moment in molecules and solids. *Phys. Rev. A*, 101(4):042501, Apr 2020.

[28] Iosif B. Khriplovich and Steve Lamoreaux. *CP Violation Without Strangeness*. Springer, 1997.

[29] A. V. Titov, N. S. Mosyagin, A. N. Petrov, and T. A. Isaev. Two-step method for precise calculation of core properties in molecules. *International Journal of Quantum Chemistry*, 104:223–239, 2005.

[30] A. N. Petrov, N. S. Mosyagin, T. A. Isaev, A. V. Titov, V. F. Ezhov, E. Eliav, and U. Kaldor. Calculation of P,T-odd effects in ^{205}TlF including electron correlation. *Phys. Rev. Lett.*, 88(7):073001, Jan 2002.

[31] Minori Abe, Takashi Tsutsui, Jörgen Ekman, Masahiko Hada, and Bhanu Das. Accurate determination of the enhancement factor X for the nuclear Schiff moment in ^{205}TlF molecule based on the four-component relativistic coupled-cluster theory. *Molecular Physics*, pages 1–7, 2020.

[32] Iosif B Khriplovich. *Parity nonconservation in atomic phenomena*. Gordon and Breach science publishers, 1991.

[33] D Cho, K Sangster, and EA Hinds. Tenfold improvement of limits on T violation in thallium fluoride. *Physical Review Letters*, 63(23):2559, 1989.

[34] Donghyun Cho, K Sangster, and EA Hinds. Search for time-reversal-symmetry violation in thallium fluoride using a jet source. *Physical Review A*, 44(5):2783, 1991.

[35] PGH Sandars. Measurability of the proton electric dipole moment. *Physical Review Letters*, 19(24):1396, 1967.

[36] Dean A Wilkening, Norman F Ramsey, and Daniel J. Larson. Search for P and T violations in the hyperfine structure of thallium fluoride. *Physical Review A*, 29(2), 1984.

[37] M.G. Kozlov and L.N. Labzowsky. Parity violation effects in diatomics. *Journal of Physics B: Atomic, Molecular and Optical Physics*, 28(10):1933, 1995.

[38] Edward A. Hinds and P.G.H Sandars. Electric dipole hyperfine structure of TlF. *Physical Review A*, 21, 1980.

[39] E. B. Norrgard, E. R. Edwards, D. J. McCarron, M. H. Steinecker, D. DeMille, S. S. Alam, S. K. Peck, N. S. Wadia, and L. R. Hunter. Hyperfine structure of the $B^3\Pi_1$ state and predictions of optical cycling behavior in the $X \rightarrow B$ transition of TlF. *Physical Review A*, 95(6):1–12, 2017.

[40] D. Cho, K. Sangster, and E. A. Hinds. Search for time-reversal-symmetry violation in thallium fluoride using a jet source. *Physical Review A*, 44(5):1–8, 1991.

[41] Brown J.M. Brown, J.M and A. Carrington. *Rotational Spectroscopy of Diatomic Molecules*. Cambridge Molecular Science. Cambridge University Press, 2003.

[42] Frank J. Lovas and Eberhard Tiemann. Microwave spectral tables i. diatomic molecules. *Journal of Physical and Chemical Reference Data*, 3(3):609–770, 1974.

[43] V. V. Flambaum, V. A. Dzuba, and H. B. Tran Tan. Time- and parity-violating effects of the nuclear Schiff moment in molecules and solids. *Phys. Rev. A*, 101(4):042501, Apr 2020.

[44] LR Hunter, SK Peck, AS Greenspon, S Saad Alam, and D DeMille. Prospects for laser cooling TlF. *Physical Review A*, 85(1):012511, 2012.

[45] Norman F. Ramsey. A molecular beam resonance method with separated oscillating fields. *Phys. Rev.*, 78(6):695–699, 1950.

[46] Norman F Ramsey and Henry B Silsbee. Phase shifts in the molecular beam method of separated oscillating fields. *Physical Review*, 84(3):506, 1951.

[47] Nicholas R Hutzler, Hsin-I Lu, and John M Doyle. The buffer gas beam: An intense, cold, and slow source for atoms and molecules. *Chemical reviews*, 112(9):4803–4827, 2012.

[48] Nathan B. Clayburn, Trevor H. Wright, Eric B. Norrgard, David DeMille, and Larry R. Hunter. Measurement of the molecular dipole moment and the hyperfine and omega doublet splittings of the $B^3\Pi_1$ state of thallium fluoride, 2020. arXiv:2007.16101.

[49] D J Berkeland and M G Boshier. Destabilization of dark states and optical spectroscopy in Zeeman-degenerate atomic systems. *Physical Review A*, 65:1–13, 2002.

[50] Dmitry Budker, Derek Kimball, Derek F Kimball, and David P DeMille. *Atomic physics: an exploration through problems and solutions*. Oxford University Press, USA, 2004.

[51] HG Bennewitz, W Paul, and Ch Schlier. Fokussierung polarer moleküle. *Zeitschrift für Physik*, 141(1-2):6–15, 1955.

[52] Robert A Berg, Lennard Wharton, William Klemperer, Alfred Büchler, and James L Stauffer. Determination of electronic symmetry by electric deflection: LiO and LaO. *The Journal of Chemical Physics*, 43(7):2416–2421, 1965.

[53] Victoria A Cho and Richard B Bernstein. Tight focusing of beams of polar polyatomic molecules via the electrostatic hexapole lens. *The Journal of Physical Chemistry*, 95(21):8129–8136, 1991.

[54] David Jiles. *Introduction to Magnetism and Magnetic Materials*. CRC Press, 3 edition, 2015.

[55] Walter Rogowski. Die elektrische Festigkeit am Rande des Plattenkondensators. *Archiv fĂĽr Elektrotechnik*, 12(1), 1923.

[56] E. Kuffel, W.S. Zaengl, and J. Kuffel. *High Voltage Engineering Fundamentals*. Newnes, Oxford, 2nd edition, 2000.

[57] S. K. Lamoreaux. Feeble magnetic fields generated by thermal charge fluctuations in extended metallic conductors: Implications for electric-dipole moment experiments. *Phys. Rev. A*, 60:1717–1720, 1999.

[58] T. W. Kornack, S. J. Smullin, S.-K. Lee, and M. V. Romalis. A low-noise ferrite magnetic shield. *Applied Physics Letters*, 90:223501, 2007.

[59] S.-K. Lee and M. V. Romalis. Calculation of magnetic field noise from high-permeability magnetic shields and conducting objects with simple geometry. *Journal of Applied Physics*, 103:084904, 2008.

[60] E. Kirilov, W. C. Campbell, J. M. Doyle, G. Gabrielse, Y. V. Gurevich, P. W. Hess, N. R. Hutzler, B. R. O'Leary, E. Petrik, B. Spaun, A. C. Vutha, and D. DeMille. Shot-noise-limited spin measurements in a pulsed molecular beam. *Phys. Rev. A*, 88(1):013844, 2013.

[61] V. Andreev, D. G. Ang, D. DeMille, J. M. Doyle, G. Gabrielse, J. Haefner, N. R. Hutzler, Z. Lasner, C. Meisenhelder, B. R. O'Leary, C. D. Panda, A. D. West, E. P. West, X. Wu, and ACME Collaboration. Improved limit on the electric dipole moment of the electron. *Nature*, 562(7727):355–360, 2018.

[62] Robert Alicki. Invitation to quantum dynamical semigroups. 2002.

[63] Vittorio Gorini, Andrzej Kossakowski, and E. C. G. Sudarshan. Completely positive dynamical semigroups of n-level systems. *Journal of Mathematical Physics*, 17(5):821–825, 1976.

[64] G. Lindblad. On the generators of quantum dynamical semigroups. *Communications in Mathematical Physics*, 48(2):119–130, 1976.

[65] J. B. Naber, A. Tauschinsky, H. B. van Linden van den Heuvell, and R. J. C. Spreeuw. Electromagnetically induced transparency with Rydberg atoms across the Breit-Rabi regime. *SciPost Phys.*, 2:015, 2017.

[66] V. Natarajan. *Modern Atomic Physics*. CRC Press, 2015.

[67] Daniel Finkelstein-Shapiro, Simone Felicetti, Thorsten Hansen, Tõnu Pullerits, and Arne Keller. Classification of dark states in multilevel dissipative systems. *Phys. Rev. A*, 99:053829, May 2019.

[68] E. Brion, L. H. Pedersen, and K. Mølmer. Adiabatic elimination in a lambda system. *Journal of Physics A: Mathematical and Theoretical*, 40(5):1033–1043, 2007.

[69] Daniel Finkelstein-Shapiro, David Viennot, Ibrahim Saideh, Thorsten Hansen, Tõnu Pullerits, and Arne Keller. Adiabatic elimination and subspace evolution of open quantum systems. *Phys. Rev. A*, 101:042102, Apr 2020.

[70] M R Tarbutt, B E Sauer, J J Hudson, and E A Hinds. Design for a fountain of YbF molecules to measure the electron's electric dipole moment. *New Journal of Physics*, 15(5):053034, may 2013.

[71] Ronny Kirste, Qiang Guo, J. Houston Dycus, Alexander Franke, Seiji Mita, Biplab Sarkar, Pramod Reddy, James M. LeBeau, Ramon Collazo, and Zlatko Sitar. 6 kW/cm2 UVC laser threshold in optically pumped lasers achieved by controlling point defect formation. *Applied Physics Express*, 11(8):082101, jul 2018.

[72] Ziyi Zhang, Maki Kushimoto, Tadayoshi Sakai, Naoharu Sugiyama, Leo J. Schowalter, Chiaki Sasaoka, and Hiroshi Amano. A 271.8 nm deep-ultraviolet laser diode for room temperature operation. *Applied Physics Express*, 12(12):124003, nov 2019.

[73] Dana Z. Anderson. Alignment of resonant optical cavities. *Appl. Opt.*, 23(17):2944–2949, Sep 1984.

[74] Tim Freegarde, Julian Coutts, Jochen Walz, Dietrich Leibfried, and T.W. Hansch. General analysis of type i second-harmonic generation with elliptical gaussian beams. *Journal of the Optical Society of America B*, 14(8):2010–2016, 1997.

[75] Irit Juwiler and Ady Arie. Efficient frequency doubling by a phase-compensated crystal in a semimonolithic cavity. *Applied optics*, 42(36):7163–7169, 2003.

[76] S. Hannig, J. Mielke, J. Fenske, M. Misera, N. Beev, C. Ospelkaus, and P. Schmidt. A highly stable monolithic enhancement cavity for second harmonic generation in the ultraviolet. *The Review of scientific instruments*, 89 1:013106, 2018.

[77] P. A. Franken, A. E. Hill, C. W. Peters, and G. Weinreich. Generation of optical harmonics. *Phys. Rev. Lett.*, 7:118–119, Aug 1961.

[78] N. Bloembergen and P. S. Pershan. Light waves at the boundary of nonlinear media. *Phys. Rev.*, 128:606–622, Oct 1962.

[79] D. A. Kleinman. Theory of second harmonic generation of light. *Phys. Rev.*, 128:1761–1775, Nov 1962.

[80] Robert W. Boyd. *Nonlinear optics*. Academic Press, Inc., 1992.

[81] P. A. Franken and J. F. Ward. Optical harmonics and nonlinear phenomena. *Rev. Mod. Phys.*, 35:23–39, Jan 1963.

[82] P. Xu and S. N. Zhu. Review article: Quasi-phase-matching engineering of entangled photons. *AIP Advances*, 2(4):041401, 2012.

[83] G. D. Boyd and D. A. Kleinman. Parametric interaction of focused gaussian light beams. *Journal of Applied Physics*, 39(8):3597–3639, 1968.

[84] A.E. Siegman. *Lasers*. University Science Books, 1986.

[85] F. Zernike and J.E. Midwinter. *Applied Nonlinear Optics*. A Wiley-Interscience publication. Wiley, 1973.

[86] R. W. P. Drever, J. Hall, F. Kowalski, James H. Hough, G. M. Ford, A. Munley, and H. Ward. Laser phase and frequency stabilization using an optical resonator. *Applied Physics B*, 31:97–105, 1983.

[87] Eric D. Black. An introduction to pound–drever–hall laser frequency stabilization. *American Journal of Physics*, 69(1):79–87, 2001.

[88] Eric B. Norrgard. *Magneto-optical trapping of diatomic molecules.* PhD thesis, 2016.

[89] F. Bertinetto, P. Cordiale, G. Galzerano, and E. Bava. Frequency stabilization of dbr diode laser against cs absorption lines at 852 nm using the modulation transfer method. *IEEE Transactions on Instrumentation and Measurement*, 50(2):490–492, 2001.

[90] Jon H. Shirley. Modulation transfer processes in optical heterodyne saturation spectroscopy. *Opt. Lett.*, 7(11):537–539, Nov 1982.

[91] Jing Zhang, Dong Wei, Changde Xie, and Kunchi Peng. Characteristics of absorption and dispersion for rubidium d2 lines with the modulation transfer spectrum. *Opt. Express*, 11(11):1338–1344, Jun 2003.

[92] D. J. McCarron, S. A. King, and S. L. Cornish. Modulation transfer spectroscopy in atomic rubidium. *Measurement Science and Technology*, 19(10):105601, aug 2008.

[93] R. K. Raj, D. Bloch, J. J. Snyder, G. Camy, and M. Ducloy. High-frequency optically heterodyned saturation spectroscopy via resonant degenerate four-wave mixing. *Phys. Rev. Lett.*, 44:1251–1254, May 1980.

[94] Fei Zi, Xuejian Wu, Weicheng Zhong, Richard H. Parker, Chenghui Yu, Simon Budker, Xuanhui Lu, and Holger Müller. Laser frequency stabilization by combining modulation transfer and frequency modulation spectroscopy. *Appl. Opt.*, 56(10):2649–2652, Apr 2017.

[95] Ch. Salomon, D. Hils, and J. L. Hall. Laser stabilization at the millihertz level. *J. Opt. Soc. Am. B*, 5(8):1576–1587, Aug 1988.

[96] B. G. Lindsay, K. A. Smith, and F. B. Dunning. Control of long-term output frequency drift in commercial dye lasers. *Review of Scientific Instruments*, 62(6):1656–1657, 1991.

[97] S. M. Jaffe, M. Rochon, and W. M. Yen. Increasing the frequency stability of single-frequency lasers. *Review of Scientific Instruments*, 64(9):2475–2481, 1993.

[98] W. Z. Zhao, J. E. Simsarian, L. A. Orozco, and G. D. Sprouse. A computer-based digital feedback control of frequency drift of multiple lasers. *Review of Scientific Instruments*, 69(11):3737–3740, 1998.

[99] Zack Lasner and D. DeMille. Statistical sensitivity of phase measurements via laser-induced fluorescence with optical cycling detection. *Phys. Rev. A*, 98:053823, 2018.

[100] BC Regan, Eugene D Commins, Christian J Schmidt, and David DeMille. New limit on the electron electric dipole moment. *Physical review letters*, 88(7):071805, 2002.

[101] S Millman. On the determination of the signs of nuclear magnetic moments by the molecular beam method of magnetic resonance. *Physical Review*, 55(7):628, 1939.

[102] S. Eckel, P. Hamilton, E. Kirilov, H. W. Smith, and D. DeMille. Search for the electron electric dipole moment using Ω-doublet levels in PbO. *Physical Review A*, 87(5):052130, May 2013.

[103] D. DeMille, F. Bay, S. Bickman, D. Kawall, L. Hunter, D. Krause Jr., S. Maxwell, and K. Ulmer. Search for the electric dipole moment of the electron using metastable PbO. In D. Budker and S.J. Bucksbaum, P.H.and Freedman, editors, *Art and Symmetry in Experimental Physics: Festschrift for Eugene D. Commins*, volume 596 of *AIP Conference Proceedings*, page 72, 2001.

[104] David Patterson and John M. Doyle. Bright, guided molecular beam with hydrodynamic enhancement. *The Journal of Chemical Physics*, 126:154307, 2007.

[105] David Patterson, Julia Rasmussen, and John M Doyle. Intense atomic and molecular beams via neon buffer-gas cooling. *New Journal of Physics*, 11(5):055018, may 2009.

[106] David Patterson and John M. Doyle. A slow, continuous beam of cold benzonitrile. *Phys. Chem. Chem. Phys.*, 17:5372–5375, 2015.

[107] Vijay Singh, Amit K. Samanta, Nils Roth, Daniel Gusa, Tim Ossenbrüggen, Igor Rubinsky, Daniel A. Horke, and Jochen Küpper. Optimized cell geometry for buffer-gas-cooled molecular-beam sources. *Phys. Rev. A*, 97:032704, Mar 2018.

[108] Y. V. Stadnik and V. V. Flambaum. Axion-induced effects in atoms, molecules, and nuclei: Parity nonconservation, anapole moments, electric dipole moments, and spin-gravity and spin-axion momentum couplings. *Phys. Rev. D*, 89:043522, 2014.

[109] Y. V. Stadnik, V. A. Dzuba, and V. V. Flambaum. Improved limits on axionlike-particle-mediated P, T-violating interactions between electrons and nucleons from electric dipole moments of atoms and molecules. *Phys. Rev. Lett.*, 120:013202, 2018.

[110] V. A. Dzuba, V. V. Flambaum, I. B. Samsonov, and Y. V. Stadnik. New constraints on axion-mediated P, T-violating interaction from electric dipole moments of diamagnetic atoms. *Phys. Rev. D*, 98:035048, 2018.

[111] D A Varshalovich, A N Moskalev, and V K Khersonskii. *Quantum Theory of Angular Momentum*. WORLD SCIENTIFIC, 1988.

Appendix A

Spherical Tensor Algebra

For the sake of completion, couple of often used formulas from spherical tensor algebra are presented. These are based on [41] and [111]. One of the most often used formula comes from the Wigner-Eckart theorem:

$$\left\langle j,m\middle|T^k_p(\mathbf{A})\middle|j',m'\right\rangle = (-1)^{j-m}\begin{pmatrix} j & k & j' \\ -m & p & m' \end{pmatrix}\left\langle j\middle\|T^k(\mathbf{A})\middle\|j'\right\rangle \tag{A.1}$$

where $T^k_p(\mathbf{A})$ is p-th component of a k-rank spherical tensor created from an operator $\mathbf{A}$ acting on j. Having put the m dependence into a 3j-symbol, one has to only evaluate the reduced matrix element. For a rank 1 tensor:

$$\left\langle j\middle\|T^1(\mathbf{A})\middle\|j'\right\rangle = \delta_{j,j'}\sqrt{j(j+1)(2j+1)}. \tag{A.2}$$

In case when we have two coupled angular momenta such that $\mathbf{j} = \mathbf{j_1} + \mathbf{j_2}$ and a spherical tensor that is a tensor product of two different spherical tensors acting on different angular momenta (i.e. $W^K(\mathbf{A_1},\mathbf{A_2}) = T^{k_1}(\mathbf{A_1}) \times T^{k_2}(\mathbf{A_2})$, where $\mathbf{A_i}$ acts on $\mathbf{j_i}$), one obtains:

$$\begin{aligned}\left\langle j_1,j_2,j\middle\|W^K(\mathbf{A_1},\mathbf{A_2})\middle\|j_1',j_2',j'\right\rangle =& \sqrt{(2K+1)(2j'+1)(2j+1)}\begin{Bmatrix} j & j' & K \\ j_1 & j_1' & k_1 \\ j_2 & j_2' & k_2 \end{Bmatrix} \\ & \left\langle j_1\middle\|T^{k_1}(\mathbf{A_1})\middle\|j_1'\right\rangle\left\langle j_2\middle\|T^{k_2}(\mathbf{A_2})\middle\|j_2'\right\rangle.\end{aligned} \tag{A.3}$$

Tensor product can also be explicitly decomposed into product of two tensors:

$$W^K_p(\mathbf{A},\mathbf{B}) = (-1)^{k_1-k_2+p}\sqrt{2K+1}\sum_{p_1p_2}\begin{pmatrix} k_1 & k_2 & K \\ p_1 & p_2 & -p \end{pmatrix} T^{k_1}_{p_1}(\mathbf{A})T^{k_2}_{p_2}(\mathbf{B}). \tag{A.4}$$

In a special case when we have a scalar product $K = 0$, $k_1 = k_2 \equiv k$, and only $p = 0$ is allowed. Then, combining Wigner-Eckart theorem with the Eq. (A.3) gives us the following:

$$\begin{aligned}\left\langle j_1, j_2, j, m\middle|T^k(\mathbf{A_1}) \cdot T^k(\mathbf{A_2})\middle|j_1', j_2', j', m'\right\rangle =&(-1)^{j_1'+j_2+j}\delta_{m,m'}\delta_{j,j'}\begin{Bmatrix} j_2' & j_1' & j \\ j_1 & j_2 & k\end{Bmatrix} \\ &\left\langle j_1\middle\|T^{k_1}(\mathbf{A_1})\middle\|j_1'\right\rangle\left\langle j_2\middle\|T^{k_2}(\mathbf{A_2})\middle\|j_2'\right\rangle.\end{aligned} \tag{A.5}$$

If both of the spherical tensors act on the same angular momentum in a coupled scheme then we can just write:

$$\left\langle j_1, j_2, j, m\middle|T^k(\mathbf{A_1}) \cdot T^k(\mathbf{B_1})\middle|j_1', j_2', j', m'\right\rangle = \delta_{m,m'}\delta_{j,j'}\delta_{j_2,j_2'}\left\langle j_1\middle\|T^k(\mathbf{A_1}) \cdot T^k(\mathbf{B_1})\middle\|j_1'\right\rangle. \tag{A.6}$$

In a different special case, if we have a matrix element of a single operator in a coupled scheme $T^{k_2}(\mathbf{A_2}) = 1$, then $k_2 = 0$ and $k_{12} = k_1$. Therefore:

$$\begin{aligned}\left\langle j_1, j_2, j\middle\|T^{k_1}(\mathbf{A_1})\middle\|j_1', j_2', j'\right\rangle =&\delta_{j_2,j_2'}(-1)^{j_1+j_2+j'+k_1}\sqrt{(2j'+1)(2j+1)}\begin{Bmatrix} j_1' & j' & j_2 \\ j & j_1 & k\end{Bmatrix} \\ &\left\langle j_1\middle\|T^{k_1}(\mathbf{A_1})\middle\|j_1'\right\rangle.\end{aligned} \tag{A.7}$$

Analogically:

$$\begin{aligned}\left\langle j_1, j_2, j\middle\|T^{k_2}(\mathbf{A_2})\middle\|j_1', j_2', j'\right\rangle =&\delta_{j_1,j_1'}(-1)^{j_1+j_2'+j+k_2}\sqrt{(2j'+1)(2j+1)}\begin{Bmatrix} j_2' & j' & j_1 \\ j & j_2 & k\end{Bmatrix} \\ &\left\langle j_2\middle\|T^{k_2}(\mathbf{A_2})\middle\|j_2'\right\rangle.\end{aligned} \tag{A.8}$$

Sometimes it is also necessary to change the frame of reference from laboratory frame to a molecular frame. To perform the transformation we use Wigner D-functions $\mathscr{D}^{(k)}_{pq}(\omega)$, which can be thought of as irreducible representation of rotation group SO(3) or SU(2) and which are eigenfunctions of the hamiltonian of spherical and symmetric rigid rotors. To go from space (p) to molecular (q) axes we write:

$$T^k_p(\mathbf{A}) = \sum_q \mathscr{D}^{(k)}_{pq}(\omega)^*\ T^k_q(\mathbf{A}).$$

One can then evaluate the reduced matrix element of the D-function. We have:

$$\left\langle J, \Omega\middle\|\mathscr{D}^{(k)}_{.q}(\omega)^*\middle\|J', \Omega'\right\rangle = (-1)^{J-\Omega}\sqrt{(2J+1)(2J'+1)}\begin{pmatrix} J & k & J' \\ -\Omega & q & \Omega'\end{pmatrix}, \tag{A.9}$$

where Ω is projection of J onto internuclear axis.

Appendix B

Rotational Branching Ratios Tables

$\lvert J, F_1, F, M_F\rangle$	$\lvert 1,\frac{1}{2},0,0\rangle$	$\lvert 1,\frac{1}{2},1,-1\rangle$	$\lvert 1,\frac{1}{2},1,0\rangle$	$\lvert 1,\frac{1}{2},1,1\rangle$	$\lvert 1,\frac{3}{2},1,-1\rangle$	$\lvert 1,\frac{3}{2},1,0\rangle$	$\lvert 1,\frac{3}{2},1,1\rangle$	$\lvert 1,\frac{3}{2},2,-2\rangle$	$\lvert 1,\frac{3}{2},2,-1\rangle$	$\lvert 1,\frac{3}{2},2,0\rangle$	$\lvert 1,\frac{3}{2},2,1\rangle$	$\lvert 1,\frac{3}{2},2,2\rangle$
$\lvert 0,\frac{1}{2},0,0\rangle$	0	2/9	2/9	2/9	4/9	4/9	4/9	0	0	0	0	0
$\lvert 0,\frac{1}{2},1,-1\rangle$	2/9	2/9	2/9	0	1/9	1/9	0	2/3	1/3	1/9	0	0
$\lvert 0,\frac{1}{2},1,0\rangle$	2/9	2/9	0	2/9	1/9	0	1/9	0	1/3	4/9	1/3	0
$\lvert 0,\frac{1}{2},1,1\rangle$	2/9	0	2/9	2/9	0	1/9	1/9	0	0	1/9	1/3	2/3
$\lvert 2,\frac{3}{2},1,-1\rangle$	1/9	1/36	1/36	0	1/72	1/72	0	1/300	1/600	1/1800	0	0
$\lvert 2,\frac{3}{2},1,0\rangle$	1/9	1/36	0	1/36	1/72	0	1/72	0	1/600	1/450	1/600	0
$\lvert 2,\frac{3}{2},1,1\rangle$	1/9	0	1/36	1/36	0	1/72	1/72	0	0	1/1800	1/600	1/300
$\lvert 2,\frac{3}{2},2,-2\rangle$	0	1/6	0	0	1/300	0	0	1/50	1/100	0	0	0
$\lvert 2,\frac{3}{2},2,-1\rangle$	0	1/12	1/12	0	1/600	1/600	0	1/100	1/200	3/200	0	0
$\lvert 2,\frac{3}{2},2,0\rangle$	0	1/36	1/9	1/36	1/1800	1/450	1/1800	0	3/200	0	3/200	0
$\lvert 2,\frac{3}{2},2,1\rangle$	0	0	1/12	1/12	0	1/600	1/600	0	0	3/200	1/200	1/100
$\lvert 2,\frac{3}{2},2,2\rangle$	0	0	0	1/6	0	0	1/300	0	0	0	1/100	1/50
$\lvert 2,\frac{5}{2},2,-2\rangle$	0	0	0	0	9/50	0	0	1/75	1/150	0	0	0
$\lvert 2,\frac{5}{2},2,-1\rangle$	0	0	0	0	9/100	9/100	0	1/150	1/300	1/100	0	0
$\lvert 2,\frac{5}{2},2,0\rangle$	0	0	0	0	3/100	3/25	3/100	0	1/100	0	1/100	0
$\lvert 2,\frac{5}{2},2,1\rangle$	0	0	0	0	0	9/100	9/100	0	0	1/100	1/300	1/150
$\lvert 2,\frac{5}{2},2,2\rangle$	0	0	0	0	0	0	9/50	0	0	0	1/150	1/75
$\lvert 2,\frac{5}{2},3,-3\rangle$	0	0	0	0	0	0	0	1/5	0	0	0	0
$\lvert 2,\frac{5}{2},3,-2\rangle$	0	0	0	0	0	0	0	1/15	2/15	0	0	0
$\lvert 2,\frac{5}{2},3,-1\rangle$	0	0	0	0	0	0	0	1/75	8/75	2/25	0	0
$\lvert 2,\frac{5}{2},3,0\rangle$	0	0	0	0	0	0	0	0	1/25	3/25	1/25	0
$\lvert 2,\frac{5}{2},3,1\rangle$	0	0	0	0	0	0	0	0	0	2/25	8/75	1/75
$\lvert 2,\frac{5}{2},3,2\rangle$	0	0	0	0	0	0	0	0	0	0	2/15	1/15
$\lvert 2,\frac{5}{2},3,3\rangle$	0	0	0	0	0	0	0	0	0	0	0	1/5

Table B.1: Branching ratios for decays from pure e-parity states $|J', F_1', F', M_F'\rangle$ (columns) in $B^3\Pi_1$ to states in $X^1\Sigma^+$ (rows)

$\lvert J, F_1, F, M_F\rangle$	$\lvert 1,\frac{1}{2},0,0\rangle$	$\lvert 1,\frac{1}{2},1,-1\rangle$	$\lvert 1,\frac{1}{2},1,0\rangle$	$\lvert 1,\frac{1}{2},1,1\rangle$	$\lvert 1,\frac{3}{2},1,-1\rangle$	$\lvert 1,\frac{3}{2},1,0\rangle$	$\lvert 1,\frac{3}{2},1,1\rangle$	$\lvert 1,\frac{3}{2},2,-2\rangle$	$\lvert 1,\frac{3}{2},2,-1\rangle$	$\lvert 1,\frac{3}{2},2,0\rangle$	$\lvert 1,\frac{3}{2},2,1\rangle$	$\lvert 1,\frac{3}{2},2,2\rangle$
$\lvert 1,\frac{1}{2},0,0\rangle$	0	2/9	2/9	2/9	1/9	1/9	1/9	0	0	0	0	0
$\lvert 1,\frac{1}{2},1,-1\rangle$	2/9	2/9	2/9	0	1/36	1/36	0	1/6	1/12	1/36	0	0
$\lvert 1,\frac{1}{2},1,0\rangle$	2/9	2/9	0	2/9	1/36	0	1/36	0	1/12	1/9	1/12	0
$\lvert 1,\frac{1}{2},1,1\rangle$	2/9	0	2/9	2/9	0	1/36	1/36	0	0	1/36	1/12	1/6
$\lvert 1,\frac{3}{2},1,-1\rangle$	1/9	1/36	1/36	0	25/72	25/72	0	1/12	1/24	1/72	0	0
$\lvert 1,\frac{3}{2},1,0\rangle$	1/9	1/36	0	1/36	25/72	0	25/72	0	1/24	1/18	1/24	0
$\lvert 1,\frac{3}{2},1,1\rangle$	1/9	0	1/36	1/36	0	25/72	25/72	0	0	1/72	1/24	1/12
$\lvert 1,\frac{3}{2},2,-2\rangle$	0	1/6	0	0	1/12	0	0	1/2	1/4	0	0	0
$\lvert 1,\frac{3}{2},2,-1\rangle$	0	1/12	1/12	0	1/24	1/24	0	1/4	1/8	3/8	0	0
$\lvert 1,\frac{3}{2},2,0\rangle$	0	1/36	1/9	1/36	1/72	1/18	1/72	0	3/8	0	3/8	0
$\lvert 1,\frac{3}{2},2,1\rangle$	0	0	1/12	1/12	0	1/24	1/24	0	0	3/8	1/8	1/4
$\lvert 1,\frac{3}{2},2,2\rangle$	0	0	0	1/6	0	0	1/12	0	0	0	1/4	1/2

Table B.2: Branching ratios for decays from pure f-parity states $|J', F_1', F', M_F'\rangle$ (columns) in $B^3\Pi_1$ to states in $X^1\Sigma^+$ (rows).

$\lvert J, F_1, F, M_F\rangle$	$\lvert 1,\frac{1}{2},0,0\rangle$	$\lvert 1,\frac{1}{2},1,-1\rangle$	$\lvert 1,\frac{1}{2},1,0\rangle$	$\lvert 1,\frac{1}{2},1,1\rangle$	$\lvert 1,\frac{3}{2},1,-1\rangle$	$\lvert 1,\frac{3}{2},1,0\rangle$	$\lvert 1,\frac{3}{2},1,1\rangle$	$\lvert 1,\frac{3}{2},2,-2\rangle$	$\lvert 1,\frac{3}{2},2,-1\rangle$	$\lvert 1,\frac{3}{2},2,0\rangle$	$\lvert 1,\frac{3}{2},2,1\rangle$	$\lvert 1,\frac{3}{2},2,2\rangle$
$\lvert 0,\frac{1}{2},0,0\rangle$	0	0.2095	0.2095	0.2095	0.3369	0.3369	0.3369	0	0	0	0	0
$\lvert 0,\frac{1}{2},1,-1\rangle$	2/9	0.2285	0.2285	0	0.0736	0.0736	0	0.4797	0.2398	0.0799	0	0
$\lvert 0,\frac{1}{2},1,0\rangle$	2/9	0.2285	0	0.2285	0.0736	0	0.0736	0	0.2398	0.3198	0.2398	0
$\lvert 0,\frac{1}{2},1,1\rangle$	2/9	0	0.2285	0.2285	0	0.0736	0.0736	0	0	0.0799	0.2398	0.4797
$\lvert 2,\frac{3}{2},1,-1\rangle$	1/9	0.0324	0.0324	0	0.1733	0.1733	0	0.0465	0.0232	0.0077	0	0
$\lvert 2,\frac{3}{2},1,0\rangle$	1/9	0.0324	0	0.0324	0.1733	0	0.1733	0	0.0232	0.0310	0.0232	0
$\lvert 2,\frac{3}{2},1,1\rangle$	1/9	0	0.0324	0.0324	0	0.1733	0.1733	0	0	0.0077	0.0232	0.0465
$\lvert 2,\frac{3}{2},2,-2\rangle$	0	0.1612	0	0	0.0471	0	0	0.2569	0.1285	0	0	0
$\lvert 2,\frac{3}{2},2,-1\rangle$	0	0.0806	0.0806	0	0.0236	0.0236	0	0.1285	0.0642	0.1927	0	0
$\lvert 2,\frac{3}{2},2,0\rangle$	0	0.0269	0.1075	0.0269	0.0079	0.0314	0.0079	0	0.1927	0	0.1927	0
$\lvert 2,\frac{3}{2},2,1\rangle$	0	0	0.0806	0.0806	0	0.0236	0.0236	0	0	0.1927	0.0642	0.1285
$\lvert 2,\frac{3}{2},2,2\rangle$	0	0	0	0.1612	0	0	0.0471	0	0	0	0.1285	0.2569
$\lvert 2,\frac{5}{2},2,-2\rangle$	0	1.77×10^{-5}	0	0	0.0544	0	0	0.0052	0.0026	0	0	0
$\lvert 2,\frac{5}{2},2,-1\rangle$	0	0.88×10^{-5}	0.88×10^{-5}	0	0.0272	0.0272	0	0.0026	0.0013	0.0039	0	0
$\lvert 2,\frac{5}{2},2,0\rangle$	0	0.29×10^{-5}	1.18×10^{-5}	0.29×10^{-5}	0.0091	0.0363	0.0091	0	0.0039	0	0.0039	0
$\lvert 2,\frac{5}{2},2,1\rangle$	0	0	0.88×10^{-5}	0.88×10^{-5}	0	0.0272	0.0272	0	0	0.0039	0.0013	0.0026
$\lvert 2,\frac{5}{2},2,2\rangle$	0	0	0	1.77×10^{-5}	0	0	0.0544	0	0	0	0.0026	0.0052
$\lvert 2,\frac{5}{2},3,-3\rangle$	0	0	0	0	0	0	0	0.0576	0	0	0	0
$\lvert 2,\frac{5}{2},3,-2\rangle$	0	0	0	0	0	0	0	0.0192	0.0384	0	0	0
$\lvert 2,\frac{5}{2},3,-1\rangle$	0	0	0	0	0	0	0	0.0038	0.0307	0.0230	0	0
$\lvert 2,\frac{5}{2},3,0\rangle$	0	0	0	0	0	0	0	0	0.0115	0.0346	0.0115	0
$\lvert 2,\frac{5}{2},3,1\rangle$	0	0	0	0	0	0	0	0	0	0.0230	0.0307	0.0038
$\lvert 2,\frac{5}{2},3,2\rangle$	0	0	0	0	0	0	0	0	0	0	0.0384	0.0192
$\lvert 2,\frac{5}{2},3,3\rangle$	0	0	0	0	0	0	0	0	0	0	0	0.0576
$\lvert 4,\frac{7}{2},3,-3\rangle$	0	0	0	0	0	0	0	1.25×10^{-5}	0	0	0	0
$\lvert 4,\frac{7}{2},3,-2\rangle$	0	0	0	0	0	0	0	0.42×10^{-5}	0.84×10^{-5}	0	0	0
$\lvert 4,\frac{7}{2},3,-1\rangle$	0	0	0	0	0	0	0	0.08×10^{-5}	0.67×10^{-5}	0.50×10^{-5}	0	0
$\lvert 4,\frac{7}{2},3,0\rangle$	0	0	0	0	0	0	0	0	0.25×10^{-5}	0.75×10^{-5}	0.25×10^{-5}	0
$\lvert 4,\frac{7}{2},3,1\rangle$	0	0	0	0	0	0	0	0	0	0.50×10^{-5}	0.67×10^{-5}	0.08×10^{-5}
$\lvert 4,\frac{7}{2},3,2\rangle$	0	0	0	0	0	0	0	0	0	0	0.84×10^{-5}	0.42×10^{-5}
$\lvert 4,\frac{7}{2},3,3\rangle$	0	0	0	0	0	0	0	0	0	0	0	1.25×10^{-5}

Table B.3: Branching ratios for decays from mixed e-parity states $\left|\widetilde{J}', \widetilde{F}_1', F', M_F'\right\rangle$ (columns) in $B^3\Pi_1$ to states in $X^1\Sigma^+$ (rows)

$\lvert J, F_1, F, M_F\rangle$	$\lvert 1,\frac{1}{2},0,0\rangle$	$\lvert 1,\frac{1}{2},1,-1\rangle$	$\lvert 1,\frac{1}{2},1,0\rangle$	$\lvert 1,\frac{1}{2},1,1\rangle$	$\lvert 1,\frac{3}{2},1,-1\rangle$	$\lvert 1,\frac{3}{2},1,0\rangle$	$\lvert 1,\frac{3}{2},1,1\rangle$	$\lvert 1,\frac{3}{2},2,-2\rangle$	$\lvert 1,\frac{3}{2},2,-1\rangle$	$\lvert 1,\frac{3}{2},2,0\rangle$	$\lvert 1,\frac{3}{2},2,1\rangle$	$\lvert 1,\frac{3}{2},2,2\rangle$
$\lvert 1,\frac{1}{2},0,0\rangle$	0	0.2385	0.2385	0.2385	0.3288	0.3288	0.3288	0	0	0	0	0
$\lvert 1,\frac{1}{2},1,-1\rangle$	2/9	0.2140	0.2140	0	0.0934	0.0934	0	0.5193	0.2597	0.0866	0	0
$\lvert 1,\frac{1}{2},1,0\rangle$	2/9	0.2140	0	0.2140	0.0934	0	0.0934	0	0.2597	0.3462	0.2597	0
$\lvert 1,\frac{1}{2},1,1\rangle$	2/9	0	0.2140	0.2140	0	0.0934	0.0934	0	0	0.0866	0.2597	0.5193
$\lvert 1,\frac{3}{2},1,-1\rangle$	1/9	0.0251	0.0251	0	0.1597	0.1597	0	0.0408	0.0204	0.0068	0	0
$\lvert 1,\frac{3}{2},1,0\rangle$	1/9	0.0251	0	0.0251	0.1597	0	0.1597	0	0.0204	0.0272	0.0204	0
$\lvert 1,\frac{3}{2},1,1\rangle$	1/9	0	0.0251	0.0251	0	0.1597	0.1597	0	0	0.0068	0.0204	0.0408
$\lvert 1,\frac{3}{2},2,-2\rangle$	0	0.1699	0	0	0.0334	0	0	0.2184	0.1092	0	0	0
$\lvert 1,\frac{3}{2},2,-1\rangle$	0	0.0849	0.0849	0	0.0167	0.0167	0	0.1092	0.0546	0.1638	0	0
$\lvert 1,\frac{3}{2},2,0\rangle$	0	0.0283	0.1132	0.0283	0.0056	0.0222	0.0056	0	0.1638	0	0.1638	0
$\lvert 1,\frac{3}{2},2,1\rangle$	0	0	0.0849	0.0849	0	0.0167	0.0167	0	0	0.1638	0.0546	0.1092
$\lvert 1,\frac{3}{2},2,2\rangle$	0	0	0	0.1699	0	0	0.0334	0	0	0	0.1092	0.2184
$\lvert 3,\frac{5}{2},2,-2\rangle$	0	7.78×10^{-5}	0	0	0.0657	0	0	0.0059	0.0030	0	0	0
$\lvert 3,\frac{5}{2},2,-1\rangle$	0	3.89×10^{-5}	3.89×10^{-5}	0	0.0328	0.0328	0	0.0030	0.0015	0.0044	0	0
$\lvert 3,\frac{5}{2},2,0\rangle$	0	1.30×10^{-5}	5.18×10^{-5}	1.30×10^{-5}	0.0109	0.0438	0.0109	0	0.0044	0	0.0044	0
$\lvert 3,\frac{5}{2},2,1\rangle$	0	0	3.89×10^{-5}	3.89×10^{-5}	0	0.0328	0.0328	0	0	0.0044	0.0015	0.0030
$\lvert 3,\frac{5}{2},2,2\rangle$	0	0	0	7.78×10^{-5}	0	0	0.0657	0	0	0	0.0030	0.0059
$\lvert 3,\frac{5}{2},3,-3\rangle$	0	0	0	0	0	0	0	0.0738	0	0	0	0
$\lvert 3,\frac{5}{2},3,-2\rangle$	0	0	0	0	0	0	0	0.0246	0.0492	0	0	0
$\lvert 3,\frac{5}{2},3,-1\rangle$	0	0	0	0	0	0	0	0.0049	0.0393	0.0295	0	0
$\lvert 3,\frac{5}{2},3,0\rangle$	0	0	0	0	0	0	0	0	0.0148	0.0443	0.0148	0
$\lvert 3,\frac{5}{2},3,1\rangle$	0	0	0	0	0	0	0	0	0	0.0295	0.0393	0.0049
$\lvert 3,\frac{5}{2},3,2\rangle$	0	0	0	0	0	0	0	0	0	0	0.0492	0.0246
$\lvert 3,\frac{5}{2},3,3\rangle$	0	0	0	0	0	0	0	0	0	0	0	0.0738
$\lvert 3,\frac{7}{2},3,-3\rangle$	0	0	0	0	0	0	0	3.62×10^{-5}	0	0	0	0
$\lvert 3,\frac{7}{2},3,-2\rangle$	0	0	0	0	0	0	0	1.21×10^{-5}	2.41×10^{-5}	0	0	0
$\lvert 3,\frac{7}{2},3,-1\rangle$	0	0	0	0	0	0	0	0.24×10^{-5}	1.93×10^{-5}	1.45×10^{-5}	0	0
$\lvert 3,\frac{7}{2},3,0\rangle$	0	0	0	0	0	0	0	0	0.72×10^{-5}	2.17×10^{-5}	0.72×10^{-5}	0
$\lvert 3,\frac{7}{2},3,1\rangle$	0	0	0	0	0	0	0	0	0	1.45×10^{-5}	1.93×10^{-5}	0.24×10^{-5}
$\lvert 3,\frac{7}{2},3,2\rangle$	0	0	0	0	0	0	0	0	0	0	2.41×10^{-5}	1.21×10^{-5}
$\lvert 3,\frac{7}{2},3,3\rangle$	0	0	0	0	0	0	0	0	0	0	0	3.62×10^{-5}

Table B.4: Branching ratios for decays from mixed f-parity states $\left|\widetilde{J}', \widetilde{F}_1', F', M_F'\right\rangle$ (columns) in $B^3\Pi_1$ to states in $X^1\Sigma^+$ (rows). States $\left|3,\frac{7}{2},4\right\rangle$ were not included due to selection rule $\Delta F = 0, \pm 1$ forbidding decays to those states. Decays to other states with $J = 3$ have non-zero branching ratios due to admixture of $J' = 2$ state in the $\widetilde{J}' = 1$ excited state.

$\lvert J, F_1, F, M_F\rangle$	$\lvert 2,\frac{3}{2},1,-1\rangle$	$\lvert 2,\frac{3}{2},1,0\rangle$	$\lvert 2,\frac{3}{2},1,1\rangle$	$\lvert 2,\frac{3}{2},2,-2\rangle$	$\lvert 2,\frac{3}{2},2,-1\rangle$	$\lvert 2,\frac{3}{2},2,0\rangle$	$\lvert 2,\frac{3}{2},2,1\rangle$	$\lvert 2,\frac{3}{2},2,2\rangle$
$\lvert 1,\frac{1}{2},0,0\rangle$	1/3	1/3	1/3	0	0	0	0	0
$\lvert 1,\frac{1}{2},1,-1\rangle$	1/12	1/12	0	1/2	1/4	1/12	0	0
$\lvert 1,\frac{1}{2},1,0\rangle$	1/12	0	1/12	0	1/4	1/3	1/4	0
$\lvert 1,\frac{1}{2},1,1\rangle$	0	1/12	1/12	0	0	1/12	1/4	1/2
$\lvert 1,\frac{3}{2},1,-1\rangle$	1/24	1/24	0	1/100	1/200	1/600	0	0
$\lvert 1,\frac{3}{2},1,0\rangle$	1/24	0	1/24	0	1/200	1/150	1/200	0
$\lvert 1,\frac{3}{2},1,1\rangle$	0	1/24	1/24	0	0	1/600	1/200	1/100
$\lvert 1,\frac{3}{2},2,-2\rangle$	1/100	0	0	3/50	3/100	0	0	0
$\lvert 1,\frac{3}{2},2,-1\rangle$	1/200	1/200	0	3/100	3/200	9/200	0	0
$\lvert 1,\frac{3}{2},2,0\rangle$	1/600	1/150	1/600	0	9/200	0	9/200	0
$\lvert 1,\frac{3}{2},2,1\rangle$	0	1/200	1/200	0	0	9/200	3/200	3/100
$\lvert 1,\frac{3}{2},2,2\rangle$	0	0	1/100	0	0	0	3/100	3/50
$\lvert 3,\frac{5}{2},2,-2\rangle$	6/25	0	0	4/225	2/225	0	0	0
$\lvert 3,\frac{5}{2},2,-1\rangle$	3/25	3/25	0	2/225	1/225	1/75	0	0
$\lvert 3,\frac{5}{2},2,0\rangle$	1/25	4/25	1/25	0	1/75	0	1/75	0
$\lvert 3,\frac{5}{2},2,1\rangle$	0	3/25	3/25	0	0	1/75	1/225	2/225
$\lvert 3,\frac{5}{2},2,2\rangle$	0	0	6/25	0	0	0	2/225	4/225
$\lvert 3,\frac{5}{2},3,-3\rangle$	0	0	0	4/15	0	0	0	0
$\lvert 3,\frac{5}{2},3,-2\rangle$	0	0	0	4/45	8/45	0	0	0
$\lvert 3,\frac{5}{2},3,-1\rangle$	0	0	0	4/225	32/225	8/75	0	0
$\lvert 3,\frac{5}{2},3,0\rangle$	0	0	0	0	4/75	4/25	4/75	0
$\lvert 3,\frac{5}{2},3,1\rangle$	0	0	0	0	0	8/75	32/225	4/225
$\lvert 3,\frac{5}{2},3,2\rangle$	0	0	0	0	0	0	8/45	4/45
$\lvert 3,\frac{5}{2},3,3\rangle$	0	0	0	0	0	0	0	4/15
$\lvert 3,\frac{7}{2},3,-3\rangle$	0	0	0	0	0	0	0	0
$\lvert 3,\frac{7}{2},3,-2\rangle$	0	0	0	0	0	0	0	0
$\lvert 3,\frac{7}{2},3,-1\rangle$	0	0	0	0	0	0	0	0
$\lvert 3,\frac{7}{2},3,0\rangle$	0	0	0	0	0	0	0	0
$\lvert 3,\frac{7}{2},3,1\rangle$	0	0	0	0	0	0	0	0
$\lvert 3,\frac{7}{2},3,2\rangle$	0	0	0	0	0	0	0	0
$\lvert 3,\frac{7}{2},3,3\rangle$	0	0	0	0	0	0	0	0
$\lvert 3,\frac{7}{2},4,-4\rangle$	0	0	0	0	0	0	0	0
$\lvert 3,\frac{7}{2},4,-3\rangle$	0	0	0	0	0	0	0	0
$\lvert 3,\frac{7}{2},4,-2\rangle$	0	0	0	0	0	0	0	0
$\lvert 3,\frac{7}{2},4,-1\rangle$	0	0	0	0	0	0	0	0
$\lvert 3,\frac{7}{2},4,0\rangle$	0	0	0	0	0	0	0	0
$\lvert 3,\frac{7}{2},4,1\rangle$	0	0	0	0	0	0	0	0
$\lvert 3,\frac{7}{2},4,2\rangle$	0	0	0	0	0	0	0	0
$\lvert 3,\frac{7}{2},4,3\rangle$	0	0	0	0	0	0	0	0
$\lvert 3,\frac{7}{2},4,4\rangle$	0	0	0	0	0	0	0	0

Table B.5: Branching ratios for decays from pure $J' = 2, F_1' = 3/2$ e-parity states $|J', F_1', F', M_F'\rangle$ (columns) in $B^3\Pi_1$ to states in $X^1\Sigma^+$ (rows).

$\lvert J, F_1, F, M_F\rangle$	$\lvert 2, \frac{5}{2}, 2, -2\rangle$	$\lvert 2, \frac{5}{2}, 2, -1\rangle$	$\lvert 2, \frac{5}{2}, 2, 0\rangle$	$\lvert 2, \frac{5}{2}, 2, 1\rangle$	$\lvert 2, \frac{5}{2}, 2, 2\rangle$	$\lvert 2, \frac{5}{2}, 3, -3\rangle$	$\lvert 2, \frac{5}{2}, 3, -2\rangle$	$\lvert 2, \frac{5}{2}, 3, -1\rangle$	$\lvert 2, \frac{5}{2}, 3, 0\rangle$	$\lvert 2, \frac{5}{2}, 3, 1\rangle$	$\lvert 2, \frac{5}{2}, 3, 2\rangle$	$\lvert 2, \frac{5}{2}, 3, 3\rangle$
$\lvert 1, \frac{1}{2}, 0, 0\rangle$	0	0	0	0	0	0	0	0	0	0	0	0
$\lvert 1, \frac{1}{2}, 1, -1\rangle$	0	0	0	0	0	0	0	0	0	0	0	0
$\lvert 1, \frac{1}{2}, 1, 0\rangle$	0	0	0	0	0	0	0	0	0	0	0	0
$\lvert 1, \frac{1}{2}, 1, 1\rangle$	0	0	0	0	0	0	0	0	0	0	0	0
$\lvert 1, \frac{3}{2}, 1, -1\rangle$	27/50	27/100	9/100	0	0	0	0	0	0	0	0	0
$\lvert 1, \frac{3}{2}, 1, 0\rangle$	0	27/100	9/25	27/100	0	0	0	0	0	0	0	0
$\lvert 1, \frac{3}{2}, 1, 1\rangle$	0	0	9/100	27/100	27/50	0	0	0	0	0	0	0
$\lvert 1, \frac{3}{2}, 2, -2\rangle$	1/25	1/50	0	0	0	3/5	1/5	1/25	0	0	0	0
$\lvert 1, \frac{3}{2}, 2, -1\rangle$	1/50	1/100	3/100	0	0	0	2/5	8/25	3/25	0	0	0
$\lvert 1, \frac{3}{2}, 2, 0\rangle$	0	3/100	0	3/100	0	0	0	6/25	9/25	6/25	0	0
$\lvert 1, \frac{3}{2}, 2, 1\rangle$	0	0	3/100	1/100	1/50	0	0	0	3/25	8/25	2/5	0
$\lvert 1, \frac{3}{2}, 2, 2\rangle$	0	0	0	1/50	1/25	0	0	0	0	1/25	1/5	3/5
$\lvert 3, \frac{5}{2}, 2, -2\rangle$	8/675	4/675	0	0	0	2/2205	2/6615	2/33075	0	0	0	0
$\lvert 3, \frac{5}{2}, 2, -1\rangle$	4/675	2/675	2/225	0	0	0	4/6615	16/33075	2/11025	0	0	0
$\lvert 3, \frac{5}{2}, 2, 0\rangle$	0	2/225	0	2/225	0	0	0	4/11025	2/3675	4/11025	0	0
$\lvert 3, \frac{5}{2}, 2, 1\rangle$	0	0	2/225	2/675	4/675	0	0	0	2/11025	16/33075	4/6615	0
$\lvert 3, \frac{5}{2}, 2, 2\rangle$	0	0	0	4/675	8/675	0	0	0	0	2/33075	2/6615	2/2205
$\lvert 3, \frac{5}{2}, 3, -3\rangle$	2/2205	0	0	0	0	2/147	2/441	0	0	0	0	0
$\lvert 3, \frac{5}{2}, 3, -2\rangle$	2/6615	4/6615	0	0	0	2/441	8/1323	10/1323	0	0	0	0
$\lvert 3, \frac{5}{2}, 3, -1\rangle$	2/33075	16/33075	4/11025	0	0	0	10/1323	2/1323	4/441	0	0	0
$\lvert 3, \frac{5}{2}, 3, 0\rangle$	0	2/11025	2/3675	2/11025	0	0	0	4/441	0	4/441	0	0
$\lvert 3, \frac{5}{2}, 3, 1\rangle$	0	0	4/11025	16/33075	2/33075	0	0	0	4/441	2/1323	10/1323	0
$\lvert 3, \frac{5}{2}, 3, 2\rangle$	0	0	0	4/6615	2/6615	0	0	0	0	10/1323	8/1323	2/441
$\lvert 3, \frac{5}{2}, 3, 3\rangle$	0	0	0	0	2/2205	0	0	0	0	0	2/441	2/147
$\lvert 3, \frac{7}{2}, 3, -3\rangle$	40/147	0	0	0	0	1/98	1/294	0	0	0	0	0
$\lvert 3, \frac{7}{2}, 3, -2\rangle$	40/441	80/441	0	0	0	1/294	2/441	5/882	0	0	0	0
$\lvert 3, \frac{7}{2}, 3, -1\rangle$	8/441	64/441	16/147	0	0	0	5/882	1/882	1/147	0	0	0
$\lvert 3, \frac{7}{2}, 3, 0\rangle$	0	8/147	8/49	8/147	0	0	0	1/147	0	1/147	0	0
$\lvert 3, \frac{7}{2}, 3, 1\rangle$	0	0	16/147	64/441	8/441	0	0	0	1/147	1/882	5/882	0
$\lvert 3, \frac{7}{2}, 3, 2\rangle$	0	0	0	80/441	40/441	0	0	0	0	5/882	2/441	1/294
$\lvert 3, \frac{7}{2}, 3, 3\rangle$	0	0	0	0	40/147	0	0	0	0	0	1/294	1/98
$\lvert 3, \frac{7}{2}, 4, -4\rangle$	0	0	0	0	0	2/7	0	0	0	0	0	0
$\lvert 3, \frac{7}{2}, 4, -3\rangle$	0	0	0	0	0	1/14	3/14	0	0	0	0	0
$\lvert 3, \frac{7}{2}, 4, -2\rangle$	0	0	0	0	0	1/98	6/49	15/98	0	0	0	0
$\lvert 3, \frac{7}{2}, 4, -1\rangle$	0	0	0	0	0	0	3/98	15/98	5/49	0	0	0
$\lvert 3, \frac{7}{2}, 4, 0\rangle$	0	0	0	0	0	0	0	3/49	8/49	3/49	0	0
$\lvert 3, \frac{7}{2}, 4, 1\rangle$	0	0	0	0	0	0	0	0	5/49	15/98	3/98	0
$\lvert 3, \frac{7}{2}, 4, 2\rangle$	0	0	0	0	0	0	0	0	0	15/98	6/49	1/98
$\lvert 3, \frac{7}{2}, 4, 3\rangle$	0	0	0	0	0	0	0	0	0	0	3/14	1/14
$\lvert 3, \frac{7}{2}, 4, 4\rangle$	0	0	0	0	0	0	0	0	0	0	0	2/7

Table B.6: Branching ratios for decays from pure $J' = 2, F_1' = 5/2$ e-parity states $\lvert J', F_1', F', M_F'\rangle$ (columns) in $B^3\Pi_1$ to states in $X^1\Sigma^+$ (rows).

$\lvert J, F_1, F, M_F\rangle$	$\lvert 2,\frac{3}{2},1,-1\rangle$	$\lvert 2,\frac{3}{2},1,0\rangle$	$\lvert 2,\frac{3}{2},1,1\rangle$	$\lvert 2,\frac{3}{2},2,-2\rangle$	$\lvert 2,\frac{3}{2},2,-1\rangle$	$\lvert 2,\frac{3}{2},2,0\rangle$	$\lvert 2,\frac{3}{2},2,1\rangle$	$\lvert 2,\frac{3}{2},2,2\rangle$
$\lvert 2,\frac{3}{2},1,-1\rangle$	3/8	3/8	0	9/100	9/200	3/200	0	0
$\lvert 2,\frac{3}{2},1,0\rangle$	3/8	0	3/8	0	9/200	3/50	9/200	0
$\lvert 2,\frac{3}{2},1,1\rangle$	0	3/8	3/8	0	0	3/200	9/200	9/100
$\lvert 2,\frac{3}{2},2,-2\rangle$	9/100	0	0	27/50	27/100	0	0	0
$\lvert 2,\frac{3}{2},2,-1\rangle$	9/200	9/200	0	27/100	27/200	81/200	0	0
$\lvert 2,\frac{3}{2},2,0\rangle$	3/200	3/50	3/200	0	81/200	0	81/200	0
$\lvert 2,\frac{3}{2},2,1\rangle$	0	9/200	9/200	0	0	81/200	27/200	27/100
$\lvert 2,\frac{3}{2},2,2\rangle$	0	0	9/100	0	0	0	27/100	27/50
$\lvert 2,\frac{5}{2},2,-2\rangle$	3/50	0	0	1/225	1/450	0	0	0
$\lvert 2,\frac{5}{2},2,-1\rangle$	3/100	3/100	0	1/450	1/900	1/300	0	0
$\lvert 2,\frac{5}{2},2,0\rangle$	1/100	1/25	1/100	0	1/300	0	1/300	0
$\lvert 2,\frac{5}{2},2,1\rangle$	0	3/100	3/100	0	0	1/300	1/900	1/450
$\lvert 2,\frac{5}{2},2,2\rangle$	0	0	3/50	0	0	0	1/450	1/225
$\lvert 2,\frac{5}{2},3,-3\rangle$	0	0	0	1/15	0	0	0	0
$\lvert 2,\frac{5}{2},3,-2\rangle$	0	0	0	1/45	2/45	0	0	0
$\lvert 2,\frac{5}{2},3,-1\rangle$	0	0	0	1/225	8/225	2/75	0	0
$\lvert 2,\frac{5}{2},3,0\rangle$	0	0	0	0	1/75	1/25	1/75	0
$\lvert 2,\frac{5}{2},3,1\rangle$	0	0	0	0	0	2/75	8/225	1/225
$\lvert 2,\frac{5}{2},3,2\rangle$	0	0	0	0	0	0	2/45	1/45
$\lvert 2,\frac{5}{2},3,3\rangle$	0	0	0	0	0	0	0	1/15

Table B.7: Branching ratios for decays from pure $J' = 2$, $F_1' = 3/2$ f-parity states $|J', F_1', F', M_F'\rangle$ (columns) in $B^3\Pi_1$ to states in $X^1\Sigma^+$ (rows).

	$\lvert 2,\frac{5}{2},2,-2\rangle$	$\lvert 2,\frac{5}{2},2,-1\rangle$	$\lvert 2,\frac{5}{2},2,0\rangle$	$\lvert 2,\frac{5}{2},2,1\rangle$	$\lvert 2,\frac{5}{2},2,2\rangle$	$\lvert 2,\frac{5}{2},3,-3\rangle$	$\lvert 2,\frac{5}{2},3,-2\rangle$	$\lvert 2,\frac{5}{2},3,-1\rangle$	$\lvert 2,\frac{5}{2},3,0\rangle$	$\lvert 2,\frac{5}{2},3,1\rangle$	$\lvert 2,\frac{5}{2},3,2\rangle$	$\lvert 2,\frac{5}{2},3,3\rangle$
$\lvert 2,\frac{3}{2},1,-1\rangle$	3/50	3/100	1/100	0	0	0	0	0	0	0	0	0
$\lvert 2,\frac{3}{2},1,0\rangle$	0	3/100	1/25	3/100	0	0	0	0	0	0	0	0
$\lvert 2,\frac{3}{2},1,1\rangle$	0	0	1/100	3/100	3/50	0	0	0	0	0	0	0
$\lvert 2,\frac{3}{2},2,-2\rangle$	1/225	1/450	0	0	0	1/15	1/45	1/225	0	0	0	0
$\lvert 2,\frac{3}{2},2,-1\rangle$	1/450	1/900	1/300	0	0	0	2/45	8/225	1/75	0	0	0
$\lvert 2,\frac{3}{2},2,0\rangle$	0	1/300	0	1/300	0	0	0	2/75	1/25	2/75	0	0
$\lvert 2,\frac{3}{2},2,1\rangle$	0	0	1/300	1/900	1/450	0	0	0	1/75	8/225	2/45	0
$\lvert 2,\frac{3}{2},2,2\rangle$	0	0	0	1/450	1/225	0	0	0	0	1/225	1/45	1/15
$\lvert 2,\frac{5}{2},2,-2\rangle$	392/675	196/675	0	0	0	2/45	2/135	2/675	0	0	0	0
$\lvert 2,\frac{5}{2},2,-1\rangle$	196/675	98/675	98/225	0	0	0	4/135	16/675	2/225	0	0	0
$\lvert 2,\frac{5}{2},2,0\rangle$	0	98/225	0	98/225	0	0	0	4/225	2/75	4/225	0	0
$\lvert 2,\frac{5}{2},2,1\rangle$	0	0	98/225	98/675	196/675	0	0	0	2/225	16/675	4/135	0
$\lvert 2,\frac{5}{2},2,2\rangle$	0	0	0	392/675	392/675	0	0	0	0	2/675	2/135	2/45
$\lvert 2,\frac{5}{2},3,-3\rangle$	2/45	0	0	0	0	2/3	2/9	0	0	0	0	0
$\lvert 2,\frac{5}{2},3,-2\rangle$	2/135	4/135	0	0	0	2/9	8/27	10/27	0	0	0	0
$\lvert 2,\frac{5}{2},3,-1\rangle$	2/675	16/675	4/225	0	0	0	10/27	2/27	4/9	0	0	0
$\lvert 2,\frac{5}{2},3,0\rangle$	0	2/225	2/75	2/225	0	0	0	4/9	0	4/9	0	0
$\lvert 2,\frac{5}{2},3,1\rangle$	0	0	4/225	16/675	2/675	0	0	0	4/9	2/27	10/27	0
$\lvert 2,\frac{5}{2},3,2\rangle$	0	0	0	4/135	2/135	0	0	0	0	10/27	8/27	2/9
$\lvert 2,\frac{5}{2},3,3\rangle$	0	0	0	0	2/45	0	0	0	0	0	2/9	2/3

Table B.8: Branching ratios for decays from pure $J' = 2$, $F_1' = 5/2$ f-parity states $|J', F_1', F', M_F'\rangle$ (columns) in $B^3\Pi_1$ to states in $X^1\Sigma^+$ (rows).

$\lvert J, F_1, F, M_F\rangle$	$\lvert 2, \frac{3}{2}, 1, -1\rangle$	$\lvert 2, \frac{3}{2}, 1, 0\rangle$	$\lvert 2, \frac{3}{2}, 1, 1\rangle$	$\lvert 2, \frac{3}{2}, 2, -2\rangle$	$\lvert 2, \frac{3}{2}, 2, -1\rangle$	$\lvert 2, \frac{3}{2}, 2, 0\rangle$	$\lvert 2, \frac{3}{2}, 2, 1\rangle$	$\lvert 2, \frac{3}{2}, 2, 2\rangle$
$\lvert 0, \frac{1}{2}, 0, 0\rangle$	0.1202	0.1202	0.1202	0	0	0	0	0
$\lvert 0, \frac{1}{2}, 1, -1\rangle$	0.0312	0.0312	0	0.1869	0.0935	0.0312	0	0
$\lvert 0, \frac{1}{2}, 1, 0\rangle$	0.0312	0	0.0312	0	0.0935	0.1246	0.0935	0
$\lvert 0, \frac{1}{2}, 1, 1\rangle$	0	0.0312	0.0312	0	0	0.0312	0.0935	0.1869
$\lvert 2, \frac{3}{2}, 1, -1\rangle$	0.2109	0.2109	0	0.0535	0.0268	0.0089	0	0
$\lvert 2, \frac{3}{2}, 1, 0\rangle$	0.2109	0	0.2109	0	0.0268	0.0357	0.0268	0
$\lvert 2, \frac{3}{2}, 1, 1\rangle$	0	0.2109	0.2109	0	0	0.0089	0.0268	0.0535
$\lvert 2, \frac{3}{2}, 2, -2\rangle$	0.0517	0	0	0.2986	0.1493	0	0	0
$\lvert 2, \frac{3}{2}, 2, -1\rangle$	0.0258	0.0258	0	0.1493	0.0746	0.2239	0	0
$\lvert 2, \frac{3}{2}, 2, 0\rangle$	0.0086	0.0345	0.0086	0	0.2239	0	0.2239	0
$\lvert 2, \frac{3}{2}, 2, 1\rangle$	0	0.0258	0.0258	0	0	0.2239	0.0746	0.1493
$\lvert 2, \frac{3}{2}, 2, 2\rangle$	0	0	0.0517	0	0	0	0.1493	0.2986
$\lvert 2, \frac{5}{2}, 2, -2\rangle$	0.1856	0	0	0.0140	0.0070	0	0	0
$\lvert 2, \frac{5}{2}, 2, -1\rangle$	0.0928	0.0928	0	0.0070	0.0035	0.0105	0	0
$\lvert 2, \frac{5}{2}, 2, 0\rangle$	0.0309	0.1237	0.0309	0	0.0105	0	0.0105	0
$\lvert 2, \frac{5}{2}, 2, 1\rangle$	0	0.0928	0.0928	0	0	0.0105	0.0035	0.0070
$\lvert 2, \frac{5}{2}, 2, 2\rangle$	0	0	0.1856	0	0	0	0.0070	0.0140
$\lvert 2, \frac{5}{2}, 3, -3\rangle$	0	0	0	0.2076	0	0	0	0
$\lvert 2, \frac{5}{2}, 3, -2\rangle$	0	0	0	0.0692	0.1384	0	0	0
$\lvert 2, \frac{5}{2}, 3, -1\rangle$	0	0	0	0.0138	0.1107	0.0830	0	0
$\lvert 2, \frac{5}{2}, 3, 0\rangle$	0	0	0	0	0.0415	0.1246	0.0415	0
$\lvert 2, \frac{5}{2}, 3, 1\rangle$	0	0	0	0	0	0.0830	0.1107	0.0138
$\lvert 2, \frac{5}{2}, 3, 2\rangle$	0	0	0	0	0	0	0.1384	0.0692
$\lvert 2, \frac{5}{2}, 3, 3\rangle$	0	0	0	0	0	0	0	0.2076
$\lvert 4, \frac{7}{2}, 3, -3\rangle$	0	0	0	3.25×10^{-5}	0	0	0	0
$\lvert 4, \frac{7}{2}, 3, -2\rangle$	0	0	0	1.08×10^{-5}	2.17×10^{-5}	0	0	0
$\lvert 4, \frac{7}{2}, 3, -1\rangle$	0	0	0	0.22×10^{-5}	1.73×10^{-5}	1.30×10^{-5}	0	0
$\lvert 4, \frac{7}{2}, 3, 0\rangle$	0	0	0	0	0.65×10^{-5}	1.95×10^{-5}	0.65×10^{-5}	0
$\lvert 4, \frac{7}{2}, 3, 1\rangle$	0	0	0	0	0	1.30×10^{-5}	1.73×10^{-5}	0.22×10^{-5}
$\lvert 4, \frac{7}{2}, 3, 2\rangle$	0	0	0	0	0	0	2.17×10^{-5}	1.08×10^{-5}
$\lvert 4, \frac{7}{2}, 3, 3\rangle$	0	0	0	0	0	0	0	3.25×10^{-5}
$\lvert 4, \frac{7}{2}, 4, -4\rangle$	0	0	0	0	0	0	0	0
$\lvert 4, \frac{7}{2}, 4, -3\rangle$	0	0	0	0	0	0	0	0
$\lvert 4, \frac{7}{2}, 4, -2\rangle$	0	0	0	0	0	0	0	0
$\lvert 4, \frac{7}{2}, 4, -1\rangle$	0	0	0	0	0	0	0	0
$\lvert 4, \frac{7}{2}, 4, 0\rangle$	0	0	0	0	0	0	0	0
$\lvert 4, \frac{7}{2}, 4, 1\rangle$	0	0	0	0	0	0	0	0
$\lvert 4, \frac{7}{2}, 4, 2\rangle$	0	0	0	0	0	0	0	0
$\lvert 4, \frac{7}{2}, 4, 3\rangle$	0	0	0	0	0	0	0	0
$\lvert 4, \frac{7}{2}, 4, 4\rangle$	0	0	0	0	0	0	0	0
$\lvert 4, \frac{9}{2}, 4, -4\rangle$	0	0	0	0	0	0	0	0
$\lvert 4, \frac{9}{2}, 4, -3\rangle$	0	0	0	0	0	0	0	0
$\lvert 4, \frac{9}{2}, 4, -2\rangle$	0	0	0	0	0	0	0	0
$\lvert 4, \frac{9}{2}, 4, -1\rangle$	0	0	0	0	0	0	0	0
$\lvert 4, \frac{9}{2}, 4, 0\rangle$	0	0	0	0	0	0	0	0
$\lvert 4, \frac{9}{2}, 4, 1\rangle$	0	0	0	0	0	0	0	0
$\lvert 4, \frac{9}{2}, 4, 2\rangle$	0	0	0	0	0	0	0	0
$\lvert 4, \frac{9}{2}, 4, 3\rangle$	0	0	0	0	0	0	0	0
$\lvert 4, \frac{9}{2}, 4, 4\rangle$	0	0	0	0	0	0	0	0

Table B.9: Branching ratios for decays from mixed $\widetilde{J}' = 2$, $\widetilde{F}_1' = 3/2$ f-parity states $\left|\widetilde{J}', \widetilde{F}_1', F', M_F'\right\rangle$ (columns) in $B^3\Pi_1$ to states in $X^1\Sigma^+$ (rows).

$\lvert J, F_1, F, M_F\rangle$	$\lvert 2, \frac{5}{2}, 2, -2\rangle$	$\lvert 2, \frac{5}{2}, 2, -1\rangle$	$\lvert 2, \frac{5}{2}, 2, 0\rangle$	$\lvert 2, \frac{5}{2}, 2, 1\rangle$	$\lvert 2, \frac{5}{2}, 2, 2\rangle$	$\lvert 2, \frac{5}{2}, 3, -3\rangle$	$\lvert 2, \frac{5}{2}, 3, -2\rangle$	$\lvert 2, \frac{5}{2}, 3, -1\rangle$	$\lvert 2, \frac{5}{2}, 3, 0\rangle$	$\lvert 2, \frac{5}{2}, 3, 1\rangle$	$\lvert 2, \frac{5}{2}, 3, 2\rangle$	$\lvert 2, \frac{5}{2}, 3, 3\rangle$
$\lvert 0, \frac{1}{2}, 0, 0\rangle$	0	0	0	0	0	0	0	0	0	0	0	0
$\lvert 0, \frac{1}{2}, 1, -1\rangle$	7.21×10^{-5}	3.61×10^{-5}	1.20×10^{-5}	0	0	0	0	0	0	0	0	0
$\lvert 0, \frac{1}{2}, 1, 0\rangle$	0	3.61×10^{-5}	4.81×10^{-5}	3.61×10^{-5}	0	0	0	0	0	0	0	0
$\lvert 0, \frac{1}{2}, 1, 1\rangle$	0	0	1.20×10^{-5}	3.61×10^{-5}	7.21×10^{-5}	0	0	0	0	0	0	0
$\lvert 2, \frac{3}{2}, 1, -1\rangle$	0.2207	0.1104	0.0368	0	0	0	0	0	0	0	0	0
$\lvert 2, \frac{3}{2}, 1, 0\rangle$	0	0.1104	0.1471	0.1104	0	0	0	0	0	0	0	0
$\lvert 2, \frac{3}{2}, 1, 1\rangle$	0	0	0.0368	0.1104	0.2207	0	0	0	0	0	0	0
$\lvert 2, \frac{3}{2}, 2, -2\rangle$	0.0194	0.0097	0	0	0	0.2518	0.0839	0.0168	0	0	0	0
$\lvert 2, \frac{3}{2}, 2, -1\rangle$	0.0097	0.0049	0.0146	0	0	0	0.1678	0.1343	0.0504	0	0	0
$\lvert 2, \frac{3}{2}, 2, 0\rangle$	0	0.0146	0	0.0146	0	0	0	0.1007	0.1511	0.1007	0	0
$\lvert 2, \frac{3}{2}, 2, 1\rangle$	0	0	0.0146	0.0049	0.0097	0	0	0	0.0504	0.1343	0.1678	0
$\lvert 2, \frac{3}{2}, 2, 2\rangle$	0	0	0	0.0097	0.0194	0	0	0	0	0.0168	0.0839	0.2518
$\lvert 2, \frac{5}{2}, 2, -2\rangle$	0.4329	0.2164	0	0	0	0.0358	0.0119	0.0024	0	0	0	0
$\lvert 2, \frac{5}{2}, 2, -1\rangle$	0.2164	0.1082	0.3247	0	0	0	0.0238	0.0191	0.0072	0	0	0
$\lvert 2, \frac{5}{2}, 2, 0\rangle$	0	0.3247	0	0.3247	0	0	0	0.0143	0.0215	0.0143	0	0
$\lvert 2, \frac{5}{2}, 2, 1\rangle$	0	0	0.3247	0.1082	0.2164	0	0	0	0.0072	0.0191	0.0238	0
$\lvert 2, \frac{5}{2}, 2, 2\rangle$	0	0	0	0.2164	0.4329	0	0	0	0	0.0024	0.0119	0.0358
$\lvert 2, \frac{5}{2}, 3, -3\rangle$	0.0337	0	0	0	0	0.4934	0.1645	0	0	0	0	0
$\lvert 2, \frac{5}{2}, 3, -2\rangle$	0.0112	0.0225	0	0	0	0.1645	0.2193	0.2741	0	0	0	0
$\lvert 2, \frac{5}{2}, 3, -1\rangle$	0.0022	0.0180	0.0135	0	0	0	0.2741	0.0548	0.3289	0	0	0
$\lvert 2, \frac{5}{2}, 3, 0\rangle$	0	0.0067	0.0202	0.0067	0	0	0	0.3289	0	0.3289	0	0
$\lvert 2, \frac{5}{2}, 3, 1\rangle$	0	0	0.0135	0.0180	0.0022	0	0	0	0.3289	0.0548	0.2741	0
$\lvert 2, \frac{5}{2}, 3, 2\rangle$	0	0	0	0.0225	0.0112	0	0	0	0	0.2741	0.2193	0.1645
$\lvert 2, \frac{5}{2}, 3, 3\rangle$	0	0	0	0	0.0337	0	0	0	0	0	0.1645	0.4934
$\lvert 4, \frac{7}{2}, 3, -3\rangle$	0.0383	0	0	0	0	0.0018	0.0006	0	0	0	0	0
$\lvert 4, \frac{7}{2}, 3, -2\rangle$	0.0128	0.0255	0	0	0	0.0006	0.0008	0.0010	0	0	0	0
$\lvert 4, \frac{7}{2}, 3, -1\rangle$	0.0026	0.0204	0.0153	0	0	0	0.0010	0.0002	0.0012	0	0	0
$\lvert 4, \frac{7}{2}, 3, 0\rangle$	0	0.0077	0.0230	0.0077	0	0	0	0.0012	0	0.0012	0	0
$\lvert 4, \frac{7}{2}, 3, 1\rangle$	0	0	0.0153	0.0204	0.0026	0	0	0	0.0012	0.0002	0.0010	0
$\lvert 4, \frac{7}{2}, 3, 2\rangle$	0	0	0	0.0255	0.0128	0	0	0	0	0.0010	0.0008	0.0006
$\lvert 4, \frac{7}{2}, 3, 3\rangle$	0	0	0	0	0.0383	0	0	0	0	0	0.0006	0.0018
$\lvert 4, \frac{7}{2}, 4, -4\rangle$	0	0	0	0	0	0.0406	0	0	0	0	0	0
$\lvert 4, \frac{7}{2}, 4, -3\rangle$	0	0	0	0	0	0.0102	0.0305	0	0	0	0	0
$\lvert 4, \frac{7}{2}, 4, -2\rangle$	0	0	0	0	0	0.0015	0.0174	0.0218	0	0	0	0
$\lvert 4, \frac{7}{2}, 4, -1\rangle$	0	0	0	0	0	0	0.0044	0.0218	0.0145	0	0	0
$\lvert 4, \frac{7}{2}, 4, 0\rangle$	0	0	0	0	0	0	0	0.0087	0.0232	0.0087	0	0
$\lvert 4, \frac{7}{2}, 4, 1\rangle$	0	0	0	0	0	0	0	0	0.0145	0.0218	0.0044	0
$\lvert 4, \frac{7}{2}, 4, 2\rangle$	0	0	0	0	0	0	0	0	0	0.0218	0.0174	0.0015
$\lvert 4, \frac{7}{2}, 4, 3\rangle$	0	0	0	0	0	0	0	0	0	0	0.0305	0.0102
$\lvert 4, \frac{7}{2}, 4, 4\rangle$	0	0	0	0	0	0	0	0	0	0	0	0.0406
$\lvert 4, \frac{9}{2}, 4, -4\rangle$	0	0	0	0	0	2.73×10^{-5}	0	0	0	0	0	0
$\lvert 4, \frac{9}{2}, 4, -3\rangle$	0	0	0	0	0	0.68×10^{-5}	2.05×10^{-5}	0	0	0	0	0
$\lvert 4, \frac{9}{2}, 4, -2\rangle$	0	0	0	0	0	0.10×10^{-5}	1.17×10^{-5}	1.46×10^{-5}	0	0	0	0
$\lvert 4, \frac{9}{2}, 4, -1\rangle$	0	0	0	0	0	0	0.29×10^{-5}	1.46×10^{-5}	0.97×10^{-5}	0	0	0
$\lvert 4, \frac{9}{2}, 4, 0\rangle$	0	0	0	0	0	0	0	0.58×10^{-5}	1.56×10^{-5}	0.58×10^{-5}	0	0
$\lvert 4, \frac{9}{2}, 4, 1\rangle$	0	0	0	0	0	0	0	0	0.97×10^{-5}	1.46×10^{-5}	0.29×10^{-5}	0
$\lvert 4, \frac{9}{2}, 4, 2\rangle$	0	0	0	0	0	0	0	0	0	1.46×10^{-5}	1.17×10^{-5}	0.10×10^{-5}
$\lvert 4, \frac{9}{2}, 4, 3\rangle$	0	0	0	0	0	0	0	0	0	0	2.05×10^{-5}	0.68×10^{-5}
$\lvert 4, \frac{9}{2}, 4, 4\rangle$	0	0	0	0	0	0	0	0	0	0	0	2.73×10^{-5}

Table B.10: Branching ratios for decays from mixed $\widetilde{J}' = 2$, $\widetilde{F}_1' = 5/2$ f-parity states $\left|\widetilde{J}', \widetilde{F}_1', F', M_F'\right\rangle$ (columns) in $B^3\Pi_1$ to states in $X^1\Sigma^+$ (rows).

$\lvert J, F_1, F, M_F\rangle$	$\lvert 2, \frac{3}{2}, 1, -1\rangle$	$\lvert 2, \frac{3}{2}, 1, 0\rangle$	$\lvert 2, \frac{3}{2}, 1, 1\rangle$	$\lvert 2, \frac{3}{2}, 2, -2\rangle$	$\lvert 2, \frac{3}{2}, 2, -1\rangle$	$\lvert 2, \frac{3}{2}, 2, 0\rangle$	$\lvert 2, \frac{3}{2}, 2, 1\rangle$	$\lvert 2, \frac{3}{2}, 2, 2\rangle$
$\lvert 1, \frac{1}{2}, 0, 0\rangle$	0.0993	0.0993	0.0993	0	0	0	0	0
$\lvert 1, \frac{1}{2}, 1, -1\rangle$	0.0259	0.0259	0	0.1472	0.0736	0.0245	0	0
$\lvert 1, \frac{1}{2}, 1, 0\rangle$	0.0259	0	0.0259	0	0.0736	0.0981	0.0736	0
$\lvert 1, \frac{1}{2}, 1, 1\rangle$	0	0.0259	0.0259	0	0	0.0245	0.0736	0.1472
$\lvert 1, \frac{3}{2}, 1, -1\rangle$	0.2319	0.2319	0	0.0561	0.0281	0.0094	0	0
$\lvert 1, \frac{3}{2}, 1, 0\rangle$	0.2319	0	0.2319	0	0.0281	0.0374	0.0281	0
$\lvert 1, \frac{3}{2}, 1, 1\rangle$	0	0.2319	0.2319	0	0	0.0094	0.0281	0.0561
$\lvert 1, \frac{3}{2}, 2, -2\rangle$	0.0568	0	0	0.3392	0.1696	0	0	0
$\lvert 1, \frac{3}{2}, 2, -1\rangle$	0.0284	0.0284	0	0.1696	0.0848	0.2544	0	0
$\lvert 1, \frac{3}{2}, 2, 0\rangle$	0.0095	0.0379	0.0095	0	0.2544	0	0.2544	0
$\lvert 1, \frac{3}{2}, 2, 1\rangle$	0	0.0284	0.0284	0	0	0.2544	0.0848	0.1696
$\lvert 1, \frac{3}{2}, 2, 2\rangle$	0	0	0.0568	0	0	0	0.1696	0.3392
$\lvert 3, \frac{5}{2}, 2, -2\rangle$	0.1742	0	0	0.0147	0.0073	0	0	0
$\lvert 3, \frac{5}{2}, 2, -1\rangle$	0.0871	0.0871	0	0.0073	0.0037	0.0110	0	0
$\lvert 3, \frac{5}{2}, 2, 0\rangle$	0.0290	0.1161	0.0290	0	0.0110	0	0.0110	0
$\lvert 3, \frac{5}{2}, 2, 1\rangle$	0	0.0871	0.0871	0	0	0.0110	0.0037	0.0073
$\lvert 3, \frac{5}{2}, 2, 2\rangle$	0	0	0.1742	0	0	0	0.0073	0.0147
$\lvert 3, \frac{5}{2}, 3, -3\rangle$	0	0	0	0.1899	0	0	0	0
$\lvert 3, \frac{5}{2}, 3, -2\rangle$	0	0	0	0.0633	0.1266	0	0	0
$\lvert 3, \frac{5}{2}, 3, -1\rangle$	0	0	0	0.0127	0.1013	0.0760	0	0
$\lvert 3, \frac{5}{2}, 3, 0\rangle$	0	0	0	0	0.0380	0.1140	0.0380	0
$\lvert 3, \frac{5}{2}, 3, 1\rangle$	0	0	0	0	0	0.0760	0.1013	0.0127
$\lvert 3, \frac{5}{2}, 3, 2\rangle$	0	0	0	0	0	0	0.1266	0.0633
$\lvert 3, \frac{5}{2}, 3, 3\rangle$	0	0	0	0	0	0	0	0.1899
$\lvert 3, \frac{7}{2}, 3, -3\rangle$	0	0	0	0.18×10^{-5}	0	0	0	0
$\lvert 3, \frac{7}{2}, 3, -2\rangle$	0	0	0	0.06×10^{-5}	0.12×10^{-5}	0	0	0
$\lvert 3, \frac{7}{2}, 3, -1\rangle$	0	0	0	0.01×10^{-5}	0.09×10^{-5}	0.07×10^{-5}	0	0
$\lvert 3, \frac{7}{2}, 3, 0\rangle$	0	0	0	0	0.04×10^{-5}	0.11×10^{-5}	0.04×10^{-5}	0
$\lvert 3, \frac{7}{2}, 3, 1\rangle$	0	0	0	0	0	0.07×10^{-5}	0.09×10^{-5}	0.01×10^{-5}
$\lvert 3, \frac{7}{2}, 3, 2\rangle$	0	0	0	0	0	0	0.12×10^{-5}	0.06×10^{-5}
$\lvert 3, \frac{7}{2}, 3, 3\rangle$	0	0	0	0	0	0	0	0.18×10^{-5}
$\lvert 3, \frac{7}{2}, 4, -4\rangle$	0	0	0	0	0	0	0	0
$\lvert 3, \frac{7}{2}, 4, -3\rangle$	0	0	0	0	0	0	0	0
$\lvert 3, \frac{7}{2}, 4, -2\rangle$	0	0	0	0	0	0	0	0
$\lvert 3, \frac{7}{2}, 4, -1\rangle$	0	0	0	0	0	0	0	0
$\lvert 3, \frac{7}{2}, 4, 0\rangle$	0	0	0	0	0	0	0	0
$\lvert 3, \frac{7}{2}, 4, 1\rangle$	0	0	0	0	0	0	0	0
$\lvert 3, \frac{7}{2}, 4, 2\rangle$	0	0	0	0	0	0	0	0
$\lvert 3, \frac{7}{2}, 4, 3\rangle$	0	0	0	0	0	0	0	0
$\lvert 3, \frac{7}{2}, 4, 4\rangle$	0	0	0	0	0	0	0	0
$\lvert 5, \frac{9}{2}, 4, -4\rangle$	0	0	0	0	0	0	0	0
$\lvert 5, \frac{9}{2}, 4, -3\rangle$	0	0	0	0	0	0	0	0
$\lvert 5, \frac{9}{2}, 4, -2\rangle$	0	0	0	0	0	0	0	0
$\lvert 5, \frac{9}{2}, 4, -1\rangle$	0	0	0	0	0	0	0	0
$\lvert 5, \frac{9}{2}, 4, 0\rangle$	0	0	0	0	0	0	0	0
$\lvert 5, \frac{9}{2}, 4, 1\rangle$	0	0	0	0	0	0	0	0
$\lvert 5, \frac{9}{2}, 4, 2\rangle$	0	0	0	0	0	0	0	0
$\lvert 5, \frac{9}{2}, 4, 3\rangle$	0	0	0	0	0	0	0	0
$\lvert 5, \frac{9}{2}, 4, 4\rangle$	0	0	0	0	0	0	0	0

Table B.11: Branching ratios for decays from mixed $\widetilde{J}' = 2$, $\widetilde{F}_1' = 3/2$ e-parity states $\left|\widetilde{J}', \widetilde{F}_1', F', M_F'\right\rangle$ (columns) in $B^3\Pi_1$ to states in $X^1\Sigma^+$ (rows).

$\lvert J, F_1, F, M_F\rangle$	$\lvert 2, \frac{5}{2}, 2, -2\rangle$	$\lvert 2, \frac{5}{2}, 2, -1\rangle$	$\lvert 2, \frac{5}{2}, 2, 0\rangle$	$\lvert 2, \frac{5}{2}, 2, 1\rangle$	$\lvert 2, \frac{5}{2}, 2, 2\rangle$	$\lvert 2, \frac{5}{2}, 3, -3\rangle$	$\lvert 2, \frac{5}{2}, 3, -2\rangle$	$\lvert 2, \frac{5}{2}, 3, -1\rangle$	$\lvert 2, \frac{5}{2}, 3, 0\rangle$	$\lvert 2, \frac{5}{2}, 3, 1\rangle$	$\lvert 2, \frac{5}{2}, 3, 2\rangle$	$\lvert 2, \frac{5}{2}, 3, 3\rangle$
$\lvert 1, \frac{1}{2}, 0, 0\rangle$	0	0	0	0	0	0	0	0	0	0	0	0
$\lvert 1, \frac{1}{2}, 1, -1\rangle$	0.0002	8.10×10^{-5}	2.70×10^{-5}	0	0	0	0	0	0	0	0	0
$\lvert 1, \frac{1}{2}, 1, 0\rangle$	0	8.10×10^{-5}	1.08×10^{-5}	8.10×10^{-5}	0	0	0	0	0	0	0	0
$\lvert 1, \frac{1}{2}, 1, 1\rangle$	0	0	2.70×10^{-5}	8.10×10^{-5}	0.0002	0	0	0	0	0	0	0
$\lvert 1, \frac{3}{2}, 1, -1\rangle$	0.4699	0.2350	0.0783	0	0	0	0	0	0	0	0	0
$\lvert 1, \frac{3}{2}, 1, 0\rangle$	0	0.2350	0.3133	0.2350	0	0	0	0	0	0	0	0
$\lvert 1, \frac{3}{2}, 1, 1\rangle$	0	0	0.0783	0.2350	0.4699	0	0	0	0	0	0	0
$\lvert 1, \frac{3}{2}, 2, -2\rangle$	0.0367	0.0183	0	0	0	0.5235	0.1745	0.0349	0	0	0	0
$\lvert 1, \frac{3}{2}, 2, -1\rangle$	0.0183	0.0092	0.0275	0	0	0	0.3490	0.2792	0.1047	0	0	0
$\lvert 1, \frac{3}{2}, 2, 0\rangle$	0	0.0275	0	0.0275	0	0	0	0.2094	0.3141	0.2094	0	0
$\lvert 1, \frac{3}{2}, 2, 1\rangle$	0	0	0.0275	0.0092	0.0183	0	0	0	0.1047	0.2792	0.3490	0
$\lvert 1, \frac{3}{2}, 2, 2\rangle$	0	0	0	0.0183	0.0367	0	0	0	0	0.0349	0.1745	0.5235
$\lvert 3, \frac{5}{2}, 2, -2\rangle$	0.1386	0.0693	0	0	0	0.0117	0.0039	0.0008	0	0	0	0
$\lvert 3, \frac{5}{2}, 2, -1\rangle$	0.0693	0.0347	0.1040	0	0	0	0.0078	0.0062	0.0023	0	0	0
$\lvert 3, \frac{5}{2}, 2, 0\rangle$	0	0.1040	0	0.1040	0	0	0	0.0047	0.0070	0.0047	0	0
$\lvert 3, \frac{5}{2}, 2, 1\rangle$	0	0	0.1040	0.0347	0.0693	0	0	0	0.0023	0.0062	0.0078	0
$\lvert 3, \frac{5}{2}, 2, 2\rangle$	0	0	0	0.0693	0.1386	0	0	0	0	0.0008	0.0039	0.0117
$\lvert 3, \frac{5}{2}, 3, -3\rangle$	0.0120	0	0	0	0	0.1620	0.0540	0	0	0	0	0
$\lvert 3, \frac{5}{2}, 3, -2\rangle$	0.0040	0.0080	0	0	0	0.0540	0.0720	0.0900	0	0	0	0
$\lvert 3, \frac{5}{2}, 3, -1\rangle$	0.0008	0.0064	0.0048	0	0	0	0.0900	0.0180	0.1080	0	0	0
$\lvert 3, \frac{5}{2}, 3, 0\rangle$	0	0.0024	0.0072	0.0024	0	0	0	0.1080	0	0.1080	0	0
$\lvert 3, \frac{5}{2}, 3, 1\rangle$	0	0	0.0048	0.0064	0.0008	0	0	0	0.1080	0.0180	0.0900	0
$\lvert 3, \frac{5}{2}, 3, 2\rangle$	0	0	0	0.0080	0.0040	0	0	0	0	0.0900	0.0720	0.0540
$\lvert 3, \frac{5}{2}, 3, 3\rangle$	0	0	0	0	0.0120	0	0	0	0	0	0.0540	0.1620
$\lvert 3, \frac{7}{2}, 3, -3\rangle$	0.1787	0	0	0	0	0.0080	0.0027	0	0	0	0	0
$\lvert 3, \frac{7}{2}, 3, -2\rangle$	0.0596	0.1191	0	0	0	0.0027	0.0036	0.0045	0	0	0	0
$\lvert 3, \frac{7}{2}, 3, -1\rangle$	0.0119	0.0953	0.0715	0	0	0	0.0045	0.0009	0.0054	0	0	0
$\lvert 3, \frac{7}{2}, 3, 0\rangle$	0	0.0357	0.1072	0.0357	0	0	0	0.0054	0	0.0054	0	0
$\lvert 3, \frac{7}{2}, 3, 1\rangle$	0	0	0.0715	0.0953	0.0119	0	0	0	0.0054	0.0009	0.0045	0
$\lvert 3, \frac{7}{2}, 3, 2\rangle$	0	0	0	0.1191	0.0596	0	0	0	0	0.0045	0.0036	0.0027
$\lvert 3, \frac{7}{2}, 3, 3\rangle$	0	0	0	0	0.1787	0	0	0	0	0	0.0027	0.0080
$\lvert 3, \frac{7}{2}, 4, -4\rangle$	0	0	0	0	0	0.1852	0	0	0	0	0	0
$\lvert 3, \frac{7}{2}, 4, -3\rangle$	0	0	0	0	0	0.0463	0.1389	0	0	0	0	0
$\lvert 3, \frac{7}{2}, 4, -2\rangle$	0	0	0	0	0	0.0066	0.0794	0.0992	0	0	0	0
$\lvert 3, \frac{7}{2}, 4, -1\rangle$	0	0	0	0	0	0	0.0198	0.0992	0.0661	0	0	0
$\lvert 3, \frac{7}{2}, 4, 0\rangle$	0	0	0	0	0	0	0	0.0397	0.1058	0.0397	0	0
$\lvert 3, \frac{7}{2}, 4, 1\rangle$	0	0	0	0	0	0	0	0	0.0661	0.0992	0.0198	0
$\lvert 3, \frac{7}{2}, 4, 2\rangle$	0	0	0	0	0	0	0	0	0	0.0992	0.0794	0.0066
$\lvert 3, \frac{7}{2}, 4, 3\rangle$	0	0	0	0	0	0	0	0	0	0	0.1389	0.0463
$\lvert 3, \frac{7}{2}, 4, 4\rangle$	0	0	0	0	0	0	0	0	0	0	0	0.1852
$\lvert 5, \frac{9}{2}, 4, -4\rangle$	0	0	0	0	0	0.36×10^{-5}	0	0	0	0	0	0
$\lvert 5, \frac{9}{2}, 4, -3\rangle$	0	0	0	0	0	0.09×10^{-5}	0.27×10^{-5}	0	0	0	0	0
$\lvert 5, \frac{9}{2}, 4, -2\rangle$	0	0	0	0	0	0.01×10^{-5}	0.15×10^{-5}	0.19×10^{-5}	0	0	0	0
$\lvert 5, \frac{9}{2}, 4, -1\rangle$	0	0	0	0	0	0	0.04×10^{-5}	0.19×10^{-5}	0.13×10^{-5}	0	0	0
$\lvert 5, \frac{9}{2}, 4, 0\rangle$	0	0	0	0	0	0	0	0.08×10^{-5}	0.20×10^{-5}	0.08×10^{-5}	0	0
$\lvert 5, \frac{9}{2}, 4, 1\rangle$	0	0	0	0	0	0	0	0	0.13×10^{-5}	0.19×10^{-5}	0.04×10^{-5}	0
$\lvert 5, \frac{9}{2}, 4, 2\rangle$	0	0	0	0	0	0	0	0	0	0.19×10^{-5}	0.15×10^{-5}	0.01×10^{-5}
$\lvert 5, \frac{9}{2}, 4, 3\rangle$	0	0	0	0	0	0	0	0	0	0	0.27×10^{-5}	0.09×10^{-5}
$\lvert 5, \frac{9}{2}, 4, 4\rangle$	0	0	0	0	0	0	0	0	0	0	0	0.36×10^{-5}

Table B.12: Branching ratios for decays from mixed $\widetilde{J}' = 2$, $\widetilde{F}_1' = 5/2$ e-parity states $\left|\widetilde{J}', \widetilde{F}_1', F', M_F'\right\rangle$ (columns) in $B^3\Pi_1$ to states in $X^1\Sigma^+$ (rows).

Appendix C

Machine Drawings

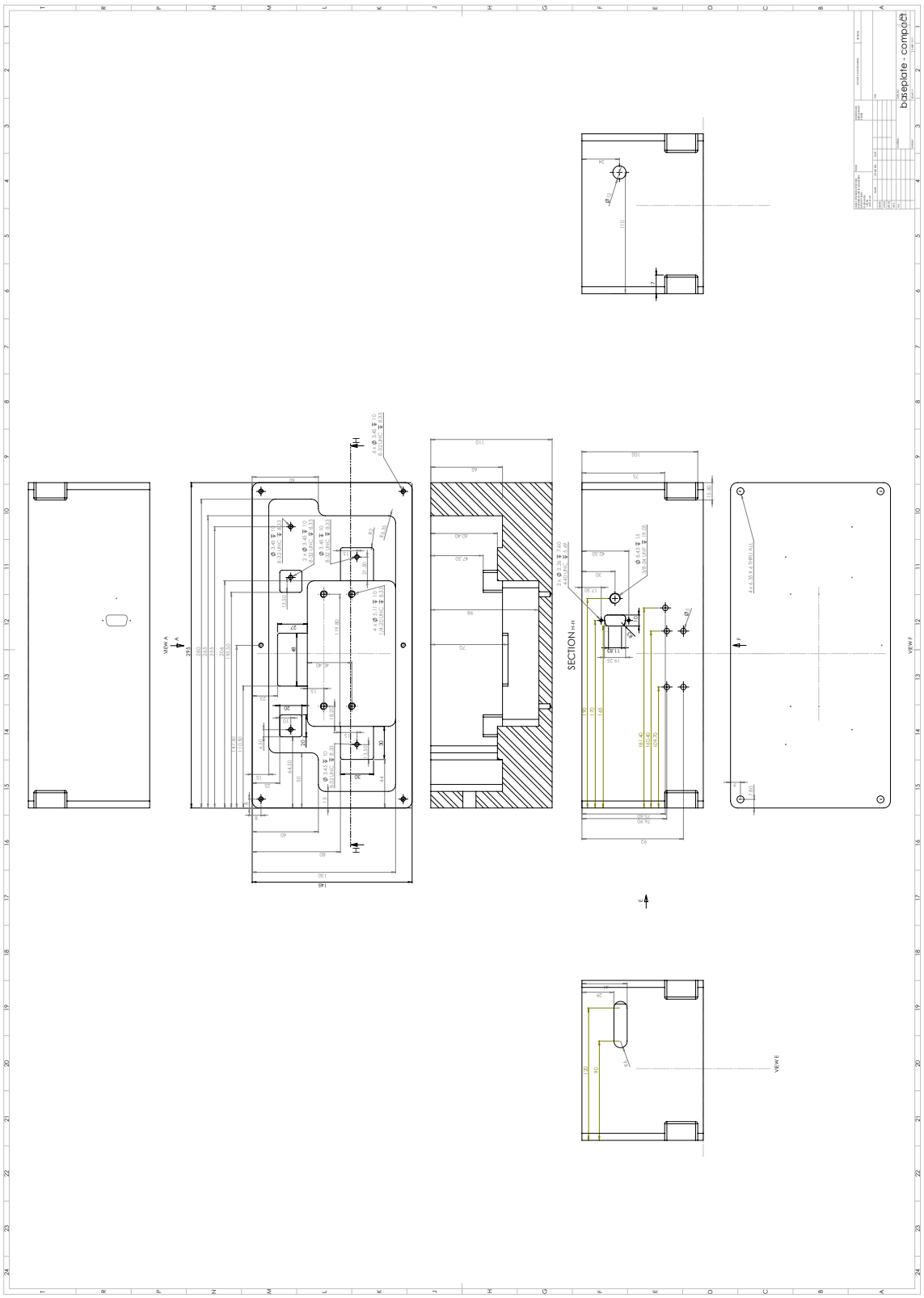

Figure C.1: Drawing of the first version of the second-harmonic generating resonant cavity.

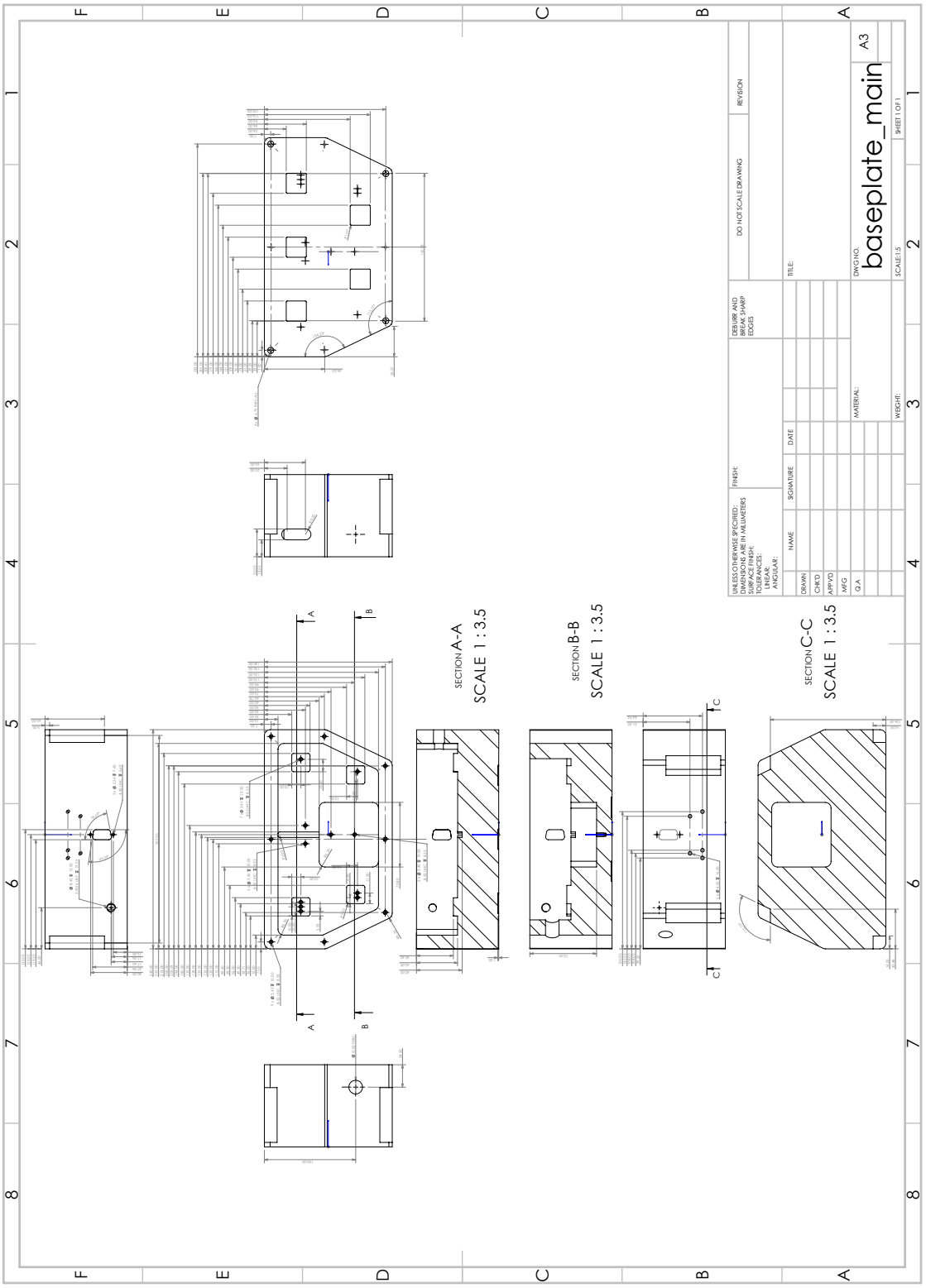

Figure C.2: Drawing of the second version of the second-harmonic generating resonant cavity.

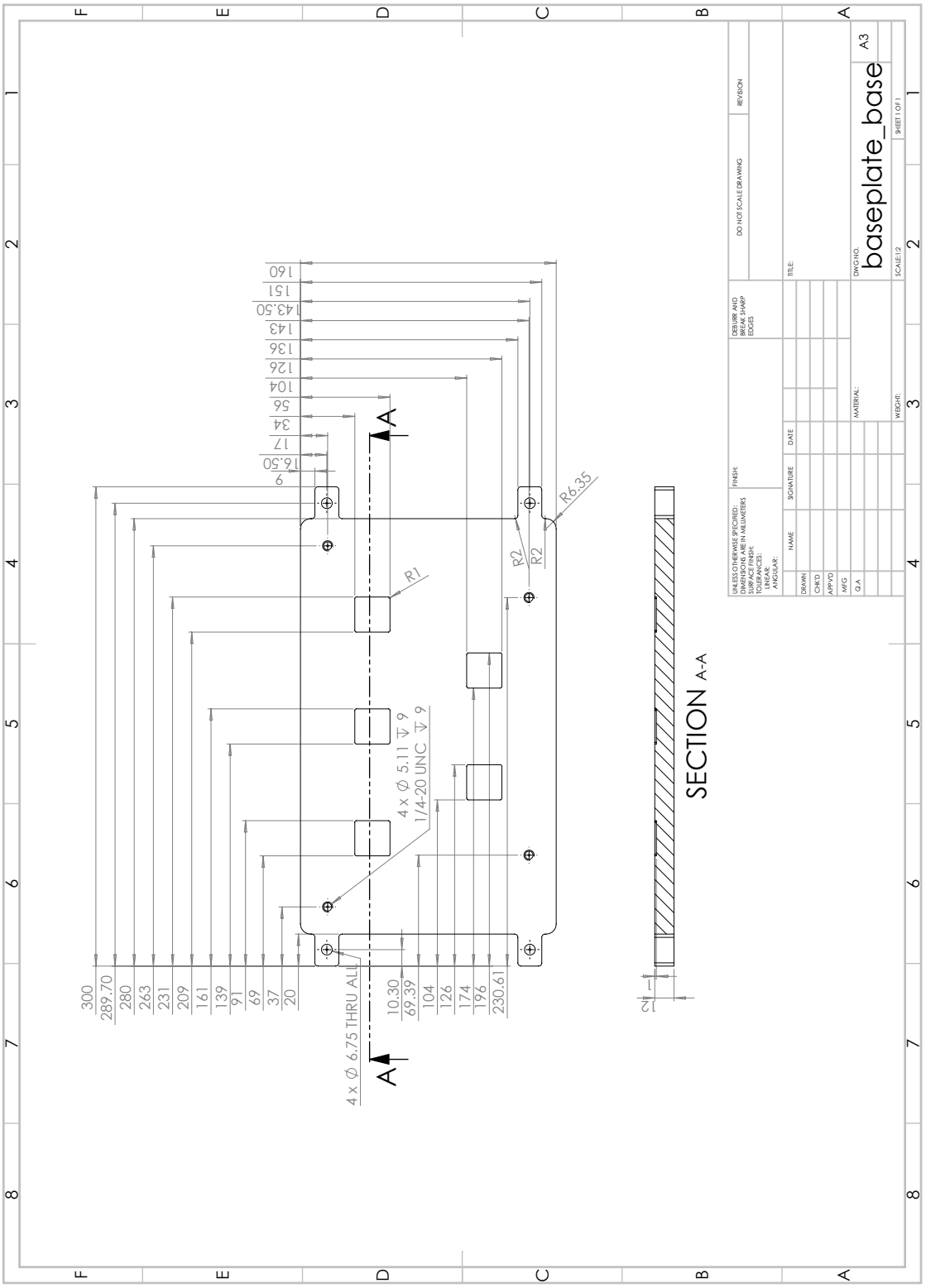

Figure C.3: Baseplate for the SHG cavity.

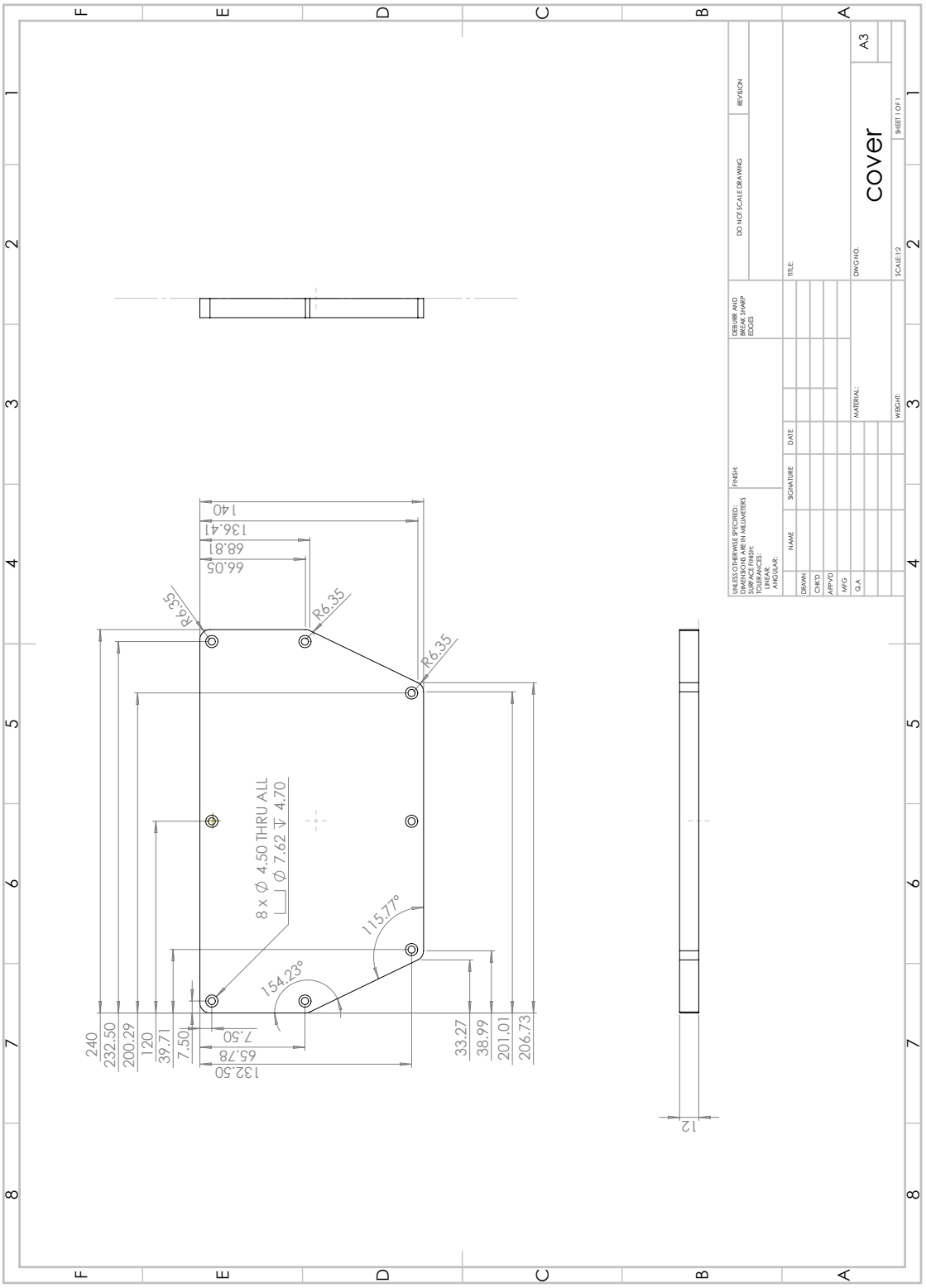

Figure C.4: Cover for the SHG cavity.

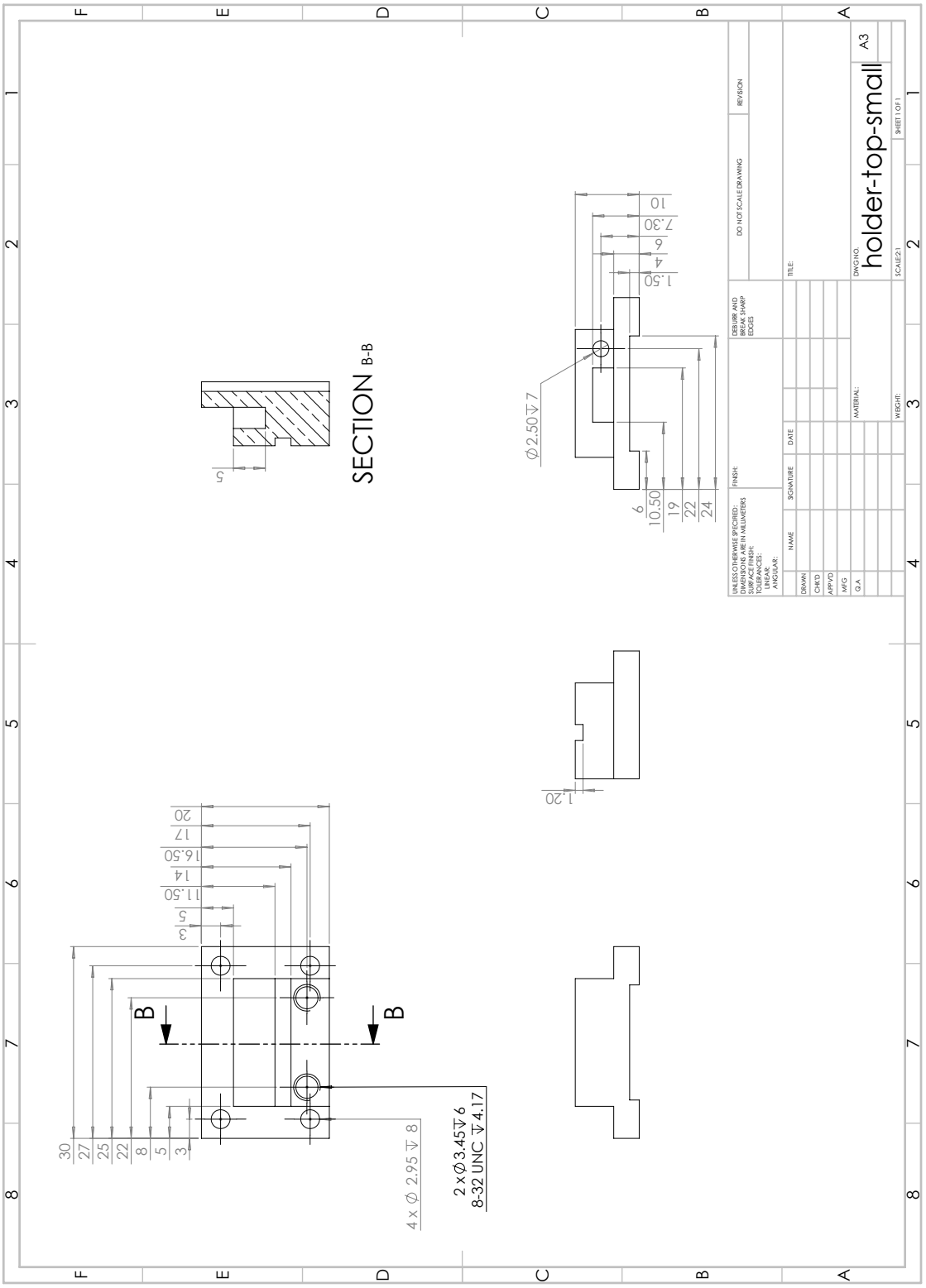

Figure C.5: KTP crystal holder.

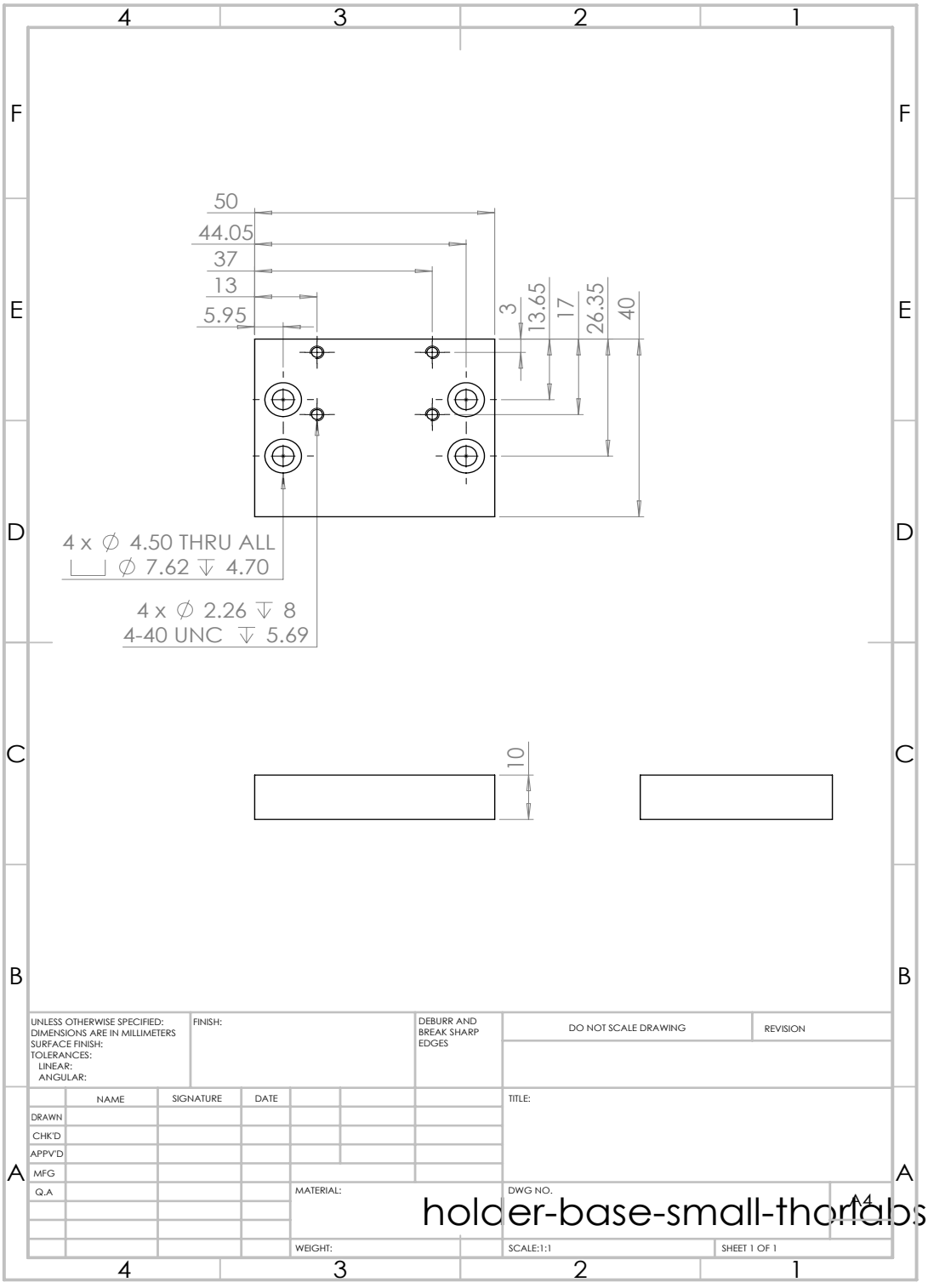

Figure C.6: Crystal holder base.

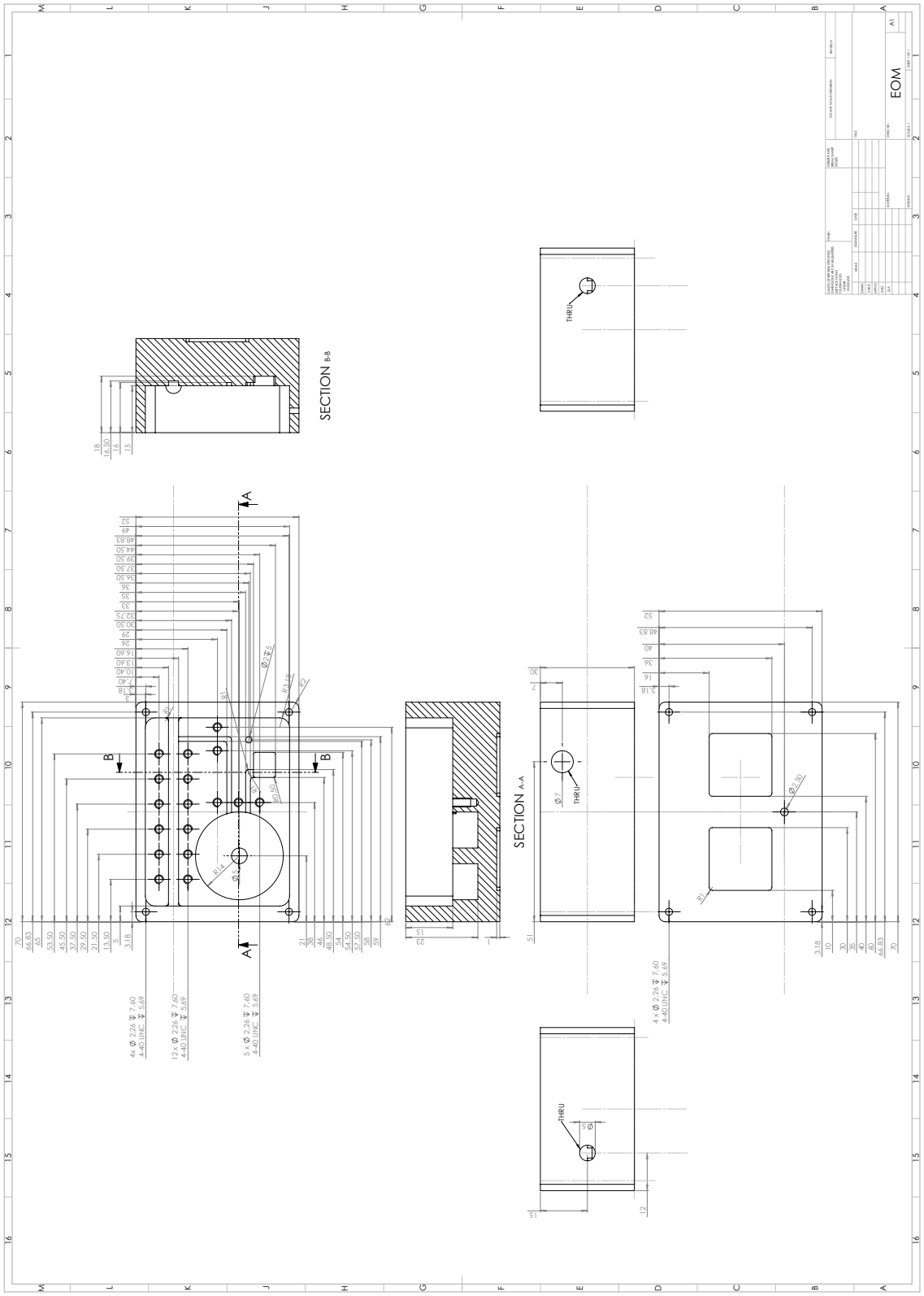

Figure C.7: Electro-optic modulator case.

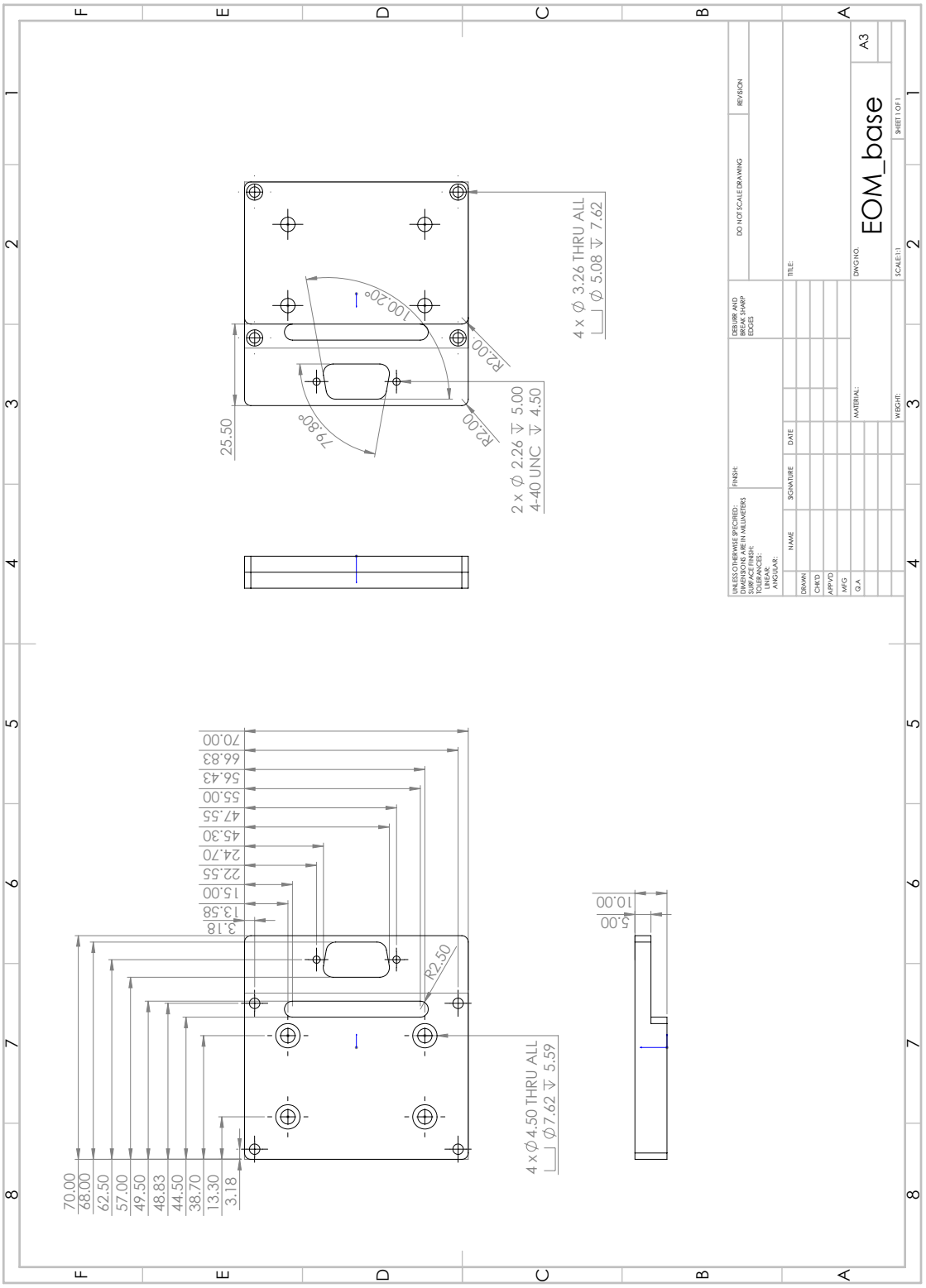

Figure C.8: Baseplate for the EOM case.

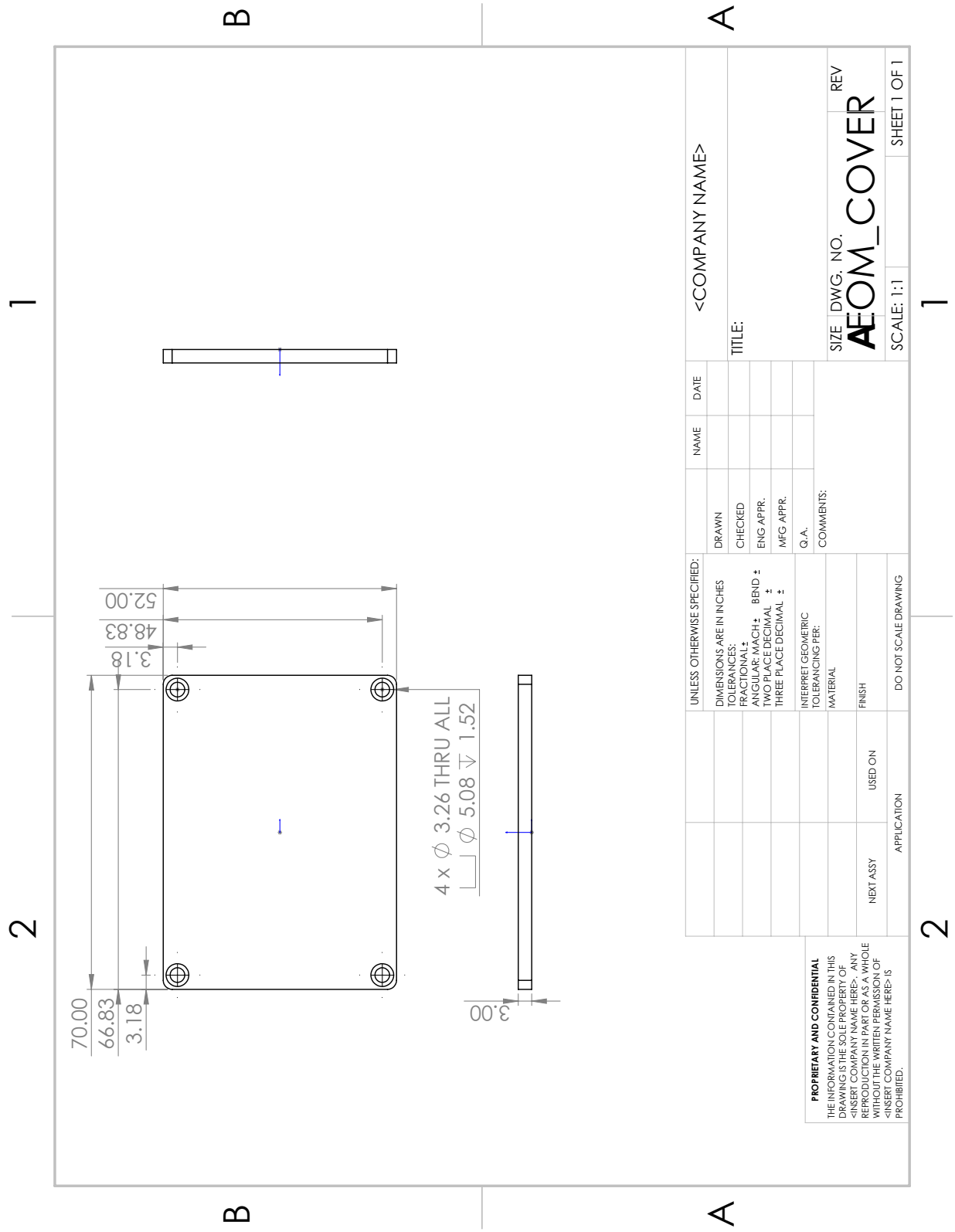

Figure C.9: Cover for the EOM case.